

Controlling drop morphology : theory, experiments and applications in printing, self-cleaning coatings and micro-fluidic systems

Citation for published version (APA):

Vrancken, R. J. (2012). *Controlling drop morphology : theory, experiments and applications in printing, self-cleaning coatings and micro-fluidic systems*. [Phd Thesis 1 (Research TU/e / Graduation TU/e), Chemical Engineering and Chemistry]. Technische Universiteit Eindhoven. <https://doi.org/10.6100/IR734491>

DOI:

[10.6100/IR734491](https://doi.org/10.6100/IR734491)

Document status and date:

Published: 01/01/2012

Document Version:

Publisher's PDF, also known as Version of Record (includes final page, issue and volume numbers)

Please check the document version of this publication:

- A submitted manuscript is the version of the article upon submission and before peer-review. There can be important differences between the submitted version and the official published version of record. People interested in the research are advised to contact the author for the final version of the publication, or visit the DOI to the publisher's website.
- The final author version and the galley proof are versions of the publication after peer review.
- The final published version features the final layout of the paper including the volume, issue and page numbers.

[Link to publication](#)

General rights

Copyright and moral rights for the publications made accessible in the public portal are retained by the authors and/or other copyright owners and it is a condition of accessing publications that users recognise and abide by the legal requirements associated with these rights.

- Users may download and print one copy of any publication from the public portal for the purpose of private study or research.
- You may not further distribute the material or use it for any profit-making activity or commercial gain
- You may freely distribute the URL identifying the publication in the public portal.

If the publication is distributed under the terms of Article 25fa of the Dutch Copyright Act, indicated by the "Taverne" license above, please follow below link for the End User Agreement:

www.tue.nl/taverne

Take down policy

If you believe that this document breaches copyright please contact us at:

openaccess@tue.nl

providing details and we will investigate your claim.

**Controlling drop morphology:
Theory, experiments and applications in printing,
self-cleaning coatings and micro-fluidic systems**

PROEFSCHRIFT

ter verkrijging van de graad van doctor aan de
Technische Universiteit Eindhoven, op gezag van de
rector magnificus, prof.dr.ir. C.J. van Duijn, voor een
commissie aangewezen door het College voor
Promoties in het openbaar te verdedigen
op maandag 18 juni 2012 om 16.00 uur

door

Robert Jan Vrancken

geboren te Heerlen

Dit proefschrift is goedgekeurd door de promotoren:

prof.dr. D.J. Broer
en
prof.dr. G. de With

Copromotor:
prof.dr.ing. C.W.M. Bastiaansen

A catalogue record is available from the Eindhoven University of Technology library

ISBN: 978-94-6191-324-1

Copyright © 2012 by Robert Jan Vrancken

Printed at: Ipskamp Drukkers, Enschede

Cover design by: Paul Verbunt and Robert Vrancken. Includes photographic image of art project States of Nature by Alex Vermeulen and Natuurkunst Foundation. Reproduced with permission.

The research described in this thesis has been financially supported by the research groups SFD and SMG of the Eindhoven University of Technology, as well as a RAAK-PRO grant from the SIA foundation (The Netherlands).

The real voyage of discovery consists not of seeking new landscapes, but of having new eyes.

Marcel Proust (1871 - 1922)

To my loved ones

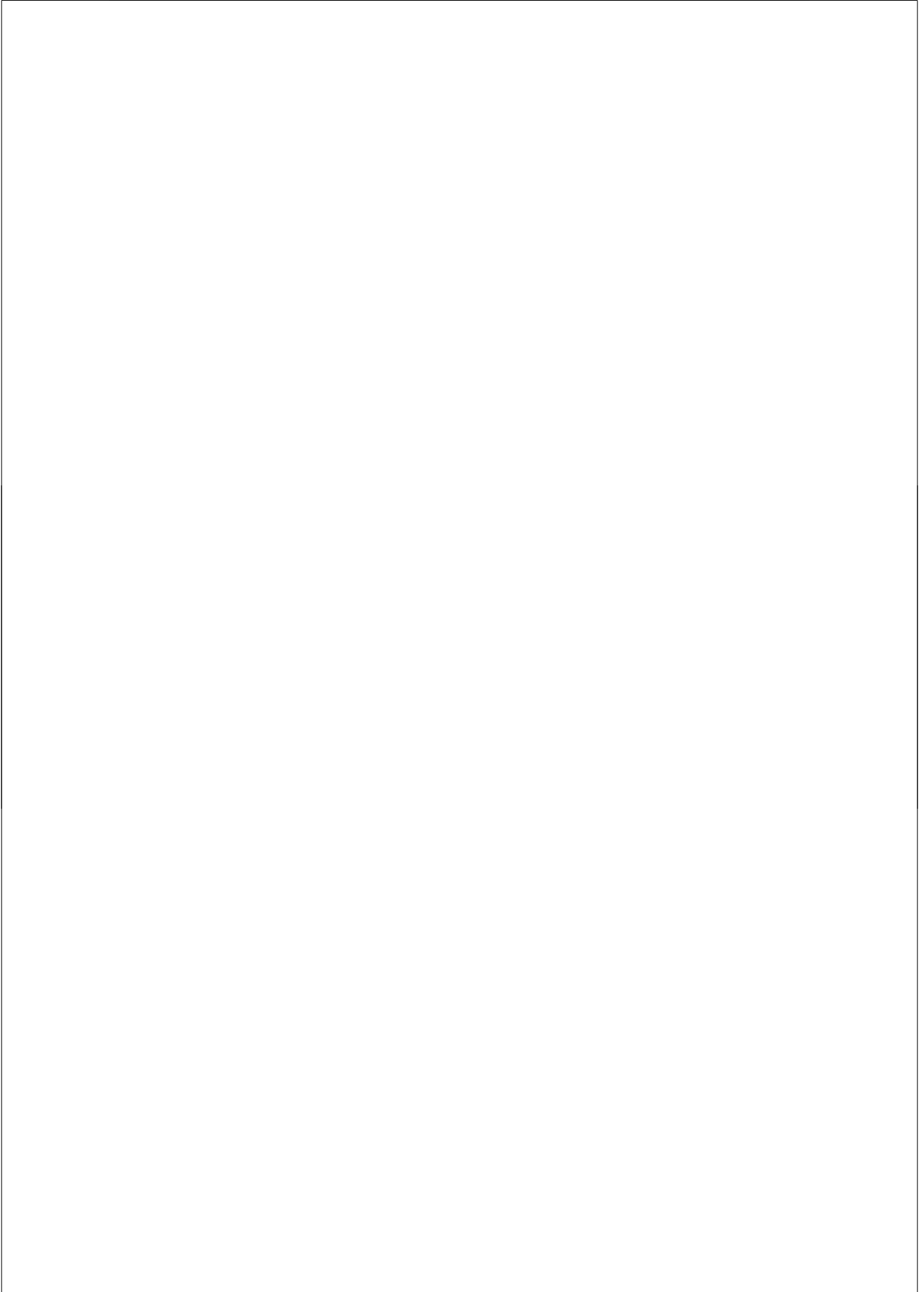


Table of contents

Table of contents	i
Summary	v
1. Introduction	1
1.1 Controlling drops of fluid.....	2
1.2 Applications of droplet control	3
1.2.1 Printing	3
1.2.2 Micro-fluidics.....	5
1.2.3 Smart functional coatings	6
1.3 Aim of the thesis	8
1.4 Structure of the thesis	8
2. Theory	11
2.1 Introduction.....	12
2.2 Thermodynamic definition of the system.....	12
2.3 Non-equilibrium conditions and hysteresis	13
2.4 Gibbs energy contributions.....	15
2.4.1 Bulk contributions	15
2.4.2 Interfacial contributions.....	16
2.4.3 Contact line contribution.....	17
2.5 Static interfacial energy models	18
2.5.1 Ideal surfaces and Young's equation.....	18
2.5.2 Laplace pressure	20
2.5.3 Surface discontinuities and Gibbs criterion.....	20
2.5.4 Wenzel equation.....	22
2.5.5 Cassie-Baxter equation.....	22
2.5.6 Gibbs energy calculations for isotropic drops and substrates	23
2.5.7 Wetting states, stability and transitions	27
2.6 Dynamic non-equilibrium models.....	28
2.6.1 Navier-Stokes equation.....	28
2.6.2 Lattice-Boltzmann simulations	29
2.7 Conclusions.....	32
3. Anisotropic drop morphologies on corrugated surfaces	33

3.1 Introduction.....	34
3.2 Experimental methods.....	35
3.3 Lattice Boltzmann simulation method	39
3.4 Anisotropic drop morphology on a corrugated surface	40
3.4.1 Experimental results.....	40
3.4.2 Simulation results.....	45
3.4.3 Discussion.....	47
3.5 Drops spreading on corrugated surfaces: understanding the contact angle measurements	47
3.5.1 Experimental results.....	47
3.5.2 Simulation results.....	50
3.5.3 Discussion.....	53
3.6 Conclusions.....	53
4. Drop shape analysis of contact printed thermotropic liquid crystal drops	55
4.1 Introduction.....	56
4.2 Theory.....	57
4.3 Experimental methods.....	59
4.4 Experimental results.....	60
4.5 Energy analysis	63
4.5.1 Two limiting cases of director profiles.....	63
4.5.2 Surface energy estimates	65
4.5.3 Bulk elastic energy estimate.....	66
4.5.4 Energy minimization via Lagrange multiplier method	67
4.6 Discussion.....	69
4.7 Conclusions.....	71
5. Fully reversible transition from Wenzel to Cassie-Baxter states on corrugated superhydrophobic surfaces	73
5.1 Introduction.....	74
5.2 Lattice Boltzmann simulation method	75
5.3 Simulation and theoretical results	76
5.4 Experimental methods.....	81
5.5 Experimental results.....	82
5.7 Discussion.....	85
5.7 Conclusions.....	86

6. Anisotropic wetting and de-wetting of drops on substrates patterned with polygonal posts.....	87
6.1 Introduction.....	88
6.2 Experimental methods.....	89
6.3 Advancing drop shape anisotropy.....	90
6.3.1 Experimental results.....	90
6.3.2 Simulation results.....	93
6.3.3 De-pinning mechanisms.....	94
6.3.4 Reproducibility of drop shapes from inkjet printing.....	95
6.3.5 Discussion.....	99
6.4 Receding contact line motion.....	99
6.4.1 Experimental results.....	99
6.4.2 Simulation results.....	101
6.4.3 Reproducibility of drop shapes from evaporation.....	101
6.4.4 De-pinning mechanisms.....	102
6.4.5 Discussion.....	105
6.5 Conclusions.....	105
7. Gibbs energy analysis of meta-stability of wetting states on dual-scale structured superlyophobic surfaces.....	107
7.1 Introduction.....	108
7.2. Hierarchical model.....	110
7.3 Single-sphere surfaces.....	116
7.3.1 Predicted wetting states and experimental comparison.....	116
7.3.2 State transitions and stability.....	119
7.3.3 Discussion.....	122
7.4 Dual-sphere surfaces.....	123
7.4.1 Wetting states and experimental comparison.....	123
7.4.2 State transitions and stability.....	126
7.4.3 Discussion.....	128
7.5 Conclusions.....	130
8. Technology assessment and future research.....	131
8.1 Introduction.....	132
8.2 Printing applications.....	132
8.3 Microfluidic devices.....	133

8.4 Superlyophobic / -lyophilic materials.....	134
8.5 Coalescence.....	135
8.6 Coffee ring effect.....	136
Appendix A: References	139
Appendix B: Nederlandse samenvatting	153
Appendix C: Acknowledgements.....	156
Appendix D: Curriculum Vitae	159
Appendix E: List of publications and patents	160
Appendix F: List of symbols	162

Summary

Controlling drop morphology: theory, experiments and applications in printing, self-cleaning coatings and micro-fluidic systems

The accurate control of drop morphology as a drop is placed on a solid surface is an important prerequisite in many applications, such as (inkjet) printing of functional materials, micro-fluidic devices and smart coatings. Carefully patterning the surface on micrometer length scales and combining this with controlled drop placement is shown to allow the creation a variety of drop morphologies in both simple and complex (liquid crystalline) fluids, which is an important parameter in the above-described fields of interest.

Starting from the governing thermodynamic equations determining the morphology of drops, the dominant energetic terms are identified for the different length scales of both the drop sizes and micro-structures in the substrate surface. For non-liquid crystalline fluids, these are gravitational potential energy, surface energy and contact line energy. To study the influence on the wetting behaviour on various patterned surfaces, the object of analysis was chosen to be a drop (or droplet) smaller than 1 mm in linear dimension. A combination of experiments, numerical modelling and theoretical analysis is used to explain the often-surprising drop shape morphologies and their dependence on the deposition method.

On surfaces patterned with parallel grooves (i.e. a corrugated surface), drops were found to elongate parallel to the grooves if the drops were deposited using a non-contact method, such as via inkjet printing or careful placement with a needle. However, if the drops were positioned in an overspread position (such as when pressed onto a surface with a contact printing technique such as micro-transfer printing), the drops elongate perpendicular to the corrugations. The key difference is that hysteresis due to contact line pinning is almost completely absent parallel to the corrugations and is present and significant perpendicular to them.

Microtransfer printing with nematic thermotropic liquid crystal monomers leads to similar perpendicular elongations under similar experimental conditions, even when the energetic contributions due to the alignment of the liquid crystal director favour elongation parallel to the corrugations in the direction of alignment.

Drops of water are shown to be able to exhibit a transition between two important wetting states by employing corrugated surfaces, combined with electrowetting and a high intrinsic contact angle of the surface. The transition from the collapsed (Wenzel) state to the suspended (also known as Cassie-Baxter) state was observed experimentally for the first time without having to heat the drop above the boiling point in order to lift it out of the

corrugations. The mechanism of this lifting transition is also investigated in detail with numerical simulations. The analysis shows that only under carefully chosen conditions, which require the elimination of contact line pinning, it is possible to have such a transition spontaneously without other forces such as vibration are employed.

The number of achievable morphologies of drops is extended to non-intuitive shapes such as octagons, hexagons, squares and quasi-triangular by employing surfaces patterned with micrometer sized posts. The modulation of the lattice according to which these posts are placed, as well as the shape of the posts itself, creates various drop shapes as the interface de-pins from the posts differently in different directions, also dependent on whether the drop is spreading or retracting. Experimental inkjet printing is combined with microscopy and numerical simulations to elucidate the local pinning of the interface.

An important application of smart coatings is self-cleaning materials in for instance windshields, textiles or ship hulls. Liquid repellent surfaces are a particular example with great industrial relevance. An analysis of the stability of the suspended drop states is presented by employing a recently created experimental surface containing raspberry-shaped silica particles covered with lyophobic polymers. By carefully studying the complex wetting states possible and the transitions between them, design rules for stable liquid repellent surfaces are derived. The method of analysis is generalised so that in the future further surfaces can be analyzed in similar fashion.

Finally, a number of new potential applications are discussed in a technology review, where also a view to future developments in the field is briefly discussed.

1. Introduction

“[...] he stretched out his arms towards the dark water in a curious way, and, far as I was from him, I could have sworn he was trembling. Involuntarily I glanced seaward – and distinguished nothing except a single green light, minute and far way, that might have been the end of a dock.”

- F. Scott Fitzgerald, “The great Gatsby”

1.1 Controlling drops of fluid

The Netherlands as a geographic region has a more than average interest in controlling fluids, as roughly one third of the country is located below sea level as shown in figure 1.1. The many terps, polders, dikes and canals are predominantly man-made structures that control water levels in order to insure the continued well-being of the Dutch people. From a macroscopic point of view, gravity is the dominant force that causes water to flow from high to low, i.e. from mountains to oceans. The tides are caused by the gravitational influence of the moon and sun, but these minor perturbations cannot change the essentially flat surface of water parallel to the horizon, neglecting of course the curvature of the earth. This flat surface is the energetic minimum configuration, and is intuitively understood from a young age.

Focussing on smaller length scales, the behaviour of liquids becomes more complex. Surface tension, which is not a bulk force but a surface ‘force’, creates the typically spherical form that people associate with liquid drops, such as rain drops or a drop of blood on the tip of a needle. If these drops become too big, they form ‘puddles’ (as used in the nomenclature of the field). These puddles are no longer spherical but flattened, due to the influence of gravity. When drops are small enough to be approximately spherical they are commonly referred to as ‘droplets’. At these length scales, surface tension and not gravity is the dominant force. Present research indicates that it is only at the nano-meter scale that other effects such as contact line tension could become dominant over the surface forces, excluding for the moment more exotic forces such as magnetism or bulk elastic forces.^{1,2}

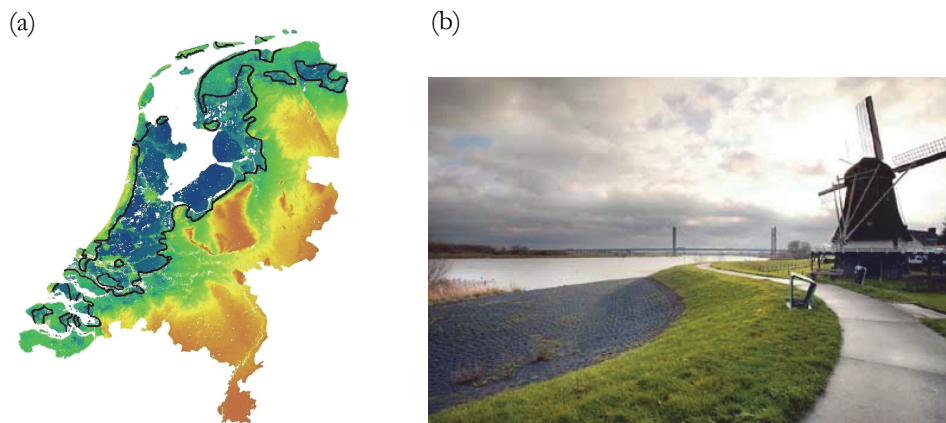


Figure 1.1: (a) Height map of The Netherlands where blue indicates the lowest lying areas and red the highest. The black height contour indicates which parts of the country are approximately below sea level.³ (b) Typical example of a Dutch dike, including a windmill which was used historically as a water pump to keep the lower lying polders dry.⁴

While gravity is the dominant factor determining the liquid morphology at larger length scales, phenomena at smaller length scales can also play an important role at the same time. For instance, the manner in which water saturates dikes or oppositely is drained from them can cause dangerous ruptures in the soil. This effect is predominantly driven by surface tension and not gravity. Whether your raincoat is permeated by water or repels it or whether your mirror fogs up when turning on the hot water faucet underneath it, are just a few more examples of microscopic phenomena which influence the macroscopic reality. In this thesis the object of analysis is the perhaps humble droplet of fluid on a structured surface, at a typical length scale of less than 1 mm and the implications of its behaviour at other length scales, which are sometimes immediate and sometimes more subtle. In many cases interesting new applications can arise from dealing with our surroundings one droplet at a time.

1.2 Applications of droplet control

1.2.1 Printing

The ability to quickly reproduce information by printing liquid inks on solid substrates was developed in the 15th century and was first used to print religious texts such as the Bible. Since then, a wide variety of printing processes have been developed, so that it is possible to print on almost any object. Printing has been used, for most of its history, only as a means to produce or multiply information like texts or graphics. The printing industry is now one of the largest industries worldwide, with over 460 billion Euro turnover annually (2009).⁵ Over time, printing techniques diversified including techniques such as letter press, intaglio printing, flexography, screen printing and more recently inkjet printing and micro-contact printing.⁶ An extension of micro-contact printing, called micro transfer printing was developed at the Eindhoven University of Technology.⁷⁻⁹ All these techniques have found their way into diverse markets, each having its particular strengths and weaknesses.

The common principle is that a liquid, the ink, is deposited on a solid substrate (for instance paper). Deposition is achieved as a thin film of liquid or as individual drops, depending on the technique. Although the way the image creation is achieved varies greatly, at the microscopic level the ink needs to be placed on the substrate in the desired way: not spreading too much or too little and only in the desired direction(s), optionally absorbing into the substrate while always adhering sufficiently. Absorption occurs only if the substrate is porous or permeable to the ink. The ink is typically a complex chemical formulation, containing pigments or dyes, solvents, binders (monomers or polymers), surfactants and also functional materials. The properties of the ink, such as viscosity, surface tension and drying behaviour have to be carefully optimized to achieve the desired result, and great industrial efforts have been spent on optimizing ink formulations. In that sense inks are closely related

to coatings, which are typically not patterned, although this is possible, in which case the distinction between both is only a matter of terminology. Efforts to optimize the surfaces to be printed on have so far been focused mostly on industrial properties such as manufacturability, cost, surface cleanliness and permeability. However, recent academic research focuses on locally modifying the geometry and chemical composition of the surface to enable new applications, which will be discussed further below.

An emerging field of interest in the printing industry is the use of printing techniques for manufacturing purposes (which sets this field apart from ‘traditional’ graphical printing). The products being manufactured by printing have industrial purposes beyond simply conveying graphical information. Typical examples are printed electronics,¹⁰ printed sensors and actuators,¹¹ printed DNA assays¹² and engineered tissues¹³ and the list of applications is growing fast. Key advantages when printing these products is the speed of production versus conventional production techniques, the low levels of waste as well as the flexibility of the printing process. While printing in some cases replaces existing less efficient production processes such as lithography, it also enables completely new applications. One of the most flexible technologies is inkjet printing, which combines additive (lossless) printing with digital capabilities, i.e. the ability to create new patterns for each new print / product. An ambitious goal that is being voiced in the industrial printing world is that in the future “anything that can be printed will be printed”.⁵

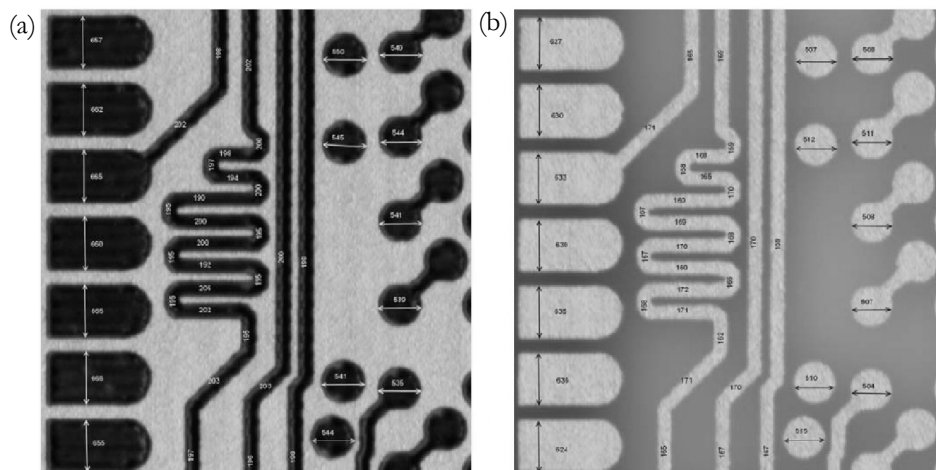


Figure 1.2: An example of extreme precision in droplet motion and flow. (a) Drops (dark areas) have been inkjet printed onto a copper PCB substrate. (b) The resulting conductive copper tracks after etching. In order to achieve the required conductivity and prevent shorts, all drops have to be printed and must stay on the print position with tolerances no greater than a few micrometers. Figure reproduced from ¹⁴.

Control of the printed patterns is for many industrial printing applications much more demanding than for graphical printing. A key challenge for instance in printed electronics is that the pattern is not interrupted anywhere (pattern fidelity), otherwise electrical contact is broken. Conversely, flowing together of structures where this is not intended creates electrical short circuits. An example is shown in figure 1.2. The impact of the printing technique (impact versus non-impact) on geometrically patterned surfaces is analyzed in chapter 3.

1.2.2 Micro-fluidics

Mainly due to the increase in micro-fabrication capabilities, interesting new applications have been developed in the field of micro-fluidics in the past decade.^{15,16} One example is lab-on-a-chip applications. Here, technologies initially developed for semi-conductor fabrication ('chips') are combined with chemical analysis ('lab'). A currently available example is a small disposable chip which can be inserted in a handheld glucose meter, which quickly and cost-effectively analyses the glucose level in the blood of an insulin patient, such as the One-Touch Ultra2^(tm) from LifeScan Inc. By combining inexpensive fabrication technology with easy-to-use chemical/biological analysis, healthcare costs are decreased while simultaneously increasing convenience for the patient, especially if patients are able to perform the analyses themselves.

Another important developing field is micro-reactors.¹⁷ The classical bulk approach to chemical manufacturing, involving large chemical plants, is not optimal for many applications. The large volumes that are concurrently processed mean that optimizing for processing conditions suffers from many practical trade-offs. Mixing of fluids, timing of the process, maximum achievable temperature change rates and many more process steps are limited in flexibility. Furthermore, large scale reactions have to be carefully controlled, as a run-away reaction can pose serious health and environmental risks. A solution to these problems is micro-reactors. Here, much smaller flows of fluid are batch or continuously processed, flowing through tight channels down to below 1 mm in diameter, depending on the application. This allows greater control over reaction parameters, parallelization driving down the minimum efficient scale of production and better safety control. However, cost-efficient production is only possible when the miniaturization of the equipment can be done efficiently.

A last example combines the two, namely micro-reactor-on-a-chip. Here, synthesis of for instance high value pharmaceuticals can sometimes be performed under precise conditions on a chemical 'reactor', not larger than a chip. The high value of the chemicals produced by such devices allows the expense of the chip.¹⁸

In these applications, liquids are typically in simultaneous contact with solids (catalysts)

and/or vapour phases, and flow batch-wise or continuously through these reactors. Controlling the wetting properties and flow mechanisms through surface control is an important tool in creating efficient micro-reactors. These flows are dominated by the surfaces and less by the bulk at these length scales. Challenges include the efficient propulsion of the fluids, especially when there is a mix of gas and fluid in the channels. An example is shown in figure 1.3. One topic being investigated to this end is the use of artificial flagellae, which can eliminate the need for external pumps or increased local mixing of multiple fluids within the channels.¹⁹

In a sense, the components available to electrical circuits on chips, such as e.g. voltage sources, delays, diodes, transistors and resistors inspire fluidic counterparts. Geometrical and chemical patterning of the surfaces in these micro-fluidic devices can help eliminate the need for external devices such as pumps. It can also increase the range of fluids that can be analysed. A number of surfaces which can inspire or form the basis of new micro-fluidic component are presented in chapters 3, 5 and 6, and their relevance is discussed in these chapters as well as summarized in chapter 8.

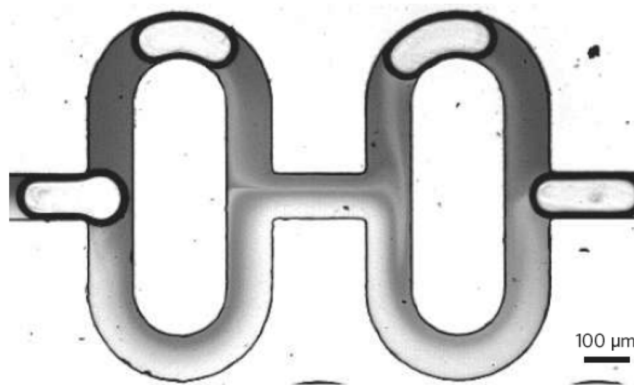


Figure 1.3: A micro-fluidic channel containing precisely measured ‘droplets’ of air (light areas), which help to efficiently mix an ink (dark fluid, top) with a surfactant (white fluid, bottom). Here, all three types of surfaces (solid-fluid, fluid-vapour and vapour-solid) are present. Reprinted by permission from Macmillan Publishers Ltd: Nature,¹⁵ copyright 2006.

1.2.3 Smart functional coatings

In the field of coatings, many academic and industrial efforts are devoted to improving the quality of existing coatings and extending their properties, as well as creating new applications with new functionality. Improving durability of coatings has been one important consideration in order to decrease overall costs and decrease the number of service intervals.

Simply put, nobody likes to paint his or her garden fence every year. One factor decreasing the lifetime and functionality of coatings is surface contamination. The simple sounding solution for this is self-cleaning or self-replenishing coatings. Inspired by nature, researchers have been active in artificially reproducing and adapting surfaces with such desirable properties found in plants and animals. These efforts are known as nature-inspired or biomimetic approaches.

A well known example of self-cleaning surface properties is found in the Lotus leaf,²⁰ as shown in figure 1.4(a). Its leaves are superhydrophobic, i.e. repellent to water. In this way, the leaves are not covered in water for long periods of time, and also when floating in a pond (its natural habitat), any dirt that accumulates on it is washed off periodically when it rains. This is crucial to capturing sufficient sunlight for photosynthesis. Smart surfaces with purposes other than self-cleaning have evolved in nature as well. For instance the water strider (a small insect) is capable of literally walking on water as it floats on the surface due to its water-repellent legs.²¹

The above mentioned Lotus leaf and the water strider legs both have a dual-scale structured surface, with the former having been mimicked successfully by raspberry-like particles, as shown in figure 1.4(b).^{22,23} Such dual-scale structuring is experimentally challenging to reproduce and there are considerable theoretical efforts underway to better understand the interactions such surfaces have with liquids drops or when submerged. In chapter 7 dual-scale structured surfaces are investigated in detail.

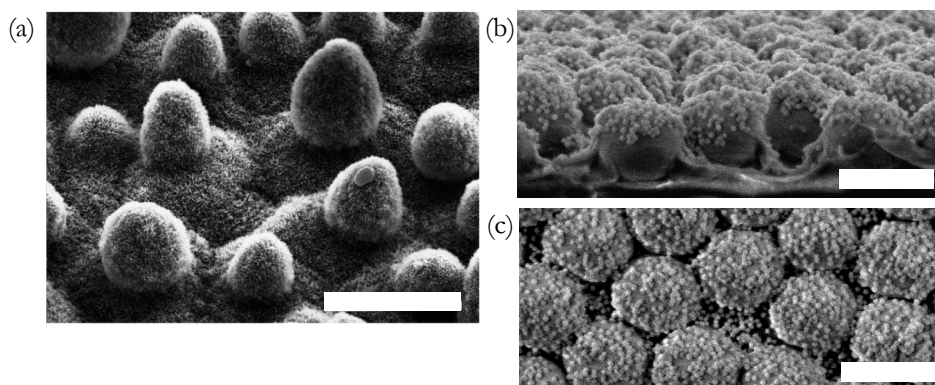


Figure 1.4. (a) SEM image of the lotus leaf, reproduced from ²⁰, showing the dual-scale structure. (b) SEM side view and (c) SEM top view of an artificially created biomimetic raspberry-like dual-scale structured surface, reproduced from ²³ with kind permission from Springer Science and Business Media; the larger first-layer particles ($d_1 \approx 700 \text{ nm}$) are covered by the second-level, smaller particles ($d_2 \approx 70 \text{ nm}$). Both surfaces exhibit superhydrophobicity due to their dual-scale roughness. The scale-bar in (a) corresponds to $20 \mu\text{m}$ and in (b) and (c) to $1 \mu\text{m}$.

Examples of applications for such surfaces are for instance self-cleaning textiles for domestic convenience or for use in dangerous environments, such as chemical spills. Other examples include low drag resistance ship hulls that decrease fuel consumption, or car windows from which the rain runs off much faster increasing visibility in poor weather conditions. One important consideration in all these examples is not only the functionality itself, but the durability of this functionality. Put more scientifically, the stability of the wetting states and the resulting drop morphologies, which will be analysed in chapters 4 and 6.

1.3 Aim of the thesis

Common challenges in the applications mentioned above deal with controlling the shape and location of the fluid (droplets) on the solid surface it interacts with. From the initial formulation of Young's equation in 1805,²⁴ describing the contact angle between a drop and the surface (defined in chapter 2), the morphology of droplets has been under constant debate. Experiments have shown that deviations from this straightforward equation are common. In fact, the drop morphology is highly dependent on the geometrical and chemical patterning of the surface the drop lies on. Furthermore, the way in which the drops are placed onto the surface influence the final stationary morphology as well. These deviations are commonly categorized as hysteresis, the understanding that the final shape of a drop is determined by both its initial shape and the evolution of this shape. In that sense, there is not necessarily a single 'equilibrium' shape, and multiple meta-stable equilibria can exist. The evolving morphology is continuously influenced by the local surface conditions that the fluid-vapour interface encounters as it moves over the surface. Therefore, a static analysis of forces or energy does not suffice.

The aim of this thesis is to investigate a number of approaches to combine drop placement methods (such as inkjet printing, micro-transfer printing) with specifically structured surfaces in such a way that control over the final droplet morphology and its stability can be achieved. Experiments, theoretical analysis and Lattice-Boltzmann numerical modelling are combined in both static and dynamic analyses. Specific attention is given to the motion (pinning and de-pinning) of the contact line, the different wetting states and the (meta-) stability of these states and morphologies. The aim is to examine the usability and limitations of the various structures as well as the research methods themselves, with a view to practical applications.

1.4 Structure of the thesis

The relevant theoretical background needed to interpret the results in this thesis is presented

in chapter 2, which serves as starting point for the subsequent investigations. First, the governing thermodynamic definition of the system is presented. From this, the relevant Gibbs energy terms are derived and simple models which are currently receiving considerable attention in the literature are presented. A lattice-Boltzmann numerical model that is frequently used in the subsequent chapters is also described.

In chapter 3, a number of fluids are deposited on corrugated surfaces (i.e. having parallel grooves and ridges in one direction), and it is shown that depending on the initial state of the drop, related to the printing technique applied (inkjet printing versus micro-transfer printing), the drop can become elongated either parallel or perpendicular to the corrugations. This unexpected result of contact angle hysteresis and breaking of the radial symmetry due to the surface serves as a good starting point to consider more advanced surface patterning.

One particular example of this elongation with practical relevance is investigated in chapter 4 for printed thermotropic nematic polymerisable liquid crystals on corrugated surfaces. It is shown that the elastic energy that is inherent to liquid crystal order, favours elongation parallel to the corrugations (which is the alignment direction). However, due to the contact printing method employed, the overall liquid crystal drops are still elongated perpendicular to the corrugations.

In chapter 5, similar corrugated substrates, coated with a fluorinated PTFE hydrophobic coating, are studied during electrowetting to make the surface temporarily much more hydrophilic to water drops. During electrowetting, the air vapour that is entrapped under the drop is pushed out, which leads the drop to go from a suspended to a so-called collapsed wetting state, which normally persists after removal of the applied voltage. For the first time, it is demonstrated experimentally that the reverse transition back from the collapsed to the suspended wetting state can spontaneously occur after removal of the voltage, and that this reverse transition is only possible under specific geometrical and energetic conditions. Since the suspended state is superhydrophobic and the drop is therefore very mobile, this reverse transition shows that simple removal of drops from a surface is possible.

In chapter 6, surfaces covered with periodic arrays of microscopic pillars are prepared, on which drops are deposited with considerable impact energy by means of inkjet printing. By changing both the lattice type arrangement of these pillars as well as the shape of the pillars to different polygons, it is shown that the drops can spread to a large number of geometrical shapes, such as squares, octagons, hexagons and triangles. Pinning and de-pinning of the contact line is observed and modelled to accurately investigate the various mechanisms of pinning, for both advancing and receding motions of the contact line. The predicted shapes of single inkjet-printed drops are observed experimentally even for very small (200 pl) and quickly evaporating water drops.

In chapter 7, a theoretical study of the stability of the different wetting states of single- and dual-scale structured surfaces is presented. One particular raspberry structure, which is a biomimetic counterpart of the Lotus leaf surface structure, is analysed in detail. Since potential applications depend crucially on the stability of this superhydrophobic state, a detailed analysis of the (meta-) stability of the different states is presented, and it is shown that these states cannot be considered simply in terms of suspended or collapsed: intermediate states are also possible, which causes an increase in possible wetting state transitions as well. The model results are compared in detail to experimental observations.

In chapter 8, the findings of the previous chapters are presented in a technology review. This also serves as a conclusion to the work and an outlook on potential future developments.

2. Theory

“There were many seas. The sea roared like a tiger. The sea whispered in your ear like a friend telling you secrets. The sea clinked like small change in a pocket. The sea thundered like avalanches. The sea hissed like sandpaper working on wood. The sea sounded like someone vomiting. The sea was dead silent.”

- Yann Martel, “Life of Pi”

2.1 Introduction

This chapter presents an overview of the main theories and models used to determine the morphology of liquid drops on a solid substrate. It summarizes the relevant theoretical background as it is known in the field, but presents no original research. The purpose of the chapter is therefore to enable the reader who is not familiar with the fields of soft matter physics and wetting science to be able to interpret the results presented in the following chapters. Readers familiar with the field may find this chapter useful to find the relevant definitions and assumptions used in this thesis.

Following a thermodynamic definition of the system in section 2.2, the phenomenon of drop shape hysteresis is discussed in 2.3. The contributions to the overall Gibbs energy of the system are systematically described in 2.4. A number of commonly employed simplifications relating the drop shape geometry to the Gibbs energy (static models) are presented in section 2.5, including a detailed discussion of equilibria, wetting states and stability of these states. In section 2.6, dynamic aspects of drop morphology are discussed including hydrodynamic effects, as well as several numerical techniques to model drops, focussing primarily on a particular lattice-Boltzmann model which will be used frequently in this thesis. The chapter ends with a brief conclusion in section 2.7. The mathematical symbols used throughout this thesis are presented for reference in appendix F.

2.2 Thermodynamic definition of the system

The model system is a drop of liquid on a solid incompressible surface, surrounded by a vapour phase, as depicted schematically in figure 2.1. The three phases are solid s , liquid l and vapour v , and are referred to as such in the subscripts. The phase boundaries are the solid-liquid interface with area Ω_{sl} , the liquid-vapour interface with area Ω_{lv} and the three-phase line L , commonly called the contact line, where the three phases meet. The substrate beyond L is Ω_{sv} , where the solid and vapour phases are in contact. The liquid has volume V defined as the volume enclosed by Ω_{sl} and Ω_{lv} , and constant on the timescales under consideration. This means that there is no evaporation of the liquid and the pressure in the vapour phase is constant. The constant volume constraint also implies constant mass M of the liquid phase, or more precisely a constant number of molecules n . The system is in thermal contact with its surroundings (the solid and vapour phases extend far beyond the drop size). Since the drop and surface are small compared to the dimensions of the surroundings with which it is in thermal contact, the temperature can be assumed constant throughout the system. It is therefore common and convenient to choose to evaluate the Gibbs energy G for this system (i.e. considering a system with constant temperature T , pressure p and number of molecules n).^{25,26} The chemical compositions of the drop and

solid surface also do not vary in time. The Gibbs energy is also known as the Gibbs free energy or the free energy, but here it shall be referred to only as the ‘Gibbs energy’ or ‘energy’. However, other choices, such as the Helmholtz (‘free’) energy, would also be correct in most cases treated in this thesis, and in literature reference is often made simply to the free energy of the system.

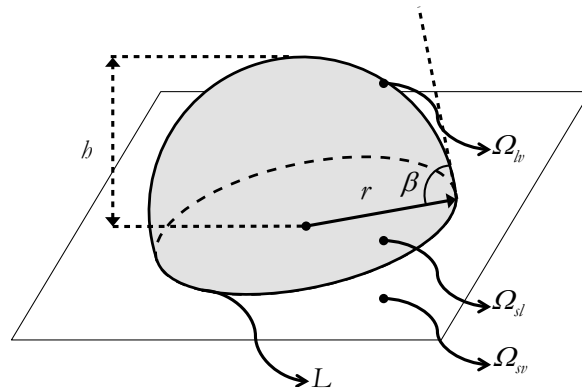


Figure 2.1: Quasi-3D view of a drop resting on a surface. The height h , the contact angle β and the radius r are indicated. Also indicated are the contact line (three-phase line) L , and the three interfaces Ω_{sv} , Ω_{sl} and Ω_{lv} . Note that the drop here has an idealized circular contact line and spherical cap shape for illustration purposes only.

There are in general three types of Gibbs energy contributions to this system: bulk contributions, interfacial contributions and contact line contributions. The total energy will be minimised in the global equilibrium drop morphology. The total energy can thus be summed as

$$G_{total} = G_{bulk} + G_{interfaces} + G_{line}. \quad (2.1)$$

In the following sections all energetic terms are presented in integral form, but first the possibility of deviations from thermodynamic equilibrium and their consequences are described.

2.3 Non-equilibrium conditions and hysteresis

An ideal, unperturbed droplet system will eventually be in a state of global equilibrium at its lowest energetic configuration, regardless of initial configuration. If the minimum energy can be calculated, given that all the relevant terms are taken into account and the system has enough time to reach equilibrium, one can determine the final state the system will be in.

This makes it possible to determine *a priori* which state the system will be in even though the system is perturbed by some means at a previous time or if it is prepared initially in a non-equilibrium state. There are however in reality many deviations from this ideal system. For instance there is always thermal and mechanical excitation unless extreme precautions are taken. Furthermore, not all allowable states may be reachable with equal probability or there are energetic barriers between the states that cannot be overcome by the energy available in the system. Also, the time needed to reach equilibrium may be too large compared to actual experimental observations. These deviations collectively manifest themselves in the present system as drop shape hysteresis, where the static state (morphology) of the system depends critically on its past states.¹ At a given static configuration, the *observed* contact angle β is as defined in figure 2.1. It is important to note that the observed contact angle β is not necessarily the same as the intrinsic contact angle δ as defined below.

From experimental practice it is well-documented that drops on a surface exhibit such morphological hysteresis.^{27–34} A particular type of hysteresis is commonly observed when forcing a drop to advance over the surface to cover a previously uncovered part of that surface (i.e. advancing motion of the contact line). This forced quasi-static motion can be induced by slowly adding liquid to the drop by means of an inserted syringe (advancing contact line). The liquid-vapour interface will be shaped differently than when the contact line moves the other way and uncovers part of the previously covered surface (receding motion), by quasi-statically removing liquid via the same syringe. When considering advancing and receding drop interfaces on a surface, a common practical measure of this hysteresis is the deviation of the macroscopic contact angle. In this case, the observed contact angle β varies when performing an experiment comparing advancing and receding motions. This hysteretic behaviour is defined as

$$\beta_h = \beta_a - \beta_r \geq 0, \quad (2.2)$$

i.e. the contact angle hysteresis is calculated by subtracting the advancing (β_a) and receding contact angles (β_r). It is therefore important to note that depending on the way a drop is placed or formed on a surface, its observed contact angle β can vary between β_a and β_r and is therefore not well defined.

It has been found that all of the following phenomena in part can account for contact angle hysteresis: contact line pinning due to surface roughness, chemical surface heterogeneity, asymmetric adsorption and desorption of liquid molecules from the surface and pre-wetting films of one or several molecular layers extending far beyond the observable drop close to the surface.²

Even while considering hysteresis, equilibrium energy calculations are still justifiable as an approximate analytical tool to gain understanding of liquid drops, as these calculations do indicate the shape the drop would *prefer* to be in. Equilibrium calculations are therefore in

common use¹ to predict many aspects of the system, including its morphology. However, in many cases non-equilibrium calculations are required, which can be quasi-static (treated in section 2.6) or dynamic (treated in section 2.7).

2.4 Gibbs energy contributions

2.4.1 Bulk contributions

The bulk contributions to the total energy of the system in the liquid phase are the gravitational energy and the intra-molecular interactions. The gravitational potential energy contribution of the liquid is

$$G_g = \sum_i^n m_i g z_i = \rho \sum_i^n z_i \Delta V_i = \rho g \iiint z dV. \quad (2.3)$$

Here the summation over individual molecules is replaced by a continuous integral and with ρ the fluid density (assumed constant throughout the liquid) and $g = 9.81 \text{ ms}^{-2}$ is the earth gravitational acceleration. As the total energy will be minimal at equilibrium, only the relative energy as function of drop shape has to be considered, and an arbitrary zero energy position can be chosen freely. Therefore, the location of $z = 0$ can be freely chosen at the solid surface, indicating that if the drop completely wets the surface (and in effect spreads to a mono-layer), this is considered as a state without potential energy.

There is also an internal energy contribution due to intra-molecular interactions.²⁵ However since n is assumed constant here, any net energy fluctuations due to this internal energy will only occur if molecules are so near to the surface that they experience a lack of attraction to other molecules 'missing' beyond the interface. However this remaining net energy is defined as the interfacial energy described in the next section, and is not a bulk term. With this common definition, the interaction energy in the bulk is in fact constant in time, and can be disregarded. By the same reasoning, bulk contributions to the other phases (solid, vapour) are also constant, so do not need to be considered.

In order to assess the relevance of gravity, a common measure in use is the capillary length, which expresses a ratio between gravity versus interfacial energy contributions. The capillary length is defined as

$$L_{cap} = \sqrt{\frac{\sigma_{lv}}{\rho g}}, \quad (2.4)$$

with σ_{lv} the liquid-vapour interface surface tension, which is formally defined in the next subsection. The common interpretation is that if the dimensions of the drop exceed the capillary length, the shape is dominated by the gravitational energy term and forms puddles, whereas if the dimensions are smaller, interfacial terms dominate and the drops form droplets, i.e. having an approximately spherical cap shape, as discussed in chapter 1. The dimensionless equivalent of the capillary length is the Bond number, presented here for a gravitational body force: $Bo = (\rho g L^2) / \sigma_{lv}$, where gravity dominates if $Bo > 1$, although for convenience and convention the capillary length is more often used. For water, with $\sigma_{lv} = 72 \text{ mJm}^{-2}$, $L_{cap} \approx 2.7 \text{ mm}$.

2.4.2 Interfacial contributions

The interfacial energies σ_{ij} are defined as

$$\sigma_{ij} = \left(\frac{\partial G}{\partial \Omega_{ij}} \right)_{T,p,n}, \quad (2.5)$$

for all interfaces ij and where the subscripts T, p, n refer to the constant temperature, pressure and number of molecules. The total interfacial energy contribution is then a straightforward summation

$$G_{interfacial} = \sigma_{lv} \Omega_{lv} + \sigma_{sl} \Omega_{sl} + \sigma_{sv} \Omega_{sv}. \quad (2.6)$$

A further simplification follows if it is considered that the change in solid-vapour and solid-liquid areas are always equal but of opposite sign, so that an equivalent and more practical definition of (2.6) is

$$\Delta G_{interfacial} = \sigma_{lv} \Omega_{lv} + (\sigma_{sl} - \sigma_{sv}) \Omega_{sl} \quad (2.7)$$

where the absolute solid-vapour interface area is removed from the equation, and only the relative Gibbs energy term is now considered.

Although σ_{sl} is formally defined by equation (2.5), the nature of the energetic interactions between the solid and liquid phases is still not fully understood. These interactions are typically grouped into two contributions: dispersive and polar, where the dispersive part is considered to be due to London-van der Waals induced-dipole-induced-dipole attractive interactions, and the polar part due to the various polar non-covalent interactions, such as dipole-dipole, dipole-induced-dipole and Lewis acid-base interactions.³⁵ Owens and Wendt³⁶, Rabel³⁷ and Kaelble³⁸ independently proposed a method (now known

as the OWRK method) to calculate the solid-liquid surface energy. The starting assumption is that surface energies consist only of dispersive and polar contributions, i.e.:

$$\sigma_{lv} = \sigma_{lv}^D + \sigma_{lv}^P \quad \text{and} \quad \sigma_{sv} = \sigma_{sv}^D + \sigma_{sv}^P \quad (2.8)$$

The interaction energy σ_{sl} is then calculated as

$$\sigma_{sl} = \sigma_{lv} + \sigma_{sv} - 2 \left(\sqrt{\sigma_{lv}^D \cdot \sigma_{sv}^D} + \sqrt{\sigma_{lv}^P \cdot \sigma_{sv}^P} \right). \quad (2.9)$$

Combining (2.9) with Young's equation (2.13) as described below leads to

$$\cos \delta = -1 + \frac{2}{\sigma_{lv}} \left(\sqrt{\sigma_{lv}^D \cdot \sigma_{sv}^D} + \sqrt{\sigma_{lv}^P \cdot \sigma_{sv}^P} \right) \quad (2.10)$$

By determining the intrinsic contact angles δ of two probe liquids with known dispersive and polar contributions to their respective σ_{lv} 's it is possible to determine both σ_{sv}^D and σ_{sv}^P for a given surface. With these surface parameters known it is possible to calculate δ and σ_{sl} of the surface for all other liquids with known dispersive and polar contributions. Care has to be taken that these calculations are at best approximations which work best when comparing liquids from specific classes (alcohols, linear alkanes, etc.) on a specific surface. If the liquid reacts chemically with the surface, the method is not applicable.

2.4.3 Contact line contribution

The edge of the drop on the surface is referred to in literature interchangeably as the contact line, three-phase line or the phase triple-point, as all three phases meet at this edge. The three-phase line boundary L_{slv} also adds a non-zero contribution to the energy of the system, which can be defined as an integral over length L as

$$G_{line} = \int_L A(\mathbf{x}) d\mathbf{x}, \quad (2.11)$$

where the contact line tension $A(\mathbf{x})$ (units Jm^{-1}) is a variable of the position of the contact line \mathbf{x} on the surface.³⁹ The magnitude and sign of this line energy can in principle be positive or negative depending on the system. This is fundamentally different to the interfacial energy, which can only be positive, due to the fact that negative interfacial energies would lead to an increase in surface area, effectively mixing the phases until no separate phases can be distinguished. Therefore no stable thermodynamic equilibrium states can exist

with negative interfacial energies. This problem does not occur with line energies, as a preferred reduction of the contact line does not necessarily lead to a disappearance of phases, and a stable equilibrium can exist. The sign and magnitude of $\mathcal{A}(\mathbf{x})$ depends locally on the geodesic curvature of the surface, assuming no discontinuities in the derivatives $\delta \mathbf{x}$ of the surface. Discontinuities are discussed in more detail in the next section.

A characteristic length scale comparing contact line energy to surface energy can be defined as

$$L_{\mathcal{A}} = \frac{\mathcal{A}}{\sigma_{lv}}. \quad (2.12)$$

Taking characteristic values for \mathcal{A} for water of 10^{-11} to 10^{-10} Jm^{-1} (experimental)³⁹ and 10^{-11} Jm^{-1} (theoretical),²⁵ it is found that $L_{\mathcal{A}} \approx 1 \text{ nm}$. Thus, the energy contribution of a line is comparable to that of a surface on the length scales of a drop that contain comparable numbers of molecules on the interface as on the contact line. Therefore, contact line energy terms can be disregarded under normal circumstances.

2.5 Static interfacial energy models

As described in section 2.2, when considering a system that exhibits hysteresis, only non-equilibrium calculations can predict the correct drop behaviour as multiple drop shapes are possible. However, with an equilibrium approach a great number of common simplifications can be made. In this section a number of these simplified theories are presented in order of increasing complexity. They all have a similar appearance in that they predict the observed contact angle and drop base diameter directly from the (interfacial) energy contributions, often disregarding gravity. These predicted parameters are also the two main geometric observables of the drop morphology which can easily be determined in simple experiments.

2.5.1 Ideal surfaces and Young's equation

The standard equation for relating surface energies to contact angles was formulated first by Young in 1805.²⁴ Assuming equilibrium, an ideally smooth surface and disregarding any other energetic contributions, the equation expresses the relationship between contact angle and surface energies.

$$\cos \delta = \frac{\sigma_{sv} - \sigma_{sl}}{\sigma_{lv}}. \quad (2.13)$$

Here, δ is called the *intrinsic* contact angle, which will only be equal to the *observed* contact angle β in case of an ideally flat and chemically homogeneous surface. When however there is any surface roughness or chemical heterogeneity, β can deviate substantially from δ . These deviations will be further detailed in the following sections and are a key topic in the remainder of this thesis as well as of ongoing academic interest. Equation (2.13) can be derived by considering an energetic minimum for a drop with a spherical geometry freely moving to its equilibrium on an ideally smooth surface. It is also possible to derive Young's equation from a mechanical point of view as a force balance. The exact derivations can be found in several textbooks.^{1,35,40} Both derivations of Young's equation can be performed locally at the contact line for an infinitesimal movement of the contact line $\delta \mathbf{x}$. This has the important consequence that the intrinsic contact angle δ (also sometimes called Young's contact angle) is found locally everywhere along the contact line, as long as the interface is stationary. This is one of the key reasons for hysteresis, as will be described further in section 2.5.3.

The simple and ubiquitous Young's equation explains why there is a preferential adherence of fluids to surfaces of high energy σ_{sv} as compared to low energy surfaces: the total energy of the system is minimised in equilibrium. For a spreading drop the increase of liquid-vapour interface area has to be compensated by an energy decrease from the surface-liquid interface interaction. Therefore, in general, high energy surfaces have low contact angles δ (so the drop adheres to surface with a large area), and vice versa.

Regarding nomenclature, surfaces on which water exhibits high observed contact angles $\beta > 90^\circ$ are called hydrophobic, and low contact angles $\beta < 90^\circ$ hydrophilic. For an ideally smooth surface this same distinction is made for the intrinsic contact angle (i.e. if $\delta > 90^\circ$ then a surface is *intrinsically* hydrophobic) which is solely a property of the molecular interactions at the surface as in equation (2.10). This subtle difference is potentially confusing, as an intrinsically hydrophilic surface may become hydrophobic (i.e. exhibit an observed contact angle $\beta > 90^\circ$) due to surface structuring and entrapment of vapour, as will be described further on. For liquids other than water, other nomenclature is in use in the literature, including lyophobic, hydrophobic or omniphobic (all indicating repellency to all liquids) and oleophobic (repellent to oil-like liquids).

Extremely water repellent surfaces, typically defined as $\beta > 150^\circ$, are referred to as superhydrophobic (and occasionally as ultrahydrophobic and other popular variants). However, it is commonly understood that for any surface to be considered extremely repellent to a given liquid, it is additionally required that these surfaces also exhibit low hysteresis $\beta_h < 20^\circ$: in particular low contact angle hysteresis according to equation (2.2). This leads to similarly low roll-off angles of the drops and associated self-cleaning properties of the surface, as is the case with for instance Lotus leaves. Superlyophobicity and superoleophobicity are defined similarly. In the case that the contact angle as well as the roll-

off angle and hysteresis are large, surfaces are said to exhibit “sticky superhydrophobicity”.⁴¹

2.5.2 Laplace pressure

A freestanding curved liquid-vapour interface under tension exerts a force on its surroundings if it is stationary. The pressure difference between both sides of the interface, required to balance this force in equilibrium is known as the Laplace pressure.⁴² It can be derived¹ to have the form

$$\Delta p = \sigma_b \left(\frac{1}{R_1} + \frac{1}{R_2} \right), \quad (2.14)$$

where R_1 and R_2 are the principal radii of curvature. For a sphere, this reduces to $\Delta p = 2\sigma_b / R$. The liquid-vapour interface is considered, as this is the only surface free to move in the system.

If the system is in equilibrium, there is constant pressure within the drop, except in the case of non-negligible gravity, when there is also an additional hydrostatic pressure component $p = \rho g b$ added to equation (2.14), which is height-dependent. The implications of the Laplace pressure are considerable, in that the curvature of the interface has to be constant at all points of the interface, including disturbances of the interface such as on defects, as this force balance has local as well as global validity. The curvature of the interface, combined with the intrinsic contact angle, uniquely determines the possible equilibrium position(s) of the interface on a given surface. Note that since the Laplace pressure is dependent on the size of the drop, the local force balance is changed due to global pressure conditions, and this establishes a unique relationship between local and global constraints.

2.5.3 Surface discontinuities and Gibbs criterion

Regarding surface roughness, Shuttleworth and Bailey⁴³ proposed that due to the mechanical force balance, the intrinsic contact angle δ is never observed on rough surfaces, but is related to the observed angle β and the local slope angle $\alpha(\mathbf{x})$ on a surface $b(\mathbf{x})$ through

$$\beta(\mathbf{x}) = \delta + \alpha(\mathbf{x}), \quad (2.15)$$

where the slope angle is defined at any point as

$$\sin(\alpha(\mathbf{x})) = [\nabla b(\mathbf{x}) \cdot \mathbf{n}_\perp(\mathbf{x})], \quad (2.16)$$

where $\mathbf{n}_\perp(\mathbf{x})$ is the vector in the horizontal plane normal to the contact line pointing towards the vapour phase. This approach requires exact knowledge of both the surface and position of the contact line, so in practise this approach is only feasible for highly defined surfaces. For rotationally symmetric surfaces, equation (2.16) was indeed found to agree with experiments.³⁴

To better understand the role of surface discontinuities, Gibbs proposed a famous criterion,⁴⁴ which is explained graphically in figure 2.2 for the case of surface roughness. In that case, the contact angle at the discontinuity can range between

$$\delta < \beta < \delta + \psi . \quad (2.17)$$

In case of an interface that is not convex but concave, the contact line will not be pinned but instead jump ahead instantaneously upon reaching the discontinuity, until it reaches another stable point that satisfies Young's equation. For chemical heterogeneity a similar mechanism occurs, where upon moving from a region of lower contact angle δ to a region of higher contact angle $\delta + \psi$, the contact line is again pinned until the contact angle increases sufficiently. In the opposite case, the contact line will again jump. This jump occurs in the direction of the contact line movement, regardless whether this is an advancing or receding motion. It can be shown mathematically that pinning also occurs on continuously varying surface slope angles or chemical compositions, but the contact line will not be completely stationary during pinning in that case.⁴⁵ Gibbs criterion has been proven experimentally³⁴ and will play an important role in chapters 3 to 6.

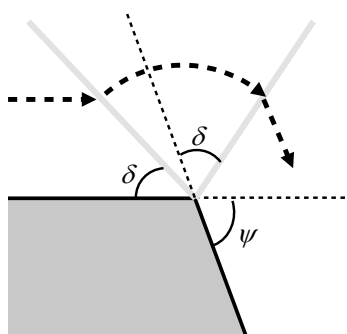


Figure 2.2: graphical illustration of Gibbs criterion. On a discontinuously rough surface, the contact line moving from left to right is pinned at the surface edge (discontinuity) until the liquid-vapour interface has deformed so far that the contact line can continue its quasi-static advance down the slope at Young's contact angle. In equilibrium the contact angle can therefore range continuously between the two angles indicated.

Young's equation, the Laplace pressure and Gibbs criterion have been called the three fundamental equations in wetting science,⁴⁵ and collectively can be used to analyze a great

number of wetting situations, especially involving the shape of the liquid-vapour interface locally near the contact line, as well as describing the causes of local contact line hysteresis. However, full energetic calculations or preferably simplified models are more applicable for finding the global drop shape, as will be discussed next. In addition, dynamic calculations are not possible with these three equations alone and applying them in non-equilibrium situations can give erroneous results.

2.5.4 Wenzel equation

In practice a simple thermodynamic approach is often used by approximating surface roughness by a roughness constant R . The surface terms Ω_{sl} and Ω_{sv} are assumed to increase straightforwardly by this factor R , defined as the ratio between true and projected (ideally smooth) surface area:

$$R = \frac{\Omega_{sl}}{A}, \quad (2.18)$$

where

$$\Omega_{sl} = \iint b(\mathbf{x}) dA \quad (2.19)$$

and where A is the projection of this surface on a smooth plane. Equations (2.18) and (2.19) can be equivalently evaluated for Ω_{sv} . By inserting these new surface terms into Young's equation the so-called Wenzel's equation is derived as:⁴⁶

$$\cos\beta = \frac{R(\sigma_{sv} - \sigma_{sl})}{\sigma_{lv}} = R \cos\delta. \quad (2.20)$$

When Wenzel proposed this equation in 1936, there was no way to verify it quantitatively, although a qualitative match was established. The advent of high-precision lithography and AFM to determine roughness on a sub-micrometer level has enabled experimental work^{33,47-49} in which the validity of the equation is reasonably established if the roughness of the surface is several (at least three to five) orders of magnitude smaller compared to the drop size and within certain limits for δ and R .

2.5.5 Cassie-Baxter equation

When the surface consists of several independent fractions of molecular species or even

several phases, Cassie and Baxter⁵⁰ proposed a similar approach as Wenzel in altering Young's equation so that

$$\cos\beta = \sum_i f_i \cos\delta_i, \quad (2.21)$$

where the respective contact angles of the surface species i are summed using the area fraction f_i of surface that each species occupies to yield the apparent contact angle β . If a flat surface consists of several chemical species, the surface coverage fractions f_i are used to determine the weighted contact angle, with the sum of all weights $\sum_i f_i = 1$. That this summation should always equal unity is a common interpretation of the Cassie-Baxter equation. However, in the spirit of the original article (the liquid-solid contact area not necessarily being flat), the weights can be allowed to sum to more than unity without loss of correctness of the equation, i.e. $\sum_i f_i \geq 1$, if the surface is patterned geometrically.

It is possible that the liquid does not completely wet the surface because a vapour fraction is entrapped in the crevices of a roughened surface. In that case the liquid is in contact with a “vapour surface”. The intrinsic contact angle of a liquid on this vapour phase is 180° for any liquid. This explains why entrapped vapour always leads to increased lyophobicity and roughening the surfaces is a common approach to achieving this. Assuming that the surface protrusions which the liquid is in contact with are planar (i.e. that $\sum_i f_i = 1$), equation (2.21) simplifies to

$$\cos\beta = f \cos\delta - (1 - f) \quad (2.22)$$

with f the fraction of surface that is wetted and $1 - f$ the fraction that is ‘covered in vapour’. Equation (2.22) is (confusingly) also referred to as the Cassie-Baxter equation, but is in fact a particular case of the general equation (2.21).

2.5.6 Gibbs energy calculations for isotropic drops and substrates

A more sophisticated approach for calculating the equilibrium drop geometry was proposed by Johnson and Dettre.^{27,28,30,31} Instead of finding an explicit relationship between β and the σ_{ij} 's via local force or energy considerations, the total Gibbs energy landscape for all contact angles between 0 and 180 degrees is calculated, after which the minimum is determined. Equilibrium, the absence of gravity and a radially symmetric spherical drop shape are still assumed, but the other improvement upon previous models is the fact that radially

symmetric model surface geometries could be implemented, and multiple local energetic minima could be determined, including the energetic barriers between them, thus giving a measure for hysteresis.

Before explaining this model in more detail, first it is instructive to compare it briefly with completely analytical models that do not take into account non-ideal surface geometries. Finding an exact solution for the minimum of the free energy terms, with the constraint of fixed volume V , can be done by minimizing an Euler-Lagrange functional,¹ while optionally also including the bulk energetic contribution of gravity.⁵¹ The coupled differential equations of the solution describe the drop surface without assuming *a priori* which shape it has, aside from rotational symmetry. A drawback is that the free energy landscape cannot be determined and only the minimum solution (as was the case with the Young, Wenzel and Cassie and Baxter equations) is found. Therefore in literature the basic approach of Johnson and Dettre has been used a number of times to gain insight into hysteresis and surface roughness.^{29,32} The derivation presented here is slightly different from that in the original article. It is described here in detail because it clearly illustrates the connection between energy models and the simpler models described before. Several intermediate results will be used in subsequent chapters.

In order to easily calculate the total interfacial energy is useful to make some minor changes to equation (2.7) by making the energy dimensionless by dividing by $\sigma_b V^{2/3}$, so that all σ 's can be substituted with the intrinsic contact angle:

$$\Delta\tilde{G}_{interfacial} = \frac{\Omega_{lv} + \Omega_{sl}\cos\delta}{V^{2/3}}, \quad (2.23)$$

where the tilde signifies that $\Delta\tilde{G}_{interfacial}$ is made dimensionless. This is the basic equation used to determine the minimum free energy.

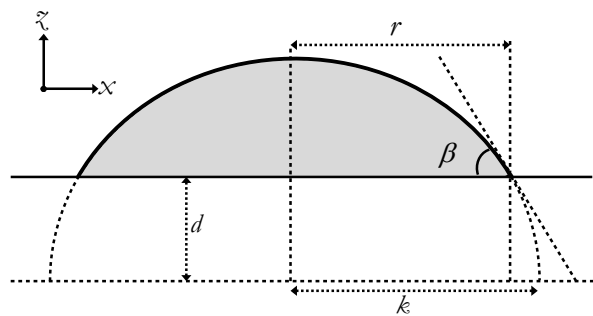


Figure 2.3: A side view of the geometry of a spherical drop, where the solid surface is at $z = d$. Indicated are the contact angle β , the drop radius r , the intrinsic curvature k and the z-axis cut-off d .

The geometrical parameters in equation (2.23) will now be written explicitly in terms of the observables r and β as schematically shown in figure 2.3. The drop is approximated with a spherical cap shape. The intrinsic curvature (principal radius) of the drop k and the cut-off distance d between the actual solid surface and the imaginary plane at the centre of the sphere needs to be determined first. From this figure the geometric relationships between β , k , d and the radius of the drop on the solid-liquid surface plane r are

$$\sin\beta = \frac{r}{k} \quad \text{and} \quad \tan\beta = \frac{r}{d}. \quad (2.24)$$

An important simplification comes from the fact that the surface roughness with height ξ , compared to the height of the drop, is $\xi \ll (k-d)$ for the model to hold. Therefore, the total volume can be calculated from the drop geometry ignoring any liquid penetration into the surface as

$$V = \iiint dV = \int_d^k A d\xi, \quad (2.25)$$

with a parameterization over ξ and the horizontal cross section of the drop, which is defined as

$$A = \pi k^2 \left(1 - \left(\frac{\xi}{k} \right)^2 \right). \quad (2.26)$$

The integral (2.25) is then evaluated with this integrand as

$$\begin{aligned} V_{sphere} &= \pi k^2 \int_d^k \left(1 - \left(\frac{\xi}{k} \right)^2 \right) d\xi \\ &= \pi k^2 \left(\frac{2k}{3} + \frac{d^3}{3k^2} - d \right) = \frac{\pi}{3} \left(\frac{r}{\sin\beta} \right)^3 (2 - 3\cos\beta + \cos^3\beta), \end{aligned} \quad (2.27)$$

where in the last step the relations of (2.24) were used. By expressing r as a function of V and β the fixed volume constraint can be expressed as

$$r = \sin\beta \left(\frac{3V}{\pi(2 - 3\cos\beta + \cos^3\beta)} \right)^{1/3}. \quad (2.28)$$

The function $h(x) = \sqrt{k^2 - x^2} - d$ defines the height of the sphere as function of horizontal position. Now the liquid-vapour interface area Ω_{lv} can be expressed as

$$\Omega_{lv} = \int_A \sqrt{1 + \left(\frac{\partial h}{\partial x}\right)^2 + \frac{1}{x^2} \left(\frac{\partial h}{\partial \phi}\right)^2} dA. \quad (2.29)$$

This integration is evaluated, considering that there is rotation symmetry around the z -axis, thus eliminating the partial derivative to ϕ . The integration limit over x is r , so that

$$\Omega_{lv} = 2\pi k \left[-\sqrt{k^2 - x^2} \right]_0^r, \quad (2.30)$$

which can be simplified further using (2.24) to

$$\Omega_{lv} = \frac{2\pi r^2}{1 + \cos\beta}. \quad (2.31)$$

Obviously for flat surfaces,

$$\Omega_{sl} = \pi r^2, \quad (2.32)$$

although for non-flat surfaces equation (2.32) may still be used as long as any significant amount of liquid penetrating the surface is accounted for by appropriate corrections to equations (2.27) and (2.28). In chapter 7 equation (2.32) will be modified to account for multi-scale surface roughness.

All terms in equation (2.23) are now written explicitly as function of r and β , and due to the fact that both Ω_{lv} and Ω_{sl} have a r^2 term, the volume V can be conveniently eliminated from the equation. Furthermore, because r is expressed explicitly as function of β due to the fixed volume constraint (2.28), $\Delta\tilde{G}$ can now be expressed *only* as function of β , which greatly facilitates the calculations.

Both the Wenzel (2.20) and Cassie-Baxter (2.21) equations have limited validity and should be used correctly only under specific circumstances. In contrast, the more general Gibbs energy model presented here can also be used calculate the energy of non-equilibrium configurations, such as meta-stable drop morphologies.

2.5.7 Wetting states, stability and transitions

When considering surfaces with increasing roughness R , there are two *generic* wetting states named after the equations that describe them: the smooth to intermediately rough ‘Wenzel’ state (typically $1 < R \lesssim 2$) and the rough to very rough (typically $R \gtrsim 2$) ‘Cassie–Baxter’ or ‘Cassie’ state. Other names for these states are the collapsed state (Wenzel) and suspended state (Cassie) and both conventions will be used in this thesis. These states are shown schematically in figure 2.4.

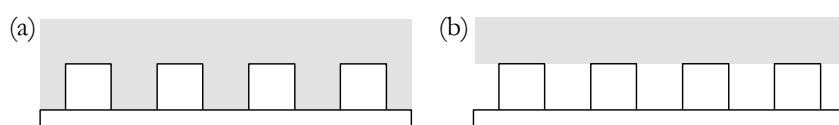


Figure 2.4: Schematic close-up of a structured surface exhibiting two generic wetting states of a liquid interacting with the surface protrusions. (a) Collapsed (or ‘Wenzel’) state, (b) Suspended (or ‘Cassie’) state.

The main qualitative difference is that in the Wenzel state no vapour phase is trapped under the drop, in contrast to the Cassie state. In the Wenzel state, contact angles increase due to a net increase in the lyophobicity of the surface and contact angle hysteresis generally increases with increasing roughness, as pinning at surface discontinuities increases. In the Cassie-Baxter state the observed contact angle is typically higher than in the Wenzel state but the contact angle hysteresis is dramatically lower, as the receding contact line is only weakly pinned on the convex ends of surface asperities. Due to this decreased interfacial contact and low pinning, drops can roll instead of slide, which decreases viscous dissipation. Transitions between rolling and sliding motion are being investigated currently.⁵² Lastly, a mixed state is also possible, where parts of the drop have collapsed between the surface protrusions, whereas other parts of the drop remain suspended. Please note that the Wenzel and Cassie-Baxter equations have limited validity and have been being hotly debated recently.^{53–56} By convention these states are referred to as Wenzel or Cassie-Baxter states, even when the similarly named equations cannot be used to calculate the observed contact angle of that state.

Lyophilic surfaces with $\delta < 90^\circ$ typically only exhibit the Wenzel state, although with smart geometric surface designs it is possible to create a meta-stable Cassie state on these surfaces as well.⁵⁷ Wetting states are considered stable if they are in their global energetic minimum whereas they are meta-stable when they are in a local energetic minimum (both have $\delta G = 0$ and $\delta^2 G \geq 0$). Saddle points or maxima in the energy landscape ($\delta G = 0$ and $\delta^2 G < 0$) are inherently unstable and are not considered viable states. The stability of a state depends on the energy barriers between the neighbouring states, and the possible pathways for a wetting state transition. Two generic transitions are the collapse transition (from a suspended to a collapsed state) and a lifting transition. In chapter 5 a full lifting transition is

demonstrated, which in combination with electrowetting and an associated collapse transition leads to the first experimentally realised surface that enables both transitions reversibly. Analysis of wetting states and transitions is a powerful tool in wetting research. For many systems, complex wetting state diagrams can be derived.^{45,58} In chapter 7 such an analysis is presented for artificial Lotus-like raspberry structures.

Typical perturbations that can lead to wetting state transitions are for instance mechanical perturbations such as drop impact on a surface with non-zero kinetic energy, vibrations or other body forces acting on the drop. Other perturbations are thermal fluctuations (typically on atomic scale), changes in surface tension (due to i.e. electrowetting) or changes in hydrostatic pressure. While perturbations and wetting state transitions can sometimes be assessed with static or quasi-static models, in many cases dynamic models are required, for instance if viscous dissipation is non-negligible or no symmetry is available to simplify the geometry of the interfaces and contact line.

2.6 Dynamic non-equilibrium models

In this section, dynamic models for wetting are described, focusing particularly on lattice-Boltzmann simulations that are employed throughout this thesis. When considering the model system in a dynamic situation, no equilibrium is assumed a priori.

2.6.1 Navier-Stokes equation

The Navier-Stokes equation is the fundamental equation in hydrodynamics. It is in fact a set of coupled non-linear partial differential equations, which can only be solved considering proper boundary conditions. Exact solutions are typically obtained by employing simplifying approximations. The equations can be expressed, with Einstein summation convention to paired indices and Greek indices representing Cartesian components of vectors. The choice for this formulation is made to link up with the description of the lattice-Boltzmann model presented further on and reads

$$\partial_t(\rho u_\alpha) + \partial_\beta(\rho u_\alpha u_\beta) = -\partial_\beta \mathbf{P}_{\alpha\beta} + \nu \partial_\beta [\rho(\partial_\beta u_\alpha + \partial_\alpha u_\beta + \delta_{\alpha\beta} \partial_\gamma u_\gamma)], \quad (2.33)$$

where ρ , \mathbf{u} , \mathbf{P} , and ν are respectively the local density, velocity, pressure tensor and kinematic viscosity. An important condition that is imposed on fluid is the continuity equation

$$\partial_t \rho + \partial_\alpha(\rho u_\alpha) = 0, \quad (2.34)$$

indicating that mass is preserved locally.

Importantly, there are several numerical simulation packages available that solve or approximate the Navier-Stokes equations by means of Computational Fluid Dynamics (CFD) methods. A state-of-the-art commercial example is COMSOL MultiPhysics, which has a dedicated micro-fluidics module offering simulations at the relevant length scale. Non-commercial software packages also exist. However, CFD approaches can have several drawbacks, including difficulties in dealing with multiple phases (liquid and vapour phases, or multiple non-mixing fluids).⁵⁹ Furthermore commercial packages are not open-source and many fundamental properties of the simulations cannot be easily verified or checked against known examples in literature. In particular numerical artefacts cannot easily be quantified.

As a last remark, it is important to point out that there is also a class of models in use which simulate drop morphologies by minimizing the surface energy by a different approach.⁶⁰ The basis of these Gibbs energy surface models is an open source program called Surface Evolver,⁶¹ which can be altered to handle specific geometries and optimization problems. The method employed involves recursively minimizing the liquid-vapour interface locally to find a (local) energetic minimum, while keeping the volume constrained. While a powerful model for qualitative understanding, this class of models suffers from a number of drawbacks, which is why they are not employed in this thesis. The most important is that while the morphology of the drops evolves as the simulation progresses, this is not a pathway based on the Navier-Stokes equations but rather on numerical optimization of the interfaces to minimize interfacial energy. Therefore, it is not possible to determine with any certainty that the (dynamic) evolution of the drop is correct, but only that (static) final morphology is a local energetic minimum. In case multiple minima are possible or suspected these can only be found by manually altering the initial surface configurations. Lastly, the varying geometries used in this thesis would have required significant additional programming to adapt the basic model to these geometries.

2.6.2 Lattice-Boltzmann simulations

Lattice-Boltzmann models are a class of meso-scale CFD models, which are receiving increasing academic interest.⁶² They have proven to simulate wetting drop systems as considered in this thesis accurately for many experimental cases described in the open literature, e.g. in ⁶³⁻⁷² and references therein. The lattice-Boltzmann simulations presented in this thesis in chapters 3, 4 and 5 are performed in collaboration with Professor Julia Yeomans at the Rudolf Peierls Centre for Theoretical Physics of Oxford University and (former) co-workers Halim Kusumaatmaja and Matthew Blow.⁷³ In the past, the dynamics of drop motion on chemically patterned surfaces was investigated,⁷⁴ as well as superhydrophobic drops on pillared surfaces.^{69,75} These and other recent results showed good qualitative agreement with experiment.

The simulation work in this thesis has been done in collaboration, meaning that determining the simulation setup and relevant parameters as well as discussing the results have been done jointly, but the conception of the model, programming and executing (including rigorous checking of the quality of the simulations) has been done exclusively by the Yeomans group. In what follows, a highly abbreviated and qualitative description of the model is given with references, while the details of the simulations are presented in their respective chapters and references therein.

The basis of models used in this thesis is a three-dimensional lattice, where the lattice points are assigned a local density as well as a local vector velocity. The local density is determined as function of time, and the system will relax to equilibrium through fluid movement governed by the Navier-Stokes (2.33) and (2.34). Note that in the model the fluid is compressible, i.e. the simplified continuity equation $\partial_\alpha u_\alpha = 0$ for incompressible liquids is not used. The latter approximation is often made in other fluid dynamic simulations, but is not valid for multi-phase simulations with variable density.

The great benefit of the model is the ability to locally investigate the forces, fluid velocities and viscous dissipation as well as the precise geometry of the fluid-vapour interface. However, there are also several limitations to the lattice-Boltzmann approach: first and foremost, there are only a limited number of lattice sites (at most some 300^3 nodes) available if the computational expense is to remain manageable in time and cost. This means that physical systems have to be approximated via numerical models with simplified geometry, often employing periodic boundary conditions or symmetry to reduce computational expense. Secondly, the difference between the vapour and liquid phase densities is unrealistically small, and the interface thickness is un-physically wide. Renormalization to physical length and timescales is possible, but the agreement between model and experiment will be qualitative, as described further below.

The lattice-Boltzmann model starts with defining a continuum energy function Ψ ,

$$\Psi = \iiint (\psi_b(\rho) + \frac{\kappa}{2}(\partial_\alpha \rho)^2) dV + \iint \psi_s(\rho_s) dS, \quad (2.35)$$

where $\psi_b(\rho)$ is a bulk free energy term taken from⁷³

$$\psi_b(\rho) = p_c(v_n + 1)^2(v_n^2 - 2v_n + 3 - 2\beta\tau_w) \quad (2.36)$$

where $v_n = (\rho - \rho_c) / \rho_c$, $\tau_w = (T_c - T) / T_c$ and ρ_c , T , T_c and p_c are the critical density, local temperature, critical temperature and critical pressure of the fluid respectively. Due to the choice of $\psi_b(\rho)$, the local density ρ has two coexisting bulk phases with densities ρ_l and ρ_v , each having an energetic minimum bulk energy. β is a numerical parameter used exclusively in the model to fix the density ratios between the fluid and vapour phases and

used here for consistency with literature, which should not be confused with observed macroscopic contact angle with the same symbol. From the context, it is made clear which β is intended.

The three terms in (2.35) model the bulk energy, the energy associated with phase boundaries and the surface interaction respectively. The second term is a function of the density gradient, which leads to a finite surface energy σ_b . The third term determines σ_{sl} , σ_{sv} and thus the intrinsic contact angle δ .

The hydrodynamics of the drop are described by the Navier-Stokes (2.33) and continuity equations (2.34), which is evaluated via a lattice Boltzmann algorithm. No-slip boundary conditions are imposed on the velocity field on the surfaces adjacent to and opposite to the drop. The thermodynamic properties of the drop are included via the pressure tensor \mathbf{P} , which is a function of density ρ and is calculated from the energy function Ψ .^{69,73,76} \mathbf{P} is defined as

$$P_{\alpha\beta} = (p_b(\rho) - \frac{\kappa}{2}(\partial_\gamma \rho)^2 - \kappa\rho\partial_{\gamma\gamma}\rho)\delta_{\alpha\beta} + \kappa(\partial_\alpha \rho)(\partial_\beta \rho), \quad (2.37)$$

with

$$p_b(\rho) = p_c(\nu_n + 1)^2(3\nu_n^2 - 2\nu_n + 1 - 2\beta\tau_n). \quad (2.38)$$

Computationally, the lattice-Boltzmann uses several distinct steps to evaluate all model parameters and to ensure physically acceptable results (local conservation of mass and momentum in particular). The simulation is then run for a number of these cycles (called time-steps), typically on the order of 10^5 steps.

The results from the model are the drop morphology and local velocity for each time step. From the morphology, the relevant geometrical parameters such as contact angles, base diameters and height can be determined. Interpolation between lattice units increases the precision of the geometrical parameters considerably. A typical example of the model results showing both geometry and local velocity is shown in figure 2.5.

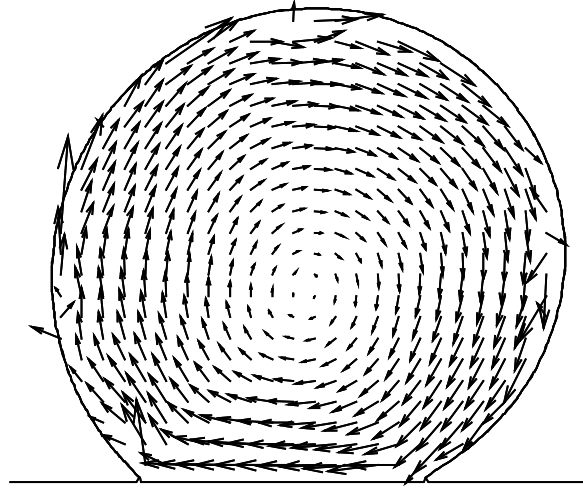


Figure 2.5: A typical example of a recent result from the lattice-Boltzmann simulations from the Yeomans group, showing drop morphology as well as the velocity distribution (in a centre-of-mass frame) of a rolling drop on a superhydrophobic surface. Figure reproduced from ⁷⁷.

Simulation and experimental parameters are related by choosing a length scale l_0 , a time scale t_0 , and a mass scale m_0 . A simulation parameter with dimensions $[L]^{n_1}[t]^{n_2}[m]^{n_3}$ can be rescaled via a factor $[l_0]^{n_1}[t_0]^{n_2}[m_0]^{n_3}$ to give the physical value.⁷¹ Since the interface widths are too large compared to experiments and the density difference between liquid and gas is too small, the result of this is that time scales are too fast.^{63,73} Comparisons with experiments so far have shown that the dynamic pathways are correct however.^{71,76,78} Changing the values of the interface width, density ratio, surface tension and viscosity only changes the speed of the dynamics, but not the pathway itself.

2.7 Conclusions

In conclusion, in this chapter the relevant theory was presented needed for the reader unversed in the field to comprehend the following chapters. Evaluation of the various energetic terms in static models has been the primary means of analysis in the field. While this has shown great merits, a more complete understanding can only be gained by including dynamic aspects of drop morphology evolution. This includes considering hysteresis, which is nearly always present, even in laboratory conditions. Therefore, in the following chapters, the Gibbs energy models presented here are often combined with force and pressure balance calculations and lattice Boltzmann (dynamic) modelling.

3. Anisotropic drop morphologies on corrugated surfaces¹

*“Two roads diverged in a yellow wood,
And sorry I could not travel both
And be one traveller, long I stood
And looked down one as far as I could
To where it bent in the undergrowth”*

– Robert Frost, “The Road Not Taken”

¹ This chapter is published in:

- H. Kusumaatmaja, R. J. Vrancken, C. W. M. Bastiaansen and J. M. Yeomans, *Anisotropic Drop Morphologies on Corrugated Surfaces*, *Langmuir* 24, 7299 (2008). Reprinted with permission. Copyright 2008 American Chemical Society.
- Mariette E. Koekoek, Thijs Meijer, Robert J. Vrancken, *Digital printing of multilevel optical variable Devices for Document Security & Brand Protection*, Proceedings of the Optical Document Conference II, 357-367, San Francisco, United States (2010)
- R. Vrancken, *Geometry of micro-transfer printed polymerised mesogen structures*, M.Sc. Thesis, Laboratory for Polymers in Advances Systems, Department of Chemical Engineering and Chemistry and Laboratory for Molecular Biosensors for Medical Diagnostics, Department of Applied Physics, Eindhoven University of Technology (2006)

3.1 Introduction

In recent years, anisotropic wetting and spreading of drops have received continued attention from the scientific community due to their relevance to micro-fluidic devices, surface coatings and bio-mimetic applications for example. Surface roughness can be exploited to significantly alter and tailor the behaviour of fluids moving over a surface. Also, it is now possible to reproduce heterogeneous surface patterns in a controlled manner on micrometer length scales. Regular arrays of chemical patches^{79–81} and posts^{58,82–84} of different shapes and sizes have been fabricated and several authors^{22,85,86} have even shown the possibilities of manufacturing multi-scale surface patterns. Recently, such patterning has been used to control the movement of drops^{87,88} and to manipulate flow in micro-channels.^{89,90}

The motion of drops on patterned surfaces is complex because of pinning and hysteresis. Surfaces with anisotropic patterns on a length scale comparable to the drop size can result in elongated drop shapes and in a different motion of drops parallel and perpendicular to the grooves. Gleiche *et al.*⁷⁹ showed that there is anisotropy in the contact angle and contact angle hysteresis on chemically nano-structured surfaces. Brandon *et al.*⁹¹ investigated the effect of drop size on chemically striped surfaces and found that the drop anisotropy and contact angle hysteresis depends on the drop volume. Elongated drop shapes were also obtained by Chen *et al.*⁶⁰ and Chung *et al.*⁹² for patterns with hydrophobic and hydrophilic grooved surfaces respectively. Narhe and Beysens⁹³ studied the growth dynamics of water drops condensing on grooved surfaces and showed that similar elongated drop shapes can be found during growth when the surface is hydrophilic, but that this elongation is absent when the surface is superhydrophobic. Pakkanen and Hirvi⁹⁴ further showed that the anisotropy still persists when surface patterning is nano-scopic. Morita *et al.*⁸⁰ and Yoshimitsu *et al.*⁸⁴ studied the dynamics of drops sliding on chemically striped and hydrophobic grooved surfaces and found that the sliding angles are considerably larger for drops moving perpendicular to the stripes. Thus similar observations and phenomena related to contact line pinning are reported for surfaces modified by chemical as well as geometrical patterning.

In this chapter a number of experiments are presented of drops spreading or de-wetting on a hydrophilic surface patterned with parallel grooves. The results are then compared to lattice Boltzmann simulations, demonstrating the importance of hysteresis and energetic barriers due to the surface patterning: because of the asymmetric behaviour of the advancing and receding contact line, the final drop shape can be elongated either along or perpendicular to the grooves.

This chapter is organised as follows. Sections 3.2 and 3.3 summarise the experimental and numerical approaches respectively. Equilibrium and quasi-static drop experiments and simulations are presented in section 3.4. In section 3.5, an investigation of the influence of

three dimensionless surface parameters is presented: the roughness factor, the aspect ratio of the barriers and the dimensions of the drop versus the dimensions of the barriers. As expected, the contact angle, particularly that of the interface lying perpendicular to the grooves, strongly depends on both the parameters of the surface and the history of the drop motion. In section 3.6 the main conclusions are presented.

3.2 Experimental methods

Two sets of experiments were performed with anisotropically grooved surfaces. In the first set of experiments, micrometer-sized droplets were placed on sub micrometer-scale corrugated polyimide surfaces. The polyimide layers were created on glass by spin-coating a commercially available mixture (JSR AL-3046) of polyimide from solvent. After spin-coating, the samples were heated for 5 minutes at 80 °C on a hotplate to evaporate the solvent, and afterwards thermally cured in a vacuum oven at 180 °C for 1.5 hours. Subsequently the samples were rubbed unidirectionally with a velvet cloth with a force $\sim 1 \text{ kg cm}^{-2}$ over a distance of 30 cm with a velocity of 10 cm s^{-1} . This created grooves between 15 to 20 nm deep and 50 to 200 nm wide, as measured by AFM and presented in figure 3.1. Non-rubbed surfaces were prepared identically, only the rubbing step was omitted. The non-rubbed surfaces are very smooth and the roughness is distributed isotropically as expected from the preparation process.

Surface energy measurements were performed on the prepared polyimide surfaces. By measuring the contact angle of water, ethylene glycol and diiodomethane drops on the surface, the surface energy was calculated to be 43.6 mJm^{-2} , employing the OWRK method from equation (2.10) extended to three probe liquids for higher accuracy.^{36–38}

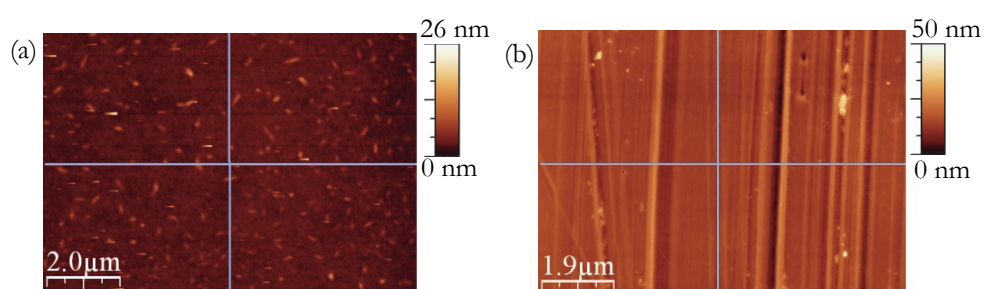


Figure 3.1: AFM topographies for an (a) unrubbed and (b) rubbed polyimide surface. The non-rubbed surface exhibits only minor isotropic roughness, whereas the rubbed surface has well-defined horizontal grooves. Notice the difference in the height scale bars.

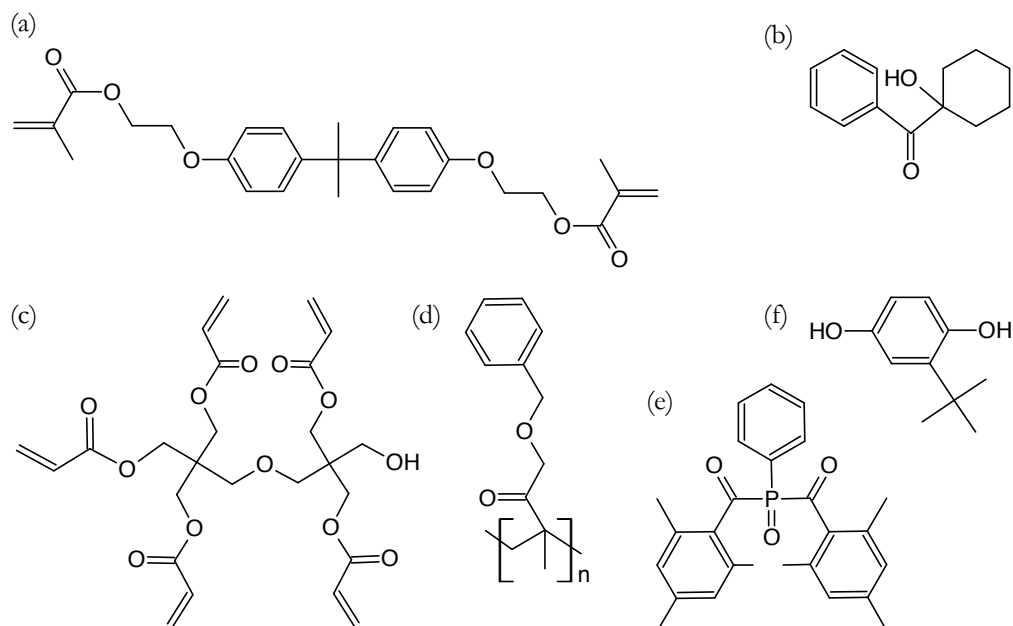


Figure 3.2: Chemicals used in this chapter. Print mixture (a-b): (a) monomer ethoxylated bisphenol-A dimethacrylate, (b) photo-initiator 1-Hydroxycyclohexyl phenyl ketone. Photo-embossing mixture (c-f): (c) monomer dipentaerythritol penta/hexa-acrylate, (d) polymer polybenzylmethacrylate, (e) photo-initiator phenyl-bis(2,4,6-trimethylbenzoyl)phosphine oxide, (f) inhibitor tert-butyl hydroquinone.

The print mixture as presented in figure 3.2(a-b) consisted of a monomer of 99.0 w% ethoxylated bisphenol-A dimethacrylate (S348L, Sartomer Europe BV), having a surface energy⁹⁵ of 39 to 44 mJm⁻², mixed with 1.0 w% photo-initiator phenyl-bis(2,4,6-trimethylbenzoyl)-phosphine oxide (Irgacure 184, Ciba Specialty Chemicals). Drops of this mixture were placed on the surface by two deposition methods. In the first method, the mixture was sprayed manually onto the polyimide surface. The resulting drops were placed randomly on the surface and were of varying size. As the drops impact the surface with additional kinetic energy, the overall process is qualitatively similar as other impact methods such as inkjet printing.

The second method employed was micro-transfer printing as presented schematically in figure 3.3.^{7,96} The stamp consists of PDMS elastomer structured with an array of trapezoidal posts with face areas of 100×100 μm which is pressed into a thin spin-coated layer of monomer mixture and afterwards pressed against the polyimide layer. Part of the mixture is transferred to the polyimide surface, after which the stamp is detached from the surface leaving an array of drops with equal size. The drops were polymerised within one minute after placement under a nitrogen environment to prevent oxygen inhibition of the photo-polymerisation reaction. This fixed the geometry of the drop and enabled analysis afterwards,

while still allowing the drop sufficient time to equilibrate. As the drops were adhered to the surface with additional pressure and contact between the stamp and the surface, micro-transfer printing belongs to the category of contact printing methods.

The drop $x-y-z$ profiles were determined by optical interferometry (Fogale Zoomsurf 3D), and the parallel and perpendicular cross-sectional height profiles were extracted and ellipse-fitted to determine the contact angles and elongation. A minimum of five drops were examined for each surface.

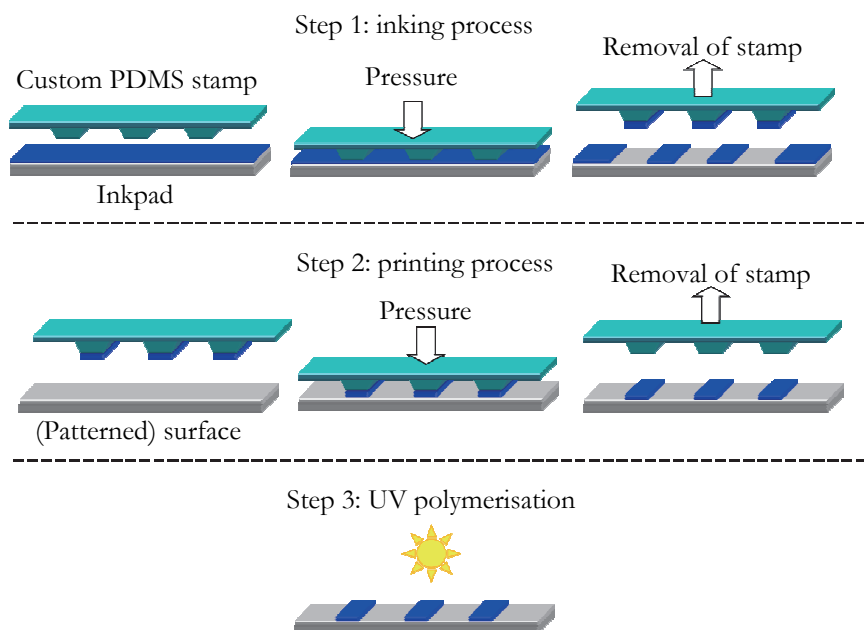


Figure 3.3: Schematic representation of micro-transfer printing, showing the three main steps of inking the soft elastomeric (PDMS) stamp, printing of the liquid onto the patterned surface and polymerisation of the resulting structure.

In the second set of experiments, corrugated polymer surfaces, were created by means of a four-step process called photo-embossing, as shown in figure 3.4(a-d).⁹⁷ In the first step a photo-polymer mixture was spin-coated on glass and a layer of $20\ \mu\text{m}$ thick was obtained. The mixture, presented in figure 3.2(c-f) consisted of 41.9 w% monomer di-pentaerythritol penta/hexa-acrylate (Sigma Aldrich), 41.9 w% polymer polybenzylmethacrylate (Mw 70 kg/mol; Scientific Polymer Products), 4.2 w% photo-initiator phenyl-bis(2,4,6-trimethylbenzoyl)phosphine oxide (Irgacure 819, Ciba Specialty Chemicals) and 12.0 w% inhibitor tert-butyl hydroquinone (Aldrich). In the second step, the layer was illuminated with UV light through a suitable lithographic mask (described below), partially polymerising the exposed parts of the layer. In the third step, the sample was heated. During heating part

of the monomers in the non-illuminated regions diffused towards the illuminated regions, creating a corrugated surface. In the last step the surface was flood-exposed with UV light under a nitrogen environment to completely polymerise the layer. The photo-embossed surfaces were found to have a surface energy of 44.7 mJm^{-2} , similar to the polyimide surfaces. A SEM image of a typical surface produced by photo-embossing is presented in figure 3.4(e).

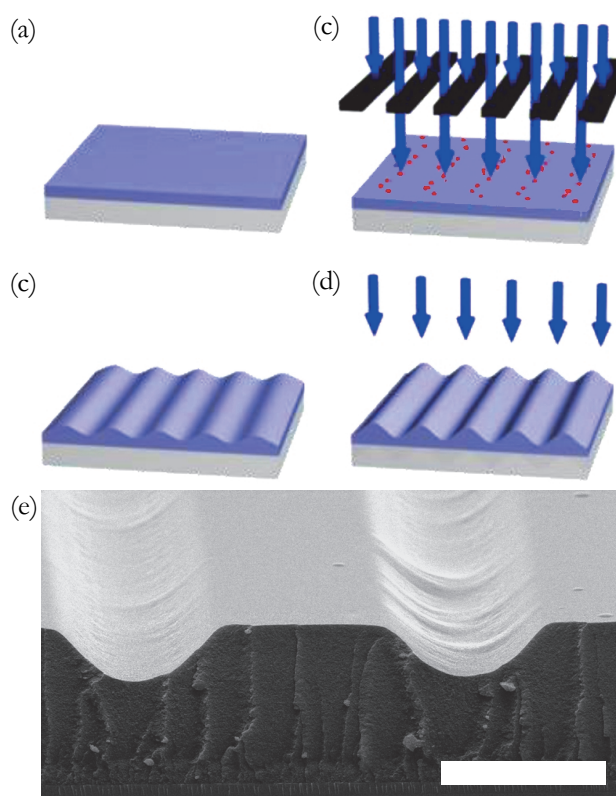


Figure 3.4: Surfaces created by photo-embossing. (a-d) Schematic representation of the photo-embossing process, reproduced from ⁹⁸, which consists of (a) spin-coating a smooth layer onto a glass slide, (b) patterned UV exposure, (c) developing step at elevated temperature and (d) UV flood exposure. (e) SEM image of a surface used in the experiments. The scale-bar in (e) indicates $20 \mu\text{m}$.

The lithographic masks employed had sizes of $1 \times 1 \text{ cm}$ and consisted of parallel stripes, where the width of the stripes was equal to the distance between the stripes, i.e. 50% of the incident light is transmitted. The resulting surface parameters are schematically defined in figure 3.5. The pitch p was varied from $10 \mu\text{m}$ to $100 \mu\text{m}$. The depth of the grooves b was varied between 100 nm and $5 \mu\text{m}$ by varying the illumination time, with the exception

that the maximum depth could only be reached with masks with pitches above 40 μm because of limitations of the photo-embossing process. The depth of the grooves was also determined with optical interferometry.

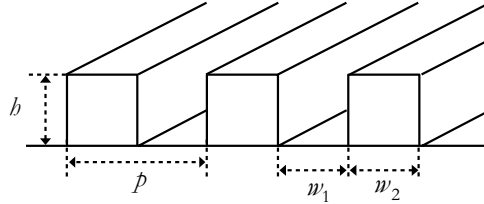


Figure 3.5: schematic of the geometric surface parameters. Indicated are the groove height h , the pitch p , which is the sum of the width of the grooves w_1 as well as the width of the corrugations w_2 .

Water drops of 4 μl were placed on the photo-embossed polymer surfaces by an automated dispensing needle (Optical Contact Angle setup, Dataphysics) at a constant height above the surface to minimize any variations in drop placement. The water used for the measurements was purified (Millipore Super-Q) and CO_2 was removed (Elix-10 UV). The drop properties were measured on the surface with the contact angle measurement setup. Both β_{\parallel} and β_{\perp} were determined, as well as the drop elongation e , defined as the ratio between parallel and perpendicular base diameters of the drop. The contact angles and base radii were determined by means of digital drop shape fitting employing an ellipse fitting algorithm.

The two sets of experiments are complementary, in that they employ different surfaces and probe liquids. The rubbed surfaces have nano-meter scale corrugations, whereas the photo-embossed surfaces have micrometer-scale corrugations. Micro-transfer printing is suitable for creating well-defined de-wetting drops, while photo-embossed surfaces have the great benefit of being smooth as well as controllable with regards to the size of the corrugations. In the following sections the results from both sets of experiments are presented next to each other, highlighting different aspects of anisotropic hysteresis.

3.3 Lattice Boltzmann simulation method

In the simulations reported here, the model described in section 2.6.2 is employed. The simulation parameters are chosen such that the relative densities of the liquid and vapour phase are $\rho_l = 4.11$ and $\rho_v = 2.89$ respectively. The intrinsic contact angle is $\delta = 70^\circ$. The typical drop and pattern sizes are of order 100 and 10 lattice spacings respectively. More specific details on the model used here, including the way complicated surface geometries are implemented, can be found in Dupuis and Yeomans.⁶⁹

The typical surface pattern used in the simulations is slightly different to that produced experimentally. In the simulations the solid surface can only be initialized with rectangular geometry, as curved surfaces cannot be implemented currently. It is therefore important to note that the aim of this chapter is to obtain a consistent qualitative understanding of the problem rather than to attempt to exactly match experiments and simulations. The shape of the grooves is taken to be rectangular, as shown in figure 3.5. The aspect ratio is defined as the ratio of the groove height b to the pitch, i.e. $\chi = b / p$. No-slip boundary conditions are imposed on the velocity field on the surfaces adjacent to and opposite to the drop and periodic boundary conditions are used in the other two directions.

3.4 Anisotropic drop morphology on a corrugated surface

In this section, the anisotropy in the final shape of a drop spreading on a corrugated surface is investigated. In section 3.4.1 an experimental comparison is presented between sprayed or micro-transfer printed drops of monomer onto the rubbed polyimide surface. In a second set of experiments water is quasi-statically added to a spreading drop prepared on a photo-embossed surface. The consistent results from both sets of experiments are then complemented by performing lattice Boltzmann simulations in section 3.4.2 to further understand the role of the surface anisotropy in determining the final shape of the drop. In 3.4.3 a comparison is made between experimental and simulation results.

3.4.1 Experimental results

Figure 3.6(b) shows a typical final shape of a liquid drop that is sprayed onto the surface, causing the drop contact line to advance to wet the corrugated surface. Since the surface patterning is not isotropic, the advancing contact line behaves differently parallel and perpendicular to the grooves. Based on Johnson and Dettre's work³⁰ no hysteresis due to the surface patterning is expected in the parallel direction as there are no energetic barriers present which could tend to pin the contact line. On the other hand, perpendicular to the grooves, surface undulations are known to pin the contact line.^{43,44,99} Contact line pinning leads to strong contact angle hysteresis and this causes the advancing contact angle β_a , to differ from that in the parallel direction.

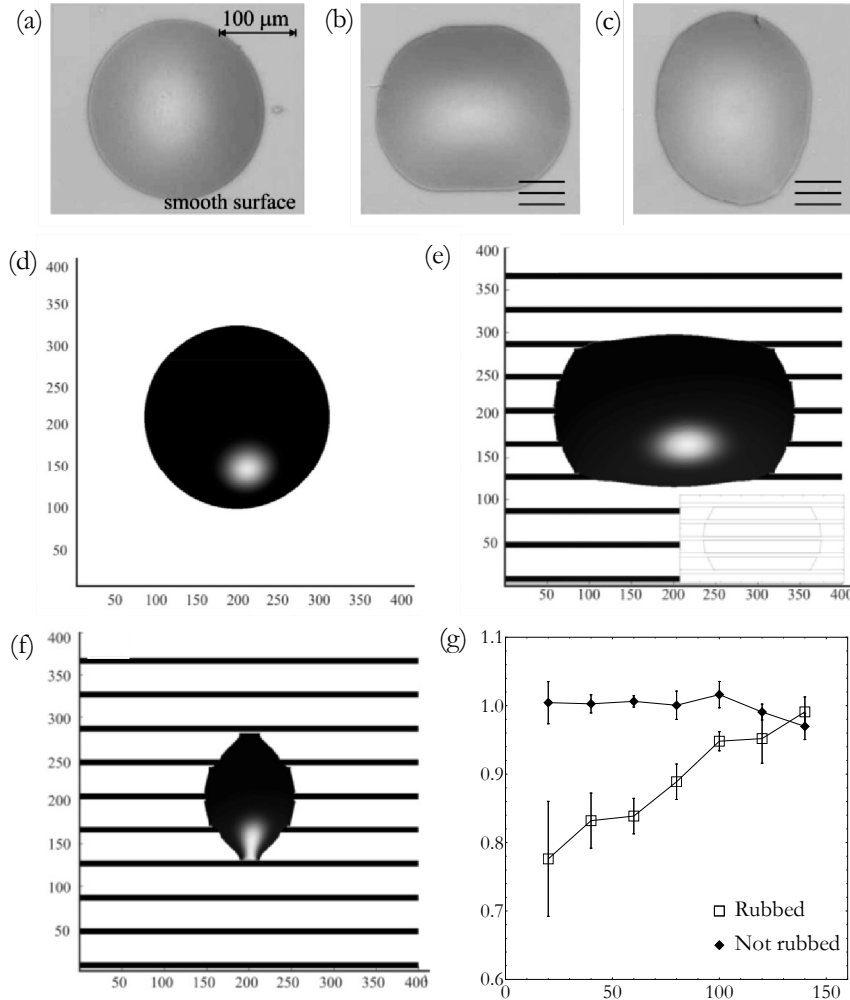


Figure 3.6: Typical drop shape observed in experiments when (a) there is no surface patterning, (b) the drop is sprayed onto the surface and spreads, and (c) the drop is stamped onto the surface and de-wets. The polyimide surfaces of (b) and (c) were patterned with sub-micrometer grooves (not visible, only schematically indicated). (d), (e) and (f) Lattice Boltzmann simulation results when (d) the drop spreads on a smooth surface, (e) and (f) the drop volume is quasi-statically (e) increased and (f) decreased. (g) Experimental measurements of the average elongation as function of printing temperature for the printed acrylate drops on rubbed and non-rubbed polyimide.

The pinning is illustrated in figure 3.7(a) as a specific instance of Gibb's criterion (section 2.5.3). For the drop contact line to advance, it has to wet the side of the grooves, which, according to the criterion occurs when $\beta_a = \delta + 90^\circ$ for rectangular ridges. More

generally $\beta_a = \delta + \alpha$ in two dimensions where α is the maximum inclination of the surface. In three dimensions, the value of the advancing (and receding - see below) angle is not as extreme as that predicted by the Gibbs criterion, due to the energy costs associated with the surface deformation from the spherical cap shape. The advancing angle perpendicular to the grooves is, nonetheless, generally larger than the advancing angle parallel to the grooves. As a consequence, it is easier for the drop to spread in the parallel direction and hence the drop shape is elongated parallel to the grooves as shown in figure 3.6(b). This is the final drop shape typically found in corrugated surface experiments.^{60,92,94} The shape of a drop on a smooth surface is also shown in figure 3.6(a) for comparison.

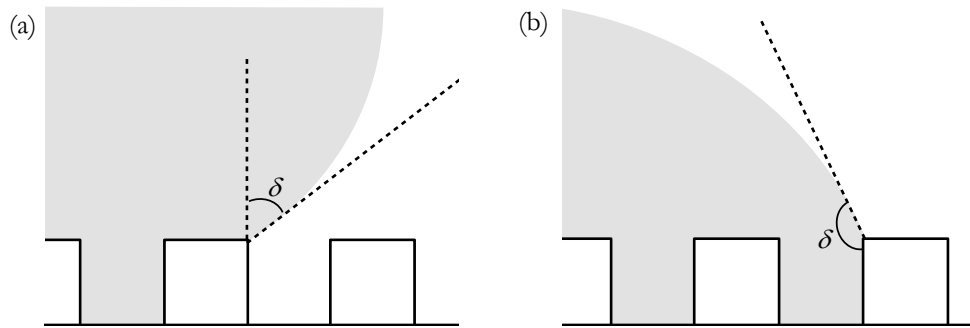


Figure 3.7: Graphical illustration of Gibbs criterion for the specific corrugated geometry employed in the simulations in this chapter, where the onset of (a) advancing and (b) receding motion of the liquid-vapour interface is depicted as the intrinsic contact angle is just reached.

When the drop is (micro-transfer) printed onto the surface, on the other hand, the drop contact line retreats to de-wet the surface, as the liquid is initially spread out much further than its equilibrium shape. This occurs when the drop contact angle is smaller than or equal to the receding contact angle. If no contact angle hysteresis is present, the final drop shape will be independent of the initial conditions. However, as discussed above, hysteresis is an important effect in the perpendicular direction and as a result the receding angles are again different parallel and perpendicular to the grooves. Contact line pinning for the receding motion is illustrated in figure 3.8(b). For the contact line to recede, the drop has to de-wet the side of the posts, which happens when $\beta_r = \delta - 90^\circ$ for rectangular ridges. For other geometries, $\beta_r = \delta - \alpha$ in two dimensions where α is the maximum inclination of the surface. Since the receding angle in the perpendicular direction is smaller than the receding angle parallel to the grooves, it is easier for the drop to de-wet in the parallel direction and the final drop shape is typically elongated perpendicular to the grooves, as shown in figure 3.6(c).

The effect of the printing temperature on the final shape of the printed drops showed

an interesting result, as shown in figure 3.6(g). With increasing temperature, the elongation perpendicular to the barriers decreases. The drops on non-rubbed surfaces have approximately spherical contact lines at all temperatures, whereas with decreasing temperatures the drops on rubbed surfaces become more and more elongated. In order to exclude the influence of temperature of the various surface energies, contact angle measurements were performed on drops over the whole temperature range. It was found that the contact angle did not change within experimental error $\pm 2^\circ$. Measurements of increasing the temperature of an individual drop gave the same result. Therefore, if any changes to the surface energies had occurred they approximately cancelled each other out.

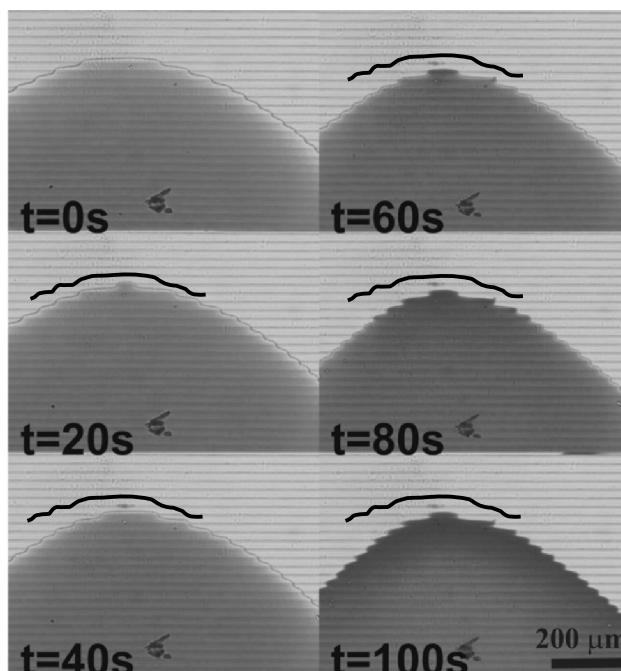


Figure 3.8: Microscope observation of the shape of the receding contact line as a water drop evaporates over time. The drop retreats predominantly parallel to the photo-embossed grooves until it becomes sufficiently distorted that it is favourable for it to retract, de-wetting one groove at a time. As a guide to the eye, the black line indicates the initial position of the contact line. 1 w/o Rhodamine-B fluorescent dye is added to the drop for visibility.

Clearly, the pinning ability of the barriers decreases at higher temperatures and the drop morphology is less affected by hysteresis. A possible explanation for this effect is that the viscosity at higher temperature decreases so that the drop in general and the contact line in particular move faster and dissipate less energy. Even without determining the exact barrier crossing mechanism, in general the interface can more easily overcome pinning on the ridges

by having more energy available for deforming its surface locally, enabling it to cross more barriers. This is further supported by simulation results, where a similar dependence of drop elongation on the drop viscosity and impact velocity is found. The typical drop elongation decreased as the drop viscosity decreased or the drop initial kinetic energy increased.

The mechanism by which the interface crosses the ridges can be envisaged as the nucleation mechanism as described by DeGennes: in this process an advancing drop will first form a nucleus in the next groove, after which the interface spreads along the grooves until a new and stable, but less elongated morphology is reached.² For drops retracting over the barrier, the inverse process occurs. The drop retreats parallel to the grooves until it becomes sufficiently distorted that it is favourable for it to retract and de-wet the outermost grooves. This retracting mechanism was also observed with evaporating water drops which were placed on a photo-embossed surface. This is shown in figure 3.8.

This interpretation of the role of contact line pinning in determining the drop shape is backed up by the experimental evidence obtained when considering a quasi-statically growing drop on a photo-embossed surface, shown in figure 3.9. The initial drop volume was 4 μl . Water was added with 0.06 μl per second causing a quasi-static, linear increase in volume. The surface had a pitch 80 μm and groove depth of 4.3 μm , i.e. an aspect ratio $\chi = 0.10$. The equilibrium contact angle of the surface was $\delta \cong 70^\circ$. The drop contact angles and base radii both parallel and perpendicular to the grooves are measured as a function of drop volume.

Three distinct features are visible in the figure: (i) the saw-tooth shaped variation with time of the perpendicular contact angle, (ii) the step-shaped variation of the perpendicular base radius and (iii) the absence of these distinct features in the parallel direction where the base radius increases continuously and the contact angle is roughly constant over the whole range of the experiment. Features (i) and (ii) are clear indications of contact line pinning in the perpendicular direction, while feature (iii) shows that pinning of the contact line due to the surface patterning does not occur in the parallel direction, leading to a significantly lower advancing contact angle. These features were reproduced for all aspect ratios and surfaces. For the receding contact line, no de-pinning was observed in the parallel direction, while de-pinning in the perpendicular direction occurred irregularly, with interfaces sometimes crossing multiple ridges at once. For this reason, reproducibly quantifying the de-pinning as function of the surface parameters was unsuccessful. It was found that, on the un-patterned surfaces, receding contact angle measurements give values of about 15° to 25° with occasional outliers of up to 50° . On the patterned surfaces, receding contact angle measurements in the parallel direction give similar values to those for the un-patterned samples, while the receding angles in the perpendicular direction are on average about 5° lower than those in the parallel direction. The high experimental scatter is attributed to the common problem of measuring very low receding contact angles, namely that incidental

pinning and de-pinning are observed even on (apparently) smooth surfaces. The base radii were also greater in the perpendicular direction, further proving that hysteresis is increased by the barriers.

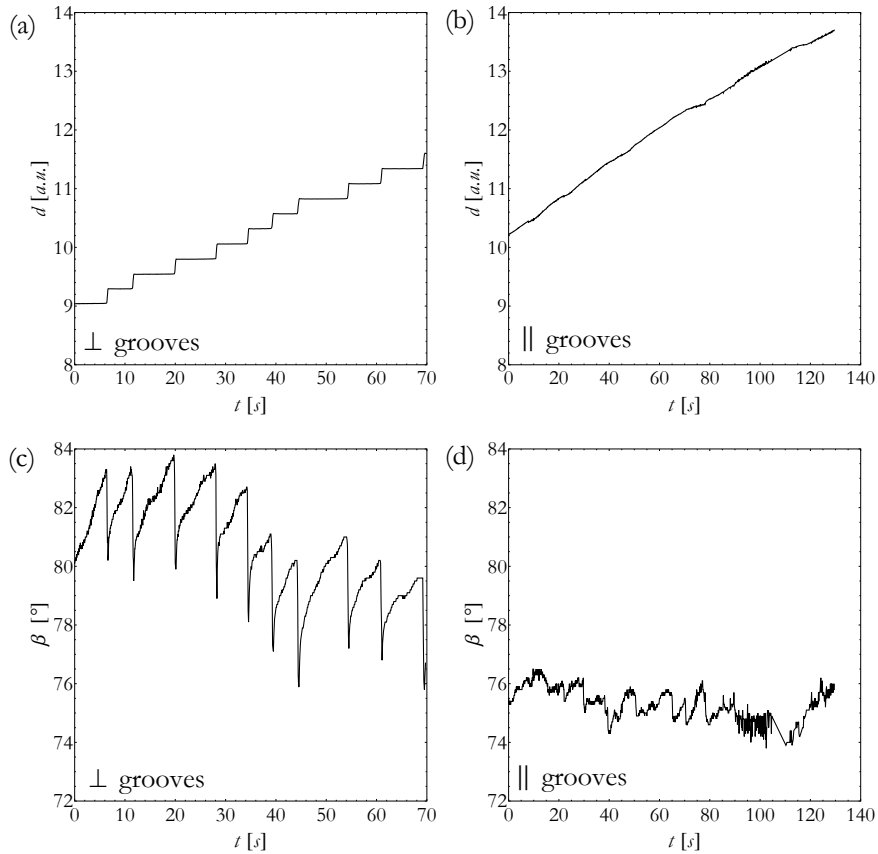


Figure 3.9: Advancing contact angle measurement for a drop of water spreading on a photo-embossed surface. (a) and (b) are measurements of the base diameter (in arbitrary units because the setup was not length-calibrated), while (c) and (d) are the contact angles as a function of time. (a) and (c) are the diameter and contact angle perpendicular to the grooves, (b) and (d) show the same variables parallel to the grooves.

3.4.2 Simulation results

In order to better understand the experimental results, lattice Boltzmann simulations were performed. A liquid drop was allowed to equilibrate on the corrugated surface. Then, using this as an initial condition, two sets of simulations were performed where the drop volume was quasi-statically increased in the first set and decreased in the second set. To do this, the liquid density was varied by $\pm 0.1\%$ from its equilibrium bulk density every 10^4 time steps.

This changed the drop volume as the system relaxed back to its coexisting equilibrium densities.

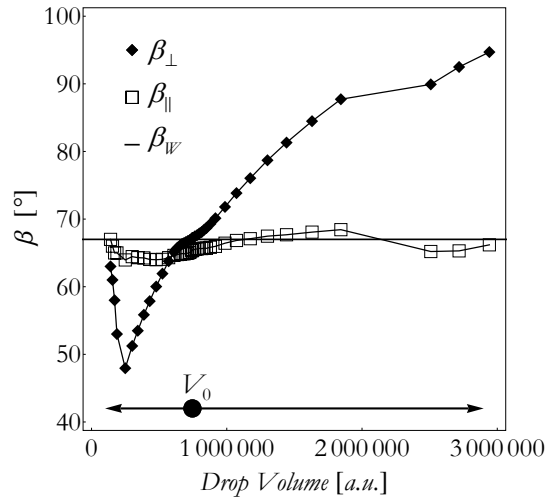


Figure 3.10: Simulations of drop contact angles on a grooved surface as a function of the drop volume for groove height $h = 3$, ridge width $w_r = 10$ and pitch $p = 40$. The solid line indicates the calculated Wenzel contact angle. The drop was initialized at $V_0 \sim 0.75 \times 10^6$ and equilibrated. Then the drop volume was either slowly decreased or increased, as indicated by the arrows.

When the drop volume is increased, the drop contact line advances. Therefore, it is expected that the first set of simulations mimics a drop sprayed onto the surface and the final drop shape to be elongated parallel to the grooves. When the drop volume is decreased, to the contrary, the drop contact line recedes. Therefore, the second set is expected to mimic a drop stamped onto the surface and the drop shape to be elongated perpendicular to the grooves. The simulation results shown in figure 3.6(d) and (e) clearly show that the drop shape is indeed elongated parallel and perpendicular to the grooves when the contact line is (d) advancing and (e) receding. The drop contact angles were also determined continuously during the simulation and the results are shown in figure 3.10. The main features indicating contact line pinning in the perpendicular direction are again reproduced: (i) the parallel contact angle stays roughly constant and (ii) a large variation in the perpendicular contact angle measurements is observed. Note, however, that due to numerical limitations, it is only possible to follow the drop as it moves over one groove so that the perpendicular contact angle in figure 3.10 shows just one period of the repeating saw tooth pattern obtained in the experiments in figure 3.9(c). In the figure the receding contact line jump in the perpendicular direction occurs at $V \sim 0.3 \times 10^6$.

3.4.3 Discussion

The experiments and lattice Boltzmann simulations are found to agree well qualitatively. No quantitative comparison was attempted, given the differences between the physical parameters of the lattice Boltzmann drops and experiments, as described in section 2.6. Also, the surface geometry used in the simulation was necessarily different than the two types of surfaces used experimentally. The overall morphology of the final drop shapes after advancing and receding contact line motion can be understood theoretically by considering the Gibbs criterion. Also for quasi-statically advancing contact lines the main features of both experiments and simulations agree well. This lends confidence to the fact that the mechanisms here described are universal, and agree with the observations in literature as cited at the beginning of section 3.4.1. The differences in surface geometry are further explored in the next section and will be discussed in more detail there.

3.5 Drops spreading on corrugated surfaces: understanding the contact angle measurements

In this section we will attempt to provide a consistent picture of the geometry of a drop spreading on corrugated surfaces as a function of a wide range of surface parameters. In particular, this sheds light on the influence of three dimensionless surface parameters: the roughness factor, the aspect ratio of the barriers and the relative ratio of the dimensions of the drop to the dimensions of the barriers. Conclusions will be drawn from both experiments (3.5.1) and lattice Boltzmann simulations (3.5.2), followed by a comparison between both (3.5.3).

3.5.1 Experimental results

In order to simplify the experimental analysis, only the two principal directions are studied: parallel and perpendicular to the grooves, since the greatest difference in contact angle is expected between these two, as determined in the previous section. Figures 3.11(a) and (b) show the experimental results on how the drop elongation and contact angles depend on the aspect ratio. In this second set of experiments, photo-embossed surfaces are prepared having different corrugations and water drops were placed onto the surfaces with a syringe. Initially, no obvious relationship between the final drop geometry and either the groove depth or the groove pitch was found. However, plotting the data against the aspect ratio of the corrugations, trends could be identified, although the scatter was significant. This is expected given the important role of hysteresis and the existence of multiple local energy minima. The data in figure 3.11 shows four features that are of interest here:

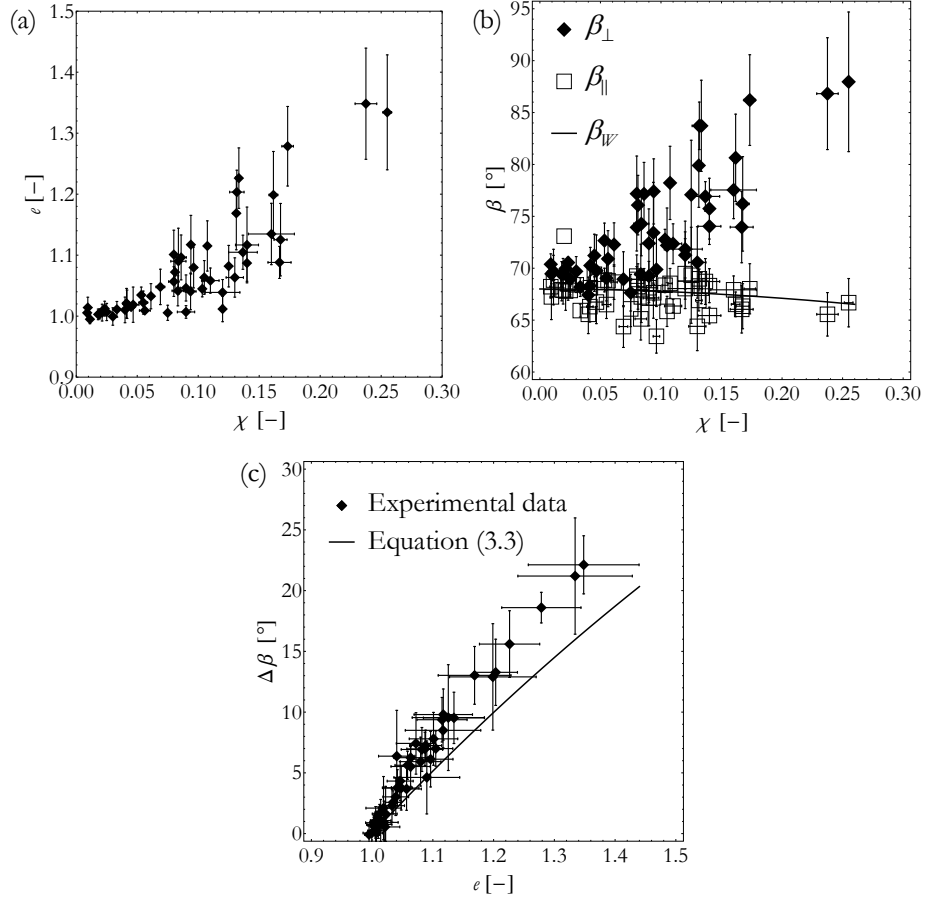


Figure 3.11: Experimental results for water drops on photo-embossed surfaces. (a) Elongation of the droplet and (b) Static β_{\parallel} and β_{\perp} as functions of the aspect ratio of the surface. Both the elongation and θ_{\perp} increase approximately monotonically with increasing χ . The solid line corresponds to the Wenzel angle. (c) $\Delta\beta = (\beta_{\perp} - \beta_{\parallel})$ as a function of elongation e . The solid line is the relation between $\Delta\beta$ and the elongation predicted by equation (3.3) and using $\beta_{\parallel} = \beta_{Wenzel}$.

(i) On chemically striped surfaces, it has been shown experimentally⁷⁹ and theoretically³⁰ that there is no contact angle hysteresis (at least due to the surface patterning) in the direction parallel to the stripes. Furthermore, Gleiche *et al.*⁷⁹ showed that the parallel contact angle is close to the Cassie-Baxter contact angle.⁵⁰ Similarly, in this study, it might be expected that the parallel angle approximately follows the Wenzel formula, as described in equation (2.20).

In the experiments the surface roughness parameter R can be approximated by

$$R \cong \frac{w_1 + \sqrt{w_2^2 + 4b^2}}{p}, \quad (3.1)$$

with the surface parameters as defined in figure 3.5. The equilibrium contact angle is $\delta \approx 68^\circ$. In figure 3.11(b) the Wenzel approximation is indeed shown to correspond well to β_{\parallel} . The same conclusion was also found by Chung *et al.*⁹²

(ii) The perpendicular contact angle, on the other hand, shows large scatter. Typically $\beta_{\perp} > \beta_{\parallel}$, and β_{\perp} tends to increase with χ . This may be explained using Gibbs criterion as discussed in the previous section. Since the drop spreads outwards on the corrugated surface, it is appropriate to consider the advancing contact line motion. Therefore, it is easier for the drop to spread parallel to the grooves. This immediately implies that the drop contact angle perpendicular to the grooves is larger than that parallel to the grooves. The maximum value of β_{\perp} is an estimate of the advancing angle in the perpendicular direction. For the two dimensional model illustrated in figure 3.7, $\beta_a = \delta + \alpha$, where α is the maximum slope on the surface. This is clearly an overestimate in three dimensions, since it neglects the energy costs associated with the surface deformation from a spherical cap. Nevertheless, from the data presented in figure 3.11, it was found that the advancing angle increases from 70° to 88° with increasing χ . This is consistent with the fact that, for the experimental substrate geometry in figure 3.4(e), the maximum slope α increases with the aspect ratio of the grooves. Similar behaviour is also observed Chung *et al.*⁹² in their figure 3.2(e).

(iii) The drop elongation e increases monotonically with χ . This result follows from the fact that the energy gain of spreading in the direction parallel to the grooves is higher for higher aspect ratio.

(iv) In figure 3.11(c), the difference between the contact angles $\Delta\beta$ as a function of the drop elongation is plotted. $\Delta\beta$ varies monotonically with drop elongation and the experimental scatter is reduced when compared to figure 3.11(a) and (b). Qualitatively this can be explained by assuming that the drop shape is close to elliptical. Assume for simplicity that the drop profiles in the two principal directions can be fitted to circles. In this case, the apparent contact angles can be written as

$$\tan(\beta_{\parallel} / 2) = b / a \quad \text{and} \quad \tan(\beta_{\perp} / 2) = b / b \quad (3.2)$$

where a and b are the drop base lengths in the two principal directions. As a result,

$$\tan(\beta_{\perp} / 2) = e \tan(\beta_{\parallel} / 2) \quad (3.3)$$

β_{\parallel} is approximately constant in the experiments and hence β_{\perp} increases monotonically with e . In figure 3.11(c), equation (3.3) is plotted assuming $\beta_{\parallel} = \beta_{\text{Wenzel}}$, and again it corresponds

well to the trend observed in the experiments.

3.5.2 Simulation results

To gain further insight into these relationships between surface and drop geometry, simulations were performed. The drop was initialised as a spherical drop just above the surface and was allowed to spread, without any external force, on the corrugated surface. The drop elongation and contact angles were then recorded after 4×10^5 time steps, by which time the drop had reached its (meta-) stable configuration. A typical final drop shape is shown in figure 3.12. As shown in figure 3.12(a) and (b) the drop cross sections in the direction parallel and perpendicular to the grooves can be fitted well with ellipses. It was attempted to fit the contact line around the base of the drop, see e.g. figure 3.12(c), but the typical fit that is obtained is poor: indeed, the top view of the drop clearly shows a corrugated contact line. The corrugation is more noticeable with increasing aspect ratio. This is because it is more advantageous to wet the sides of the grooves the higher the aspect ratio. This is similar to changing the wettability ratio between the hydrophilic and hydrophobic stripes on chemically striped surfaces.

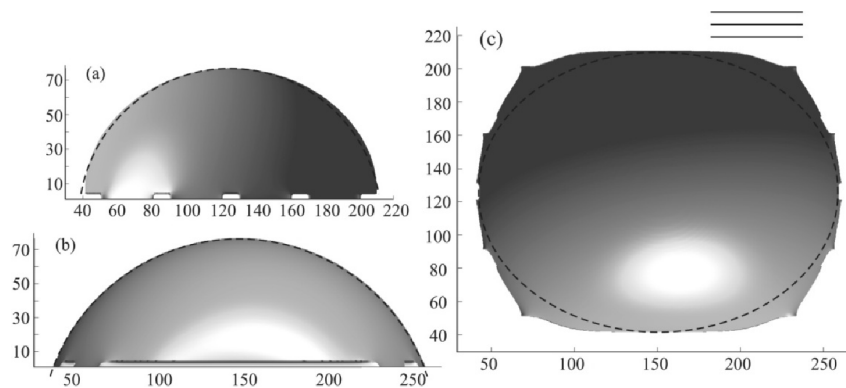


Figure 3.12: A typical drop shape observed in simulations. The drop cross sections in the direction perpendicular (a) and parallel (b) to the grooves. (c) Top view of the drop, with the direction of the corrugations indicated in the top right corner. The dashed lines are fits to a circle (a-b) or an ellipse (c).

Table 3.1: Drop contact angles and elongation for different groove heights for a drop left to spread unforced. The drop volume is $V \sim 7.47 \times 10^5$ and the groove width and pitch are kept constant at 30 and 40 lattice units, respectively. β_{Wenzel} is the theoretical Wenzel angle. Here the drops only lie on 4 grooves.

w_1	h	β_{\perp}	β_{\parallel}	β_{Wenzel}	e
10	3	67.2	65.4	66.8	1.03
10	5	65.9	61.7	64.7	1.08
10	8	62.8	57.5	61.4	1.11
10	10	58.8	52.9	59.1	1.13
10	15	43.6	37.4	53.2	1.18

The simulation results are presented in table 3.1 and figure 3.13. In interpreting the data it is important to note that there were two differences to the experiments dictated by computational requirements. Firstly, the dimensions of the simulated drop were comparable to the dimension of the grooves so that a drop lies on only 4 to 5 barriers. Secondly, the ridges were taken to be rectangular so that the maximum slope $\alpha = 90^\circ$ was independent of χ . The groove depth varied but the other parameters were kept the same. In the simulations

$$R = 1 + \frac{2b}{p}. \quad (3.4)$$

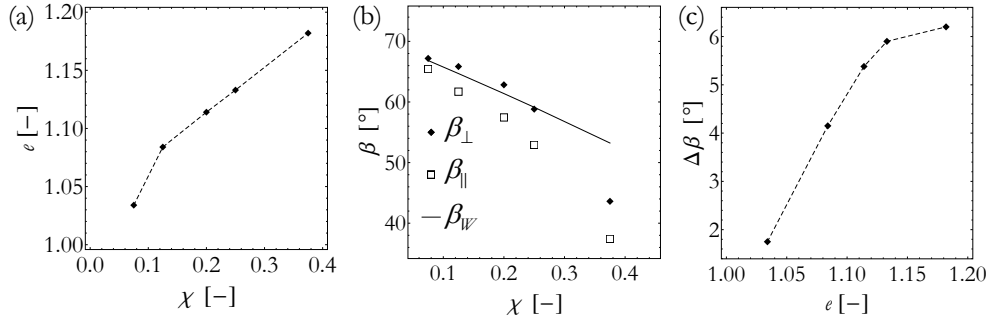


Figure 3.13: Lattice Boltzmann simulation results for drops spreading unforced on a corrugated surface. (a) Elongation of the droplet and (b) β_{\parallel} and β_{\perp} as function of the aspect ratio χ of the surface. The elongation increases monotonically with increasing aspect ratio, but both β_{\parallel} and β_{\perp} decrease. The straight line corresponds to the Wenzel equation. (c) $\Delta\beta$ as a function of the elongation e . (The dotted lines in (a) and (c) are guides to the eye.)

Of the experimental features listed in the previous subsection, (iii) the drop elongation increases with increasing χ , and (iv) $\Delta\beta$ increases with increasing e , and are reproduced in

the simulations as shown in figure 3.13(a) and (c). These trends are observed for the same reasons as in the experiments. The experimental trends (i) and (ii) are, however, not reproduced by the simulations for the following reasons:

(i) $\beta_{\parallel} \cong \beta_{Wenzel}$: in the simulations, shown in figure 3.13(b), the Wenzel angle is a poor approximation for the parallel contact angle, even though both simulations and experiments are in the same aspect ratio regime. The reason for this discrepancy is that the size of the heterogeneities is of the same order as the size of the drop. Since the drop only lies on a small number of grooves, the Wenzel equation is not applicable. For this reason a second set of simulations was performed where the size of the ridges is an order of magnitude smaller than the drop, as shown in table 3.2 and figure 3.14, which found that Wenzel equation is indeed a reasonable approximation to the parallel contact angle. In this case, the size of the ridges is comparable to the width of the interface in the lattice Boltzmann simulations and the roughness factor is much higher than that obtained in the experiments. In other words, as long as the typical length scale of the corrugation is much smaller than the drop size, the Wenzel equation is a good estimate of the parallel contact angle. The other main trends in figure 3.13(a) and (c) are again reproduced by this second set of simulations as expected.

Table 3.2: Drop contact angles and elongation for different groove widths for a drop left to spread unforced. The drop volume is $V \sim 7.42 \times 10^5$ and the barrier width and height are kept constant at 4 lattice units each. β_{Wenzel} is the theoretical Wenzel angle.

w_1	p	β_{\perp}	β_{\parallel}	β_{Wenzel}	e
4	8	57.6	45.4	46.8	1.31
6	10	61.0	52.0	52.0	1.21
8	12	59.3	54.7	55.2	1.10

(ii) $\beta_{\perp} > \beta_{\parallel}$ and β_{\perp} on average increases with increasing aspect ratio: from figure 3.11(b) it is indeed found that $\beta_{\perp} > \beta_{\parallel}$, however, from the data gathered so far, increasing the aspect ratio is not followed by an increase in β_{\perp} ; instead a decrease was found. The reason for this is believed to be the following: in the experiments, the roughness factor is close to 1 (at most 1.06, from equation (3.1)) and hence β_{\parallel} is typically just below δ . Furthermore, β_a increases with the aspect ratio since α increases with the aspect ratio. Since $\beta_{\parallel} < \beta_{\perp} < \beta_a$, β_{\perp} increases with increasing aspect ratio. In the simulations, on the other hand, R is considerably larger than 1 (between 1.15 and 2) and hence β_{\parallel} is much smaller than δ . Since the lower limit of the allowed values of β_{\perp} is decreased, it is plausible to find β_{\perp} decreasing with increasing aspect ratio in figure 3.11(b).

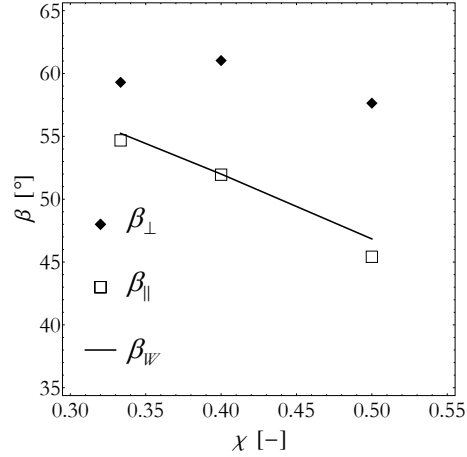


Figure 3.14: β_{\parallel} and β_{\perp} as a function of the aspect ratio χ of the surface. Here the size of the ridges is much smaller than the size of the drop. The solid line is the theoretical Wenzel angle.

3.5.3 Discussion

Of the four main qualitative aspects of the experimental data, three are clearly reproduced by the simulations. In order to show aspect (i), that the Wenzel angle is a fair approximation to the parallel contact angle $\beta_{\parallel} \cong \beta_{\text{Wenzel}}$, a second set of simulations had to be performed in order to increase the number of corrugations underneath the drop. The fact that this increase indeed led to the same behaviour as in the experiments further demonstrates that the Wenzel approximation of (2.20) is indeed only valid if the surface can be considered isotropic as far as the parallel contact line is concerned, since it can move freely over the surface to its minimum energy shape. The sole qualitative difference between experiments and simulations was the increase (experiments) versus the decrease (simulations) of β_{\perp} with increasing aspect ratio, which could be explained well in terms of the overall difference in surface roughness R . This difference indicates that the comparison between experiments and simulations has its limitations, but it is possible to explain these differences from theory.

3.6 Conclusions

In this chapter experiments and simulations were used to investigate the behaviour of drops on surfaces patterned with sub-micrometer and micrometer-scale parallel grooves. It was found that the final drop shape is highly dependent on the path by which it is achieved. Drops which advance across the surface are elongated parallel to the grooves whereas drops that de-wet the surface are elongated perpendicular to the grooves. This behaviour is

explained in terms of the pinning of the contact line on the groove edges. It should be stressed that it is not possible to measure a single contact angle for a drop on a patterned surface. The contact angle varies around the rim of the drop, with its position on the surface and with its dynamic history.

Contact angles and base dimensions were measured for drops spreading on corrugated surfaces. This was done for a large number of drops and substrate geometries. The data was quite noisy, underlining the prevalence of hysteresis on patterned surfaces. However, several conclusions could be drawn from the results. Firstly, the parallel contact angle is close to the Wenzel angle. The Wenzel angle in return depends on the roughness factor of the surface. Pinning effects render results for the perpendicular contact angles noisy but they are, in general, greater than the parallel angles and tend to increase with increasing aspect ratio. The difference between parallel and perpendicular contact angles increases with the drop elongation while the drop elongation increases with the aspect ratio. This behaviour is explained, again by considering contact line pinning, and by noting that the drop spreads more quickly in the parallel direction on surfaces with higher aspect ratio.

Lattice Boltzmann simulations of drop motion were of great use in interpreting the experiments. The same relation between the direction of elongation of the drop and its direction of motion over the surface was immediately apparent in the simulations, and it was possible to probe the pinning perpendicular to the grooves. Differences in detail between the simulations and experiments arose because the simulations are limited to drops lying on a small number of grooves. In particular, it is found that the Wenzel angle no longer provides a good estimate of the parallel angle when the drop dimensions are comparable to the dimensions of the corrugation. An interesting future project would be to perform experiments on wider grooves where a quantitative match to the simulations may be possible.

4. Drop shape analysis of contact printed thermotropic liquid crystal drops²

The sea closed over me. And then I heard plainly in my ears the sign of the god.

– Mary Renault, “The King Must Die”

² This chapter is published in:

- R. J. Vrancken, C. W. M. Bastiaansen, G. de With, D. J. Broer, *Drop shape analysis of contact printed thermotropic liquid crystal drops*, In preparation (2012)
- Mariette E. Koekoek, Thijs Meijer, Robert J. Vrancken, *Digital printing of multilevel optical variable Devices for Document Security & Brand Protection*, Proceedings of the Optical Document Conference II, 357-367, San Francisco, United States (2010)
- C. W. M. Bastiaansen, T. Meijer, R. J. Vrancken, *Security device with multiple authentication features*, PCT/EP2008/001924, Applicant Eindhoven University of Technology, Priority date filing 13-3-2007
- C. W. M. Bastiaansen, T. Meijer, R. J. Vrancken, *Inkjettable polymerisable liquid crystalline mixture*, PCT/EP2008/001868, Applicant Eindhoven University of Technology, Priority date filing 13-3-2007
- R. Vrancken, *Geometry of micro-transfer printed polymerised mesogen structures*, M.Sc. Thesis, Laboratory for Polymers in Advances Systems, Department of Chemical Engineering and Chemistry and Laboratory for Molecular Biosensors for Medical Diagnostics, Department of Applied Physics, Eindhoven University of Technology (2006)

4.1 Introduction

Since their invention polymerisable liquid crystals,^{100–104}, also known as reactive mesogens, have attracted significant academic interest over the past three decades. These materials typically possess useful anisotropic mechanical and optical properties arising from the liquid crystalline order. For practical applications utilizing these properties it is often a requirement that liquid crystal structures (drops, layers, etc.) can be ‘frozen in’, which can be achieved via the polymerisation. Their polymerisability also enables ease of processing in the monomer state and subsequent fixation into a solid state via photo- or thermal polymerisation. These properties therefore enable a number of interesting applications, including printed security features,^{105–108} micro-mechanical actuators driven by light¹¹ and patterned optical elements such as retarders and wavelength selective reflectors which can be used in for instance display applications.¹⁰⁹

A novel method of patterning is micro-transfer printing, which can enable these and other new applications.¹¹⁰ A key aspect of these applications is the need to control the morphology of the printed drops to achieve the desired optical, mechanical or other properties. Furthermore, the local orientation (alignment) of the liquid crystal molecules also has to be controlled for this reason.

In this chapter polymerisable liquid crystals are micro-transfer printed in the same manner as the isotropic liquid monomers (i.e. amorphous) in chapter 3. The alignment of these polymerisable LC’s is often achieved by using rubbed polyimide with the same nanometer-size corrugations as in chapter 3. The effect of these anisotropic substrates is investigated experimentally and theoretically to distinguish between the effects of substrate anisotropy and anisotropy caused by the liquid crystal structure. From the literature it is known that this order significantly affects the shape of liquid crystal drops suspended in solution, but a theoretical description of sessile thermotropic liquid crystal drops on a surface is not available.¹¹¹ The analyses offer insight into the possibilities and limitations of drop morphology control required in the various demanding applications. The analysis is generally valid also for non-polymerisable liquid crystals, as will be shown below.

This chapter is structured as follows. In section 4.2 the relevant theory for the thermodynamic energetic contributions to the surface and bulk energies for these thermotropic nematic polymerisable liquid crystals is presented. In section 4.3 the experimental methods are described including the optical analysis of the type of alignment. In section 4.4 the micro-transfer printing results are presented. As these drops display elongation similar to those in chapter 3, the energetic analysis is then extended to include the liquid crystalline surface and bulk energies in section 4.5. The theoretical predictions are compared to the experimental results in section 4.6 and discussed in the context of the above-mentioned applications, followed by conclusions in section 4.7.

4.2 Theory

Liquid crystals are a class of liquids which exhibit certain ordering at the molecular scale analogous to regular crystals, except retaining the ability to flow as a liquid. The liquid crystal phase is found in a temperature range between a pure fluid (isotropic phase) and the solid phase. Pure materials with such a phase (or phases) are called thermotropic liquid crystals. Alternatively, certain materials exhibit liquid crystalline behaviour when dissolved in a solvent, which are called lyotropic liquid crystals. Multiple thermotropic liquid crystalline phases have been found, depending on the particular materials or mixtures of materials studied. The shape of the molecules is of influence on the type of ordering in the liquid crystalline phase. The most common shapes are rod-like and discotic (disk-shaped).¹¹² In figure 4.1 the two most relevant classes of rod-like phases are indicated schematically, namely nematic and smectic. The smectic phases exhibits long-range positional order in one direction as well as rotational order, whereas the nematic phase only exhibits rotational order. There are various types of nematic and smectic phases. In the following only thermotropic rod-like nematic liquid crystals are considered.

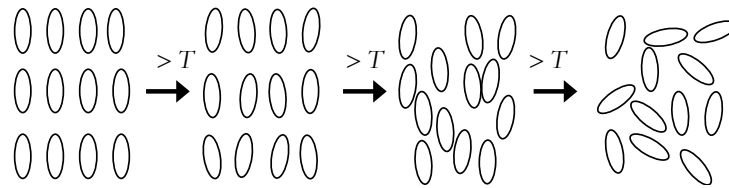


Figure 4.1: The various phases thermotropic liquid crystals can go through upon heating from left to right: (1) crystalline, (2) smectic, (3) nematic and (4) isotropic. The smectic and nematic phases are referred to as liquid crystalline phases as they have both an inherent order, but also translational freedom common to liquids. Not all liquid crystals exhibit both smectic and the nematic phases. Figure reproduced from ¹¹³.

Misalignment of the molecules in the bulk or at the surface requires more energy than being perfectly aligned. The orientation-dependent interaction energy terms between the molecules in the bulk, at the interfaces and at the contact line will now be described mathematically. This increases the number of Gibbs energy terms from section 2.4 which need to be considered to find the equilibrium shape of a drop on a surface.

The additional energy contribution associated with the local orientation of the molecules in the bulk is known as the elastic energy. In the case that the liquid crystals are uniformly aligned in the bulk, this elastic energy is constant. Only elastic energy contributions due to deviations from uniform alignment are further considered just like the average intra-molecular interactions described in section 2.4.1, which could also be disregarded for being constant. The elastic energy is defined as a volume integral

$$G_e = \frac{1}{2} \iiint \left(k_1 (\nabla \cdot \mathbf{n})^2 + k_2 (\mathbf{n} \cdot \nabla \times \mathbf{n})^2 + k_3 [\mathbf{n} \times (\nabla \times \mathbf{n})]^2 \right) dV, \quad (4.1)$$

where the elastic constants are associated with the three main types of deformation (misalignment), namely splay (k_1), twist (k_2) and bend (k_3) types of deformations, as shown schematically in figure 4.2. The local orientation is described by the director $\mathbf{n}(\mathbf{x})$, which is a vector defined locally at \mathbf{x} in the direction of the long axis of the elongated liquid crystal molecules. This equation is commonly known as the Frank-Oseen equation.^{114,115} When the orientation of the molecules is known locally as well as the elastic constants for the particular liquid crystal, the integral can be evaluated either analytically or numerically.

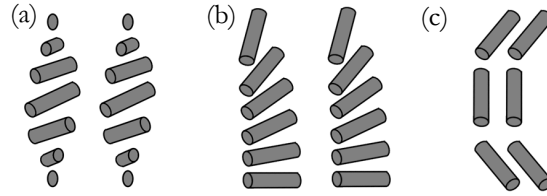


Figure 4.2: Three types of deformation of liquid crystals: (a) twist, (b) splay and (c) bend deformation.

The liquid crystal interfacial energy term is more complex than for isotropic liquids because of the various ways liquid crystals can align at the interface. Because this alignment is energetically determined, a straightforward way of describing the interfacial energy is commonly used in literature, known as the Rapini-Papoular equation¹¹⁶

$$G_{ij} = \sigma_{ij} \int \left(1 + \omega_{ij} (\mathbf{q} \cdot \mathbf{n})^2 \right) d\Omega_{ij}, \quad (4.2)$$

where the interfacial energy σ_{ij} can denote both the solid-liquid and liquid-vapour interfaces over area Ω_{ij} . Equation (4.2) is a generalisation of equation (2.7) specifically for liquid crystal surfaces. The first term between brackets is equivalent to the isotropic contribution to the surface energy. The energy associated with the anisotropic molecular alignment at the surface is found in the second term, where it scales with the inner product between the molecule orientation director \mathbf{n} and the surface normal \mathbf{q} . The dimensionless anchoring strength ω_{ij} indicates whether the molecules favour a position tangential ($\omega_{ij} > 0$) or normal to the surface ($\omega_{ij} < 0$). Tangential alignment is known as planar alignment, and a surface-normal orientation as homeotropic.

The contact line energy term for the local molecular alignment of a liquid crystal drop on a molecularly aligned substrate will vary locally as the contact line bends to form a drop. For this anisotropic contribution no formal description was found in literature, even though

it could be regarded as a surface line defect added to the regular line tension as was done empirically for interfacial contributions.¹¹² Considering that the contribution of molecular anisotropy to the total contribution (bulk, interface, line) is typically smaller than or on the order of the isotropic contribution, and that the contact line energy is not significant for the systems under consideration here, this contribution is disregarded.

4.3 Experimental methods

The liquid crystal drops were micro-transfer printed on rubbed and non-rubbed polyimide surfaces (JSR AL-3046). The printing method and surface preparation were identical to the methods described in detail in chapter 3. The only difference is that the print mixture consisted of polymerisable liquid crystal monomers instead of amorphous (isotropic) monomers. This enables quantitative comparison between the results. The print mixture consisted of 99.0 w%, polymerisable liquid crystal monomer 1,4-phenylene-bis-(4-[3-acryloyloxy]propyloxy]benzoate (known as C3M and obtained from Merck & Co GmbH under trade name RM257) and 1.0 w% photo-initiator 2-Benzyl-2-(dimethylamino)-4'-morpholinobutyrophenone (Irgacure 369, Ciba Specialty Chemicals) No planarization surfactants were added to the printed mixture. The molecular structures are shown in figure 4.3. Note that the isotropic monomer used in chapter 3 has structural similarity to the liquid crystal monomer.

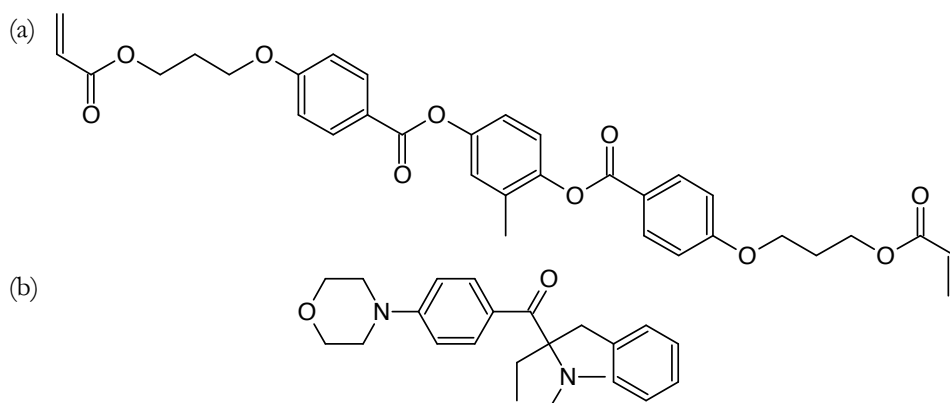


Figure 4.3: Molecular structure (a) polymerisable liquid crystal monomer 1,4-phenylene-bis-(4-[3-acryloyloxy]propyloxy]benzoate and (b) photo-initiator 2-Benzyl-2-(dimethylamino)-4'-morpholinobutyrophenone.

Due to their anisotropic bulk orientation, liquid crystals can exhibit anisotropic optical, mechanical and in certain cases electrically conductive properties. If all molecules are aligned along one axis, and the molecules are optically anisotropic, the resulting layer exhibits birefringence: the layer has different indices of refraction depending on the direction of propagation of light relative to the alignment of the molecules. For rod-like liquid crystals considered in this thesis, there are two indices of refraction n_o (the ‘ordinary’ index of refraction) and n_e (the ‘extraordinary’ index), the latter being parallel to the local orientation of the director \mathbf{n} .

It is possible to determine if and how liquid crystals are aligned locally by means of Polarised Optical Microscopy (POM), making use of the above described birefringent properties of liquid crystals. POM is described schematically in figure 4.4. Unpolarised light enters via a first linear polariser to linearly polarise the light. After passing through the birefringent liquid crystal sample, the light becomes elliptically polarised. The exact elliptical polarisation depends on the birefringence, sample thickness and the angle between the incoming polarised light and the optical axes of the liquid crystal sample. Finally the light passes through a second linear polariser known as the analyser, which has a polarisation direction turned 90° relative to the first polariser. If the front polariser is aligned with either the ordinary or extra-ordinary index of refraction (perpendicular or parallel to the director, respectively), no light will be transmitted. Thus, if the liquid crystals are aligned perfectly and exhibits no defects, the POM images will be completely dark under certain angles of rotation of the sample and will be uniformly bright under other angles. Multi-domain alignment or defects will be visible as areas of varying light intensity and without having a clear dark-state.

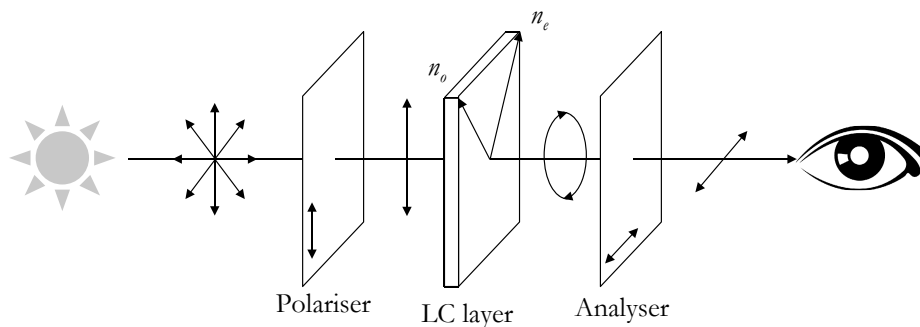


Figure 4.4: (a) Optical setup of Polarised Optical Microscopy (POM). Indicated are the ordinary n_o and extra-ordinary n_e refractive index of a uniformly aligned liquid crystalline layer.

4.4 Experimental results

In figure 4.5 the elongation as function of temperature is presented, which is similar to figure

3.4(g). The trend is consistent with the findings in the previous chapter: drops printed on the corrugated (rubbed) polyimide have $e < 1$ and drops printed on non-corrugated surfaces have $e \approx 1$. The order of magnitude of elongation is also similar, as is the increase in elongation with increasing temperature on the corrugated surfaces. However, the liquid crystal structure can potentially influence the shape of the drops, as the rubbed polyimide induces alignment in the liquid crystals. This is experimentally verified in figure 4.6 by means of Polarised Optical Microscopy as described in figure 4.4. Comparison with drops printed on non-rubbed polyimide (figure 4.5(c)) shows that these drops are also locally aligned, but there exist multiple separate ‘domains’, and turning the sample relative to the polarisers does not modulate the average transmitted intensity per drop as it does for the aligned drops (comparing (a) to (b)). This is indicative of multi-domain alignment, so that averaged over the drop there is no directional preference either parallel or perpendicular to the corrugations due to the liquid crystal structure.

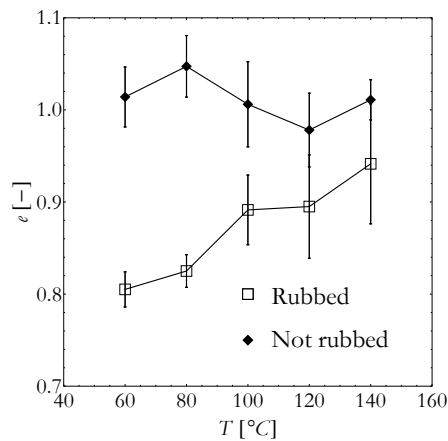


Figure 4.5: Elongation of micro-transfer printed liquid crystal drops on rubbed and non-rubbed polyimide. The elongation on rubbed polyimide decreases with increasing printing temperature.

The practical relevance of this elongation is considerable, as shrinkage of up to 20% ($e = 0.8$) requires considerable adjustments to the print patterns to be able to reproducibly recreate patterns. For instance, printing lines of equal thickness in both parallel and perpendicular directions will require placing the drops closer together in the parallel direction to ensure full coalescence and proper line formation. On the other hand, pinning of the interface on the grooves and ridges perpendicular to the rubbing direction can also decrease coalescence perpendicular to rubbing. Both these complications were observed in practice when printing patterns.

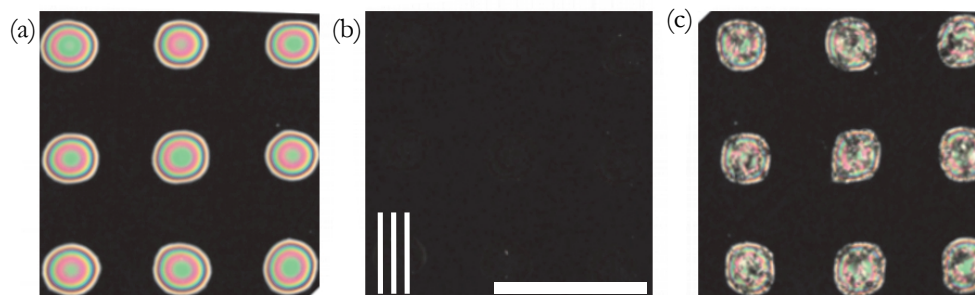


Figure 4.6: Printed liquid crystal drops observed with Polarised Optical Microscopy (POM), with the sample aligned at (a) 45° and (b) 0° to the front polariser. The rubbing direction in (a) and (b) is vertical. Also printed structures on non-rubbed polyimide (c) are shown. The drops printed on rubbed polyimide are elongated perpendicular to the direction of rubbing ($e \approx 0.82$), whereas the drops in (c) are not elongated on average. The scale bar in the bottom right corner of (b) indicates $400 \mu\text{m}$. The printing temperature was 80°C and the photo-polymerisation temperature was 20°C .

Two control experiments were performed to further validate the observations presented above. No variation in contact angles as function of temperature was found, examined with the same method and with the same result as for the isotropic monomers in section 3.4.1.

It was also determined that polymerisation shrinkage did not occur for these drops. Polymerisation shrinkage is often stronger for LCP's in the direction parallel to the director than perpendicular to it, typically on the order of 6% and 2% respectively.¹¹⁷ The absence of shrinkage was determined by two methods, namely by observing drop shapes pre- and post-polymerisation with microscopy, as well as performing real-time contact angle and base diameter measurements on macroscopic drops. In both instances, no shrinkage due to polymerisation was observed. There are two possible explanations for this absence. Firstly, at 20°C the degree of polymerisation will not be high, limiting the possible shrinkage. Secondly, the large surface-liquid contact area which pins the drop sufficiently so that no additional shrinkage is possible.

It is interesting to note that in practical applications it is therefore possible that polymerisation shrinkage induces latent stress in the material, which can be a cause for concern in applications where the substrate is flexible and will be concavely and especially convexly bent on a regular basis. Such applications can include e.g. flexible displays, and flexible anti-counterfeiting labels used on various product packaging or in banknotes and passports.

A tentative experimental observation was also made that micro-transfer printed drops of $10\text{--}15 \mu\text{m}$ elongate slightly parallel to the rubbing direction ($e \cong 1.05\text{--}1.10$), while printed on the same corrugated polyimide. This is clearly against the trend presented in figure

4.5 for the larger drops as well as the results in chapter 3. This result may indicate that there is a potentially significant counteracting elongation parallel to the corrugations due to the liquid crystalline order. However, the experimental setup in use currently is not accurate enough to determine the elongation reproducibly, since the force of application is poorly controlled, and furthermore only a minor drift of a few μm of the stamp during contact will introduce a high experimental noise. Manual application of the stamp or a slight angle between stamp and substrate can introduce such lateral shift. For the larger drops of figure 4.5 and 4.6 these factors were found to be the cause of some of the scatter in the data, but still giving reproducible and significant results. For this reason no statistical analysis of the elongation for smaller drops was performed. Therefore, the present results for smaller drops can be considered tentative at best, as will be further considered in the discussion (section 4.6).

4.5 Energy analysis

4.5.1 Two limiting cases of director profiles

In order to assess if the liquid crystalline order indeed influences the elongation of the drops, in this section an analysis of the energetic terms is performed. These terms determine whether and in which manner elongation is enhanced or decreased by the liquid crystalline order. Since the governing equations (4.1) and (4.2) are complex and no rotational symmetry is present, precise results will presumably only be obtained with numerical methods, which is beyond the scope of this chapter. Therefore in the following a simplified estimation is presented based on length scale arguments and omitting numerical pre-factors.

The first step is to describe the drop geometry and alignment in simple terms. The perfect dark state in figure 4.6(b) indicates that the director is aligned parallel to the rubbing direction (polar angle in the horizontal plane) at every point in the drop. This corresponds to the schematic in figure 4.7(a). Via polarised microscopy it could also be determined that the alignment at both interfaces was not homeotropic but planar or near-planar. Homeotropic alignment would be undesirable for most applications described before, and is not considered here further. For this reason $\omega_{ij} > 0$ at both interfaces is assumed in the following.

From literature it is known that lyotropic¹¹¹ as well as thermotropic¹¹⁸ liquid crystal drops can exhibit bipolar director configurations. The formation of such a structure depends on the interplay between surface anchoring and the various bulk elastic energetic terms, where effectively the surface anchoring dominates over the bulk deformation. No bipolar drops were found with POM. Such a bipolar configuration would resemble the schematic in figure 4.7(b). This configuration would be clearly distinguishable via polarised microscopy, as the drop would not exhibit a complete dark state (which was observed) but instead exhibit a

characteristic intensity profile (which was not observed). Furthermore, a quantitative investigation of the optical retardation for micro-transfer printed drops was presented in ^{105,109}, also confirming the absence of this bipolar configuration. The reason for this absence is ascribed to the strong anchoring of the liquid crystals at the solid-liquid interface.

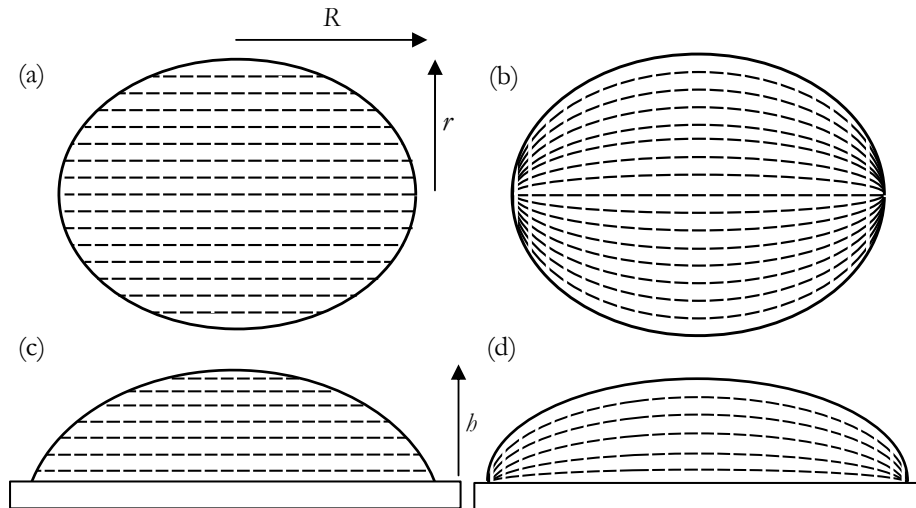


Figure 4.7: Different types of anisotropic director fields and their alignment to the surfaces. Top view of (a) a drop with planar parallel director alignment and (b) planar bipolar alignment. Side view of (c) Case 1 and (d) Case 2, as defined in the text. Note that Indicated are the parallel base radius R , the perpendicular base radius r and height h .

By excluding homeotropic and bipolar drops, only two director profiles are possible which agree with experimental data, as indicated in the top view configuration of figure 4.7(a). These cases are displayed schematically in figure 4.7(c) and (d) and are

- 1) the director profile \mathbf{n} in the bulk is aligned horizontally (planar) parallel to the alignment direction of the solid surface (4.7(c)) and
- 2) the director profile \mathbf{n} in the bulk is curved with liquid crystal alignment parallel to the alignment at the solid surface and also parallel to the liquid-vapour interface (4.7(d)). Note that Case 2 is *not* a bipolar drop. Although it resembles a bipolar configuration in side view, in top view it corresponds to figure 4.7(a) and *not* to 4.7(b).

For both cases, the geometric variables of the drop are also indicated in figure 4.7. These are an elliptic base with axis R parallel to the corrugations and r in the perpendicular direction. The height of the drop as measured from the surface is h . The horizontal elongation is $e = R/r$ and the dimensionless height is $\zeta = h/r$. The volume V is fixed and known and can be approximated as $V \approx Rrh = e\zeta r^3$ by omitting all numerical pre-factors in order to

simplify the expression. Such omissions will be made consequently further on as well.

Based on the microscopy data, deviations from the fully planar orientation in Case 1 due to dominance of the liquid-vapour surface anchoring energy over bulk elastic energy cannot be excluded. The reason that this is not easily observed with polarised microscopy is that $\zeta \ll 1$ so that only very detailed observations under small angles would enable determining whether Case 2 alignment would occur. This justifies the need to investigate Case 2 as well. Cases 1 and 2 can therefore be considered as the limiting cases for the director profile.

4.5.2 Surface energy estimates

First consider the interaction energy at the solid-liquid interface, which can be described equally for Case 1 and 2. The vector product is $(\mathbf{q} \cdot \mathbf{n}) = 1$ in case of planar alignment with the polar angle of the director fully aligned with the rubbing direction and zero azimuthal angle. Note that this was implicitly assumed in both Case 1 and 2. The polyimide used experimentally is chosen as it is known to induce planar alignment with only a small pre-tilt azimuthal angle of around 3° , although the exact pre-tilt does depend on the method of rubbing and is not determined in detail here. Even if the alignment is not perfectly planar but homogeneous over the surface, this product will be constant.

Therefore, equation (4.2), combined with (2.7), simplifies to

$$\tilde{G}_{sl} \approx \frac{((\sigma_{sl}(1 + \omega_{sl}) - \sigma_{sv})\Omega_{sl})}{\sigma_{lv}V^{2/3}} = e^{1/3}\zeta^{-2/3} \left(\left(\frac{\omega_{sl}\sigma_{sl}}{\sigma_{lv}} \right) - \cos\delta \right) \quad (4.3)$$

This definition is made dimensionless, as signified by the tilde on \tilde{G} , with respect to the liquid-vapour surface energy. This makes the definition independent of volume. Considering equation (4.3) it is likely that \tilde{G}_{sl} is negative, since it is assumed that $\delta < 90^\circ$, which is the case for the experimental results presented in figure 4.5 and in general desirable for printing applications. So unless $\omega_{sl}\sigma_{sl} > \sigma_{lv}$, i.e. ω_{sl} is on the order of one, increasing the elongation or decreasing the height actually gains energy, of course at the expense of increasing the liquid-vapour interfacial energy. If however $\omega_{sl} \sim 1$ then \tilde{G}_{sl} can be positive or negative, so that the impact of e and ζ on the total energy via \tilde{G}_{sl} can vary in that case.

Considering the alignment at the liquid-vapour interface, for Case 2 there is perfect alignment and $(\mathbf{q} \cdot \mathbf{n})^2 = 0$ in equation (4.2). For Case 1, an approximation of the vector product is made following¹¹¹ as

$$(\mathbf{q} \cdot \mathbf{n}) = \frac{b}{R} \frac{r}{R} = \frac{\zeta}{e^2}, \quad (4.4)$$

where an approximate average over the polar and azimuthal angles is multiplied. The liquid-vapour interface is estimated as $\Omega_{lv} = \Omega_{sl}(1 + \zeta)$, so expressing it as a function of the dimensionless height. This estimate is exact for $\zeta = 0$ and $\zeta = 1$ if $e = 1$ (this corresponds to $\delta = 90^\circ$), with the overall trend being correct for increasing ζ .

Combining the above, we find

$$\tilde{G}_{lv} \approx \left(1 + \omega_{lv} \left(\frac{\zeta}{e^2}\right)^2\right) \frac{e(1 + \zeta)r^2}{V^{2/3}} = e^{1/3} (\zeta^{-2/3} + \zeta^{1/3}) \left(1 + \omega_{lv} \left(\frac{\zeta}{e^2}\right)^2\right). \quad (4.5)$$

We can find Case 2 by setting $\omega_{lv} = 0$ in equation (4.5), even though it should be noted that this is perhaps misleading as the anchoring energy is actually so high that in fact the vector product (4.4) becomes zero). The dependence on e in (4.5) is complex: if $\omega_{lv} \ll 1$ (i.e. weak anchoring), increasing e will lead to an overall energy increase, but if the product of ω_{lv} and ζ^2 becomes of the order 1 then increasing e will lower this term and decrease the overall liquid-vapour energy. The summed term with two powers of ζ indicate that there is a minimum at intermediate ζ 's, which can easily be understood by considering that in the isotropic case there would also be an energetic optimum for an intermediate ζ since $0^\circ < \delta < 90^\circ$.

4.5.3 Bulk elastic energy estimate

Secondly, the elastic energy from alignment in the bulk is considered. In Case 1 there is perfect parallel alignment and the elastic energy is negligible. In Case 2, the mean radii of curvature of the drop in the direction of the alignment can be taken as an estimate of the typical length scales of the curvature of \mathbf{n} and used to estimate the derivatives in equation (4.1).¹¹¹ The mean radius of curvature for the splay deformation scales as $R = e \cdot r$, while the mean radius of curvature for the bend deformation scales as $e^2 r / \zeta$. Given the types of alignment, no twist deformation is expected as this would break symmetry and increase overall energy. It is not observed experimentally either. The individual elastic contributions can then be estimated as

$$\begin{aligned} G_{e,splay} &\approx \frac{k_1 V}{(er)^2} = \frac{k_1 \zeta r}{e} \\ G_{e,bend} &\approx \frac{k_3 V}{(e^2 r / \zeta)^2} = \frac{k_3 \zeta^3 r}{e^3}. \end{aligned} \quad (4.6)$$

In order to simplify further, the equal constants approach $k_1 = k_3 = K$ is employed, which is often applied and is justified by experiments where these values are commonly found to be within a factor 3 of each other (and since numerical pre-factors are already omitted).^{112,119} Making the energy dimensionless by dividing by the liquid-vapour interface energy yields

$$\tilde{G}_e = \frac{K}{\sigma_{lv}} \frac{1}{r} \left(\zeta^{1/3} e^{-5/3} + \zeta^{7/3} e^{-11/3} \right). \quad (4.7)$$

With increasing elastic constant K the elastic energy increases as expected. The drop can decrease this energy increasing its overall volume, as this decreases the radii of curvature, as becomes clear from the r in the denominator. At constant volume and for a given K , the drop can lower its elastic energy by decreasing its drop height or increasing its elongation, as both will reduce the intrinsic curvatures in the direction of the director field. While for the splay contribution (the first term in brackets) the dependency on drop height is not very strong, the bend deformation is quite sensitive to both elongation and drop height.

4.5.4 Energy minimization via Lagrange multiplier method

Now that simplified expressions for the various energetic contributions have been derived, the approximate energetic minima for Cases 1 and 2 can be calculated by using the Lagrange multiplier method using the volume as constraint. For Case 1 this results, after some calculations in

$$e \propto \left(5\zeta^2 + 6\zeta^3 \right)^{1/4} \left(\frac{\omega_{lv}}{1 + \frac{\omega_{sl}\sigma_{sl}}{\sigma_{lv}} - \cos\delta} \right)^{1/4}. \quad (4.8)$$

Note that e is independent of V (i.e. r), as is expected since only surface terms are considered (which all scale equally relative to the volume). With increasing ζ the elongation increases slightly less than linearly. With increasing anchoring strength ω_{lv} the elongation increases as well, more strongly if $\omega_{sl} \ll 1$ and $\delta \rightarrow 0^\circ$. Thus, with increasing ζ and δ the elongation increases. This is expected as both increase the overall curvature and thus average mismatch of the director at the surface. Increasing ω_{sl} will decrease the elongation however.

For Case 2 a more complex relationship is found:

$$e \propto \zeta^{1/2} \left(\frac{K + (K^2 + 6K\zeta r \sigma_{lv} (1 + \frac{\omega_{sl} \sigma_{sl}}{\sigma_{lv}} - \cos \delta))^{1/2}}{r \left(1 + \frac{\omega_{sl} \sigma_{sl}}{\sigma_{lv}} - \cos \delta \right) \sigma_{lv}} \right)^{1/2}. \quad (4.9)$$

Equation (4.9) is the reason for not considering an intermediate case between 1 and 2 with both strong liquid-vapour interface anchoring and high elastic energy, as the Lagrange minimization becomes unwieldy and offers only little further insight. With increasing ζ and K , the elongation increases, as the former increases the average curvature and the latter the energetic cost of curvature. Unfortunately the volume dependence on e is not easily perceived from (4.9) and it is easier to consider it from equation (4.7). Just as with the capillary length a relevant length scale here is the ‘elastic length’

$$L_e = \frac{K}{\sigma_{lv}}. \quad (4.10)$$

Table 4.1: Overview of the various constants and their impact on the director profile and drop elongation. Note that for $\omega_{sl} \ll 1$ it is still assumed that the surface induces sufficient alignment to avoid multi-domain director profiles.

ω_{sl}	ω_{lv}	L_e	Director profile	Impact on e
$\ll 1$	$\ll 1$	$L_e \gtrsim r$	Case 1 or 2 indetermined, possibly multi-domain	$e \sim 1$
$\gtrsim 1$	$\ll 1$	$L_e \gtrsim r$	Case 1 or 2 indetermined	$e \sim 1$
$\ll 1$	$\gtrsim 1$	$L_e \gtrsim r$	Case 2	$e > 1$
$\ll 1$	$\ll 1$	$\ll r$	Case 1	$e > 1$
$\gtrsim 1$	$\gtrsim 1$	$L_e \gtrsim r$	Case 2	$e > 1$
$\gtrsim 1$	$\ll 1$	$\ll r$	Case 1	$e > 1$
$\ll 1$	$\gtrsim 1$	$\ll r$	Intermediate between case 1 and 2	$e > 1$
$\gtrsim 1$	$\gtrsim 1$	$\ll r$	Intermediate between case 1 and 2	$e > 1$

The bulk elastic energy is significant for drops smaller than L_e . This is somewhat counter-intuitive, since in the case of gravity, the bulk contribution dominates at length scales

larger than the capillary length. The reason for this is that in the case of bulk elastic energy, the bulk energy per unit volume decreases with increasing drop dimensions due to the decrease in average curvature. As shown in (4.6) the elastic energy scales with r , whereas the surface energy scales with r^2 .

For both cases a number of relevant constants of proportionality and length scales are simultaneously relevant. Instead of discussing an exhaustive list per case, the main results from the energy analysis are summarized in table 4.1. The most important conclusion to be drawn from table 4.1 is that the liquid crystalline order, when planar or near-planar, will induce elongation parallel to the rubbing direction. For none of the cases considered here will elongation perpendicular to the surface be favourable with regards to the liquid crystal energetic contributions.

4.6 Discussion

The experimental observations indicate that drops of $\sim 150 \mu\text{m}$ consistently elongate perpendicular to the corrugations, although the degree of elongation decreases with increasing temperature. This data is quantitatively consistent with isotropic drops as experimentally and theoretically investigated in chapter 3. For drops that are an order of magnitude smaller, the tentative experimental data indicates that the drops elongate parallel to the corrugations instead. Energy analysis indicates that it is possible that this increase in elongation for smaller drops is caused by the bulk elastic energy. In this section the experiments and energy analysis are compared in more detail and discussed in the context of relevant applications.

In order to quantify the impact of the various energetic terms, it is necessary to use literature^{111,112,119} values as no exact data is available for the reactive mesogens used here. Typical order of magnitude values for non-reactive liquid crystals are $\omega_{sl} \sim \omega_{sl} \sim 10^{-5} - 10^{-3}$, $K \sim 10^{-13} - 10^{-11} \text{ N}$ and $\sigma_h \sim 10^{-2} \text{ Jm}^{-2}$. What is known for polymerisable liquid crystals is that highly splayed configurations can be achieved with very similar molecules by employing homeotropic alignment layers or surfactants which act at the liquid-vapour interface.¹¹ Such layers are typically tens of micrometers thick and can be up to several square centimetres large. Even though in no surfactant was used and no homeotropic alignment was found, it is not *a priori* certain that in the experiments bulk energy terms dominate over surface anchoring at either interface.

Anchoring at the solid-liquid interface was strong, as evidenced by the complete absence of bipolar orientation within the drop. Increasing the drop elongation in either direction does not decrease the total amount of solid-liquid anchoring energy, as it does not decrease the amount of solid-liquid surface. For this reason, even though $\omega_{sl} > 0$, this does not directly cause elongation but rather by imposing orientation on the director field it may

cause elongation indirectly via the other anisotropic contributions.

The impact of bulk elastic energy can be assessed from the literature values of non-reactive liquid crystals, by calculating $L_e \approx 10^{-11} - 10^{-9}$ m. These values indicate that both types of experimental drops presented above were considerably larger than L_e and that the tentative parallel elongation for the smaller drops would not be caused by the bulk elastic deformation. A very crude estimate is that an elongation of 10% would require r to be at most than one order of magnitude larger than L_e , which is still three order of magnitude smaller than the actual drop size. Furthermore, bulk elastic energy would only cause elongation if liquid-vapour anchoring energy is dominant (Case 2), as will now be discussed.

The most difficult parameter to quantify is ω_b . What has been done for suspended lyotropic drops of liquid crystals is to determine the shape of a drop together with the overall volume and then to observe the director profile.¹¹¹ These results are then used to fit ω_b . In the context of the present work this is not a viable approach, since the solid surface with its corrugations influences the drop shape. Also the available elongation data for the smaller drops is not of sufficient accuracy.

There are two reasons why ω_b is most likely too small to cause the parallel elongation:

The distinct perpendicular elongation found for the large drops. Since surface anchoring is an energetic term that is independent of volume it causes equal elongation on any length scale as long as the director is sufficiently aligned throughout the drop (Case 1). Secondly, the detailed experiments and simulations on surface corrugations indicate that decreasing the length scale of the drop one order of magnitude does not significantly decrease the effect of the surface corrugations as long as these corrugations are significantly smaller than the drop size in both instances. Therefore the effect on elongation of both surface corrugations and ω_b are independent of the size of the drops.

The literature values of $\omega \approx 10^{-5} - 10^{-3}$ indicate that the total effect of surface anchoring is at best three order of magnitude smaller than the ‘regular’ liquid-vapour interfacial energy. Since elongation clearly increases the liquid-vapour interface if the other drop parameters remain the same, a crude estimate would be that since $\Omega_b \propto r^2$ then $e \sim \sqrt{1 + O(10^{-3})} \approx 1 + O(10^{-3})$, which is much smaller than observed, within experimental error and lastly not crucial for most applications.

Considering the above, the tentative conclusion is that the observed parallel elongation for small drops is presumably caused by the printing setup and not by the influence of the liquid crystal alignment. It is therefore recommended to improve the micro-transfer printing setup to minimize human handling and placement of the sample and stamp to prevent any lateral shifts. A potentially more efficient method would be to use sprayed drops, as in chapter 3, on non-corrugated aligning surfaces such as linearly photo-polymerisable polymers (LPP’s), which are smooth surfaces that induce alignment purely by molecular interactions.

It is also recommended to quantitatively determine the surface anchoring energies and elastic constants for the polymerisable liquid crystal used in this chapter. The energy analysis presented above is sufficiently accurate to estimate the order of magnitude of elongation if these material constants are known. If elongation were to be desirable to a particular application, the analysis shows that liquid crystals with high elastic constants and/or high surface anchoring are required. In that case, the use of surfactants to increase ω_b is another option to increase the range of applicable liquid crystals.

4.7 Conclusions

The influence of liquid crystalline order on drop morphology was studied by micro-transfer printing of polymerisable liquid crystalline drops. It was found that drops of approximately 150 μm in diameter elongate perpendicular to the direction of the corrugations, comparable to non-liquid crystalline drops. However, anchoring of the liquid crystal director at either interface as well as the elastic energy needed for deformations in the bulk of the liquid crystal were shown theoretically to be able to induce preferential elongation parallel to the rubbing direction. From this theoretical energy analysis it is shown that tentative results for smaller drops of around 10 μm in diameter showing parallel elongation are likely due to experimental error and not from the liquid crystalline order. Suggestions to improve the experiments are presented, as well as a discussion on various potential consequences for industrial applications.



5. Fully reversible transition from Wenzel to Cassie-Baxter states on corrugated superhydrophobic surfaces³

“The river was clear and smoothly fast in the early morning. Down about two hundred yards were three logs all the way across the stream. They made the water smooth and deep above them.”

– Ernest Hemingway, “Big two-hearted river”

³ This chapter is published in:

- R.J. Vrancken, H. Kusumaatmaja, K. Hermans, A. M. Prenen, O. Pierre-Louis, C.W. M. Bastiaansen and D. J. Broer, *Fully Reversible Transition from Wenzel to Cassie-Baxter States on Corrugated Superhydrophobic Surfaces*, *Langmuir*, 26(5), 3335–3341 (2010). Reprinted with permission. Copyright 2010 American Chemical Society.

5.1 Introduction

The wetting properties of liquids have been a topic of interest for centuries.² Recently, it became clear that both the static and dynamical properties can be controlled via surface patterning. Superhydrophobicity is perhaps the prime example: by making the surface rough, the contact angle of a hydrophobic surface can be increased to more than 150° .^{120,121} The two possible states i.e. collapsed⁴⁶ and suspended⁵⁰ states on structured surfaces, exhibit clear differences in drop mobility. For a variety of applications (e.g. fluid motion control in microfluidics),¹⁶ it is therefore of great interest that reversible transitions between these states can be induced at will. Furthermore, in many cases, it is possible to render the surface effectively hydrophilic when the drop is in the collapsed state and as a result, the contact angle switches from close to 0° (superhydrophilic) to close to 180° (superhydrophobic). This active control of the wetting properties may be induced in a number of ways, for example, by electrowetting, light irradiation, or a change in temperature or pH.¹²²

Unfortunately, however, a reversible transition from collapsed to suspended states is normally difficult to achieve, due to the existence of (Gibbs) energy barriers between the states.^{123,124} In particular, it is the transition from the collapsed to suspended state that proves problematic, because the base of the liquid drop in the collapsed state cannot detach from the solid surface, as one needs to replace one interface (liquid-solid) with two interfaces (liquid-gas and gas-solid). In other words, this transition must occur via a different pathway. It is therefore the aim of this chapter to demonstrate a new and simple design paradigm, consisting of parallel grooves of appropriate aspect ratio that allows for a controlled, barrierless, and reversible switching of the wetting states upon the application of electrowetting. In this chapter a direct observation is reported of the barrierless dynamical pathway for the transition from the Wenzel (collapsed) to the Cassie-Baxter (suspended) state and a theory that accounts for the transition is presented.

So far, to the best of the author's knowledge, only Krupenkin *et al.* have unambiguously demonstrated a lifting transition by rapid heating of the substrate and evaporating part of the liquid into a vapour blanket beneath the droplet.¹²⁵ From here on, the collapsed to suspended state transition shall be called a *lifting* transition and the opposite transition as a *collapse* transition. Although this proves the concept of a lifting transition, the evaporation of liquid is impractical in closed systems such as switchable lenses,¹²⁶ micro-fluidic devices,¹²⁷ and displays.¹²⁸ Thus, a more practical dynamic pathway is desired for many applications.

Inspired by the findings in the previous chapter that parallel to a corrugated surface the surface patterning does not introduce any significant energy barrier for the moving liquid-vapour interface,^{78,80,92} in this chapter the possibility of the lifting transition occurring on such surfaces is investigated. To induce the transitions between the aforementioned wetting states, electrowetting is used,^{129,130} which has been shown to be applicable on

superhydrophobic surfaces.^{131,132} Lattice Boltzmann simulations are employed to identify the dynamical pathway of the lifting transition and estimate the conditions required to observe it. The outcomes of the simulations are used to assist in choosing the relevant experimental parameters to realize reversible and repeatable cycles of lifting and collapse transitions. These transitions are observed indirectly via contact angle measurements and directly by monitoring the motion of liquid/air interfaces under the water droplet during electrowetting.

5.2 Lattice Boltzmann simulation method

In the simulations reported here, the liquid drop and its surrounding vapour are again modelled using a one-component, two-phase fluid. The following parameters, as described in section 2.6.2, are chosen for the simulations: $\beta = 0.1$, $\kappa = 0.004$, $p_c = 1/8$, $\rho_c = 3.5$, and $\tau_w = 0.3$. These parameters give an interfacial thickness $\xi = 1.8$ lattice units, surface tension $\sigma_{lv} = 7.7 \times 10^{-4}$, liquid density $\rho_l = 4.1$, gas density $\rho_v = 2.9$ and liquid viscosity $\nu = 0.69$ (all in lattice Boltzmann units). The density ratio between liquid and gas is considerably smaller than in real systems. It is important to point out again here that a problem with many meso-scale simulations of liquid–gas systems is that interface widths are too large compared to experiments and the density difference between liquid and gas is too small. The result of this is that time scales are too fast,^{63,74} though comparisons with experiments so far have shown that the dynamic pathways are correct.^{71,74,76,78} This is actually advantageous since in this chapter the main interest is in the criterion for the lifting transition. Changing the values of the interface width, density ratio, surface tension and viscosity only changes the speed of the transition (i.e. how fast it occurs), but not the criterion itself. It is expected that the dynamics of the lifting transition to be slow close to the transition line. To minimize this dynamical effect, the lattice Boltzmann simulations are run for 10^6 time steps. For simulation parameters that allow the lifting transition, it is typically achieved in 2 to 4×10^5 time steps.

The lattice Boltzmann simulations are initialised as follows. A hemi-cylindrical drop with radius $R = 110$ lattice spacings, which is large compared to the size of the grooves, is placed in the Wenzel state on a grooved surface for a given intrinsic contact angle δ (local contact angle without application of electrowetting) and aspect ratio, defined as the height h divided by the width w of the groove. Then, the drop is equilibrated for 10^6 time steps. Simulating a cylindrical drop rather than a full, three dimensional, spherical drop makes it possible to reduce the system size and hence the computational requirements, while preserving the important physics, in particular a two dimensional curvature of the interface in the direction parallel to the grooves. The simulations are run for different values of δ and h/w . The simulation parameters for the surface contact angle and its corrugation are given in table 5.1. Further on a comparison to full three-dimensional simulation results is presented.

Table 5.1: Summary of the lattice Boltzmann simulations parameters.

δ	w	h	Lifting transition	δ	w	h	Lifting transition
110 °	10	15	Yes	120 °	30	8	No
110 °	10	14	No	130 °	40	20	Yes
110 °	10	12	No	130 °	40	16	No
110 °	10	10	No	130 °	40	14	No
110 °	10	5	No	130 °	40	12	No
120 °	30	30	Yes	130 °	40	10	No
120 °	30	27	Yes	140 °	50	15	Yes
120 °	30	24	Yes	140 °	50	10	No
120 °	30	22	No	140 °	50	5	No
120 °	30	15	No				

5.3 Simulation and theoretical results

In this section, the lattice Boltzmann simulation results are presented (figure 5.1) and it is shown how this leads to a simple criterion for the lifting transition to occur. The typical dynamical pathway for the lifting transition shows that, as the drop de-wets, the contact line moves considerably slower on top of the barriers than in the grooves, and the shape of the liquid-vapour interface that connects the two sides of the groove walls does not change much. The surface geometry is shown in figure 5.2(a). As the contact line recedes by dx , the system is essentially replacing $(2b + w_1)dx$ of liquid-solid interface along each groove of width w_1 with $(2b + w_1)dx$ of solid-vapour interface and w_1dx of liquid-vapour interface. Working out the surface energy balance, and employing Young's equation it is found that if:

$$\cos \delta < -\frac{1}{1 + 2(b/w_1)}, \quad (5.1)$$

the transition is energetically favourable. One can see from equation (5.1) that lifting only happens for $\delta > 90^\circ$, since $\cos \delta$ is always < 0 .

A lifting transition diagram is shown in figure 5.1(d) as a function of the aspect ratio b/w_1 and contact angle δ . Regions where the transition occurs and is suppressed are shown by diamonds and circles, respectively. The data points are obtained from the hemi-cylindrical lattice Boltzmann simulations detailed in table 5.1, where the solid black line is the analytical result given in equation (5.1). The agreement between simulation and theory is good, except that in the simulations for a given value of δ , the transition occurs at a slightly higher aspect ratio.

This discrepancy can be accounted for by further taking into account the finite size effects of the drop volume into account in the analytical model of (5.1). As in the simulations, a cylindrical drop is now considered instead of only the local interfaces in the channel. Furthermore, for simplicity, two assumptions are made. Firstly, the contact angle of the cylindrical cap is close to the Cassie-Baxter contact angle. Secondly, the shape of the liquid-gas interface in the groove can be approximated by a simple plane.

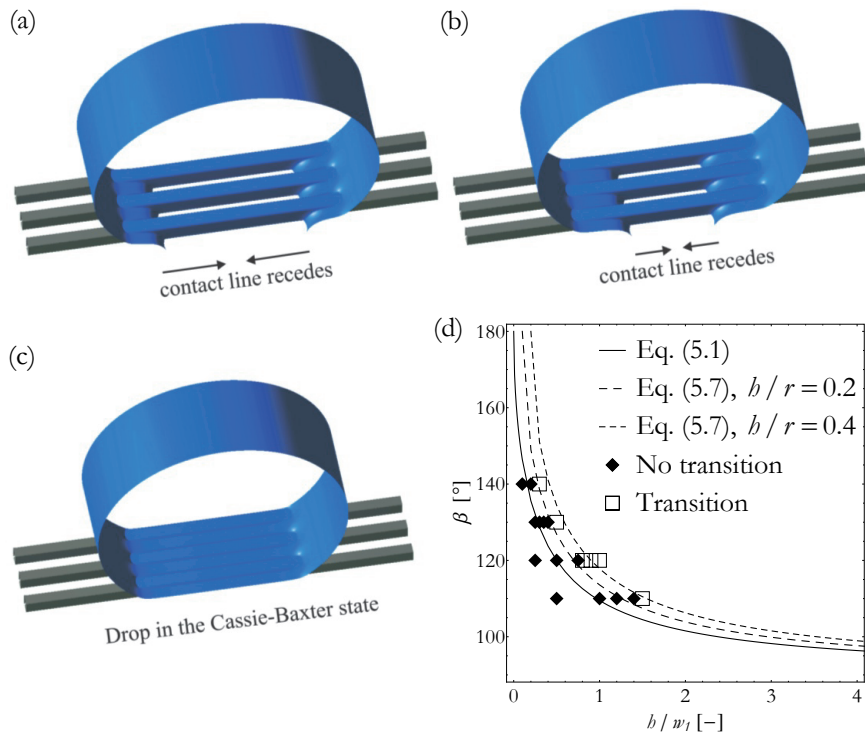


Figure 5.1: Lattice Boltzmann simulation results showing a lifting transition. The simulation results for cylindrical drops on parallel grooves: the drop de-wets the grooves and undergoes a lifting transition. The shape of the cylindrical drop is shown at (a) $t = 10^5$, (b) 1.5×10^5 , and (c) 2.5×10^5 . (d) The lifting transition diagram as a function of groove aspect ratio and contact angle. The solid line represents the theoretical prediction of equations (5.1) and (5.7). The lattice Boltzmann simulations results are shown in squares, where the transition occurs, and in diamonds where it does not occur.

For the geometry shown in the figure 5.2, the Cassie-Baxter contact angle is given by

$$\cos \beta_{CB} = \frac{\eta \cos \delta - 1}{\eta + 1}, \quad (5.2)$$

where $\eta = w_1 / w_2$ and the Cassie-Baxter parameter $f = \eta / (\eta + 1)$ according to equation (2.22). Under the assumptions described above, the total volume of the drop is given by

$$V = w_1 \left(\frac{1+\eta}{2} (2\pi - \theta + \sin \theta) r^2 + bl \right), \quad (5.3)$$

and the total energy reads (the energy of the bare substrate is subtracted):

$$E = (2\pi - \theta)(1 - \eta)w_1 r \sigma_{lv} + (2r \sin(\theta / 2) - l)w_1 [\sigma_{lv} + \eta(\sigma_{sl} - \sigma_{sv})] + 2bw_1 \sigma_{lv} + l[(w_1(1 + \eta) + 2b)(\sigma_{sl} - \sigma_{sv})]. \quad (5.4)$$

The four terms in the above equation account for the liquid-gas interface of the cylindrical cap, the base of the drop in contact with the composite solid/gas substrate, the liquid-gas interface in the channel, and the liquid-solid interface in the channel respectively. The angle θ is related to the Cassie-Baxter angle via

$$\theta = 2(\pi - \beta_{CB}). \quad (5.5)$$

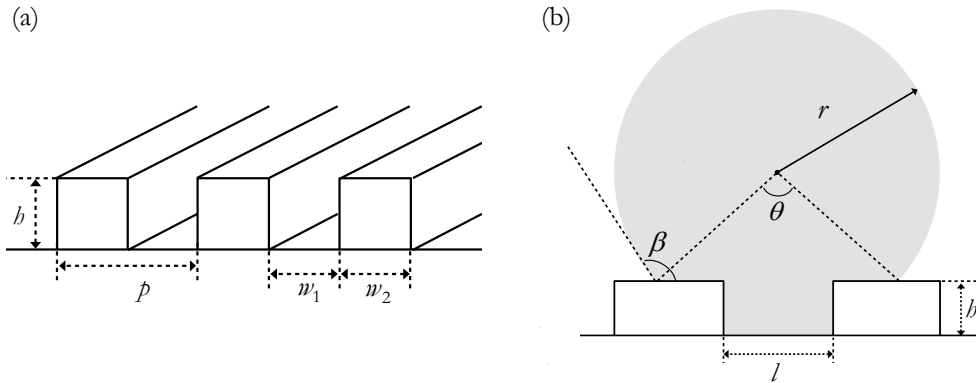


Figure 5.2: Schematic diagram of the geometry. (a) The surface pattern viewed along the corrugation. (b) The side view of the drop viewed perpendicular to the corrugations, where a part of the channel with length l has filled with liquid. Please note that $l \neq w_1$, as the (a) and (b) views of the surface are at a 90° angle. The geometric parameters of the finite size correction model are defined in the figures.

The Wenzel to Cassie-Baxter lifting transition occurs when $\partial_l E > 0$. Calculating the first derivative of E with respect to l and taking into account the volume constraint, we obtain

$$\partial_l E = w_1 \sigma_b \left(-\frac{h}{r} - 1 - (1 + 2h/w_1) \cos \delta \right). \quad (5.6)$$

The lifting transition requirement $\partial_l E > 0$ leads to the criterion:

$$\cos \delta < -\frac{1 + h/r}{1 + 2h/w_1}. \quad (5.7)$$

Compared to equation (5.1), the finite size effect of the drop volume adds an extra term h/r in the numerator. In figure 5.1(d) equation (5.7) is plotted for several values of h/r . The match between simulation results and analytical theory is improved considerably: the h/r term shifts the lifting transition to higher aspect ratio for a given intrinsic (Young's) contact angle. In other words, a smaller drop requires a more extreme geometry (higher aspect ratio) to enable the transition from the collapsed to the suspended state.

Qualitatively, these results provide a manufacturing guideline. For a lifting transition to occur there must be a dynamical pathway on which there is little contact line pinning (or contact angle hysteresis). When pinning or hysteresis is a dominant factor, e.g. in the direction perpendicular to the grooves or when the surface is patterned with rectangular posts, this type of dynamical pathway cannot be realized and the lifting transition cannot occur. Indeed, for the full three dimensional simulations of a lifting transition, it is observed that the contact line *only* de-wets in the parallel direction. Perpendicular to the grooves, the contact line is pinned. Equations (5.1) and (5.7) also dictate that the grooves aspect ratio must be high enough so that the suspended state is preferable.

In figure 5.3, a lattice Boltzmann simulation of the lifting transition is shown for a full, three-dimensional drop of radius 110 lattice spacings. At the beginning of the simulation (a), the drop is in the Wenzel state. The surface's intrinsic contact angle is 80° and the aspect ratio of the corrugations is $h/w_1 = 12/8 = 1.5$. The intrinsic contact angle is then changed to 120° and the drop undergoes a transition to the Cassie-Baxter state. Initially, the drop relaxes to a more spherical shape. Then (b) the contact line on top of the barriers halts its inward motion and does not move considerably any further. The liquid-vapour fronts inside the grooves, however, continue to recede in (c-e). In other words, the channels are filled with vapour. This motion can be seen by closely observing the indicated lighter parts of the channel. These regions decrease inward with time until finally (f) the two liquid-vapour interfaces annihilate each other. The lifting transition is now completed.

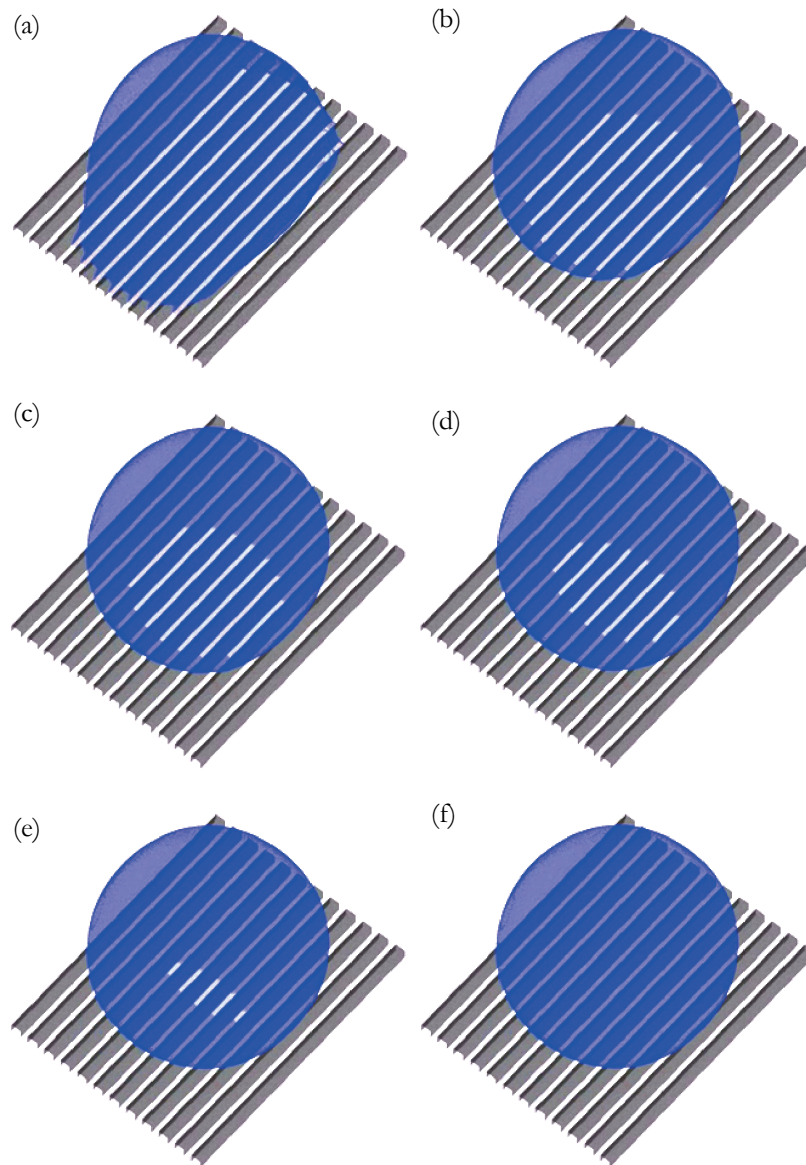


Figure 5.3: 3D lattice Boltzmann simulation of the uplifting transition. Starting in the collapsed state (a), with clear shape anisotropy (i.e. an elongated drop parallel to the corrugations) and filled channels, the drop slowly lifts up from the surface (b–e) as vapour is filling into the channels from the sides of the drop, visible as a decrease of the length of the wetted grooves (light areas underneath the drop). When the transition is complete (f) the whole channel is filled with vapour and the drop is in the suspended state and nearly spherical and not elongated.

5.4 Experimental methods

Photolithography was used to prepare corrugated surfaces with the desired aspect ratio as well as reference samples. Indium tin oxide (ITO) coated glass surfaces were coated with a thin layer of SU8 negative photoresist (MicroChem Corp.), the molecular structure of which is presented in figure 5.4, followed by a heating step (1 minute at 65 °C and 2 minutes at 95 °C). This first layer of SU8 was flood exposed with UV light to promote adhesion of the textured SU8 layer to the ITO surface. After crosslinking (1 minute at 65 °C and 2 minutes at 95 °C), a second SU8 layer with a thickness of 18 μm was applied. After a heating step, the SU8 photo-resist was patterned (30 μm line pattern) via standard photolithography which resulted in an aspect ratio b/w of approximately 1.4. A 300–500 nm PTFE coating (Teflon-AF, Dupont) was applied from solution on top of the structure to increase the hydrophobicity of the surface. The contact angle of the coated surface was $\delta = 110^\circ$.

Scanning electron microscopy (XL 30 ESEM-FEG, Philips) was used to image the surface structures. Before the SEM analysis, a 15 nm gold layer (K575 XD Turbo Sputter Coater, Emitech Ltd.) was applied on the sample to improve electron conduction. The aspect ratio was determined using confocal microscopy, (Sensofar, PL μ 2300) with a 50x objective.

To investigate the wetting behaviour of water droplets on the surfaces, the contact angle was measured (OCA-30, DataPhysics Germany) upon reversibly applying an electric potential of up to 150 V, by means of attaching the anode to the ITO layer and inserting the cathode (a small conductive pin) in the droplet from the top. The voltage was supplied by a Delta Electronica ES0300-0.45 power supply. Common tap water was used, having a moderate loading of dissolved ions. The anode clamp was attached to the ITO layer on the side of the sample.

To directly and unambiguously observe the lifting transition, optical microscopy was performed while performing electrowetting experiments on water drops *in situ*. The microscope was a Leica DM6000M (5x objective with 2x magnification), equipped with a Leica DFC 420C camera, used in bright field transmission mode. The transition was filmed in camera mode at 100 frames per second and saved as an uncompressed AVI file. Images from the movie were exported as JPEG via the VirtualDub editing freeware (version 1.9.0). The stills were prepared as TIFF figures in Corel PhotoPaint X3, converting to 32bit CMYK and resized to the appropriate resolution. No alterations to the contrast or intensity were made and care was taken to not introduce any visual artefacts.

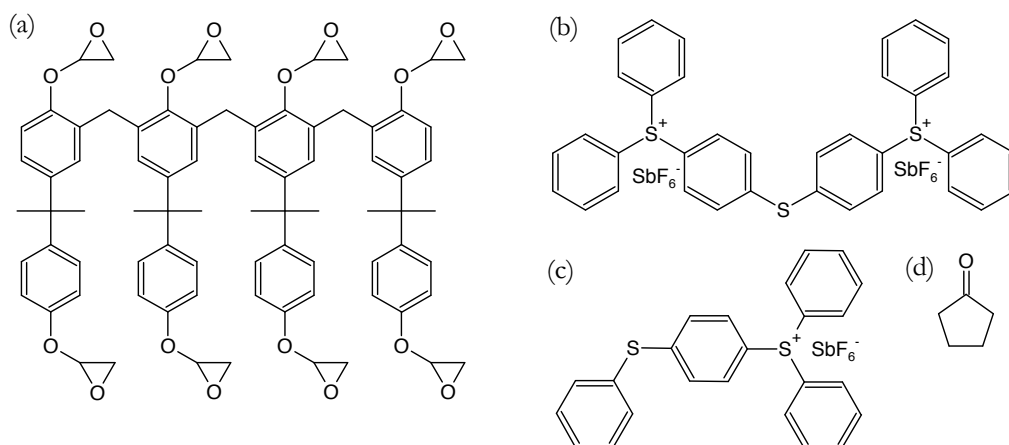


Figure 5.4: SU8 formulation as supplied. (a) SU8 monomer with 8 epoxy groups, (b-c) photo-initiators triarylsulfonium salts and (d) solvent cyclopentanone.

5.5 Experimental results

To investigate the wetting vapour of water droplets on the corrugated PTFE surface as shown in figure 5.5(a), the contact angle is measured upon reversibly applying an electric potential of 150 V DC. The electric voltage is increased linearly from 0 to 150 V in 30 s, kept at this voltage for 20 s for the drops to equilibrate, after which the voltage is reduced back to 0 V in 30 s. Figure 5.5 (b-d) shows the contact angle as a function of time on respectively a non-corrugated and corrugated coated surface. The water droplet goes through the above described electrowetting cycle multiple times. None of the surfaces displays any visual signs of degradation due to e.g. pinhole conductive paths in the coatings. The measurements show that the electrowetting effect on a smooth surface is nicely reproducible and with a large range of contact angles from 110° to 60° . This smooth and repeatable transition is also achieved on the corrugated surface. When the voltage is 0 V, the drop is in the suspended state, in agreement with equation (5.1). In fact, the value of the contact angle agrees well with the Cassie-Baxter angle of equation (2.22), with $f \sim 0.5$ and $\delta \sim 110^\circ$, we obtain $\beta_{CB} \sim 130^\circ$.

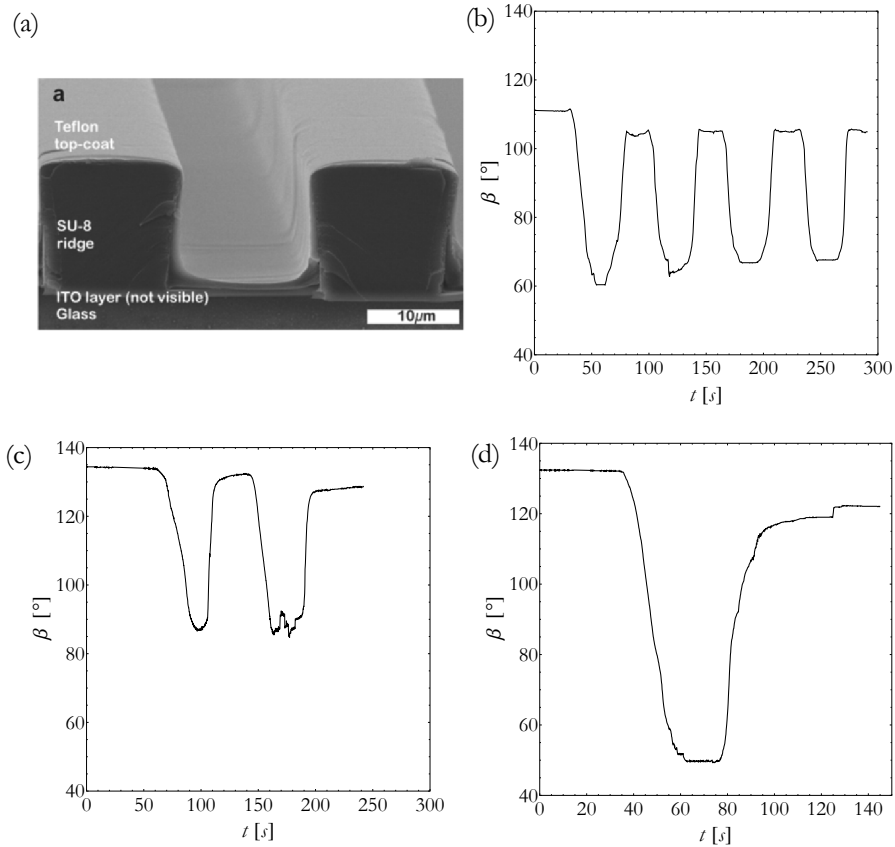


Figure 5.5: (a) SEM cross-section of a corrugated surface used in the electrowetting experiments. Contact angle measurements on a non-patterned (b) surface show that the contact angle varies between 110° and 60° , whereas on a patterned (c-d) surface the contact angle can be reversibly switched between 130° and 90° (perpendicular) / 50° (parallel) during electrowetting cycles. Contact angle measurements were done by automated contact angle fitting, employing an ellipsoidal drop profile. Using this method, the typical fitting error is $\pm 3^\circ$. The measurements in (c) and (d) are taken perpendicular and parallel to the grooves. Slight hysteresis does occur due to surface defects.

On the other hand, when the electrowetting potential is switched on, the surface acts as a hydrophilic surface with an intrinsic contact angle of 60° . The suspended state is no longer preferable and the liquid drop collapses. It should be noted that the drop shape in the collapsed state is quite elongated along the direction of the corrugations, and the contact angles are considerably different parallel and perpendicular to the corrugations, as expected from the results from chapter 3. The contact angles measured perpendicular to the corrugations (i.e. viewed along the corrugations) are shown in figure 5.5(c) as a function of

time. The contact angle varies from 130° to 90° . The contact angle measurements parallel to the corrugations are shown in figure 5.5(d) for one electrowetting cycle. In the Wenzel state, contact angle measurements yield distinct results parallel ($\sim 50^\circ$) and perpendicular ($\sim 90^\circ$) to the grooves. This is due to pinning of the contact line on the ridges, which prevents the drop from spreading out perpendicular to the channels.⁷⁸ In figure 5.6, this difference in elongation is shown from images captured by the OCA-30 contact angle setup during experiments.

Another important aspect of drops on surfaces is their sliding angle, i.e. the tilt angle at which a drop spontaneously starts moving due to gravity. While a fully controlled sliding angle experiment was difficult to perform since the cathode needle had to be kept properly inserted in the drop, the preliminary results confirm our expectations. Drops in the Wenzel state are stuck on the surface even when the tilt angle is increased to up to 90° . In contrast, drops in the Cassie-Baxter state exhibit motion for a sliding angle of less than 10° . Furthermore no significant difference is observed between the parallel and the perpendicular sliding angle for drops in the Cassie-Baxter state.



Figure 5.6: Side view of water drops during electrowetting experiment on a corrugated surface. The needle is seen inserted from the top. (a) The Cassie-Baxter (suspended) drop at $0V$ before actuation, with a base radius of approximately 1 mm . The Wenzel (collapsed) drop at $150V$ during electrowetting, viewed (b) perpendicular and (c) parallel to the grooves. The elongation of the drop parallel to the channels is clearly visible from the difference in base length and contact angle between (b) and (c).

As further evidence that the lifting transition has occurred, optical microscopy was performed on the drop while the drop underwent subsequent collapse and uplifting transitions. In figure 5.7, a drop is shown imaged by microscopy on a corrugated PTFE surface upon the application of an electrowetting cycle. At the beginning $t = 0:00$ of the experiment, an electrowetting potential of 150 V is applied. The water drop undergoes a collapse transition. This is observed from the outward movement of the liquid-vapour interface fronts in the channels. These fronts are black as they reflect light away from the optical path. Furthermore, the drop elongates along the direction of the channels. After maintaining the voltage at 150 V briefly until $t = 0:30$ when the voltage is reduced to 0 V Similar to figure 5.3, the drop then relaxes to a more spherical shape (higher contact angle state). The sample state is slightly repositioned to keep the drop in the frame. Starting at

$t = 1:41$, the liquid-vapour front start moving in the channel from the edge of the drop inwards, filling the channel with vapour. Contrary to the simulations, these fronts do not appear symmetrically from both ends of the channel, nor do they proceed at equal speeds. This is due to pinning of the interfaces in the channels, which is caused by defects and surface roughness in the channels. Nonetheless, it was clearly observed that in a number of channels the fronts from each side of the drop collide and annihilate one another. At the end of the experiments at $t = 4:55$, all channels are filled with vapour and the lifting transition is complete. After this the drop is motionless.

In the supporting information of ¹³³, available online via ¹³⁴ figures 5.3 and 5.7 are also available as movies.

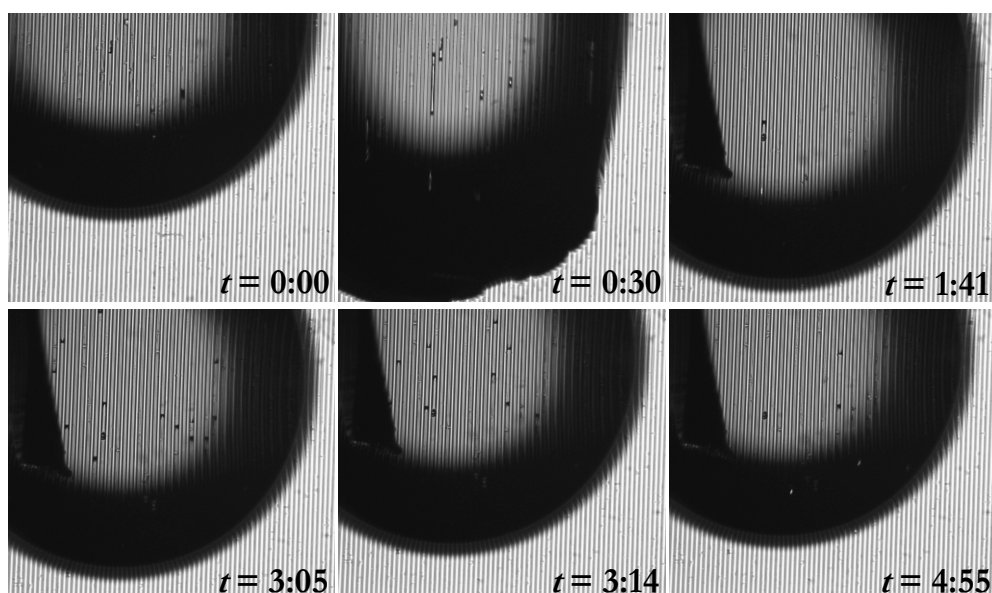


Figure 5.7: Optical microscopy images of the subsequent collapse and lifting transitions of a water drop at different times as indicated, starting with the application of 150 V at $t = 0:00$ and removal of the voltage at $t = 0:30$. The collapse and lifting transitions can be observed by monitoring the movement of the liquid-vapour interfaces underneath the water drop, which show up as dark spots in the channel due to refraction of light away from the optical path in the microscope due to the curvature (which also causes the dark edges of the drop).

5.7 Discussion

The possibility of a Wenzel-to-Cassie transition can be calculated from energetic arguments for this particular grooved geometry. The transition is possible if the channels are deep enough. The calculation disregards any viscous dissipation or local pinning of the contact

line in the channel. For this reason, quasi-2D as well as full 3D lattice Boltzmann simulations were performed including viscous dissipation, which agree well with the theoretical predictions. These results enabled the determination of the minimum aspect ratio of the channel to perform the experiments, which compared well with the theoretical prediction as long as corrections for the finite size of the channels were made.

The transition was observed experimentally for the first time using only electrowetting and spontaneous recovery. In the experiments viscous dissipation combined with local pinning were the causes of the long time scales (over 30 seconds) needed for the channels to be filled by air. Pinning in particular caused the speed and timing of the filling process to vary considerably from channel to channel as well as for a single channel. Finally all channels were filled with air and the process could be repeated several times.

The complementary nature of energy analysis, simulations and experiments was clearly demonstrated in this chapter. It will be of interest to further consider the effects of viscosity and pinning with these methods in order to optimize the experimental results. More complex geometries, such as radially oriented channels may be considered, even though these may have more limited applications. One particular benefit is the fact that if the drop is placed in the middle of this radial pattern, it will remain approximately circular during the electrowetting cycle. For use in optical elements this may be a useful property.

Combinations of parallel and radial corrugations are also possible, as long as these do not intersect, as this would cause a natural pinning site. Lattice Boltzmann simulations may be employed to guide future experiments to determine if and how many pinning sites are still acceptable for a drop to transition to the Cassie state or if this would lead to mixed wetting states.

5.7 Conclusions

In this chapter, it was demonstrated that repeatable and reversible transitions between the Cassie-Baxter and Wenzel states can be induced by using a combination of a corrugated surface and electrowetting. The directionality of the surface patterning is key here as it allows the contact line to de-wet the grooves with little or no energy barrier in the parallel direction, while it remains pinned in the perpendicular direction. By using lattice Boltzmann simulations as a guide in determining the required conditions the transition is realized experimentally on a PTFE coated surface patterned with parallel grooves. The transitions are verified by contact angle measurements and by direct observation using an optical microscope. Since both surface patterning and electrowetting are already commonly used, the design paradigm presented here is believed to be highly practical and it offers a clear opportunity to manipulate fluids in potential areas of applications, such as in the design of smart materials in micro-fluidics.

6. Anisotropic wetting and de-wetting of drops on substrates patterned with polygonal posts⁴

“Pythagoras: In all this world, no thing can keep its form. For all things flow; all things are born to change their shapes. And time itself is like a river, flowing on an endless course. Witness: no stream and no swift moment can relent; they must forever flow; just as wave follows wave, and every wave is pressed, and also presses on the wave ahead; so, too, must moments always be renewed. What was is now no more; and what was not has come to be; renewal is the lot of time.”

– Ovid, “Metamorphoses”

⁴This chapter is published in:

- R. J. Vrancken, M. Blow, H. Kusumaatmaja, K. Hermans, A. Prenen, C. W. M. Bastiaansen, D. J. Broer, J. M. Yeomans, *Anisotropic wetting and de-wetting of drops on substrates patterned with polygonal posts*, in preparation (2012)

6.1 Introduction

Driven by developments in surface patterning methods, there has been significant academic interest in recent years to control the spreading and flow of liquids using the surface properties of the solids with which they are in contact. It is now possible to produce complex surfaces with regions or patches of varying compliances, wettabilities and/or topological features.^{57,79,82,83,135–138} Not only do these structured surfaces provide useful model systems to explore fundamental issues such as contact angle hysteresis^{30,70,139} and three-phase contact line motion,^{140–143} but also understanding how liquids move on structured surfaces has led to many practical applications. In particular, one rapidly growing area of applications is micro-fluidics. For examples, chemically patterned surfaces may be exploited to generate mono-disperse drops,¹⁴⁴ or to separate drops⁸⁷ and capsules^{145,146} of particular sizes or stiffness in open micro-fluidic geometries; ratcheted posts have been designed to allow preferential fluid flow in one direction;^{140,147–150} numerous superhydrophobic surfaces have been fabricated to reduce drag and contact angle hysteresis.^{151,152}

In this chapter, our focus is to investigate the movement of the contact line of a fluid on surfaces patterned with polygonal posts. Courbin et al.¹⁵³ showed that the final shape of a drop spreading on a surface patterned with posts strongly depends on the arrangement of the posts: square drops are obtained when the posts are in a square lattice, and hexagonal drops when the posts are in a triangular lattice. The shape of the posts was not explored in the study of Courbin et al., but it was later investigated by Blow et al.^{154,155} using lattice Boltzmann simulations. It was found that the post shapes indeed play a role due to the anisotropy in the de-pinning mechanisms around the posts. Two distinct de-pinning mechanisms were described for a fluid being imbibed by this type of surfaces. Here we experimentally validate the existence of anisotropic wetting on surfaces with lattices of polygonal posts, as well as both de-pinning mechanisms. Furthermore, we extend the analysis to the retracting motion of the contact line as the fluid evaporates, which also exhibits two related de-pinning mechanisms. Interestingly we find that the preferential directions for spreading and retraction are the same for the surfaces investigated.

For our purposes a suitable experimental method for depositing the drops is inkjet printing, which is increasingly used as a versatile research tool.^{10,156–158} Here it allows us to deposit one or multiple drops on the patterned surfaces in a very controlled fashion. In this way we are able to quickly create a large number of drops with near identical conditions, in order to study small drops across multiple surfaces as well as obtain high reproducibility on a single surface, even for pico-liter droplets. A further advantage is being able to vary the total drop volume by printing multiple drops on one location of the surface, thereby looking at the evolution of the drop shape (in particular the contact line) with increasing volume.

The experimental results are compared to lattice Boltzmann simulations. The lattice

Boltzmann method is a meso-scale simulation technique which has been proven to be successful in predicting and understanding numerous wetting situations.^{74,78,159–161} The particular model we use is detailed in ^{72,73,162} (see also section 2.6.2). Alternative models are also available in the literature, see e.g. ^{67,163–165}.

This chapter is structured as follows: after a description of the experimental details of inkjet printing and surface preparation in section 6.2, an analysis of the various shapes of the advancing contact line for drops inkjet-printed onto variously patterned surfaces is presented in section 6.3. Also included in this section is a comparison to our previous lattice Boltzmann simulation results, including a detailed description of the related de-pinning mechanisms on a surface patterned with triangular posts on a hexagonal lattice. In section 6.4 the analysis is extended to retracting contact lines via evaporation experiments and simulations, combined with a theoretical analysis of the de-pinning mechanisms of the contact line. Finally in section 6.5 the main conclusions are briefly presented.

6.2 Experimental methods

Printing was performed using a MicroDrop inkjet printing system with a MD-K-140 glass capillary and nozzle of $98\ \mu\text{m}$ diameter (MicroDrop GmbH, DE). The electrical pulse supplied to the piezo-element was $100\ \text{V}$, with a $140\ \mu\text{s}$ pulse length. Deionised water was used as printing fluid, which created highly reproducible drops of around $200\ \text{pl}$, and the drops were ejected from the nozzle at $6\ \text{ms}^{-1}$, determined by the integrated camera system and software of the lab-scale inkjet printer. Substrates (see below) were placed under the inkjet nozzle in a fixed position, and a pre-set number of drops (up to 225) were printed onto the surface. Print frequencies varied from 1 to 200 Hz, so within just over 1 second even the largest surface drops studied here were completely formed. The stand-off distance between the nozzle and the surface was $1\ \text{mm}$.

The surfaces were created as in previous work^{133,166} by means of photo-lithography of SU8. First, a thin layer of negative photoresist of 3 to $5\ \mu\text{m}$ (SU8, MicroChem Corp.) was spin-coated from a solution of cyclopentanone onto standard laboratory glass slides which were cleaned in ethanol and subsequently dried in nitrogen. Secondly a heating sequence on a hotplate was performed (1 minute at $65\ ^\circ\text{C}$ followed by 2 minutes at $95\ ^\circ\text{C}$) to remove the solvent, while the sample was simultaneously flood exposed with UV light (Exfo UV source) to promote adhesion of the SU8 surface texture. Subsequently a second layer with a thickness of $18\ \mu\text{m}$ was again applied and dried without exposure to flood-UV. Then, the SU8 layer was exposed to UV-light via contact lithography with a quartz-chrome custom lithographic mask. The mask was patterned with various post geometries (circle, square, triangle, hexagon) and two lattice types (hexagonal, square) at various post sizes and lattice spacings, while the post height remained fixed by the layer thickness of $18\ \mu\text{m}$. Following

exposure, a second heating sequence similar to before was employed to crosslink the exposed areas of the layer, followed by slow cooling. The non-exposed parts were then removed by a custom developer (mr-dev 600, MicroChem Corp.), after which the sample was rinsed by isopropanol and blown dry with a mild nitrogen flow. Reference samples of SU8 with a smooth flat surface were created via the same procedure without the second patterning step.

The intrinsic contact angle δ was measured by contact angle measurement setup (OCA30, DataPhysics Germany) to be $80 \pm 3^\circ$. After printing, the drops were imaged by optical microscopy using a Leica DM6000 M (20x objective with 1x additional magnification), equipped with a Leica DFC420C camera in bright field transmission mode. Images from the movie were exported as jpeg files via VirtualDub video editing freeware (version 1.9.0) and subsequently analyzed.

The sample with water drop printed on top was moved to the microscope manually with care, within 20 to 30 seconds after printing was completed. The drop and surface were subjected during movement to minor mechanical vibrations. The impact of these mechanical vibrations was found to be negligible, as reproducibility of the drop shape during several identical experiments was found to be within experimental error. Similarly, by moving the same sample with drop multiple times, no differences in drop shape were observed. One reason for this is the fact that after printing, the drops are in the collapsed ('Wenzel') state,⁴⁶ which means that a large portion of the total drop interface is in contact with the surface and such Wenzel states are known to be quite immobile due to contact line pinning and hysteresis.

After being placed under the microscope, the drops start to evaporate considerably faster than under ambient conditions, due to the heat of the additional transmitted light. While this heat flux is not strictly regulated, it is constant per unit time during a measurement and between measurements as long as the optics of the microscope (diaphragm, light intensity, magnification) are not changed. Typical evaporation times are between 30 seconds and 5 minutes, depending on drop volume. This increased evaporation is beneficially utilized in the experiments with receding contact lines.

6.3 Advancing drop shape anisotropy

6.3.1 Experimental results

Drops which are inkjet-printed on surfaces patterned with polygonal posts exhibit a variety of typical shapes, depending on the lattice type, post shape and size. In figure 6.1, a number of typical shapes are shown.

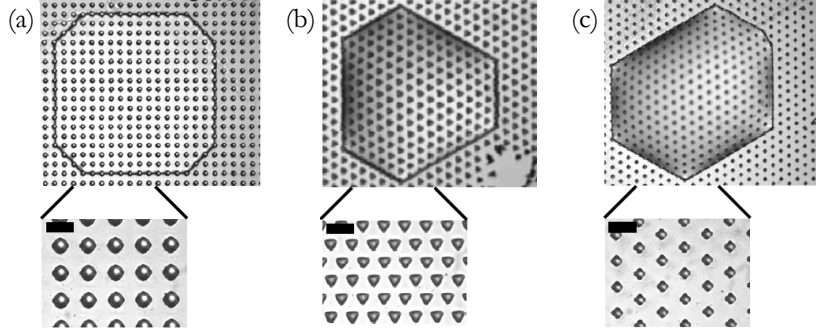


Figure 6.1: Microscopic images of various drop shapes on different types of lattice. An inset with a magnification of the posts is placed below each image. The black scale bar indicates $20\ \mu\text{m}$. (a) An octagonal drop on a square lattice with diamond shaped posts, $b = 10\ \mu\text{m}$, $d = 20\ \mu\text{m}$. (b) A drop with a shape intermediate between a hexagon and an equilateral triangle on a hexagonal lattice with triangular posts, $b = 7.5\ \mu\text{m}$, $d = 15\ \mu\text{m}$. (c) An irregular hexagon on a hexagonal lattice with diamond shaped posts, $b = 7.5\ \mu\text{m}$, $d = 20\ \mu\text{m}$. Due to curvature of the liquid-vapour interface, the posts below the drop in (b) and (c) look slightly distorted and out of focus, whereas the drop in (a) was imaged after prolonged evaporation just prior to initial retraction of the contact line (due to de-pinning) and therefore had a nearly horizontal liquid-vapour interface.

From studying the various shapes of the drops in figure 6.1, and other drops on a variety of surface geometries, we find that the primary determinant of drop shape is the lattice type and the secondary determinant is the post shape. Due to the lattice type, the shape of drops on square lattices is typically square or octagonal, whereas on hexagonal lattices drops are typically shaped close to regular hexagons. These observations agree with and further confirm the mechanisms previously elucidated, e.g. in ^{70,153,154}. When spreading on a surface patterned with posts, the contact line has to overcome an energetic penalty in order to wet the next row of posts. When it is finally able to reach such a new row, the adjacent posts are quickly wet, akin to the unzipping mechanism identified by Sbragaglia *et al.*¹⁶¹

As a consequence, the rotational symmetry of the drop shape is typically the same as the symmetry of the lattice. In 6.1(a) and 6.1(b), the rotational symmetry of the lattice is 4-fold and 3-fold respectively. The edges and faces of the posts are aligned to the lattice with the same rotational symmetry, and as a consequence the drop shapes are indeed approximately 4-fold and 3-fold symmetrical. In 6.1(c), the edges and faces of the posts are not aligned with the same symmetry as the lattice. The overall surface therefore only has two mirror symmetries, and drops placed on it only display this 2-fold symmetry. Note for instance that the drop with 3-fold symmetry in 6.1(b) will not occur on the surface of 6.1(c). However, the actual drop shown in 6.1(c) is perfectly 2-fold symmetrical but spans multiple additional

posts to the upper right corner. Such deviations do occur occasionally during experiments. The deviations are attributed to either mechanical vibrations, local deviations from ideal shapes of the posts and other minor influences such as the drop being ejected by the inkjet nozzle at an angle ('satellite drops' or 'side shooters'). The reproducibility of the drop shapes is generally quite high though, and can be analysed statistically as will be done further on.

Regarding the influence of the posts, comparing 6.1(b) and 6.1(c) is instructive. Since the posts are shaped and placed on the lattice in 6.1(b) in a way corresponding to the lattice symmetry, it influences the shape of the interface considerably, as the contact line is able to reach the next row of posts more easily in the direction of the sharp edges of the triangular pillars. Such a distinct difference in wetting is not observed in 6.1(c), as the preferred wetting directions are much less pronounced. We further note that circular posts on a hexagonal lattice (introducing no preferred lattice directions) were used in the experiments by Courbin *et al.*,¹⁵³ and in that case regular hexagons (which possess the lattice 6-fold rotational symmetry) were observed.

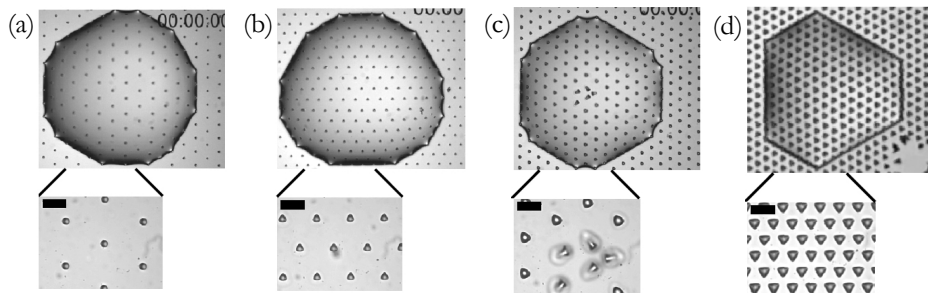


Figure 6.2: Microscopic images of various drop shapes on a hexagonal lattice with differently shaped and spaced posts. An inset with a magnification of the posts is placed below each image. The scale bar in black is $20 \mu\text{m}$. (a) A nearly round drop on a sparse lattice of small round pillars, $b = 5 \mu\text{m}$, $d = 40 \mu\text{m}$. (b) A drop with a shape intermediately between sphere, a hexagon and a triangle (pointing upward), on a sparse lattice of small triangular posts, $b = 7.5 \mu\text{m}$, $d = 30 \mu\text{m}$. (c) A drop with an approximately hexagonal shape on an intermediately filled lattice with triangular posts, $b = 10 \mu\text{m}$, $d = 30 \mu\text{m}$. (d) A drop shaped intermediately between a regular hexagon and a triangle, on a dense lattice with relatively thick triangular posts, $b = 7.5 \mu\text{m}$, $d = 15 \mu\text{m}$. (Note that figure 6.2(d) is identical to figure 6.1(b).)

To further investigate the influence of the shape and arrangement of the posts, a systematic variation of posts on a hexagonal lattice is presented in figure 6.2. The drop on round pillars (6.2(a)) has a nearly round contact line shape. Increasing the post size (6.2(b) to 6.2(c)) or also decreasing the post spacing (6.2(c) to 6.2(d)) lead to progressively more strongly anisotropic contact line shapes. The primary determinant is the lattice (type and spacing), but a clear modulation is created by choosing the parameters of the pillar shape,

and orientation.

From studying figures 6.1 and 6.2, the shape of the contact line is clearly found to deviate from the circular shape. This deviation is determined besides the lattice type by the relationship between three geometric parameters: the post height h , post width b and lattice spacing d (i.e. the inter-post distance), which we define as in ¹⁵⁵. While we did not vary the post height, the dimensionless parameters of h/b , b/d and h/d were effectively varied by varying the post width and lattice spacing.

In general when the posts are small compared to the lattice spacing and relatively far apart (i.e. low b/d and low h/d), the contact line more closely resembles a circle. If however one of or both these two ratios are high, the contact line also approximately resembles a circle. For h/d an increase in de-pinning with increasing h/b was previously reported in ¹⁵⁵ as a consequence of the interface reaching the next post without an energetically costly decrease in local liquid-vapour surface curvature. This effect is also expected for high b/d and is consistent with the experimental results for wide posts (i.e. $b/d \gg 0.75$), where the contact line was also found to resemble a circle. Therefore, the drops are most anisotropic and de-pinning is the dominant factor in determining contact line shape in an intermediate range of b/d and h/d , which will be studied here.

6.3.2 Simulation results

Previous lattice Boltzmann simulation results and analysis for advancing imbibition were presented in ^{154,155}. We will first briefly revisit these findings for the purpose of comparison with the deposition experiments presented in this chapter. The details of the simulation method employed in this chapter are presented in section 2.6.2. For reference, we choose as numerical parameters $\kappa = 0.01$, $p_c = 0.125$, $\rho_l = 3.5$, $\tau_w = 0.3$ and $\beta = 1.0$, which result in an interfacial thickness $\chi = 0.9$ and surface tension $\gamma = 0.029$ (in lattice Boltzmann units). The density ratio $\rho_l / \rho_v = 3.42$ and the viscosity ratio is $\eta_l / \eta_v = 7.5$. Slightly different boundary conditions are used compared to the simulations in 2.6.2, which are detailed in ^{45,72}, which do not affect the simulation results, as the simulations presented here are derived quasi-statically and the boundary conditions only affect the dynamics of the contact line. We concentrate most of our attention on substrates patterned with hexagonal arrays of posts with equilateral triangles as cross-sections. The posts have height $h = 20 l.u.$ (lattice units), side length $b = 20 l.u.$, and centre-to-centre separation $d = 40 l.u.$. The posts and the base substrate have the same intrinsic angle δ .

Simulating a large drop feeding imbibition among an array of posts (with intrinsic contact angle $\delta = 55^\circ$) beneath it is computationally expensive. Since we are only interested in the details of flow amongst the posts, it is expedient to feed imbibition from a ‘virtual reservoir’, a small circular region of radius ~ 6 lattice units at the centre of the box. Using this simulation geometry, we were able to capture a number of interesting spreading

behaviours. For examples, a drop spreading on a square array of triangular posts, with edges pointing in the $+x$ and $\pm y$ directions is able to advance in these same directions, via the connected contact line (CCL) mechanism (see below), but is barred from advancing in the $-x$ direction. On a square array of hexagonal posts with post edges pointing in the $\pm x$ directions, liquid is permitted to advance along this $\pm x$ again via the CCL mechanism but is barred along $\pm y$, hence a stripe of fluid is formed. For a hexagonal array of triangular posts, the spreading liquid quickly facets into a hexagon, which further forms a drop, shaped intermediate between a regular hexagon and a triangle as shown in figure 6.3(a-c), indeed very similar to our experimental observation in figure 6.1(c).

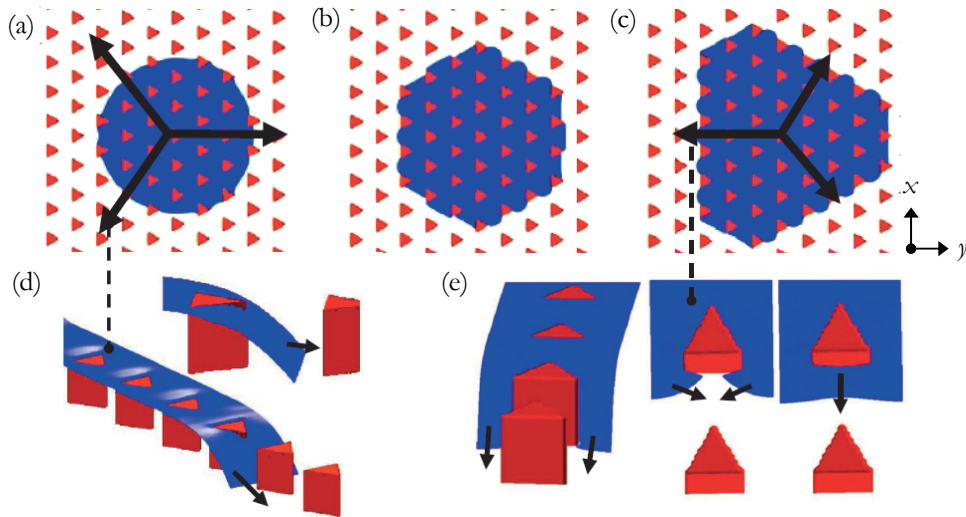


Figure 6.3: Lattice Boltzmann simulations of drops spreading via imbibition on a surface covered with triangular posts in a hexagonal array. These results were reported previously in ¹⁵⁵. (a–c) Evolution of the drop shape and contact line as function of time, showing the evolution of the drop from (a) approximately spherical to (b) hexagonal to (c) a shape intermediate between hexagonal and triangular. (d) Side view of the connected contact line (CCL) de-pinning mechanism, for a simulation with a narrow periodic geometry. The movement of the contact line is indicated with arrows, with the interface moving past the post with a connected contact line. (e) Side view of disconnected contact line (DCL) de-pinning, where the contact line is disconnected and only connects as it de-pins from the post. The dashed lines link the two de-pinning mechanisms with the corresponding lattice directions indicated in (a) and (c).

6.3.3 De-pinning mechanisms

To understand the spreading anisotropy, we further analyse the contact line de-pinning mechanisms. We find two distinct types, connected and disconnected contact line, mechanisms, as indicated in figure 6.3 (d) and (e) respectively, as we will now discuss. At its

boundary facing outwards in the $+x$ direction in figure 6.3(a-c), the film is of height b at the back face of the leading triangle, completely wetting this face. Beyond this, the height of the film decreases, such that the interface meets the substrate with the Young angle δ , as illustrated in figure 6.3(d). The interface will remain pinned if this condition can be geometrically satisfied without the contact line reaching the next row of posts. If the interface is flat, it can be seen that pinning will occur if $\delta > \tan^{-1}(b/d)$, although we showed in ¹⁵⁴ that the curvature of the interface (arising from the Laplace pressure) needs to be taken into account to obtain a more accurate prediction. Because the contact line is unbroken, this means of pinning is called the connected contact line (CCL) mechanism.

On the other hand, for the film edge facing the $-x$ direction in figure 6.3(a-c), pinning can occur with the interface spanning the gaps between the post faces, as shown in figure 6.3(e). In this situation, the contact line along the base substrate is punctuated by these faces, so we use the term disconnected contact line (DCL) mechanism. Whether the contact line will be pinned or advance depends on the balance of the interfacial free energy cost of creating interface against the free energy reduction of wetting the hydrophilic substrate. The latter will outweigh the former when δ is sufficiently small. As δ is lowered, the interface creeps around the corners of the post face. Once it comes into contact with the neighbouring portion of interface, it readily wets up the post face and across the base substrate to the next row of posts (see figure 6.3(e)).

In general the threshold values of δ for the two pinning mechanisms differ, giving rise to an intermediate range of δ in which spreading is permitted in only certain directions, and is thus highly anisotropic.

6.3.4 Reproducibility of drop shapes from inkjet printing

We first compare the simulation result of figure 6.3 with the experimental results shown in figure 6.2, especially (d). We note that there are significant differences in the circumstances represented: 6.2(d) shows a Wenzel drop having a dome-shaped cap extending above the posts, which has impacted onto the substrate with substantial kinetic energy, while 6.3(c) shows an imbibed film (a thick, flat film with the same height as the posts, but not wetting their top faces) which has been introduced quasi-statically. Despite these differences, the figures show qualitatively similar shapes, intermediate between an equilateral triangle and a regular hexagon.

The experimental variations in drop shape in figures 6.1 and 6.2 can be explained well in terms of the analysis of the lattice, combined with the CCL and DCL de-pinning mechanisms. For posts spaced more closely together, or with larger widths relative to the lattice spacing, the contact line shape modulation due to the anisotropy of the posts increases. This causes the contact line motion due to de-pinning to become relatively more important to the zipping-unzipping motion between rows of normal isotropic posts on a

lattice, thus leading to more anisotropic shapes. The fact that the experiments and simulations compare well, indicates that the mechanisms involved in drop spreading remain comparable even though in inkjet printing the advancing contact line has initial kinetic energy and the drop is also not fully imbibed into the pillars, but rather forms a curved liquid-vapour interface wetting also the tops of the posts. We will come back to these differences further on.

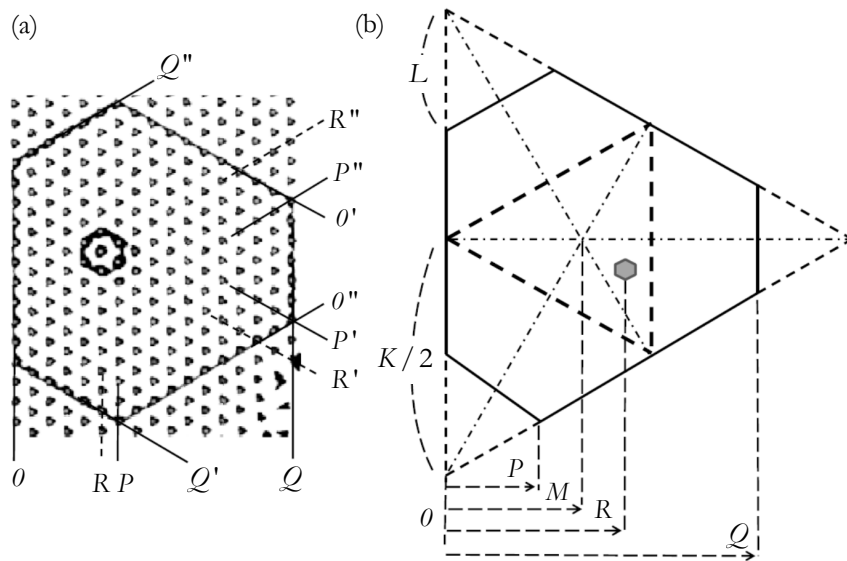


Figure 6.4: Schematic of the shape analysis of the hexagonal drops. (a) Two super-imposed microscopic images of the contact line of an experimental drop, with the outer initial contact line outline after advancing. Also shown is the inner last position just prior to the drop being completely evaporated. The positions P , Q and R are natural numbers of rows of the lattice, as counted from the left. The position R is the middle post of the last remaining part of the drop. Because of the threefold symmetry, positions P' and P'' are defined similar to P , and also for Q and R . (b) An equilateral triangle with side K , relating observables P , Q and R to K and the position of the theoretical middle M . Also shown is the length L which the side that an irregular hexagon would have to be extended to form an equilateral triangle. Note that M is not the same as the actual end point of evaporation R , which is indicated in as a small filled hexagon.

As a specific surface to analyze in more detail in order to quantify the effects of post anisotropy we choose the surface with triangular posts on a hexagonal lattice presented in figure 6.1(c). The experimental surface parameters are $b = 18 \mu\text{m}$, $b = 10 \mu\text{m}$ (i.e. one of the sides of the triangle being $10 \mu\text{m}$) and $d = 15 \mu\text{m}$. The schematics presented in figure 6.4 indicate a number of geometric relationships required to analyse the drop shape anisotropy in detail.

Following the definitions of α , β and γ in the schematic of figure 6.4(a), the primary geometric data from the microscopy images is collected. For further analysis we also establish a number of geometric relations of the contact line shape, which are presented in figure 6.4(b). $L = 0$ indicates an equilateral triangle while $L = K/3$ indicates a regular hexagon. Intermediate values of L indicate an intermediate shape which shall be referred to as irregular hexagons. A convenient dimensionless parameter to distinguish between these two shapes is

$$\lambda = \frac{2L}{K} = \frac{2P}{P+Q}. \quad (6.1)$$

In figure 6.4 (b) x , y and z from figure 6.4(a) are also indicated as well as the symmetrical middle M of the irregular hexagon by extending its sides to a triangle and constructing the symmetrical middle of the triangle.

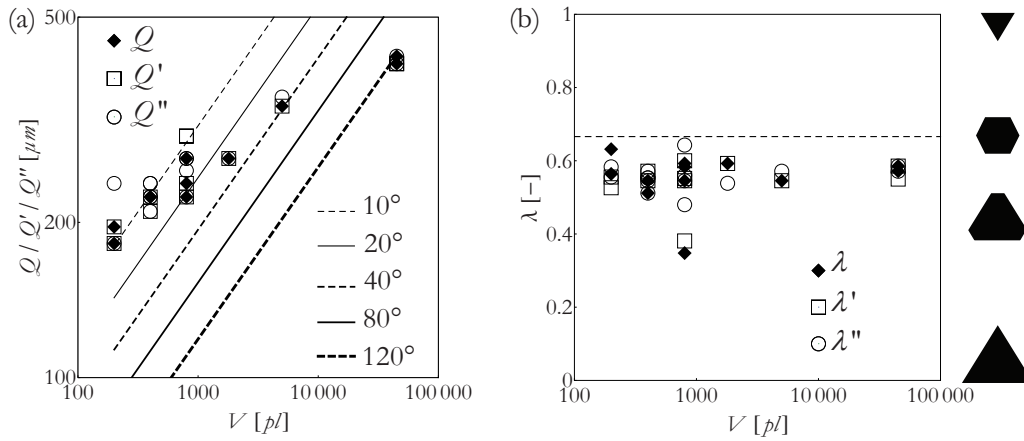


Figure 6.5: (a) Drop size Q as function of drop volume V as measured in the three principal lattice directions (according to the legend) plotted on double logarithmic scale. Also plotted is the theoretical curve of the drop diameter for a spherical drop according to equation (6.2) as defined in the legend. (b) Drop shape parameter λ as function of V for the three principal lattice directions according to the legend, plotted on log-linear scale. Note that the three lowest measured points with $\lambda < 0.5$ are from one single observed drop which more closely resembled a triangle than all other drops. The drop shapes corresponding to their equivalent λ are indicated to the right of (b), where for instance $\lambda = 2/3$ indicates a regular hexagon, which is also plotted as a dashed line.

Figure 6.5 demonstrates the effects of drop volume on drop shape, in particular how the drop size and shape evolve as more inkjet-printed drops are added to the drop on the

surface. The three most important observations from the figure are that: (i) the drop size increases much less than expected by the increase in volume, (ii) in general the contact line shapes are very similar whether consisting of 1 printed drop of 200 pl up to drops of more than 5 nl consisting of 225 printed drops and (iii) the data exhibit a high degree of reproducibility. We shall now discuss points (i) and (ii) in detail.

In figure 6.5(a), the theoretical curves for the radius of a perfectly spherical drop are plotted for a given volume and contact angle. This relationship is known from geometry as

$$r = \sin \delta \left(\frac{3V}{\pi(2 - 3\cos\delta + \cos^3\delta)} \right)^{1/3}, \quad (6.2)$$

with r the drop radius, V the volume and δ the intrinsic contact angle. While a spherical drop with a circularly shaped contact line is an approximation, it serves our purpose here, as a hexagonal or triangular drop has 6-fold or 3-fold rotational symmetry, so that the deviation is not too large. As can be clearly seen, a single printed drop is initially overstretched considerably due to pinning by the posts so that its effective contact angle is below $\sim 20^\circ$, whereas the intrinsic contact angle of the surface is 80° . However, as the number of inkjet-printed drops added to the surface drop increases, the drop eventually exceeds the intrinsic contact angle, since the contact line is pinned by the posts. Close analysis of the microscopy images confirms that the spherical cap of the drop overhangs beyond the contact line on the surface, indicating that the contact angle exceeds 90° .

The initial overspreading of the drop is due to the excess kinetic energy as it impacts the surface. With the increasing number of inkjet drops added sequentially to the surface drop, the net available energy at the contact line decreases per new added drop, as increasingly this energy will be absorbed by the fluid reservoir of the main drop and dissipated viscously. Considering the differences in contact angle and kinetic energy at the contact line, the reproducibility of the drop shape as shown in figure 6.5(b) is somewhat surprising. The average of λ is $\mu_\lambda = 0.55$, with a standard deviation of only $\sigma_\lambda = 0.06$, which indicates a clear deviation from a regular hexagon. The irregular hexagon is also three-fold rotationally symmetric: the data for λ and y are equally distributed for all three principal lattice directions.

From these results it can be concluded that the preference of the contact line for CCL de-pinning compared to DCL de-pinning persists outside the quasi-static situation of the simulations even if ample amounts of kinetic energy are available. Another conclusion is that the contact line shape is not sensitive to the curvature in the liquid-vapour interface, which becomes progressively more dome-shaped and extends further above the pillars as more inkjet drops are added. For computational reasons this situation is not currently feasible to simulate via lattice Boltzmann methods, especially for very high contact angles.

This result is remarkable, considering the following: assume that the first drop on the surface has constant height h , then it would have a volume $V \approx hQ^2$. Then, from a 200 pL drop, the average height is $h \approx 5 \mu\text{m}$, which is about one-third of the height of the posts. Eventually at 225 drops, the contact angle exceeds 90° so that the liquid-vapour interface in fact arcs outward beyond the posts on which it is pinned. Thus the described pinning mechanisms is valid not only for liquid-vapour interfaces which wet up to the post height, but also for interfaces that wet only up to part of the pillars or extend above the pillars. These results indicate that local contact line deviations determine to a large extent the overall drop shape and it is possible to create distinctly anisotropic shapes which are unfavourable energetically compared to a spherical drop on a non-patterned surface. However, if the spherical cap starts to extend well beyond the contact line, this difference in shape becomes less pronounced, as now only the liquid-vapour interface near the contact line will be distorted and the dome on top of the drop resembles a spherical drop more closely.

6.3.5 Discussion

To our knowledge, this observation of similar shapes between single drops deposited in a controlled way and larger compound drops has not been made before. The correspondence between simulated and experimentally observed drop shapes is pleasing. The CCL and DCL pinning mechanisms, which have now for the first time been studied experimentally, appear to be applicable to a broad range of post geometries. By considering the local pinning mechanisms which can be studied in detail with the experiments, the experimental results for various types of posts can be understood.

The high degree of reproducibility of the inkjet printed drops as they spread on the surface is surprising. This opens up the possibility for new possible wetting experiments with fluids in the pico-liter range with inkjet printing, which despite being an impact deposition method can yield reproducible results that can be compared to quasi-static experiments and simulations. It is important to take into account that while the contact line shape is largely unaffected by the amount of drops, the initial kinetic energy does lead to variations in contact angle due to pinning, which is an interesting topic in itself to study as it is related to such phenomena as the coffee drop effect and drop coalescence.

6.4 Receding contact line motion

6.4.1 Experimental results

The de-pinning mechanisms of advancing contact lines are now compared to those of receding lines. To simplify the discussion of the experimental results for these receding contact lines, only data for the most investigated geometry are presented in figure 6.6(a), as

these observations are generally valid also for other surfaces. During evaporation of the water drops, the spherical cap of liquid above the outer contact line evaporates while the outer contact line is observed to be completely pinned. The contact line remains pinned typically until the tops of the outermost posts are de-wetted, with the latter clearly observed with microscopy due to the sudden contrast change of the posts. It is important to note that the retraction process does not necessarily start after all tops are de-wetted but typically starts while some of the posts are still wetted. The drop then proceeds to de-wet post by post (or several posts at a time) with a typical jumping motion of the contact line, until only a small group of posts is wetted. This last group normally consists of 6 posts in a hexagonal pattern with one further post in the middle, such as the small inner outline in figure 6.6(a). At that point, the drop evaporates quickly and completely.

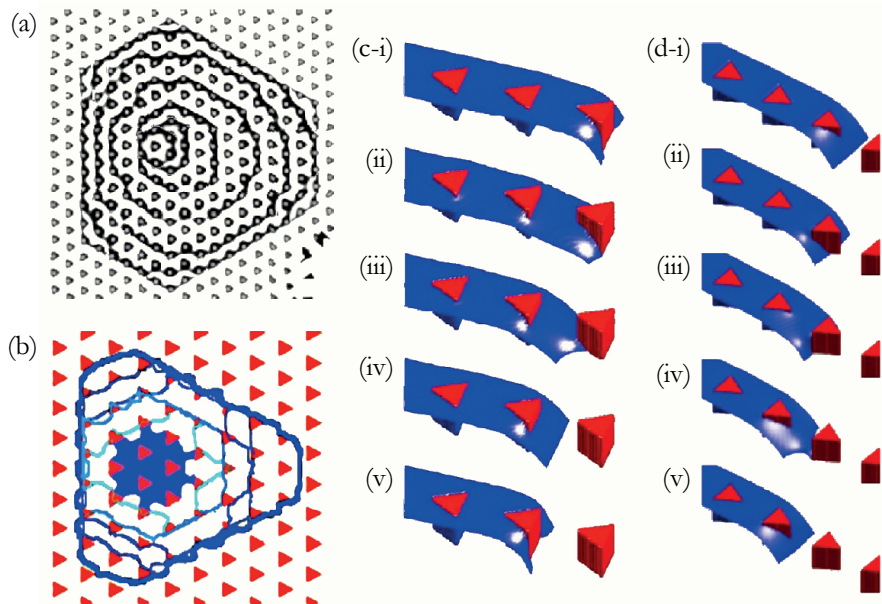


Figure 6.6: (a) Experimental and simulation (b-d) results of receding contact lines on surfaces patterned with triangular posts on a hexagonal lattice. (a) Time superposition microscopy images of the evaporating drop. The various concentric lines moving inward indicate the subsequent positions of the contact line at various times during evaporation. (b) time superposition image of a 3D lattice Boltzmann simulation of quasi-static evaporation, defined similar to (a) and exhibiting similar behaviour. (c-d) Quasi-2D simulations of (c) disconnected contact line (DCL) de-pinning and (d) mixed connected and disconnected contact line (CCL/DCL) de-pinning for a receding contact line. The roman numerals indicate increasing time, at (v) the contact line has moved exactly one lattice spacing from (i).

During de-wetting, the contact line changes in shape from the initial irregular hexagon to a round shape. Regular hexagons are not normally found to form exactly because the contact line starts to become rounded at the edges before this is possible. Different irregular shapes can form, and symmetry is often broken as one side of the drop starts to move inward while another side is still be pinned, as in figure 6.6(a) where the effective middle of the drop moves in the $-x$ direction slightly more lattice spacings than would be expected due to symmetry. The irregular shapes found at the final stage of evaporation indicate that kinetics and surface defects play dominant roles for small liquid volumes (higher evaporation rates).

6.4.2 Simulation results

To investigate receding de-pinning mechanisms by evaporation with lattice Boltzmann simulations we again take an imbibed film as the starting point in our simulation. We begin with the configuration reached by quasi-statically advancing the contact line in figure 6.3(c), but instead of using a virtual drain, we gradually reduce the volume of the film, by subtracting a small amount of mass from the liquid phase at given intervals, such that quasi-static evaporation is simulated. This corresponds more closely to the experimental situation.

An equivalent time superposition image of the simulation is presented in figure 6.6(b) for $\delta = 55^\circ$. The simulation suffers from some anisotropy resulting from the cubic discretisation used in the lattice Boltzmann, which breaks the natural three-fold symmetry of the physical system, so that retraction in the x direction is slightly slower than that in the two diagonal directions. However, if we ignore this artefact, the overall trend is that the film retracts preferentially towards the edges of the triangles compared to the faces. This effect is sufficiently strong to undo the anisotropy gained in the spreading phase. One of the intermediate contact line contours in 6.6(b) is a regular hexagon, indicating that the drop reverts back to this original shape during evaporation, before proceeding to smaller shapes. The final residual hexagon, towards the end of evaporation, is shown in the last panel. The overall mechanism and shape of the contact line in the simulation agrees well with the experimental observations.

6.4.3 Reproducibility of drop shapes from evaporation

While the advancing anisotropy can be described by λ , the preferred direction of retraction is more difficult in a 3-fold symmetric geometry as considered here. On ideal surfaces, the drop will retract to M in figure 6.4(b). For the experimental drops, \bar{x} (the actual position of the 'last de-wetted post') was measured in the three lattice directions. Also, M is calculated via

$$M = \frac{K}{2} \tan(30^\circ) = \frac{P + Q}{3} = \frac{2}{3(2 - \lambda)}. \quad (6.3)$$

Comparing R/Q (i.e. made dimensionless with regards to drop size) to M/R (theoretical middle of the drop) gathered for the drops at various volumes shows that the retraction process does not have a preferred lattice direction: the overall averaged value is $\mu_{R/Q} = 0.45$ versus $M/R = 0.46$. The scatter in the data is considerable, with $\sigma_{R/Q} = 0.15$. The simulation results are $(R/Q)_{sim} = 0.39 \pm 0.10$, which is also well within the predicted range, where the spread is solely caused by the fact that the initial drop in the simulations is placed over an even number of posts in each lattice direction, so that symmetry is broken at the last post which cannot be in the exact middle. Symmetry breaking is facilitated by minor discretisation errors as discussed above.

The retraction motion is a slow process compared to the advancing motion where excess kinetic energy is available, and it follows the unzipping mechanism described above. De-pinning was observed to be a cascading process under the microscope, with the retraction from one pillar often followed by neighbouring pillars being de-wet. For this reason, small variations in post size can influence local 'jumping' significantly, thus increase the experimental scatter in the data. Still, the average above gives confidence that this type of shape analysis of experimental data can be applied to other surface geometries, optionally combined with statistical analysis. For practical applications it appears that exploiting drop shape anisotropy from advancing motion or at least from motion with excess kinetic energy (e.g. by micro-pumps in micro-fluidic circuits) is strongly preferred to employing retraction anisotropy in order to achieve more reproducible results. Also, evaporation of the liquid is often not desirable in practical applications.

6.4.4 De-pinning mechanisms

We now look at the de-pinning mechanisms in detail. To reduce computational expense and to isolate particular pinning behaviour, we use simplified simulation geometries as indicated in figure 6.6(c) and (d). We take $x = 0$ as a plane of reflectional symmetry, so that all the triangles are pointing towards (6.6(a)), or away from (6.6(b)) the origin.

Contact line de-pinning follows the following stages in 6.6(c): as the transition from c(i) to c(ii) indicates, the contact line remains pinned to the bottom vertices of the posts while the interface de-wets the post vertically. Once the height of the interface around the final post has dropped significantly, the contact line finally de-pins from the corners of the posts, but c(iii) demonstrates that there is still a barrier to retraction, with the interface being significantly distorted around the post. The barrier can be understood in terms of the free

energy cost of the increasing interfacial area in the widening gap. When the contact line finally reaches the apex of the triangle, it snaps back into a straight, connected configuration, as shown in c(iv). The contact line then further retracts, de-wetting the back face of the next post, until it is in a disconnected state as shown in c(v), equivalent to its starting configuration in c(i) only one lattice spacing inward, and the cycle repeats. This mechanism can be considered as disconnected contact line (DCL) de-pinning, as the front face of the post has to be de-wet first forming a disconnected contact line, requiring considerable distortions of the liquid-vapour interface as in the case of DCL de-pinning for advancing contact lines.^{154,155}

When the triangular posts are pointing away from the origin, on the other hand, de-pinning proceeds as follows (figure 6.6(d)). From the connected configuration in d(i), the contact line retreats until it is punctuated by the posts in d(ii). From there, the liquid de-wets the two front faces of the posts, so that the contact line is level with the back, as shown in d(iii). As d(iv) demonstrates, de-wetting the back face of the post is the main obstacle to de-pinning, with the interface being greatly distorted. Once this face has de-wetted, the contact line springs back into position d(v), which is again morphologically equivalent to position d(i), completing the mechanism. Unlike the mechanisms previously discussed, this mechanism exhibits stages of pinning where the contact line is connected (d(i)-d(ii)) and where it is disconnected(d(ii)-d(v)), so it is best seen as a mixed CCL/DCL mechanism. This is contrast to the advancing case where the contact line is only pinned in its connected form.

It is found in the simulations, as in the experiments, that for a retracting contact line the mixed CCL/DCL de-pinning mechanism is energetically favourable than DCL de-pinning. The lattice direction in which mixed CCL/DCL de-pinning is favoured is the same lattice direction for which advancing contact lines favour CCL de-pinning. Therefore the drop preferentially advances and retracts along the same lattice direction and the receding motion restores the approximately round shape of the contact line. For this particular geometry it is not possible to further increase the shape anisotropy via retracting contact line motion. However it is expected that for suitably chosen geometries it will be possible to obtain anisotropic drop shapes from retracting motion as well, since the motion is shown to be determined by the competition between the de-pinning mechanisms in the various directions of a given surface.

To complete our discussion of the evaporation simulation results, we consider another important parameter analogous to the advancing contact line case. In the evaporation experiments, the height of the liquid-vapour interface can be higher but also lower than the post height, which corresponds in drop shape to the case of single or few inkjet-printed drops, but not to the case of multiple drops where the interface forms a dome-shaped cap above the pillars. However, during evaporation it is observed with microscopy that the spherical cap shrinks until the observed contact angle is far below 90° at the onset of the

retracting motion. We further recall from ¹⁵⁵ that the degree of advancing anisotropy is dependent on δ .

To identify the effect of the drop height on receding anisotropy, we perform simulations with varying δ . To better understand the evaporation process, we use the simulations to simultaneously investigate both mechanisms of de-pinning under the retraction of the film. We use a similar simulation geometry as before, except now we remove the mirror symmetry at $x = 0$, which was used to reduce the computational burden of the simulations. We initialise the system with a strip of liquid filling the substrate to the tops of the posts, as in a state of imbibition, and again simulate evaporation by slowly subtracting mass.

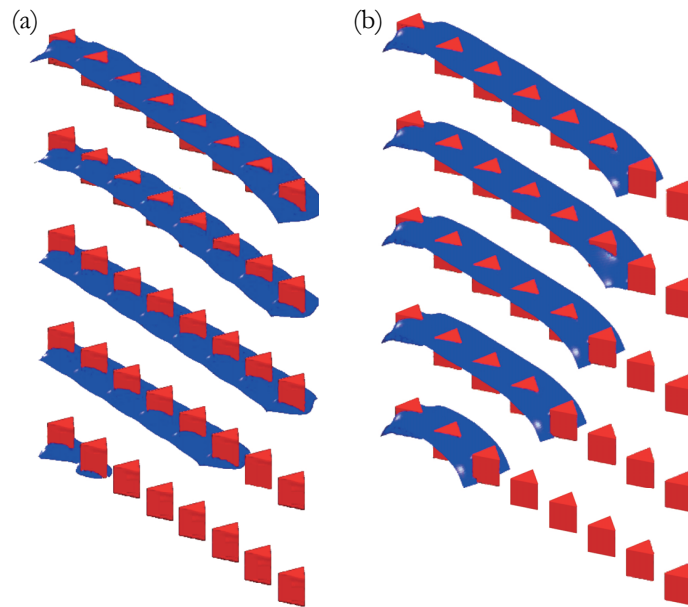


Figure 6.7: Receding behaviour of a quasi-2D lattice Boltzmann drop without mirror symmetry, for increasing time from top to bottom. (a) For $\delta = 30^\circ$, the drop remains pinned until the tops of the posts are de-wetted. Then, the interface de-pins from the face of the triangle. (b) For $\delta = 55^\circ$, de-pinning from the face occurs before de-pinning from the top of the interface and the drop retains constant height away from the contact line.

Figure 6.7(a) shows the simulation results for the case $\delta = 30^\circ$. We find that for this lower δ , de-pinning from the outer posts is inhibited in *both* x directions. Instead, the film decreases in thickness as it evaporates, remaining at a constant length. This can be understood from the increased energy cost of de-wetting a more hydrophilic substrate. The film only begins to retract when it is very thin: less than half of b . It does however retract

only in the direction of CCL de-pinning indicating that also for films of less than b the preference in de-pinning direction persists. For $\delta = 55^\circ$ in figure 6.7(b), the simulation results from figure 6.5 are qualitatively reproduced, with the film thickness remaining constant at h , and a preference for CCL de-pinning again manifests itself. Increasing δ up to 70° was also performed, and no qualitative change from the $\delta = 55^\circ$ case was found.

In general, the contact angle sensitivity for retraction is less than that for advancing contact lines. No regime was discovered where retraction in the face direction occurred preferentially to that in the edge direction. This is different from the advancing contact line scenario where Blow and Yeomans¹⁵⁵ showed that CCL and DCL de-pinning may be preferred depending on the contact angle and the ratio of post height and separation. In the receding case, the contact line exhibits DCL de-pinning in one direction and mixed CCL/DCL de-pinning in the other direction instead of pure CCL de-pinning. CCL de-pinning is much more sensitive to the intrinsic contact angle as explained by Blow and Yeomans. This explains the lower sensitivity of the retraction motion to the intrinsic contact angle.

6.4.5 Discussion

The agreement between experiments and simulations regarding the retracting motion of the contact line is good, although for the advancing contact line the agreement in contact line shape was stronger. The reason for this difference is considered to be due to the slower movement of the contact line with less energy during retraction. Detachment of the interface from a post when it is only attached on a single vanishing spot will also be more sensitive to the exact local shape of this post. Retraction is therefore a less desirable method to use experimentally, but through statistical analysis it is shown that the key trends from the simulations are well reproduced. In studying the de-pinning mechanisms, it was found that the same general CCL and DCL mechanisms occur during retraction, although it was discovered that in this case the mechanisms can be mixed. Since there is a clear difference in sensitivity to the intrinsic contact angle for both mechanisms, control over drop shapes in for instance micro-fluidic applications has to be carefully considered if these drops also recede across structured interfaces.

6.5 Conclusions

In this chapter, we presented experiments and lattice Boltzmann simulations of drops imbibing into surfaces patterned with polygonal posts as well as imbibed drops which slowly evaporate. Complex drop shapes with 3, 4 and 6-fold symmetry were observed. Both simulations and experiments demonstrate that besides the lattice type also the post shape can

have a considerable influence on the spreading and retraction behaviour of the drops. Depending on the direction of the contact line motion with respect to the post shape, one of two distinct de-pinning mechanisms occurs. We identified these mechanisms as connected contact line (CCL) de-pinning and disconnected contact line (DCL) de-pinning mechanisms, and it was shown that these mechanisms occur for contact line de-pinning for both advancing and retracting drops.

Apart from addressing fundamental issues of drops spreading on complex surfaces, our study indicates that polygonal posts may be exploited to control liquid motion. It may, for example, lead to new design options in micro-fluidic devices. In fact, there is in principle no need for a regular lattice on which the posts are placed (the case here), and variations in lattice type or even non-periodic placement of posts can lead to new drop shapes. Varying the post shapes locally or the post orientation relative to the lattice creates even more design freedom.

Finally, the synergy between lattice Boltzmann simulations and experiments using inkjet printing is particularly encouraging. On one hand, it shows the strength of lattice Boltzmann method to guide experiments on wetting phenomena. On the other hand, inkjet printing was shown to be a viable technique for continued research in this direction, leading to reproducible results for drops as small as 10 pico-liter.

7. Gibbs energy analysis of meta-stability of wetting states on dual-scale structured superlyophobic surfaces⁵

“There was only one catch and that was Catch-22.”

- Joseph Heller, “Catch-22”

⁵ This chapter is published in:

- R. J. Vrancken, B. G. H. van Loenen, G. de With, W. Ming , *Gibbs Energy Analysis of Meta-Stability of Wetting States On Dual-Scale Structured Superlyophobic Surfaces*, in preparation (2012)
- W. Ming, D. Wu, R. Vrancken, B. van Loenen, R. van Benthem, G. de With, *Nature-Inspired Superhydrophobic Coatings*, Proceedings of the Smart Coatings Conference, Orlando Florida (2007)
- D. Wu, R. J. Vrancken, B. G. H. van Loenen, R. A. T. M. van Benthem, G. de With, W. Ming, *Lipophobicity on Hierarchically Structured Superhydrophobic Surfaces*, Polym. Mat. Sci. Eng., 97, 419 (2007)
- R. Vrancken, *Geometry of micro-transfer printed polymerised mesogen structures*, M.Sc. Thesis, Laboratory for Polymers in Advances Systems, Department of Chemical Engineering and Chemistry and Laboratory for Molecular Biosensors for Medical Diagnostics, Department of Applied Physics, Eindhoven University of Technology (2006)

7.1 Introduction

Superlyophobicity (or superhydrophobicity¹⁶⁷), the property of a surface to be extremely repellent to water (superhydrophobic) and oil (superoleophobic), has been receiving increasing experimental^{57,168–178} as well as theoretical^{1,167,178,179} attention recently. Promising applications include self-cleaning coatings and low friction surfaces. It is highly desirable for a self-cleaning surface that is repellent with respect to water to also be repellent to oil-like substances in order to maintain its self-cleaning property. It appears that a key ingredient for superlyophobicity is entrapping vapour (normally air) in between a corrugated structured surface.

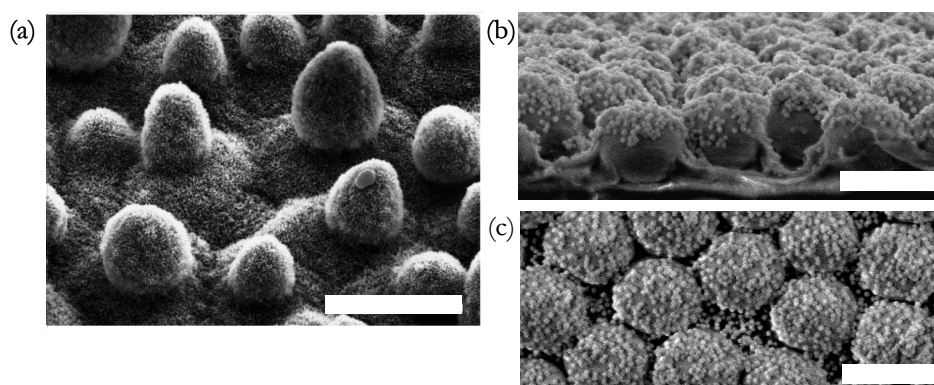


Figure 7.1. (a) SEM image of the lotus leaf, reproduced from ²⁰, showing the dual-scale structure. (b) SEM side view and (c) SEM top view of an artificially created biomimetic raspberry-like dual-scale structured surface, reproduced from ²³ with kind permission from Springer Science and Business Media; the larger first-layer particles ($d_1 \approx 700 \text{ nm}$) are covered by the second-level, smaller particles ($d_2 \approx 70 \text{ nm}$). Both surfaces exhibit superhydrophobicity due to their dual-scale roughness. The scale-bar in (a) corresponds to $20 \mu\text{m}$ and in (b) and (c) to $1 \mu\text{m}$.

Another feature of superlyophobicity is less well understood: the roll-off angle (or more precisely the gravitational force) required to move a liquid drop has to be very low. This leads to the famous “Lotus effect”,²⁰ where drops of water simply roll off the lotus leaf, thereby removing all contamination on the leaf. The lotus leaf is dual-scale structured, as shown in figure 7.1(a), meaning that the surface roughness has two characteristic length scales: the first length scale is of the order of micrometers, on which a secondary roughness with a sub-micrometer length scale is superimposed. In previous work, a nature-inspired raspberry-like dual-scale structured surface (figure 7.1(b)) was proven to be superhydrophobic and also highly oleophobic and robust.^{22,23} Many other recent attempts^{180–182} have been made recently to obtain superhydrophobic surfaces by mimicking the lotus

surface.

Young's equation,²⁴ defining the intrinsic contact angle δ of a drop resting on an ideally smooth surface as a function of the surface energies σ of all three interfaces: solid-liquid (sl), solid-vapour (sv) and liquid-vapour (lv), is defined in equation (2.13). In this chapter, the term oleophobic will be used to describe repellency of surfaces (with observed contact angles of $\beta > 90^\circ$) to a broad class of low surface tension (σ_{lv}) liquids such as hexadecane, paraffin oil and sunflower oil. A common characteristic of these 'oils' is that $\delta < 90^\circ$ on virtually all smooth surfaces, which is one of the main input parameters of the model described below. Mixtures of water and ethanol in various weight ratios (to lower σ_{lv}) as well as pure hexadecane are used as probe liquids. It is important to note that repellency to all oil-like fluids cannot be determined by the model, as comparison is only made between fluids of similar intrinsic contact angle. The terms oleophobicity and superoleophobicity as used in this chapter are therefore limited to a general tendency to repel oil-like liquids and not a universal tendency. For the adjective *super-oleophobic*, the empirically accepted definition is $\beta > 150^\circ$ and a roll-off angle lower than 10° . Only surfaces which repel all liquids, even if $\delta \sim 0^\circ$ can be considered universally oleophobic, a property which to the best knowledge of the author no surface has yet displayed. In this chapter these terms are used as described above and as is common in literature, and the reader is urged to consider the limitations of the terms.

A well-known modification to Young's equation was made by Wenzel, who considered the effect of surface roughness on the surface.⁴⁶ Later, Cassie and Baxter took into account composite surfaces with regions having different intrinsic contact angles or optionally entrapped vapour.^{50,183} In case a vapour fraction is entrapped in the crevices of a roughened surface, the "vapour surface" is commonly assumed to have an intrinsic contact angle of 180° for any liquid. If a flat surface consists of several chemical species, the surface coverage fractions f_i are used to determine the weighted contact angle, with the sum of all weights $\sum_i f_i = 1$. The key drawback of the Wenzel and Cassie-Baxter equations is that they relate the contact angle of the drop to experimental surface parameters which are presumed to be known exactly, which for realistic surfaces is not always the case. Furthermore, they only describe equilibrium situations. Deviations from equilibrium are not considered and generalizations of these equations to more complex surface geometries are often cumbersome mathematically.

These drawbacks were overcome by the work of Johnson and Dettre,^{27,28,30,31} who calculated the Gibbs energy G of a drop as a function of contact angle for a radially symmetric sinusoidally corrugated surface as well as a radially symmetric chemically patterned surface. At a Gibbs energy minimum, the drop is in equilibrium. Multiple minima can exist, and the Wenzel and Cassie-Baxter cases can be particular cases found with the Johnson and

Detre method. In addition, deviations from equilibrium can be calculated as well as the energy penalty for these deviations. Furthermore, energy barriers between different (metastable) equilibria can be calculated.

A more recent model was proposed by Bormashenko *et. al.*,¹⁸⁴ who employed an energy variation model to determine the apparent contact angle of a raspberry-like surface with slightly different geometry. The model was found to predict the contact angles of experimental structures accurately. However, wetting state transitions and the amount of liquid penetration into the crevices were not considered, as well as intermediate wetting states (where only the first or second level is wetted by the liquid).

In order to analyze dual-scale structured surfaces and the robustness of oleophobic wetting states in greater detail a Gibbs energy model is presented in this chapter, based on generalized hierarchically structured surface descriptions. The purpose is to explain the (super-) lyophobicity of dual-scale structured raspberry surfaces in detail. Aside from predicting equilibrium contact angles, the metastability of the various superlyophobic states as well as the energy barriers between this state and other (metastable) states are predicted and compared to experimental results.

The chapter is organised as follows. Section 7.2 describes the generalized hierarchical surface model. The remainder of section 7.2 describes in detail how these generalized equations are evaluated for the particular case of a raspberry-like dual-scale surface. In section 7.3, the results of this model for single sphere surfaces are discussed and compared to experimental results. Also discussed are the state transitions, the energy barriers between the states and their stability for these single-structured surfaces. In section 7.4, the results for dual-scale raspberry surfaces are presented and compared in detail to experimental results. Intermediate wetting states are found to occur before the structure is completely wetted. The chapter ends with conclusions in section 7.5.

7.2. Hierarchical model

The model described in this section is based on a number of assumptions. The dual-scale structured surfaces considered here are isotropic on the scale of the drop. The exact locations of the first and second levels of spheres on the surface are not taken into account, but an ‘averaged’ quasi-isotropic surface is considered covered with small particles of negligible size. Penetration of the liquid into the crevices is therefore not included in the model. Furthermore, only radially symmetric drops are described. Moreover, contact line energy terms are not included here. The magnitude and even the sign of the contact line energy (commonly known as line tension) of water on a surface is not known except for a few cases.³⁹ In general, energetic estimates predict that contact line energy effects only become significant for nanometre-sized droplets using the order of magnitude estimates of

the scarce experimental data available. Important to note is that for suspended states the total length of three-phase contact line, at the locations where the liquid-vapour interface touches the surface asperities underneath it, increases greatly compared to a fully collapsed state. However, since these contact lines are distributed isotropically over the surface, the total contact line energy can be averaged over the surface. It is therefore effectively a surface energy and can be included in the regular surface energy terms of the model. Finally, gravity effects are not included, as the drops under consideration are presumed to have radii well below the capillary length. Only interfacial energy terms are included in the model and, therefore, the total Gibbs energy can be made dimensionless conveniently.

The general equation for drops dominated by interface energy is

$$G = \sigma_{lv}\Omega_{lv} + (\sigma_{sl} - \sigma_{sv})\Omega_{sl}, \quad (7.1)$$

where G is the Gibbs energy of the drop-on-a-surface system, Ω_{ij} 's are the interface areas of the liquid-vapour (lv), solid-liquid (sl) and solid-vapour (sv) interface. Note that only the energy of the drop itself is calculated, i.e. the contact line is the boundary of the system under consideration.

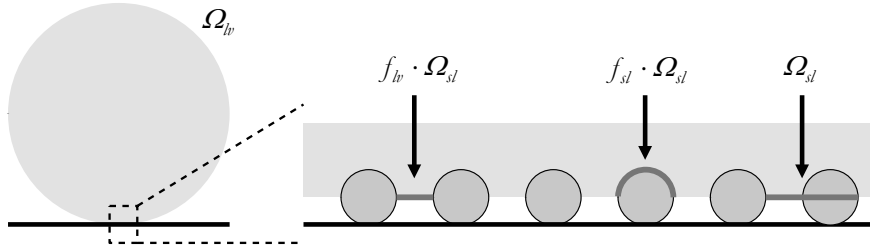


Figure 7.2: Schematic image of a drop on a solid surface, where the liquid-vapour interface Ω_{lv} is indicated (left) and a close-up of the solid-liquid interface Ω_{sl} , where both the solid-liquid fraction f_{sl} and the liquid-vapour fraction of the surface f_{lv} are visually defined for one of the iterated sections of the total surface.

A schematic of the particular surface under consideration is shown in figure 7.2. As shown, f_{lv} and f_{sl} are defined as the area factors by which the solid-liquid surface (which is defined as being flat) needs to be multiplied to obtain the true surface areas for the energy calculation. Note that f_{lv} and f_{sl} do not correspond to the well-known parameters f and R for the Cassie-Baxter and Wenzel equations. For other surface geometries (half-spheres, pillars, cones, pyramids, etc.) it is possible to define f_{lv} and f_{sl} functions analogously, and the model below can be used to describe such other multi-scale surfaces as well.

Equation (7.1) is modified to include f_{lv} and f_{sl} as

$$\tilde{G}_1 = \frac{\Omega_{lv} + (f_{lv} - f_{sl} \cos \delta) \Omega_{sl}}{V^{2/3}}. \quad (7.2)$$

where the subscript 1 denotes that the equation describes any single-scale structured surface. Furthermore the intrinsic contact angle δ was introduced by substituting all σ 's and making the energy dimensionless by dividing by $\sigma_{lv} V^{2/3}$. The tilde signifies that \tilde{G}_1 is dimensionless.

Dual-scale structured surfaces can then be described by extending the equation so that any solid fraction of a single-structured surface $f_{sl,1}$ is replaced with a new composite surface $f_{sl,1}f_{lv,2} + f_{sl,1}f_{sl,2}$, which consists of a solid surface and an entrapped vapour fraction, so that

$$\tilde{G}_{1,2} = \frac{\Omega_{lv} + (f_{lv,1} + f_{sl,1}f_{lv,2} - f_{sl,1}f_{sl,2} \cos \delta) \Omega_{sl}}{V^{2/3}}, \quad (7.3)$$

where subscript 2 refers to the secondary structure placed on top of the primary structure 1. The role of the dual-scale structure becomes immediately clear from these equations: the total amount of liquid-vapour interface per projected drop-surface interface area increases, whereas the total amount of liquid-solid surface may increase but also decrease, depending on whether the different fractions $\sum_i f_{sl,i} \geq 1$. Equation (7.3) is only valid if the absolute height (valley-peak) of the surface roughness of the second level is much smaller than that of the first level, which in turn should be much smaller than the drop base radius. Extending equation (7.3) to higher order hierarchical structures is straightforward from the above derivation, and will be analyzed further in future work.

To calculate the Gibbs energy in (7.3), expressions are needed for the total surface areas Ω_{ij} as a function of drop volume V , base radius ρ and the observed contact angle β . These expressions have been derived in literature before¹⁸⁵ by means of volume and surface integrations. Two of the three parameters (volume, base radius and contact angle) determine the third, through the following relationship:

$$\rho = \sin \beta \left(\frac{3V}{\pi(2 - 3 \cos \beta + \cos^3 \beta)} \right)^{1/3}, \quad (7.4)$$

assuming that the amount of liquid entrapped in the surface crevices is negligible. Furthermore, the expressions for the surfaces are

$$\Omega_{sl} = \pi\rho^2, \quad (7.5)$$

and

$$\Omega_h = \frac{2\pi\rho^2}{1 + \cos\beta} \quad (7.6)$$

By substituting equations (7.4), (7.5) and (7.6) into (7.2) or (7.3), the $V^{2/3}$ term is eliminated from the expression so that the model is volume independent. It is important to note that for the calculated observed contact angle β no consideration is given to contact angle hysteresis. In this chapter the experimental drops are prepared by controlled drop deposition onto the surface. Therefore the common approximation that $\beta \sim \beta_a$ (the advancing contact angle) is made for these drops.

Explicit functions for the fractions f_{lv} and f_{sl} also have to be derived. Inspired by the experimental surfaces prepared previously,²² the surface is defined as a layer of spheres covered by a second layer of much smaller spheres, for which the same fundamental functions f_{lv} and f_{sl} are valid.

A key parameter in a surface covered in spheres is the areal packing factor η , which is defined as the ratio between the vertical projection of the spheres on the surface and the unit surface area. For square packing this can be calculated straightforward as $\eta = \pi r^2 / 4r^2 = \pi / 4 \approx 0.79$, with r being the radius of the sphere. For hexagonally close packed spheres, the densest packing of spheres possible on a two-dimensional surface is $\eta = \pi / (2\sqrt{3}) \approx 0.91$.

Both the solid fraction and the vapour fraction depend on the penetration of the liquid into the structures. b is defined as the vapour height as in figure 7.3, which ranges from 0 to $2r$. At $b = 2r$ the liquid rests entirely on top of the spheres; at $b = 0$ the liquid has penetrated the gaps between the spheres totally and also wets the original flat surface at the base of the spheres.

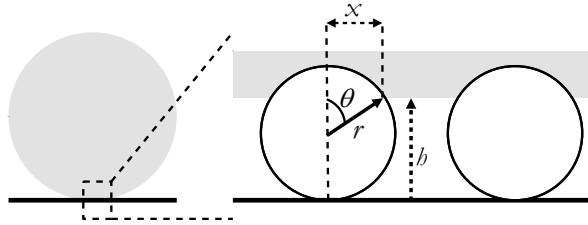


Figure 7.3: Schematic of the parameters used in calculating the area of the cap of a single sphere at height b .

The area of a single sphere that is covered by liquid, A_{sphere} (figure 7.3) is calculated as

$$A_{sphere} = 2\pi \int_0^{\tilde{x}} x \sqrt{1 + \left(\frac{\partial \tilde{x}}{\partial x}\right)^2} dx = 2\pi r^2 (1 - \cos\theta), \quad (7.7)$$

where this surface of revolution is calculated as a surface integral ranging over parameter x from 0 to \tilde{x} , with $x = r \sin\theta$ and $\tilde{x} = \sqrt{r^2 - x^2}$. The height b of the liquid-vapour interface as a function of θ is $b = r(1 + \cos\theta)$. It is useful to replace b with $\tilde{b} = b/2r$, the dimensionless height ranging from 0 to 1. The solid fraction $f_{sl,sphere}$ can then be expressed by substituting $2(1 - \tilde{b}) = (1 - \cos\theta)$ into (7.7) to find the area coverage of the spheres in terms of b as

$$f_{sl,sphere} = 4\eta(1 - \tilde{b}) + H(-\tilde{b}), \quad (7.8)$$

where the packing factor is also taken into account. The Heaviside function H is defined in the usual way and takes into account the discontinuity at $\tilde{b} = 0$, where the bottom surface is assumed to be wetted instantaneously as soon as the fluid level reaches $\tilde{b} = 0$. Note that this description of f_{sl} is independent of the absolute size r of the spheres. The expression for the vapour fraction f_{lv} is found by considering that only the horizontal cross-section of the sphere at height \tilde{b} should be subtracted from the total projected area to find

$$f_{lv,sphere} = 1 - \eta(1 - (2\tilde{b} - 1)^2) - H(-\tilde{b}), \quad (7.9)$$

which is again dimensionless. Both $f_{sl,sphere}$ and $f_{lv,sphere}$ are plotted in figure 7.4. For brevity, $f_{sl,sphere}$ and $f_{lv,sphere}$ will be referred to as f_{sl} and f_{lv} in the following, as this is the only surface geometry considered from now on.

The combined equations derived above were evaluated as a function of the intrinsic contact angle δ and the packing factors η for the structured surface. The results for the single structure, \tilde{G} , β and \tilde{b} , were found by numerical (iterative) minimization of \tilde{G} as a function of β and \tilde{b} (single-scale structure) or \tilde{b}_1 and \tilde{b}_2 (dual-scale structure) to find the lowest point on the Gibbs energy landscape. Since it is not known *a priori* in which state the drop is in, all wetting states were evaluated simultaneously and the ‘true’ state chosen as the state with the lowest \tilde{G} . For single structures, the ‘Wenzel’ and ‘Cassie’ states are possible; for the dual-scale structured surfaces, ‘Wenzel-Wenzel’, ‘Wenzel-Cassie’, ‘Cassie-Wenzel’ and ‘Cassie-Cassie’ states are possible, where the order of states mentioned is ‘Primary-Secondary’.

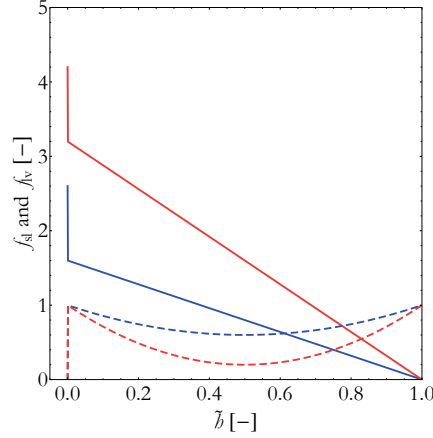


Figure 7.4: Solid-liquid (f_{sl} , solid line) and liquid-vapour (f_{lv} , dashed line) fractions as a function of the relative vapour height (\tilde{h}) for a surface structured with a monolayer of spheres. Notice the discontinuous jumps at $\tilde{h} = 0$, where the interface is wetted as the liquid-vapour interface reaches the bottom of the spheres. Blue lines represent low packing ($\eta = 0.3$), and red lines represent high packing ($\eta = 0.9$).

A typical example of a Gibbs energy landscape found for single-scale structured surfaces is shown in figure 7.5(a). A drop which is deposited surface starts initially at $\beta = 180^\circ$ and $\tilde{h} = 1$, i.e. the drop has not spread yet and no liquid has penetrated the spheres initially. The drop will then proceed to move towards the minimum position via a path through the energy landscape by spreading along the actual surface (thus decreasing β) as well as increasingly penetrating the surface (thus decreasing \tilde{h}). In the process the drop loses its excess surface and kinetic energy through viscous dissipation, and can be assumed to follow the path of steepest descent. Note that at $\beta = 180^\circ$, the Gibbs energy curve is constant (i.e. independent of \tilde{h}). In this limiting case the drop only makes contact with the surface on an infinitesimally small area and none of the surface parameters matter as there is no energetic interaction between drop and surface.

The model has a practical feature that is valid for all surface geometries: in figure 7.5(b), it is shown that the minima in the Gibbs energy landscape, for any given type of surface lie on a single monotonous curve in the plot of Gibbs energy versus β . The curve has a number of interesting features:

- i. approximately no offset, i.e. $\tilde{G} \rightarrow 0$ as $\beta \rightarrow 0^\circ$;
- ii. an almost horizontal plateau in \tilde{G} for $\beta \rightarrow 180^\circ$ and
- iii. a large approximately linear regime for $0^\circ < \beta < 100^\circ$.

Gibbs energy values below zero indicate complete wetting of the surface. Feature (ii) indicates that β for lyophobic surfaces is very sensitive to small disturbances in \tilde{G} . Experimentally, for high apparent contact angles the energetic differences are small, which

can easily cause scatter in the contact angle data (aside from the known difficulties in accurately measuring very high contact angles). Due to the monotonous relationship between \tilde{G} and β , it is possible to plot only the more intuitive β and refrain from also plotting the Gibbs energy separately.

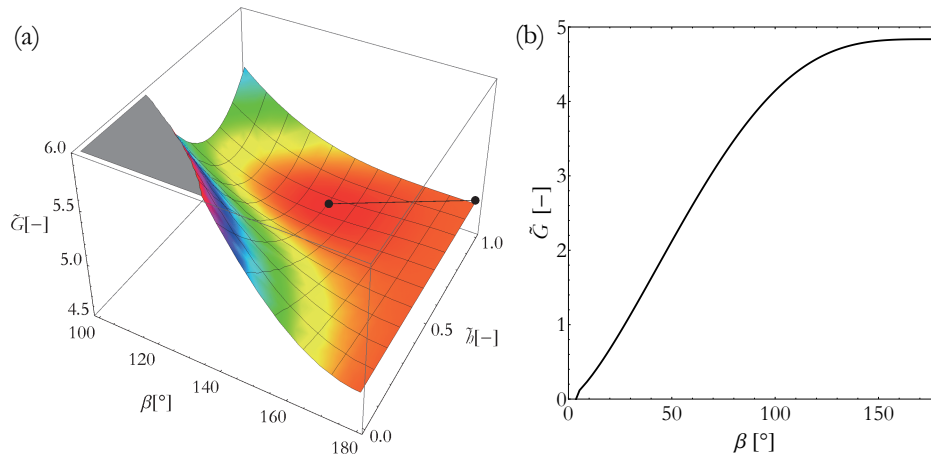


Figure 7.5: Typical model results. (a) Gibbs energy landscapes for the single-scale structured Cassie state with $\delta = 120^\circ$ showing the dimensionless relative Gibbs energy as a function of apparent contact angle as well as vapour height for two different packing factors. The Gibbs energy minimum is indicated with a black dot, at $\tilde{h} = 0.75$, $\beta = 140^\circ$ as well as the path towards this minimum from the initial drop position at $\tilde{h} = 1$, $\beta = 180^\circ$. (b) Gibbs energy as a function of β for all surface geometries.

7.3 Single-sphere surfaces

7.3.1 Predicted wetting states and experimental comparison

The model results for the single-scale sphere model are depicted in figure 7.6, where δ and η are varied systematically. As shown in 7.6(a), for $\delta = 120^\circ$ at $\eta = 0.9$ in the Cassie state the apparent contact angle $\beta = 140^\circ$, and further increases to 158° as η is reduced to 0.3. For both high and low packing the Wenzel state $\beta = 180^\circ$, and since it has a higher contact angle, it is also the higher energy state according to figure 7.5(b). For completeness the whole range of δ 's is plotted, although realizing that for water on smooth surfaces, intrinsic contact angles greater than 120° (for perfluorinated surfaces) have not been observed experimentally. For decreasing δ the most energetically favourable state becomes the Wenzel state. Near the cross-over point drops in the Wenzel state still have very high contact angles, but decreasing δ further leads to a rapid decrease in apparent contact angle and eventually between $60^\circ < \delta < 95^\circ$, depending on packing, drops in the minimum-

energy Wenzel state will completely wet the surface.

These results compare favourably with experimental data from both PDMS^{22,23,186} and perfluorodecyl-modified surfaces with single sphere geometry as shown as the data-points in 7.6(a).¹⁸⁷ In particular RfSi (1H,1H,2H,2H-perfluorodecyltrichlorosilane), exhibits high intrinsic contact angles for many fluids^{182,186} as it forms a fluorocarbon self-assembled monolayer (SAM) on the surface that is very lyophobic. The experimental results were measured on surfaces have been prepared in a variety of ways, with spheres of between 70 to 800 nm diameter and packing factors approximately $0.6 < \eta < 0.8$. Considering these experimental differences, the internal consistency of the experimental data as well as to the model results is pleasing. The size of the particles, even though varied over one order of magnitude, is not found to influence the apparent contact angle. This is consistent with the model, which does not consider the absolute size of the particles.

It is not possible from the limited amount of experimental data to distinguish conclusively between the Wenzel and Cassie states for this particular contact angle range as the apparent contact angles for both states are quite close together for most packing factors. Contact angle hysteresis according to (2.2) was measured to be $\sim 40^\circ - 50^\circ$, which is neither very high nor low and therefore does not give a clear indication of the state. However, a comparison can be made to samples where the layer of PDMS-covered spheres is embedded partly into an epoxy bottom layer for improved mechanical stability. These samples with spheres embedded to up to $\tilde{h} \sim 0.4$ in the layer exhibited very similar apparent contact angles and contact hysteresis.^{23,186} In figure 7.6(b) it can be seen that for $\delta \sim 105^\circ$, the liquid will have penetrated into the surface only up to $\tilde{h} \sim 0.6$ in the Cassie state. Therefore it is most likely that the drops were in the meta-stable Cassie state, since otherwise the degree of embedding would most likely cause differences in both β and β_b .

In figure 7.6(c) it can be seen clearly that lyophobicity increases with decreasing packing. Higher packing leads to more surface roughness, but also to decreased vapour entrapment. This is consistent with both the Wenzel and Cassie-Baxter equations, which predict that higher intrinsic contact angles, greater surface roughness and vapour entrapment all increase the apparent contact angle.

With regards to packing, it is shown in figure 7.6(a) that the transition from the Cassie state to the Wenzel state for lower η occurs at higher δ ($\sim 110^\circ$ for $\eta = 0.3$). This means that while lowering the packing might lead to higher β 's in the Cassie state (desired for lyophobicity), the transition to the Wenzel state for higher δ 's in fact leads to *lyophilicity*. In 7.6(c) it can be seen that for very low packing, the Wenzel state is actually the most favourable state even for very high intrinsic contact angles. Figure 7.6(c) therefore demonstrates clearly that the packing cannot be lowered too far until for very high intrinsic contact angles the stable state will be the Wenzel state. This is unfortunate since high δ 's are desirable for lyophobicity.

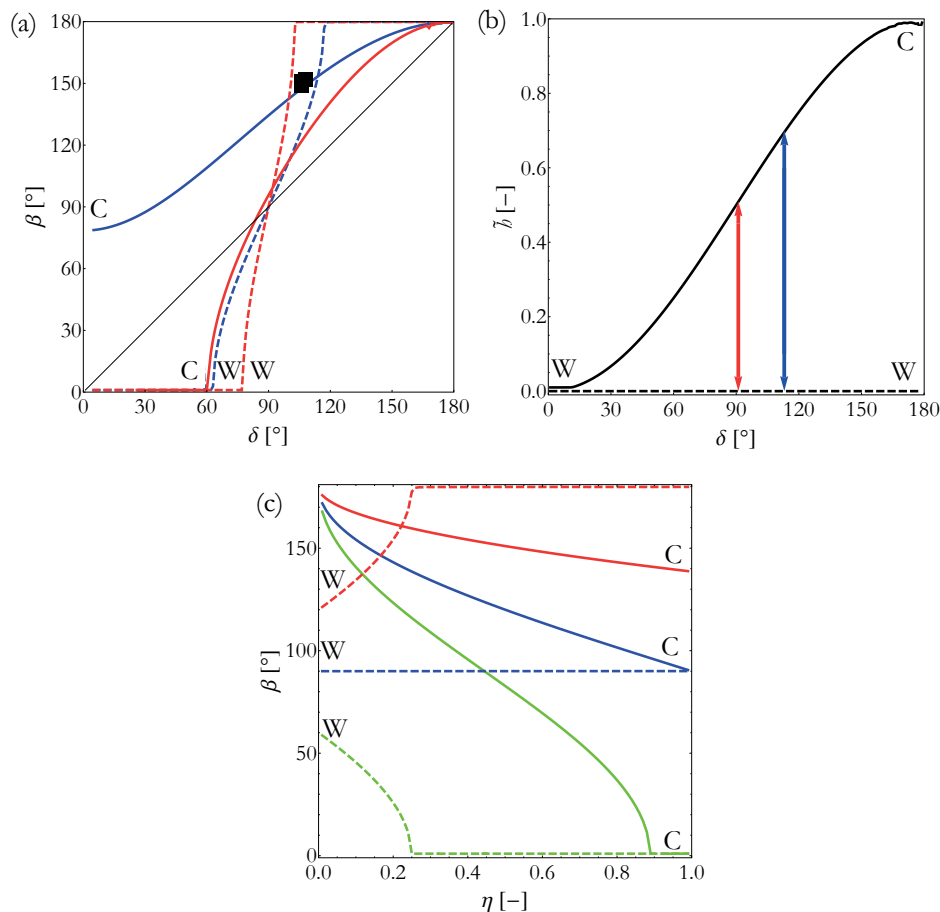


Figure 7.6: Model results for a surface with a monolayer of spheres. In (a) and (b) blue lines represent low packing ($\eta = 0.3$), red lines represent high packing ($\eta = 0.9$). The solid lines denote represent the Cassie state (indicated with 'C') and the dashed lines denote the Wenzel state ('W'). (a) β as a function of δ . The experimental data (solid squares) are taken from ^{22,23,186}. (b) \tilde{h} as a function of δ . The arrows indicate where the preferred state is C (to the right) or W (to the left), where the colour corresponds to the packing as above. (c) β as a function of η , where green $\delta = 60^\circ$, blue $\delta = 90^\circ$ and red $\delta = 120^\circ$.

For high δ 's the sensitivity to variations in local packing is low, but for lower δ 's this sensitivity is much higher. Therefore, for stable oleophobicity it will not only be important to achieve a robust meta-stable Cassie state, but also to have sufficient control over packing factor uniformity across the surface, as too large deviations can easily lead to much lower than intended β . The experimental results in figure 7.6(a) are found on surfaces with relatively high packing factors $0.6 < \eta < 0.8$, which in part explains the reproducible contact angle data found on these surfaces. Note that the particles are deposited without any explicit

patterning mechanism so that local variations in packing are likely to occur.

7.3.2 State transitions and stability

Since decreasing the packing is preferable for lyophobicity, it is interesting to see at which point lowering the packing jeopardizes the stability of the Cassie state, as in the limit of zero packing there clearly cannot be a suspended state any more. In this section, the energy barriers between the Wenzel and Cassie state are calculated based on the model. These results are analysed as function of δ and η and the likelihood of a transition between the states is determined.

In figure 7.7 the results of energy barrier calculations for a single sphere surface are presented. Figure 7.7(a) shows \tilde{G} as a function of \tilde{h} . There are two local minima for both the Cassie and Wenzel ($\tilde{h} = 0$) states. Also, the Wenzel state in this particular case has lower overall energy. However, as the drop has to penetrate the full layer of spheres to reach the bottom, an energetic barrier has to be overcome. These (dimensionless) energetic barriers are defined as:

$$\tilde{B}_{C \rightarrow W} = \tilde{G} \Big|_{\tilde{h} \downarrow 0} - \tilde{G}_C \quad \text{and} \quad \tilde{B}_{W \rightarrow C} = \tilde{G} \Big|_{\tilde{h} \downarrow 0} - \tilde{G}_W. \quad (7.10)$$

Besides the barriers, the differential Gibbs energy $\Delta \tilde{G}_{C \leftrightarrow W}$ between the two states is indicated. When the Wenzel state is energetically favourable, $\Delta \tilde{G}_{C \rightarrow W} = \tilde{G}_C - \tilde{G}_W > 0$ and vice versa. Note that $\Delta \tilde{G}_{C \rightarrow W} = -\Delta \tilde{G}_{W \rightarrow C}$.

In figure 7.7(b) the energy curves for the various terms of equation (7.10) are shown for intermediate $\eta = 0.6$. For $\delta \gtrsim 100^\circ$, all three curves lie very close together, indicating that the energetic difference between the states as well as the barriers between them is small. This may seem counter-intuitive at first, as it seems to imply that the surface can be in either state just as likely, where for high δ a suspended state is expected. However, as was shown in figure 7.5(b), at this very high \tilde{G} the apparent contact angle of these states is 180° , so that the drop scarcely touches the surface and is very mobile. For this reason the drop will be in the Cassie state, or at least act indistinguishable from it. The Wenzel line decreases to $\tilde{G} < 0$ already for $\delta \approx 72^\circ$, and is the energetically favoured state for $\delta < 100^\circ$.

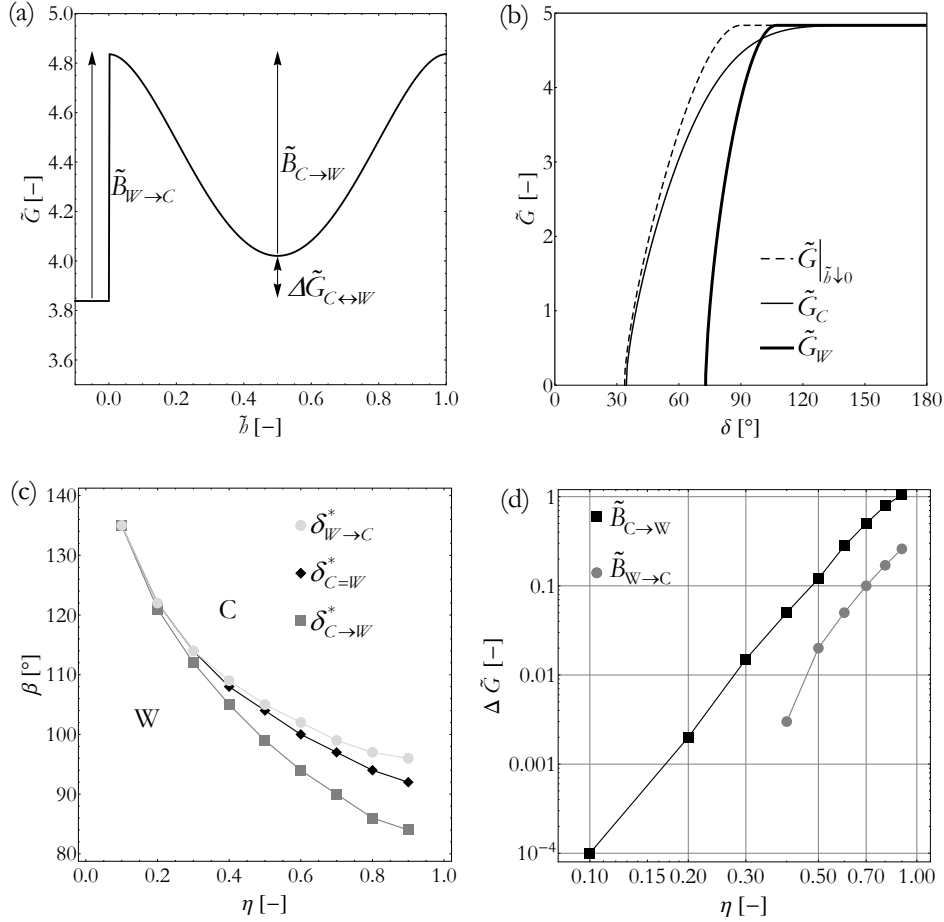


Figure 7.7: Energy barriers for wetting state transitions for single-scale structured surfaces with spheres. (a) \tilde{G} as a function of \tilde{h} , for a drop with $\delta = 90^\circ$ and $\eta = 0.9$. Indicated are the energetic barriers $\tilde{B}_{C \rightarrow W}$ and $\tilde{B}_{W \rightarrow C}$, as well as differential relative Gibbs energy $\Delta \tilde{G}_{C \leftrightarrow W}$ as defined in (7.10). (b) \tilde{G} as function of δ for the Cassie, Wenzel and $\tilde{h} \downarrow 0$ states. (c) State diagram: the intrinsic contact angle at which a state transition occurs as function of packing, for the cases of equation (7.11) and also where the Cassie and Wenzel state have equal energy ($\delta_{C=W}^*$). Also indicated with ‘C’ and ‘W’ is the stable state. (d) The energy barrier heights $\tilde{B}_{C \rightarrow W}$ and $\tilde{B}_{W \rightarrow C}$ at the point where these barriers equal the energetic gain $\Delta \tilde{G}_{C \rightarrow W}$ for the transition, as function of packing on a double-logarithmic scale.

When a drop in the Cassie state collapses, it first needs to gather sufficient energy to reach the $\tilde{G}|_{\tilde{h} \downarrow 0}$ curve, which lies close to the \tilde{G}_C curve for both low and high intrinsic contact angle, but deviates considerably from it at intermediate δ .

In order to efficiently analyse these curves for various packing factors, characteristic

cross-over points for the transitions are defined as:

$$\begin{aligned}
 \delta_{C \rightarrow W}^* & \quad \text{at} \quad \tilde{B}_{C \rightarrow W} = \Delta \tilde{G}_{C \rightarrow W} \\
 \delta_{C=W}^* & \quad \text{at} \quad \Delta \tilde{G}_{C \rightarrow W} = 0 \\
 \delta_{W \rightarrow C}^* & \quad \text{at} \quad \tilde{B}_{W \rightarrow C} = \Delta \tilde{G}_{W \rightarrow C}
 \end{aligned} \tag{7.11}$$

The importance of these cross-over points to the stability of the state can be understood as follows: the model considers the surface isotropic, so that the energy considerations are as valid locally as they are for the overall drop. It is possible that locally the liquid-vapour interface deviates from the average penetration depth, for instance due to a surface defect. From this initial site, the interface may spread further into the surface if this is energetically favourable. As the contact line moves forward a cascade of neighbouring spheres transition one by one. This spreading motion then causes the wetting transition, even though the initial energy required for the transition is much smaller than is needed for the whole drop to transition instantaneously.

The advancing motion is energetically neutral at the cross-over point $\delta_{C=W}^*$. However, the local energy barrier still has to be overcome. For this reason, consider for instance the Cassie-to-Wenzel transition. At $\delta_{C \rightarrow W}^*$ the net energy gain per unit surface equals the energy barrier that needs to be crossed. The significance of this cross-over point can be seen as an analogue of the activation energy for a chemical reaction, which is supplied by an exothermal reaction. Note that in this simple model effects such as pinning and curvature of the contact line and viscous dissipation are ignored, for which fluid-dynamic models are required as for instance used in chapter 5.

In figures 7.7(c) the three cross-over points from equation (7.11) are plotted as function of packing, so that it is in effect a state diagram with the stable state indicated in the figure. The boundaries of the states are defined by the cross-over points. With increasing packing, all δ^* 's decrease monotonously and with similar trends. For the Cassie to Wenzel transition at high packing, the crossing point lies 8° (from 92° to 84°) lower than state equilibrium, which is not spectacular but still increases the fluid latitude for which robust metastability is feasible. For decreasing packing all δ^* data points lie closer together, making both transitions likely to occur already for liquids which deviate only slightly from $\delta_{C=W}^*$.

The absolute energy barrier at the cross-over point is plotted in 7.7(d) on a double-logarithmic scale. What is remarkable in this plot is that the height of the barriers decrease as a power law $\tilde{B} \propto \eta^\alpha$, with exponent $\alpha \approx 4 - 5$. For the Cassie to Wenzel transition this power law is valid for over four orders of magnitude of the barrier energy. While an analytical derivation of the exact relationship is in principle possible, it is outside of the scope of the present work. The result shows that decreasing η leads to very rapidly decreasing stability of the wetting states, as will be further discussed below.

7.3.3 Discussion

The model results will now be discussed in terms of practical relevance compared to the experimental results. The model results show the most potential for lyophobicity at low packing, as in figure 7.6(a). On the other hand, at these low packing factors there are a range of less desirable effects as well:

- i. the liquid penetrates quite far into the structures (figure 7.6(b));
- ii. the sensitivity to local packing increases (figure 7.6(c));
- iii. the contact angle range of feasible metastability ($\delta_{C \rightarrow W}^* - \delta_{C=W}^*$) decreases (figure 7.7(c) and
- iv. the absolute value of the energy barrier decreases swiftly (figure 7.7(d)).

For this reason, an optimum between lyophobicity and stability is expected at intermediate packing. The experimental results indicate that indeed such surfaces exhibit stable and reproducible contact angle and hysteresis data, consistent with the model predictions.

Wetting state stability is not only a matter of packing and intrinsic contact angle. Given the fact that liquids are influenced by the environment, such as being contaminated by minute amounts of surfactants or oils, it is very desirable to have a bandwidth of intrinsic contact angles for which the wetting state remains stable. However even for surfaces that are kept chemically clean, many other factors can affect the intrinsic contact angle: (a) changes in humidity¹⁸⁸ can affect δ at least 8° , (b) changes in temperature¹⁸⁹ up to 5° , (c) changes in pH¹⁹⁰ up to 30° to name just a few examples reported in literature. Therefore, the range of δ 's that are determined as stable for a given packing should be tested with regards to fluctuations in the environment.

A further concern for low η surfaces, and not included in the present model, is the possibility that the liquid-vapour interface between the surface spheres bends downward under the influence of hydrostatic pressure. For a stationary drop this bending is caused solely by the Laplace pressure, which increases as the drop volume decreases.¹ As an estimate, for a water drop with a radius in air of 1 mm, the Laplace pressure $\Delta p = 2\sigma_{lv} / R_{drop}$ (equation (2.14)) will be the same everywhere inside the drop and also between the spheres. Considering spheres of 70 to 800 nm diameter as in the experimental results presented in 7.6(a), the maximum distance between the spheres will approximately be the same as the drop diameter for moderate packing. The greatest bending distance will be in the middle between two spheres. From geometry, it can be derived that the ratio of bending to the distance between the spheres is of the same order of magnitude as the ratio between the distance between the spheres and the principal curvature of the drop R_{drop} , which is at least 3 orders of magnitude. Therefore bending of the interface for these surfaces under *static* conditions can be disregarded in the model for the present particle diameters. One reason why wetting transitions induced by pressure have attracted considerable attention in the past, is that smaller drops and much larger structures on the order of tens of micrometers were

considered.¹⁹¹

The Wenzel to Cassie transition is in fact quite unlikely for this geometry as was shown in chapter 5,¹³³ where it was shown that a transition from a Wenzel to Cassie state can occur if the surface has little to no locations where the liquid-vapour interface inside the surface structure can become pinned. However as shown in figure 7.7(d), the energetic barrier for the uplifting transition is approximately a factor of 4 lower than the collapse transition for a given η and with approximately the same exponent α . Given this surprising result, it would be interesting to investigate if such an uplifting transition is possible experimentally, for instance by means of electrowetting. This is however outside of the scope of the present work.

7.4 Dual-sphere surfaces

7.4.1 Wetting states and experimental comparison

By adding a second level structure, the number of relevant surface parameters is increased from two to three: δ and packing factors η_1 and η_2 for both levels. The model results are plotted in figure 7.8 together with experimental data from previous work. The number of possible states has increased to four. For ease of reading, from here on CC will indicate the Cassie-Cassie state and similar for the CW, WC and WW states, where the first letter denotes the first, i.e. the lower lying, primary level of the structure. Therefore, also the number of possible wetting state transitions has increased significantly, as will be discussed further on.

Before discussing the apparent contact angles from the model and experiments in figure 7.8(a), it is instructive to first look briefly at figures 7.8(b) and (c), where it is shown that the vapour height for the second-level structure is not dependent on η_1 , η_2 and \tilde{h}_1 . The second layer therefore acts as if it were a lyophobic coating to the first layer. The CW state \tilde{h}_1 is extremely high for high δ 's, but decreases faster with decreasing δ than the CC state. The packing of the second layer clearly influences the vapour height in the first layer and the behaviour of this secondary layer can be determined independently from other surface parameters. Only the limiting cases of packing are presented, i.e. low packing ($\eta_1 = \eta_2 = 0.3$) on both levels as well as high packing ($\eta_1 = \eta_2 = 0.9$). For all intermediate combinations, intermediate values for β , \tilde{h}_1 and \tilde{h}_2 are found. This means that the model is stable with respect to the input parameters, and interpolations can be made.

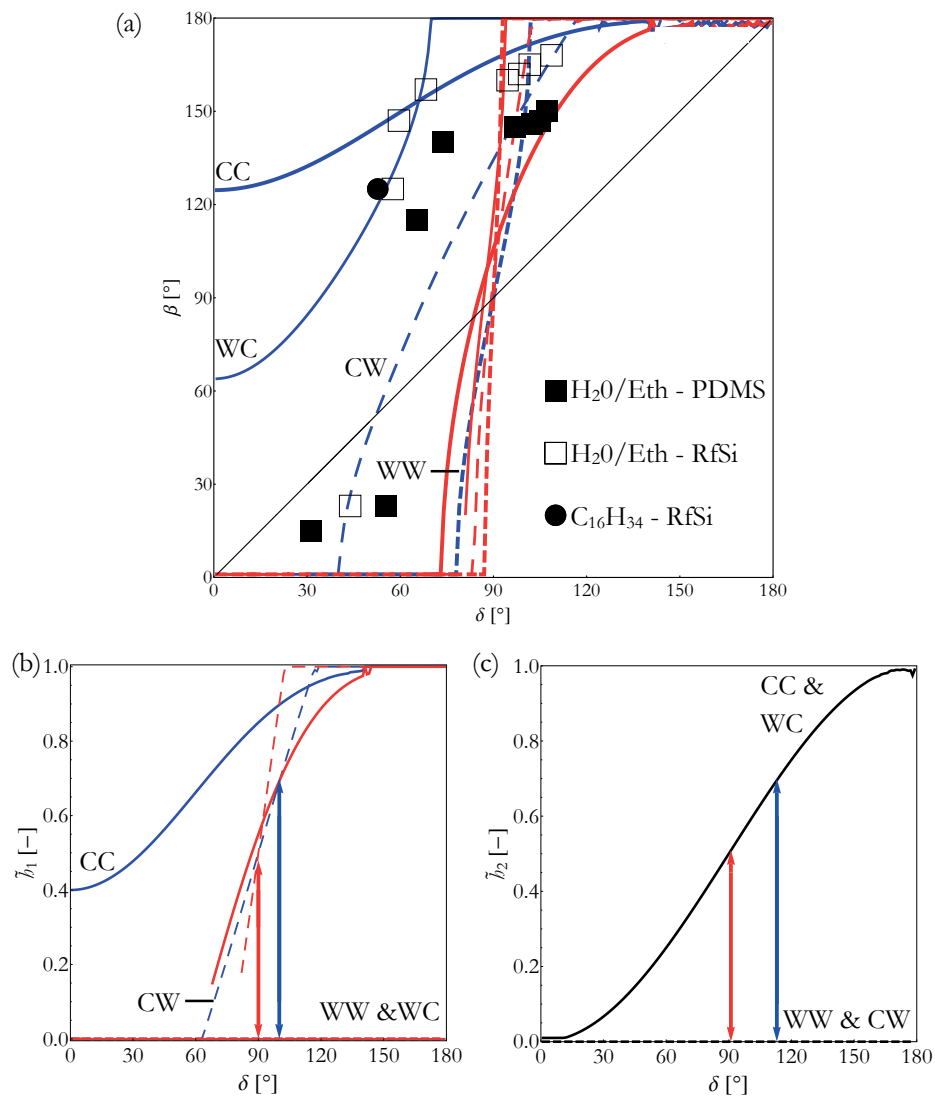


Figure 7.8: Model results for a surface packed with dual-scale, raspberry-like structure. Blue lines represent low packing ($\eta_1 = \eta_2 = 0.3$), red lines represent high packing ($\eta_1 = \eta_2 = 0.9$). The various states are only indicated for low packing but have equivalent line styles (thickness, dashing) for high packing. (a) β as a function of δ . The experimental data is reproduced from^{182,186}. (b and c) The arrows indicate where the preferred state is suspended (to the right) or collapsed (to the left) for the given height, where the colour corresponds to the packing as above. (b) \tilde{h}_1 as a function of δ . (c) \tilde{h}_2 as a function of δ . Note that for \tilde{h}_2 the CC and WC states lie on a single curve, as do the WW and CW states.

In figure 7.8(a) the relationships between δ and β are plotted for the various dual-structured states, analogous to figure 7.7(a). The experimental data agree well with the model results for low packing surfaces, even though in practice the experimental surfaces are determined via electron microscopy to have intermediate packing $\eta_1 \sim \eta_2 \sim 0.5 - 0.6$. This decrease in packing compared to the single structured surfaces is presumably in part due to the hindrance of the spontaneous self-organisation in the primary caused by adding the second layer. The experimental dual-structured surfaces have a primary layer of 700 nm (equal to the single-structure surfaces from figure 7.6(a)) and a secondary layer of 70 nm. The data are gathered from contact-angle measurements for a variety of mixtures of water and ethanol in various volume fractions to systematically decrease the liquid-vapour surface tension of the probe liquid. The intrinsic contact angle measurements were made on smooth reference surfaces.

Comparing the experimental PDMS- to RfSi-covered surface, it can be seen that the PDMS samples have overall lower β 's, but the overall trend through the data-points is pleasingly similar to that of RfSi. Both are monotonously increasing with increasing δ as would be expected. A plausible explanation for the absolute difference in β is that the PDMS surface layer that is chemically bonded onto the structure is thicker. This causes the crevices between the surface spheres to be filled more with PDMS, in particular for the second layer (for which the particles only have 70 nm diameter). The data for RfSi shows that it is in a meta-stable state for $60^\circ < \delta \leq 90^\circ$, because if it were in the WW state it would exhibit $\beta = 0^\circ$. The PDMS data on the other hand shows a transition to low contact angles already at $\delta \sim 70^\circ$. Therefore, the RfSi-functionalised surfaces are relatively more oleophobic to water/ethanol mixtures.

The experimental data from both β and β_b indicates that with decreasing δ , the wetting transitions occur as CC \rightarrow WC \rightarrow WW. This is based on four observations:

- i. For PDMS, the two data-points with high β that lie on the intersect of the CC and the WC curves (at $\beta = 140^\circ$ and $\beta = 110^\circ$) exhibit high hysteresis of 95° and 100° degrees as well, which corresponds to a partially collapsed state such as WC or CW and not to a fully suspended CC state.
- ii. For RfSi, the data point with $\beta = 125^\circ$ exhibits hysteresis of 55° and the closely lying hexadecane data point exhibits roll-off angles $> 60^\circ$, which is consistent with the water/ethanol mixture with similar intrinsic contact angle. The hexadecane measurement also clearly demonstrates the oleophobic nature of these structures, although the high sliding angle shows that the surface cannot be considered superoleophobic or self-cleaning with respect to hexadecane.
- iii. For both PDMS and RfSi, all data points at higher δ 's than mentioned in (i) and (ii) exhibit low hysteresis and roll-off angles below 10° , corresponding well to suspended wetting states and the CC-state is the only truly suspended state for

which such low hysteresis would be expected.

- iv. For low δ the data indicate a fully wetted surface even though $\beta \sim 20^\circ$ and not 0° (i.e complete wetting), which is predicted for the WW state. The drops exhibit high hysteresis $> 100^\circ$ as well. It is most likely that the drop is in the WW state, and that due to local pinning, the drop cannot completely wet the surface since the movement of the contact line is pinned by surface defects. It is also possible that the drop is in fact slowly being imbibed into the surface, corresponding well with the slow movement of the imbibition process, which leaves a residual drop of low contact angle on the surface for long timescales.²

In conclusion, the experimental data agree well with the model results with intermediate to low packing, and show that as the intrinsic contact angle of a probe liquid decreases, the observed contact angles found experimentally match with different simulated wetting states. High packing surfaces are actually predicted to exhibit poor oleophobicity, as all states (even the CC state) will have $\beta \downarrow 0^\circ$ for $\delta \leq 70 - 80^\circ$. These high-packed states lie close together and will be difficult to distinguish in experiments based on contact angles alone. Low packing surfaces are predicted to exhibit very high apparent contact angles even for very low δ 's. The CC and to a lesser extent the WC states exhibits very high contact angles also for all intrinsic contact angles below 90° , but these states are meta-stable.

7.4.2 State transitions and stability

Because the experimental data indicates consistently that the drops are in meta-stable wetting states, the same analysis on the state transitions and stability used for single-sphere surfaces (section 7.3.2) is applied here to the more complicated dual-scale structured surface. There are five possible transitions (collapse and uplifting) to consider: between the CC and CW state, the CW and WW state, the CC and WC state, the WC and WW state and finally and between the CC and WW state. Between the CW and WC states no single transition is considered, as this would involve simultaneous uplifting on one layer and collapse on another, which is highly unlikely. In figure 7.9, the transitions are plotted in the same manner as in figure 7.7(c) and (d), however the number of plots is doubled as both η_1 and η_2 are varied independently. Again figures 7.9(a) and 7.9(b) can be interpreted as state diagrams, where for legibility the actual states are not plotted on the graph. For instance, in 7.9(a), given a coordinate (δ, η_1) , the stable state can be reasoned from the surrounding transitions. In the upper right corner the state will be CC, and in the lower left corner WW. While the interested reader could work out the exact stable state at each point of the figure, the more relevant trends for the various transitions will now be discussed.

The results in 7.9 correspond well with the general trends already found for single sphere surfaces in 7.7, namely that δ^* for the collapse transition is lower than for state equilibrium which is in turn lower than for the uplifting transition. This holds true for all

transitions and packing factors considered. The energetic barriers for the collapse transitions are again higher than for the uplifting transition and again follow a power-law dependence as function of packing. This indicates self-consistency in the model. There are some minor numerical artefacts due to rounding which causes some mild scatter in the data, but the effect is less than 1° for δ^* or 5% for \tilde{B} , which is insignificant for the present discussion.

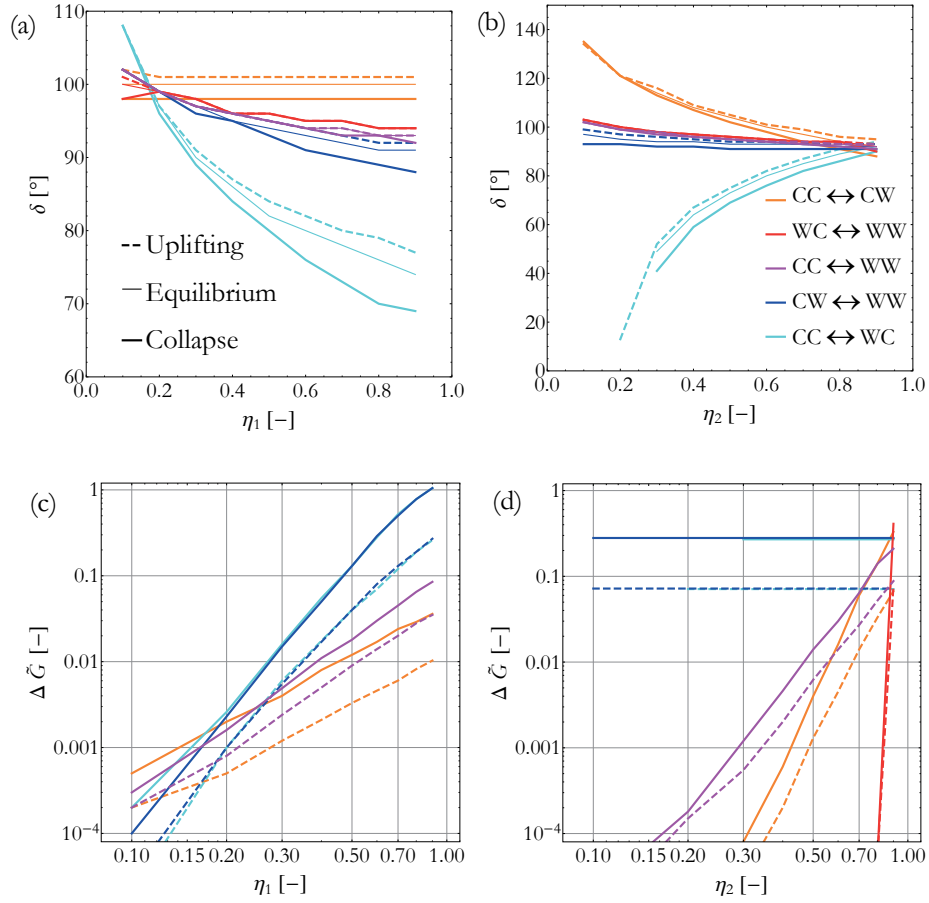


Figure 7.9: Wetting state transitions for dual-structured raspberry structures. The legends in (a) and (b) apply to all panels. (a) the δ 's according to equation 7.12 as function of η_1 with $\eta_2 = 0.6$. (b) same as (a) except as function of η_2 with $\eta_1 = 0.6$. (c) the energy barriers \tilde{B} for the various transitions as function of η_1 with $\eta_2 = 0.6$ and (d) the energy barriers \tilde{B} as function of η_2 with $\eta_1 = 0.6$. Note the double-logarithmic scale in (c) and (d).

A number of important conclusions can be drawn from figure 7.9, but most importantly, the energy barrier analysis indicates that the $CC \rightarrow WC$ transition can only

occur for almost all packing factors at lower δ^* and has to overcome higher energetic barriers than the CC \rightarrow CW transition. Recall that this is not in agreement with the experiments which agrees best with a CC \rightarrow WC transition. Furthermore, by studying the WC \rightarrow WW transition, it can be seen that this transition occurs at *higher* δ^* than the transition CC \rightarrow WC, and has extremely low energetic barriers. The reason for this is the high relative energy cost of the WC state, which has a large amount of entrapped vapour all around each primary sphere. The model therefore indicates that the WC state would be highly unstable and would collapse to the WW state almost immediately given the very low barriers.

Therefore, the barrier analysis predicts the collapse transition pathway to occur via the CW state instead of the WC state. For this reason, whether the actual drop transitions in the experiments via either the CW or WC state cannot be determined unambiguously from the presently available results. While the experimental data match better with the predicted WC contact angles than the CW curves, the observations (i-iv) are also consistent with an CC \rightarrow CW \rightarrow WW transition. Either way, the model indicates that the transition is a multi-step process.

The results presented in figure 7.9(a) and (b) indicate that δ^* for the collapse transition is only 4 – 5° lower than state equilibrium for most transitions. The CC \rightarrow WC transition is an interesting exception for a number of reasons:

- i. At high η_1 the acceptable fluid range is extended up to 8°.
- ii. At low η_2 the model predicts *no* transition at all since the energetic barrier between the states is higher than the potential energy gain.
- iii. δ^* of the collapse is found to actually *decrease* with decreasing packing (against the trend for all other transitions), while the energetic barrier does not decrease. This is caused by the fact that while decreasing the second level packing, the energy gained by the transition decreases but the barrier decreases by *exactly* the same amount, which is an incidental result of the particular definition (equation (7.11)) of the cross-over point.

7.4.3 Discussion

By comparing the model results for dual-structured surfaces to the experimental data it becomes clear that firm conclusions regarding the exact wetting states cannot be drawn yet even though the contact angle data matches well. A number of tentative conclusions are possible and several new experiments are suggested by the model to further elucidate the different wetting states. Both will now be discussed.

The transition from fully suspended to fully collapsed is very likely a multi-step process. However, the exact order cannot be established from the presently available data, as the most likely fit of the experimental contact angle data to the model contact angles does not agree

with the predicted stable state as predicted by the energy barrier analysis. When disregarding the barrier analysis however, the contact angle and hysteresis data are consistent with the model predictions. The additional effects of pinning and viscous dissipation, which are not included in the model, offer some additional insight. Pinning of the interface by the spheres is expected to improve the robustness of the metastable Cassie state on the second level more than on the first level as there are many more pinning sites which would increase the stability of a meta-stable wetting state by preventing the local transition. Equally, viscous dissipation will also be higher for the smaller inter-sphere gaps on the second level. This could be a further explanation why the WC state might be preferred over the CW state regardless of the idealized barrier calculations.

The barrier analysis results for the CC \rightarrow WC transition are intriguing. No experimental results were obtained so far in the low η_2 range. The model predictions for this transition seem hard to believe, especially in the limit of $\eta_2 \rightarrow 0$, but it is worthwhile to experimentally vary η_2 . Both preparation methods for these raspberry structures, i.e. attaching the small spheres to the larger spheres before attaching the raspberry to the surface,²² or creating the structure in a layer-by-layer approach as in figure 7.1¹⁸⁶ lend themselves well to varying η_2 . Systematic variation of the packing on both levels can then also aid in determining whether the intermediate state is either WC or CW, as the effect on packing variation would be quite different for each state. Another possibility to consider is that the experimental drops with high hysteresis are in fact partially in the WC and partially in the CW state (i.e. a mixed state) which may also be borne out by such experiments.

The model also has an important practical limitation: no correction for the finite size ratio between the primary and secondary structures (i.e. r_1 / r_2) was included. Consider the radius of curvature of the larger spheres as the curvature of the plane on which the smaller spheres lie: if the size ratio is sufficiently large, the smaller spheres will effectively be surrounded by neighbouring particles on a nearly smooth plane. In that case no correction is needed. More detailed calculations have shown that for ratios of 10 or larger the model results discussed above are accurate. Below a size ratio of 10, the results start to deviate noticeably, and certainly below a size ratio of 5 the results presented in this section should not be used without correcting for the size ratio.

Lastly, a brief comparison to Lotus leaf structures (figure 7.1(a)) shows that low packing on at least the first level structures appears optimal for hydrophobicity (from evolutionary arguments). Comparison between the PDMS (with slightly more filled crevices due to the thicker PDMS layer) to the RfSi data, indicates that lower packing of the RfSi surface increases lyophobicity while retaining sufficient stability (when compared on the basis of intrinsic contact angle). This preference for lower packed surfaces corresponds well with previously reported experimental findings by Bormashenko *et al.*,¹⁸⁴ who used gold-coated dual-structured surfaces with similar geometry. Observed water contact angles ($\delta \approx 60^\circ$) up

to 160° were reported for relatively open structures, while complete wetting was reported for structures packed closely on both levels. These results are consistent with the model presented here as there are no states available at $\delta = 60^\circ$ and high packing which are not completely wetting.

7.5 Conclusions

The model presented in this chapter shows that dual-scale structured (super)lyophobic surfaces can be described by means of a Gibbs energy model, which generally agree well with experimental results. Key features of the model are its simplicity, the possibility to make straightforward adaptation to different geometries (on either level) and the focus on predicting not only the wetting states but also the transitions between them. The addition of the second level structure to the primary structure improves the potential for achieving superoleophobicity through the Cassie-Cassie state. It was demonstrated that this state is metastable for intrinsic contact angles below 90° .

Low packing of the spheres on both levels of the structure is needed for true superoleophobicity, which leads to more unstable wetting state than higher-packed surfaces. The experimental data as well as model indicate that the transition from Cassie-Cassie to Wenzel-Wenzel wetting states proceeds via at least one intermediate state. Whether this transition occurs via the Wenzel-Cassie or Cassie-Wenzel intermediate state cannot be concluded with certainty at the moment. Especially the Wenzel-Cassie state appears unlikely at first glance, but could be crucial in preventing collapse of the Cassie-Cassie state at lower intrinsic contact angles. Further experimental optimisation of the packing of the spheres on the second level in particular appears worthwhile for superlyophobicity, while at the same time shedding more light on the exact states and transitions.

8. Technology assessment and future research⁶

“Après Nous le déluge!”

– Louis Quatorze

⁶ This chapter is published in:

- M. E. Koekoek, T. Meijer, R. J. Vrancken, *Digital printing of multilevel optical variable Devices for Document Security & Brand Protection*, Proceedings of the Optical Document Conference II, 357-367, San Francisco, United States (2010)
- C. W. M. Bastiaansen, T. Meijer, R. J. Vrancken, *Security device with multiple authentication features*, PCT/EP2008/001924, Applicant Eindhoven University of Technology, Priority date filing 13-3-2007
- Danqing Liu, Robert J. Vrancken, Jolke Perelaer, Ulrich S. Schubert, Dirk J. Broer, Jaap den Toonder, *Coffee rings in a three-component inkjet printed drop with binder, solvent and magnetic nanoparticles*, in preparation (2012)
- M. A. H. van Dongen, R. Vrancken, F. Horsten, P. Ketelaars, J. Bernards, *UV-mediated coalescence and mixing of inkjet printed drops*, in preparation (2012)

8.1 Introduction

The work described in this thesis can aid in the development of current or new applications. In this chapter the results of this thesis are discussed in the context of relevant applications (8.2-8.4) and two new research directions (8.5-8.6) with particular relevance to these applications are also briefly described, including preliminary results.

8.2 Printing applications

Findings from this thesis on the spreading of liquids on micro-patterned surfaces (i.e. with length scales at least approximately one order of magnitude smaller than the droplet size) can have important applications in the field of printing. Many of the surfaces printed onto have patterning, from the porous structures of many papers, to the micro-/nano-structures that many polymer substrates obtain during processing into films. In Chapter 3 it was shown that even nanometre-size grooves in polyimide layers can significantly elongate drops. Since the elongation is dependent on the initial drop shape, corrections for this effect will be different for impact and non-impact printing techniques.

For industrial printing applications, such as printed electronics or printed OLED-displays, the work in this thesis (Chapters 3 and 6) shows that substrate anisotropy can significantly influence drop shapes. Problems may arise when the substrates employed in the process are anisotropic due to the fabrication process, but this anisotropy is not carefully controlled. Examples of such surfaces are glass, copper PCB plates, flexible polymers for flexible displays and flexible solar cells. Chapter 6 shows that even for situations in which a single drop has a large impact velocity on the surface and therefore a lot of excess energy, the movement of the contact line can be determined locally by a subtle interplay between pinning and de-pinning mechanisms. Therefore, specification in advance of tolerances in surface anisotropy (both chemical and topographical) is important to ensure the development of a robust process.

It was shown in chapters 3 and 4 that drop shape anisotropy also occurs in (micro-transfer and inkjet) printed polymerisable liquid crystalline drops. Surface patterning by creating nano-scale corrugations is one of the main techniques used in practice to align the liquid crystals. As explained in chapter 4, such alignment is needed to generate the special optical effects which liquid crystals are used for in applications such as LCD displays. An interesting new application is inkjet printed polymerisable liquid crystal anti-counterfeiting products, which provide a flexible means to achieve high levels of resistance to counterfeiting combined with secure digitally printed unique information. This provides secure track & trace functionality, which is particularly suited to prevent counterfeiting of high value products in global supply chains.¹⁰⁶⁻¹⁰⁸ These security features have recently been

produced on an industrial scale for the first time, as presented in figure 8.1.

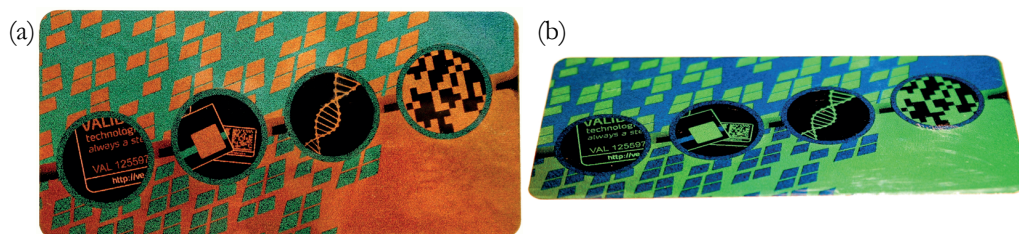


Figure 8.1: example of inkjet printed polymerisable liquid crystal based security label. (a) front view, (b) view from a tilted angle. At an angle, the label exhibits a colour shift of the chiral nematic structures: both a red-to-green and a green-to-blue shift depending on the local concentration of chiral dopant. The self-adhesive label further includes high resolution text, sensitivity to circularly polarised light, a unique barcode and a tamper-evident label construction, all of which increase the security level considerably.

8.3 Microfluidic devices

Microfluidic flows are dictated by surface energy and external forces such as pressure differences via micro-pumps. The work in this thesis employs a drop as a model system, which has a large free liquid-vapour surface on an open horizontal surface. Chapters 3, 5 and 6 present results relevant for micro-fluidic applications, even though micro-fluidic devices typically have closed surfaces and often deal with filled channels of liquid. During filling, or if there is batch processing, the contact lines of internal liquid-vapour surfaces follow a path through the device. Chapter 3 shows the importance of the Gibbs criterion and strong influence on the shape and mobility of liquid-vapour interfaces of pinning. This pinning was shown to be relevant even on surfaces with only tens of nanometre deep grooves, which are normally not detectable by optical means and can easily be introduced unknowingly in the fabrication processes of such devices.

Chapter 5 shows a particular configuration of corrugated surfaces with a practical means of creating a collapsed-to-suspended state drop. Within the context of a micro-fluidic device, such an element enables the temporary stopping or slowing down of the liquid-vapour interface within the device. Electrowetting is well-known in the micro-fluidic research community, but the opportunities of guiding a fluid in the locally suspended state (i.e with entrapped vapour in the surface structure) could lead to reversible switching between a high and a low flow resistance mode, for which the latter could potentially require considerably less pressure. Effecting a temporary collapse transition also allows the creation of an equally temporary fluid buffer, acting like a fluidic delay. The location and timing of this delay can be chosen flexibly, contrary to the now common in-channel filters.¹⁶⁶

Chapter 6 shows that the shape of drops can be determined by the flow mechanism of the contact line which moves through an array of micro-posts. The movement of the contact line through the posts is dominated by two distinct types of pinning behaviour, connected and disconnected contact line de-pinning. Independent work, both experimental and with lattice Boltzmann modeling is continuing^{148,192-196} on enclosed systems which are directly useable as micro-fluidic applications, and which show that indeed these pinning types can affect the motion of the interface in a delicate way. This could lead to elements that have high or low hysteresis depending on the direction that the contact line is moving, enabling elements such as one-way fluidic diodes. Such elements could also respond differently depending on the fluid, or be actively modulated through electrowetting, as the effect is found to be dependent on the intrinsic contact angle of the fluid.

In conclusion, careful structuring of the surfaces within a micro-fluidic device can beneficially employ pinning and de-pinning of the liquid-vapour interface and modulation of the liquid-solid interfaces to control the fluids within the device, just as the morphology of drops is controlled in the model system considered in this thesis. This widens the array of possible elements in micro-fluidic circuits, such as e.g. diodes, delays, resistors and pumps.

8.4 Superlyophobic / -lyophilic materials

Chapter 4 demonstrates a surface design which exhibits recovery from complete wetting, as it allows for a Wenzel-to-Cassie state transition. The Cassie state is shown to have superhydrophobic properties. The ability to switch between wetting states via electro-wetting enables surfaces to alternate between self-cleaning and attractive to contamination.

Chapter 7 presents a model for a novel biomimetic superlyophobic surface made up of a raspberry-like dual-structured surface morphology. The model describes the already experimentally realized surface, and points in directions to further optimise it. It also details the constraints that have to be imposed on the surface to retain a stable superlyophobic wetting state. A number of factors can easily compromise this stability. Contamination of the surface with oily substances is a known problem, as these have lower intrinsic contact angles and can sometimes infiltrate the surface structure or collapse via a wetting transition into this structure. A larger energy barrier between the collapsed and fully suspended state will create less instability for the meta-stable suspended state, which is the desired state for superlyophobicity. Another destabilizing factor is defect formation in the coating structure, either during creation or due to mechanical wear and tear effects such as scratches and abrasion. Work to include many of the known types of instability in such coatings into the model is underway.¹⁹⁷

The structure of the model can be easily adapted to different morphologies and extended in a hierarchical way to triple- or even higher-structured surfaces. Initial results of

triple-structured surfaces are underway,¹⁹⁸ both experimentally and based on the model. Another interesting approach is to use as a first structure level textile fibres, which are inherently structured due to their curvature and weaving. Functionalizing these fibres can lead to very lyophobic textiles, and initial results are promising.¹⁷²

Interestingly, by learning more about the way surfaces repel liquids, knowledge is also gathered on surfaces that absorb wetting liquids in optimal ways. Surfaces with hierarchical roughness have the potential to create very strong bonds with adhesives if the completely wetted Wenzel-Wenzel state is reached everywhere, although this could be at the expense of mechanical robustness of the solid surface. For such applications, low energetic barriers between the wetting states are desirable.

8.5 Coalescence

Coalescence is a topic not treated in detail in this thesis but is of great importance in many of the above mentioned applications. While there are real-world examples of single drops or perfectly formed layers of water coming into contact with a surface, in reality it is often the case that multiple drops are required to coalesce into a layer or line structure. Inkjet printing is a particular example, where all structures are formed one drop at a time. For instance, the multi-colour inkjet printed label presented in figure 8.1 had to be carefully designed to prevent excessive coalescence.

Coalescence has been studied, with particular interest in the power laws governing the formation of the 'bridge' between the drops at early times.^{199–206} Three interesting questions in connection to coalescence are: (a) how do the deposition (printing) methods influence the dynamics and final state of coalesced drops, (b) how well are the drops mixed after coalescence, and is this dependent on the final state alone or also the dynamics and (c) what influence does surface structuring have on coalescence.

Preliminary results^{207,208} show that it is possible to study the mixing aspect of coalescence by means of two different fluorescent markers, as shown in figure 8.2. By making fluorescent microscopic images, and renormalizing to central emission wavelengths, it is possible to study coalescence as well as mixing, both in real-time and after inkjet printing. The structures were photo-polymerised after coalescing to fixate the drop shape and degree of mixing and facilitate subsequent analysis.

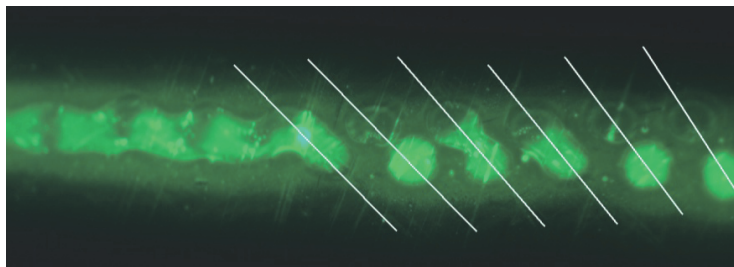


Figure 8.2: fluorescent microscopy image of two lines of drops printed close together under a small angle. From left to right, the spacing between the drops increases slightly, and the drops become less and less coalesced. By adding a fluorescent marker to the drops printed in one of the lines, it can be observed that with decreasing coalescence, the fluids in the drops also become less mixed. Via optical analysis it is possible to determine the degree of mixing quantitatively. The white lines are guides to the eye.

It was found that indeed with increasing coalescence, mixing increases but remains incomplete as long as a distinct bridge exists between the drops. The influence of substrate temperature was two-fold: on the one hand, increasing the temperature increased coalescence and mixing due to lower viscosity, as could be expected, but the increased evaporation of solvent increased the overall viscosity of the printed drop as well. For a given material (liquid crystals in this particular case, as described in chapter 4) and solvent concentration levels, an optimum can be found for the maximum degree of coalescence and mixing. Using grooved polyimide substrates, similar to those described in chapter 3, it was found unexpectedly that no significant differences were found between grooved and smooth surfaces with regards to the degree of drop coalescence and mixing. Work to complete these lines of research is ongoing.²⁰⁸

8.6 Coffee ring effect

Also researched, but outside the scope of this thesis, is the so-called coffee ring effect (also known as the coffee drop, or coffee stain effect). This effect was first investigated by Deegan *et al.* after observing that drying drops of coffee form rings of deposit at the contact line, instead of depositing uniformly.²⁰⁹ The driving force is a combination of evaporation of the solvent (in this case water), a pinned contact line, and a spherical cap shape, which has to be maintained by effectively creating a radially outward flow, which carries the particles to the contact line. The contact line is then pinned even further due to the accumulation of particles, called self-pinning. While in this thesis the focus is on structured (anisotropic) substrates, the research goal of the work on the coffee ring effect was to investigate a situation commonly found in practice, but not described in literature: a drop consisting of three generic components, a non-evaporating liquid binder, an evaporating solvent and solid

particles. So far in literature either a binder-solvent or a solvent-particle system was investigated. The surprising initial results²¹⁰ show that even with low weight percentages of solvent (below 20 w%), a considerable portion of the particles can still accumulate at the contact line. Examples are shown in figure 8.3.

This result has many practical implications, because the ink formulations commonly used in the printing industry are complex chemical products, which typically consist of the three components mentioned above. The coffee ring effect could be detrimental to many applications, and poses technical constraints on the use of solvents in particular. This effect can however also be used beneficially to enable new applications. The first are meta-materials (such as optical or magnetic meta-materials),²¹¹ which require fine periodic structures of for instance rings to create material properties such as negative indices of refraction. The particular benefits from using the coffee ring effect are that the due to self-organisation the efforts to pattern the material is greatly reduced. Employing inks with all three components has the additional benefit that the particle deposition pattern is embedded in a binder, which can then optionally be thermally or UV-cured. This binder can provide a durability that a structure of solid particles can only achieve via some chemical or thermal treatment such as sintering.

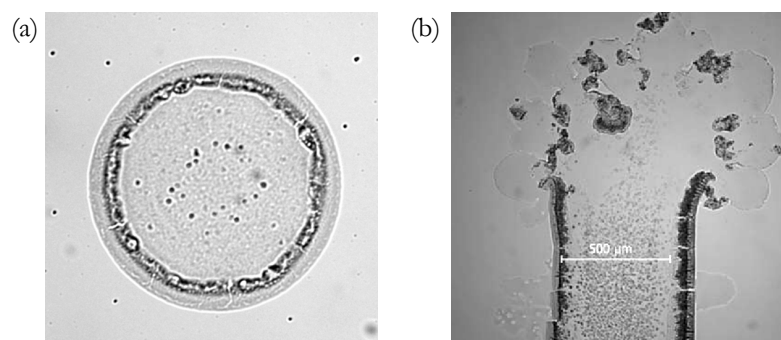
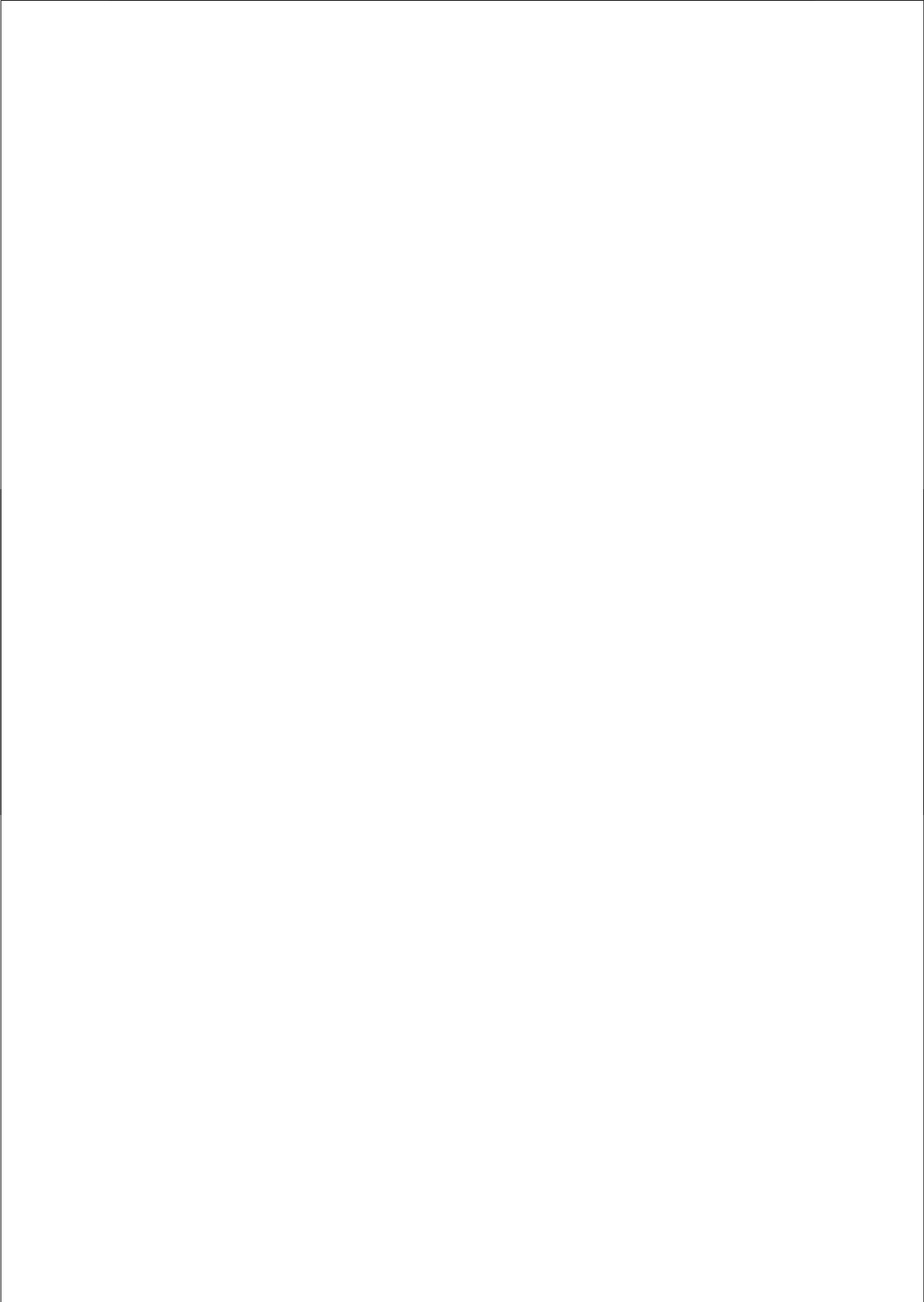


Figure 8.3: Coffee ring effect for inkjet printed drops with three components: acrylate binder, solvent and Fe-nanoparticles. (a) Single drop with diameter $\sim 60 \mu\text{m}$ showing clear build-up at the contact line. (b) Print pattern $\sim 500 \mu\text{m}$ consisting of multiple drops, showing the potential detrimental effects of the coffee ring effect on pattern fidelity: the top part of the structure is ruptured by the build-up of internal Laplace pressure.

The purpose of this chapter was to show the great application potential as well as the many new research challenges that exist in the field, and to which the work in this thesis has attempted to contribute. I can only hope to have imbued in the reader who has made it to the end of this thesis some of the enthusiasm and joy with which I have worked in this exciting field with inspiring mentors, colleagues and friends.



Appendix A: References

- (1) DeGennes, P. G.; Brochard-Wyart, F.; Quere, D. *Capillarity and Wetting Phenomena: Drops, Bubbles, Pearls, Waves*; 1st ed.; Springer, 2003.
- (2) DeGennes, P. G. Wetting: statics and dynamics. *Rev. Mod. Phys.* **1985**, *57*, 827–863.
- (3) Het Waterschapshuis www.ahn.nl/viewed (accessed Oct 11, 2011).
- (4) Rijkswaterstaat <http://www.rijkswaterstaat.nl/water/veiligheid/bescherming%5Ftegen%5Fhet%5Fwater/waterkeringen/dijken/> (accessed Oct 11, 2011).
- (5) Slot, M. PrintValley and High Tech Top projects: an introduction <http://global.oce.com/oce-innovation/open-innovation/printvalley/printvalley-symposium.aspx> (accessed Nov 11, 2011).
- (6) Tien, J.; Xia, Y.; Whitesides, G. M. Microcontact printing of SAMs. In *Self-Assembled Monolayers of Thiols*; Thin Films; Academic Press: San Diego, CA, 1998; Vol. 24.
- (7) Verbakel, F. High resolution contact printing of functional polymers and liquid crystals. M.Sc. thesis, Eindhoven University of Technology, 2004.
- (8) Houten, van, T. Micro-transfer printing of reactive mesogens. M.Sc. thesis, Eindhoven University of Technology, 2005.
- (9) Sanchez, C.; Bastiaansen, C. W. M.; Broer, D. J.; Verbakel, F. Microstructuring of Mesogens Using Contact Printing. *Patent application 2004, US20050631959 20050711; US20040587045P 20040713; WO2005NL00495 20050711*.
- (10) Perelaer, J.; Smith, P. J.; Mager, D.; Soltman, D.; Volkman, S. K.; Subramanian, V.; Korvink, J. G.; Schubert, U. S. Printed electronics: the challenges involved in printing devices, interconnects, and contacts based on inorganic materials. *Journal of Materials Chemistry* **2010**, *20*, 8446.
- (11) Oosten, van, C. L. Responsive liquid crystal networks. Ph. D. thesis, Eindhoven University of Technology, 2009.
- (12) Barbulovic-Nad, I.; Lucente, M.; Sun, Y.; Mingjun, Z.; Wheeler, A. R.; Bussmann, M. Bio-Microarray Fabrication Techniques—A Review. *Critical Reviews in Biotechnology* **2006**, *26*, 237–259.
- (13) Campbell, P. G.; Weiss, L. E. Tissue engineering with the aid of inkjet printers. *Expert Opinion on Biological Therapy* **2007**, *7*, 1123–1127.
- (14) Bakker, M. Presentation on a technology developed by Océ Technologies B.V. and Mutracx B.V. <http://global.oce.com/oce-innovation/open-innovation/printvalley/printvalley-symposium.aspx> (accessed Oct 11, 2011).

- (15) Whitesides, G. M. The origins and the future of microfluidics. *Nature* **2006**, *442*, 368–373.
- (16) Squires, T. M.; Quake, S. R. Microfluidics: Fluid physics at the nanoliter scale. *Rev. Mod. Phys.* **2005**, *77*, 977–1026.
- (17) *Micro Process Engineering: A Comprehensive Handbook*; Hessel, V.; Renken, A.; Schouten, J. C.; Yoshida, J., Eds.; 1st ed.; Wiley-VCH, 2009.
- (18) Watts, P.; Haswell, S. J. Chemical Synthesis in Microreactors. In *Microengineering in Biotechnology*; Hughes, M. P.; Hoettges, K. F., Eds.; Humana Press: Totowa, NJ, 2010; Vol. 583, pp. 109–120.
- (19) Liu, D.; Bastiaansen, C. W. M.; Broer, D. J.; Onck, P.; Toonder, J. d. Inkjet printing of magnetic/non-magnetic polymer microfluidic actuators. *Proceedings of 14th International Conference on Miniaturized Systems for Chemistry and Life Sciences* **2010**, 515–517.
- (20) Barthlott, W.; Neinhuis, C. Purity of the sacred lotus, or escape from contamination in biological surfaces. *Planta* **1997**, *202*, 1–8.
- (21) Gao, X.; Jiang, L. Biophysics: Water-repellent legs of water striders. *Nature* **2004**, *432*, 36.
- (22) Ming, W.; Wu, D.; van Bentem, R.; de With, G. Superhydrophobic Films from Raspberry-like Particles. *Nano Letters* **2005**, *5*, 2298–2301.
- (23) Wu, D. Nature-inspired superlyophobic surfaces. Ph. D. thesis, Eindhoven University of Technology, 2007.
- (24) Young, T. An Essay on the Cohesion of Fluids. *Philosophical Transactions of the Royal Society of London* **1805**, *95*, 65–87.
- (25) Rowlinson, J. S.; Widom, B. *Molecular Theory of Capillarity*; Dover Publications, 2003.
- (26) Paula, de, J.; Atkins, P. *Atkins' Physical Chemistry*; 9th Revised ed.; Oxford University Press, 2009.
- (27) Dettre, R. H.; Johnson, R. E. Contact Angle Hysteresis. In *Contact Angle, Wettability, and Adhesion*; Fowkes, F. M., Ed.; American Chemical Society: Washington, D.C., 1964; Vol. 43, pp. 136–144.
- (28) Dettre, R. H.; Johnson, R. E. Contact Angle Hysteresis. IV. Contact Angle Measurements on Heterogeneous Surfaces¹. *J. Phys. Chem.* **1965**, *69*, 1507–1515.
- (29) Huh, C.; Mason, S. G. Effects of surface roughness on wetting (theoretical). *Journal of Colloid and Interface Science* **1977**, *60*, 11–38.
- (30) Johnson, R. E.; Dettre, R. H. Contact Angle Hysteresis. III. Study of an Idealized Heterogeneous Surface. *J. Phys. Chem.* **1964**, *68*, 1744–1750.

- (31) Johnson, R. E.; Dettre, R. H. Contact Angle Hysteresis. In *Contact Angle, Wettability, and Adhesion*; Fowkes, F. M., Ed.; American Chemical Society: Washington, D.C., 1964; Vol. 43, pp. 112–135.
- (32) Li, W.; Amirfazli, A. A thermodynamic approach for determining the contact angle hysteresis for superhydrophobic surfaces. *Journal of Colloid and Interface Science* **2005**, *292*, 195–201.
- (33) Miwa, M.; Nakajima, A.; Fujishima, A.; Hashimoto, K.; Watanabe, T. Effects of the Surface Roughness on Sliding Angles of Water Droplets on Superhydrophobic Surfaces. *Langmuir* **2000**, *16*, 5754–5760.
- (34) Oliver, J. P.; Huh, C.; Mason, S. G. An experimental study of some effects of solid surface roughness on wetting. *Colloids and Surfaces* **1980**, *1*, 79–104.
- (35) Israelachvili, J. N. *Intermolecular and Surface Forces*; Academic Press, 2011.
- (36) Owens, D. K.; Wendt, R. C. Estimation of the surface free energy of polymers. *Journal of Applied Polymer Science* **1969**, *13*, 1741–1747.
- (37) Rabel, W. Einige Aspekte der Benetzungstheorie und ihre Anwendung auf die Untersuchung und Veränderung der Oberflächeneigenschaften von Polymeren. *Farbe u. Lack* **1971**, *77*, 997.
- (38) Kaelble, D. H. Dispersion-Polar Surface Tension Properties of Organic Solids. *The Journal of Adhesion* **1970**, *2*, 66–81.
- (39) Pompe, T.; Herminghaus, S. Three-Phase Contact Line Energetics from Nanoscale Liquid Surface Topographies. *Phys. Rev. Lett.* **2000**, *85*, 1930–1933.
- (40) Holmberg, K. *Handbook of Applied Surface and Colloid Chemistry*; 2 volume set.; Wiley-Blackwell, 2001.
- (41) Liu, B.; Lange, F. Pressure induced transition between superhydrophobic states: Configuration diagrams and effect of surface feature size. *Journal of Colloid and Interface Science* **2006**, *298*, 899–909.
- (42) Laplace, de, P. S. *Oeuvres completes de Laplace, t IV, Supplement au livre X du traite de la mecanique celeste.*
- (43) Shuttleworth, R.; Bailey, G. L. J. The spreading of a liquid over a rough solid. *Discuss. Faraday Soc.* **1948**, *3*, 16–22.
- (44) Gibbs, J. W. *The Scientific Papers of J. Willard Gibbs, Vol. 1: Thermodynamics*; Ox Bow Pr, 1993.
- (45) Blow, M. L. Wetting on flexible and anisotropic surfaces. D. Phil. thesis, University of Oxford, 2010.
- (46) Wenzel, R. N. Resistance of solid surfaces to wetting by water. *Ind. Eng. Chem.* **1936**, *28*, 988–994.

- (47) He, B.; Lee, J.; Patankar, N. A. Contact angle hysteresis on rough hydrophobic surfaces. *Colloids and Surfaces A: Physicochemical and Engineering Aspects* **2004**, *248*, 101–104.
- (48) Peltonen, J.; Järn, M.; Areva, S.; Linden, M.; Rosenholm, J. B. Topographical Parameters for Specifying a Three-Dimensional Surface. *Langmuir* **2004**, *20*, 9428–9431.
- (49) Jeong, H. E.; Lee, S. H.; Kim, J. K.; Suh, K. Y. Nanoengineered Multiscale Hierarchical Structures with Tailored Wetting Properties. *Langmuir* **2006**, *22*, 1640–1645.
- (50) Cassie, A. B. D.; Baxter, S. Wettability of porous surfaces. *Trans. Faraday Soc.* **1944**, *40*, 546–551.
- (51) Behroozi, F. The profile of a dew drop. *American Journal of Physics* **1996**, *64*, 1120.
- (52) Mognetti, B. M.; Kusumaatmaja, H.; Yeomans, J. M. Drop dynamics on hydrophobic and superhydrophobic surfaces. *Faraday Discuss.* **2010**, *146*, 153–165.
- (53) Gao, L.; McCarthy, T. J. How Wenzel and Cassie Were Wrong. *Langmuir* **2007**, *23*, 3762–3765.
- (54) Panchagnula, M. V.; Vedantam, S. Comment on How Wenzel and Cassie Were Wrong by Gao and McCarthy. *Langmuir* **2007**, *23*, 13242.
- (55) Marmur, A.; Bittoun, E. When Wenzel and Cassie Are Right: Reconciling Local and Global Considerations. *Langmuir* **2009**, *25*, 1277–1281.
- (56) Gao, L.; McCarthy, T. J. An Attempt to Correct the Faulty Intuition Perpetuated by the Wenzel and Cassie “Laws.” *Langmuir* **2009**, *25*, 7249–7255.
- (57) Tuteja, A.; Choi, W.; Ma, M.; Mabry, J. M.; Mazzella, S. A.; Rutledge, G. C.; McKinley, G. H.; Cohen, R. E. Designing Superoleophobic Surfaces. *Science* **2007**, *318*, 1618–1622.
- (58) Seemann, R.; Brinkmann, M.; Kramer, E. J.; Lange, F. F.; Lipowsky, R. Wetting morphologies at microstructured surfaces. *Proceedings of the National Academy of Sciences of the United States of America* **2005**, *102*, 1848–1852.
- (59) Tu, D.; Tu, J.; Yeoh, G. H.; LIU, C. *Computational Fluid Dynamics: A Practical Approach*; 1st ed.; Butterworth-Heinemann, 2007.
- (60) Chen, Y.; He, B.; Lee, J.; Patankar, N. A. Anisotropy in the wetting of rough surfaces. *Journal of Colloid and Interface Science* **2005**, *281*, 458–464.
- (61) Brakke, K. A. The surface evolver. *Experimental Mathematics* **1992**, *1*, 141–165.
- (62) Succi, S. *The Lattice Boltzmann Equation for Fluid Dynamics and Beyond*; Oxford University Press, USA, 2001.

- (63) Diotallevi, F.; Biferale, L.; Chibbaro, S.; Pontrelli, G.; Toschi, F.; Succi, S. Lattice Boltzmann simulations of capillary filling: Finite vapour density effects. *The European Physical Journal Special Topics* **2009**, *171*, 237–243.
- (64) Sbragaglia, M.; Benzi, R.; Biferale, L.; Succi, S.; Toschi, F. Surface Roughness-Hydrophobicity Coupling in Microchannel and Nanochannel Flows. *Phys. Rev. Lett.* **2006**, *97*, 204503.
- (65) Yeomans, J. M. Mesoscale simulations: Lattice Boltzmann and particle algorithms. *Physica A: Statistical Mechanics and its Applications* **2006**, *369*, 159–184.
- (66) Bouzidi, M.; Firdaouss, M.; Lallemand, P. Momentum transfer of a Boltzmann-lattice fluid with boundaries. *Physics of Fluids* **2001**, *13*, 3452–3459.
- (67) Benzi, R.; Biferale, L.; Sbragaglia, M.; Succi, S.; Toschi, F. Mesoscopic modeling of a two-phase flow in the presence of boundaries: The contact angle. *Phys. Rev. E* **2006**, *74*, 021509.
- (68) Benzi, R.; Biferale, L.; Sbragaglia, M.; Succi, S.; Toschi, F. Mesoscopic Modelling of Heterogeneous Boundary Conditions for Microchannel Flows. *Journal of Fluid Mechanics* **2006**, *548*, 257–280.
- (69) Dupuis, A.; Yeomans, J. M. Modeling Droplets on Superhydrophobic Surfaces: Equilibrium States and Transitions. *Langmuir* **2005**, *21*, 2624–2629.
- (70) Kusumaatmaja, H.; Yeomans, J. M. Modeling Contact Angle Hysteresis on Chemically Patterned and Superhydrophobic Surfaces. *Langmuir* **2007**, *23*, 6019–6032.
- (71) Kusumaatmaja, H. Lattice Boltzmann studies of wetting and spreading on patterned surfaces. D. Phil. thesis, University of Oxford, 2008.
- (72) Pooley, C. M.; Kusumaatmaja, H.; Yeomans, J. M. Contact line dynamics in binary lattice Boltzmann simulations. *Phys. Rev. E* **2008**, *78*, 056709.
- (73) Briant, A. J.; Wagner, A. J.; Yeomans, J. M. Lattice Boltzmann simulations of contact line motion. I. Liquid-gas systems. *Phys. Rev. E* **2004**, *69*, 031602.
- (74) Kusumaatmaja, H.; Léopoldès, J.; Dupuis, A.; Yeomans, J. M. Drop dynamics on chemically patterned surfaces. *Europhysics Letters (EPL)* **2006**, *73*, 740–746.
- (75) Dupuis, A.; Yeomans, J. M. Droplets on patterned substrates: water off a beetle's back. *International Journal for Numerical Methods in Fluids* **2006**, *50*, 255–261.
- (76) Léopoldès, J.; Dupuis, A.; Bucknall, D. G.; Yeomans, J. M. Jetting Micron-Scale Droplets onto Chemically Heterogeneous Surfaces. *Langmuir* **2003**, *19*, 9818–9822.
- (77) Mognetti, B. M.; Kusumaatmaja, H.; Yeomans, J. M. Personal communications.
- (78) Kusumaatmaja, H.; Vrancken, R. J.; Bastiaansen, C. W. M.; Yeomans, J. M. Anisotropic Drop Morphologies on Corrugated Surfaces. *Langmuir* **2008**, *24*, 7299–7308.

- (79) Gleiche, M.; Chi, L.; Gedig, E.; Fuchs, H. Anisotropic Contact-Angle Hysteresis of Chemically Nanostructured Surfaces. *ChemPhysChem* **2001**, *2*, 187–191.
- (80) Morita, M.; Koga, T.; Otsuka, H.; Takahara, A. Macroscopic-Wetting Anisotropy on the Line-Patterned Surface of Fluoroalkylsilane Monolayers. *Langmuir* **2004**, *21*, 911–918.
- (81) Dupuis, A.; Leopoldes, J.; Bucknall, D. G.; Yeomans, J. M. Control of drop positioning using chemical patterning. *Applied Physics Letters* **2005**, *87*, 024103–024103–3.
- (82) Öner, D.; McCarthy, T. J. Ultrahydrophobic Surfaces. Effects of Topography Length Scales on Wettability. *Langmuir* **2000**, *16*, 7777–7782.
- (83) Bico, J.; Tordeux, C.; Quéré, D. Rough wetting. *Europhysics Letters (EPL)* **2001**, *55*, 214–220.
- (84) Yoshimitsu, Z.; Nakajima, A.; Watanabe, T.; Hashimoto, K. Effects of Surface Structure on the Hydrophobicity and Sliding Behavior of Water Droplets. *Langmuir* **2002**, *18*, 5818–5822.
- (85) Zhu, L.; Xiu, Y.; Xu, J.; Tamirisa, P. A.; Hess, D. W.; Wong, C.-P. Superhydrophobicity on Two-Tier Rough Surfaces Fabricated by Controlled Growth of Aligned Carbon Nanotube Arrays Coated with Fluorocarbon. *Langmuir* **2005**, *21*, 11208–11212.
- (86) Gao, X.; Yao, X.; Jiang, L. Effects of Rugged Nanoprotrusions on the Surface Hydrophobicity and Water Adhesion of Anisotropic Micropatterns. *Langmuir* **2007**, *23*, 4886–4891.
- (87) Kusumaatmaja, H.; Yeomans, J. M. Controlling Drop Size and Polydispersity Using Chemically Patterned Surfaces. *Langmuir* **2006**, *23*, 956–959.
- (88) Fidalgo, L. M.; Abell, C.; Huck, W. T. S. Surface-induced droplet fusion in microfluidic devices. *Lab on a Chip* **2007**, *7*, 984–986.
- (89) Ou, J.; Rothstein, J. P. Direct velocity measurements of the flow past drag-reducing ultrahydrophobic surfaces. *Physics of Fluids* **2005**, *17*, 103606–103606–10.
- (90) Joseph, P.; Cottin-Bizonne, C.; Benoît, J.-M.; Ybert, C.; Journet, C.; Tabeling, P.; Bocquet, L. Slippage of Water Past Superhydrophobic Carbon Nanotube Forests in Microchannels. *Phys. Rev. Lett.* **2006**, *97*, 156104.
- (91) Brandon, S.; Haimovich, N.; Yeager, E.; Marmur, A. Partial wetting of chemically patterned surfaces: The effect of drop size. *Journal of Colloid and Interface Science* **2003**, *263*, 237–243.
- (92) Chung, J. Y.; Youngblood, J. P.; Stafford, C. M. Anisotropic wetting on tunable micro-wrinkled surfaces. *Soft Matter* **2007**, *3*, 1163–1169.

- (93) Narhe, R. D.; Beysens, D. A. Nucleation and Growth on a Superhydrophobic Grooved Surface. *Phys. Rev. Lett.* **2004**, *93*, 076103.
- (94) Hirvi, J. T.; Pakkanen, T. A. Wetting of Nanogrooved Polymer Surfaces. *Langmuir* **2007**, *23*, 7724–7729.
- (95) Powers, J. M.; Pratten, D. H.; Collard, S. M.; Cowperthwaite, G. F. Spreading of oligomers on polymers. *Dental Materials* **1991**, *7*, 88–91.
- (96) Sánchez, C.; Verbakel, F.; Escuti, M. J.; Bastiaansen, C. W. M.; Broer, D. J. Printing of Monolithic Polymeric Microstructures Using Reactive Mesogens. *Advanced Materials* **2008**, *20*, 74–78.
- (97) Hermans, K.; Wolf, F. K.; Perelaer, J.; Janssen, R. A. J.; Schubert, U. S.; Bastiaansen, C. W. M.; Broer, D. J. High aspect ratio surface relief structures by photoembossing. *Applied Physics Letters* **2007**, *91*, 174103–174103–3.
- (98) Hermans, K. Latent Structured Thermally Developed Reliefs: Principles and Applications of Photoembossing, Eindhoven University of Technology, 2009.
- (99) Oliver, J. .; Huh, C.; Mason, S. . Resistance to spreading of liquids by sharp edges. *Journal of Colloid and Interface Science* **1977**, *59*, 568–581.
- (100) Broer, D. J.; Mol, G. N.; Challa, G. In situ photopolymerization of an oriented liquid-crystalline acrylate, 2. *Die Makromolekulare Chemie* **1989**, *190*, 19–30.
- (101) Broer, D. J.; Finkelmann, H.; Kondo, K. In-situ photopolymerization of an oriented liquid-crystalline acrylate. *Die Makromolekulare Chemie* **1988**, *189*, 185–194.
- (102) Broer, D. J.; Boven, J.; Mol, G. N.; Challa, G. In-situ photopolymerization of oriented liquid-crystalline acrylates, 3. Oriented polymer networks from a mesogenic diacrylate. *Die Makromolekulare Chemie* **1989**, *190*, 2255–2268.
- (103) Broer, D. J.; Hikmet, R. A. M.; Challa, G. In-situ photopolymerization of oriented liquid-crystalline acrylates, 4. Influence of a lateral methyl substituent on monomer and oriented polymer network properties of a mesogenic diacrylate. *Die Makromolekulare Chemie* **1989**, *190*, 3201–3215.
- (104) Broer, D. J.; Mol, G. N.; Challa, G. In-situ photopolymerization of oriented liquid-crystalline acrylates, 5.. Influence of the alkylene spacer on the properties of the mesogenic monomers and the formation and properties of oriented polymer networks. *Die Makromolekulare Chemie* **1991**, *192*, 59–74.
- (105) Koekoek, M. E.; Meijer, T.; Vrancken, R. J. Digital printing of multilevel optical variable Devices for Document Security & Brand Protection. In *Proceedings of Optical Document Conference*, San Francisco, USA, 2010; pp. 357–367.
- (106) Bastiaansen, C. W. M.; Meijer, T.; Vrancken, R. J. Inkjettable polymerizable liquid crystalline mixture. *Patent application* **2007**, PCT/EP2008/001868.

- (107) Bastiaansen, C. W. M.; Meijer, T.; Vrancken, R. J. Polarization selective scattering security device and method for manufacturing. *Patent application* **2007**, PCT/EP2008/001867.
- (108) Bastiaansen, C. W. M.; Meijer, T.; Vrancken, R. J. Security device with multiple authentication features. *Patent application* **2007**, PCT/EP2008/001924.
- (109) Meijer, T. Optical properties of inkjet printed and micro-transfer printed structures of reactive mesogens. M.Sc. thesis, Eindhoven University of Technology, 2006.
- (110) Sanchez, C.; Bastiaansen, C. W. M.; Broer, D. J.; Verbakel, F. Microstructuring of Mesogens Using Contact Printing.
- (111) Prinsen, P.; van der Schoot, P. Shape and director-field transformation of tactoids. *Physical Review E* **2003**, *68*.
- (112) DeGennes, P. G.; Prost, J. *The Physics of Liquid Crystals*; 2nd ed.; Oxford University Press, USA, 1995.
- (113) Hermans, K. Luminescent solar concentrator based on the alignment of fluorescent dye in liquid crystals. M.Sc. thesis, Eindhoven University of Technology, 2004.
- (114) Frank, F. C. I. Liquid crystals. On the theory of liquid crystals. *Discuss. Faraday Soc.* **1958**, *25*, 19–28.
- (115) Oseen, C. W. The theory of liquid crystals. *Transactions of the Faraday Society* **1933**, *29*, 883.
- (116) Rapini, A.; Papoular, M. Distorsion d'une lamelle nématique sous champ magnétique conditions d'ancrage aux parois. *Le Journal de Physique Colloques* **1969**, *30*, 3.
- (117) Hikmet, R. A. M.; Zwerver, B. H.; Broer, D. J. Anisotropic polymerization shrinkage behaviour of liquid-crystalline diacrylates. *Polymer* **1992**, *33*, 89–95.
- (118) *Liquid Crystals In Complex Geometries: Formed by Polymer And Porous Networks*; Crawford, G. P.; Zumer, S., Eds.; 1st ed.; Taylor & Francis, 1996.
- (119) Yeh, P.; Gu, C. *Optics of Liquid Crystal Displays*; 1st ed.; Wiley-Interscience, 1999.
- (120) Quéré, D. Non-sticking drops. *Reports on Progress in Physics* **2005**, *68*, 2495–2532.
- (121) Quéré, D. Rough ideas on wetting. *Physica A: Statistical Mechanics and its Applications* **2002**, *313*, 32–46.
- (122) Xia, F.; Zhu, Y.; Feng, L.; Jiang, L. Smart responsive surfaces switching reversibly between super-hydrophobicity and super-hydrophilicity. *Soft Matter* **2008**, *5*, 275–281.
- (123) Kusumaatmaja, H.; Blow, M. L.; Dupuis, A.; Yeomans, J. M. The collapse transition on superhydrophobic surfaces. *EPL (Europhysics Letters)* **2008**, *81*, 36003.
- (124) Ishino, C.; Okumura, K.; Quéré, D. Wetting transitions on rough surfaces. *Europhysics Letters (EPL)* **2004**, *68*, 419–425.

- (125) Krupenkin, T. N.; Taylor, J. A.; Wang, E. N.; Kolodner, P.; Hodes, M.; Salamon, T. R. Reversible Wetting–Dewetting Transitions on Electrically Tunable Superhydrophobic Nanostructured Surfaces. *Langmuir* **2007**, *23*, 9128–9133.
- (126) Liu, C.-X.; Park, J.; Choi, J.-W. A planar lens based on the electrowetting of two immiscible liquids. *Journal of Micromechanics and Microengineering* **2008**, *18*, 035023.
- (127) Brassard, D.; Malic, L.; Normandin, F.; Tabrizian, M.; Veres, T. Water-oil core-shell droplets for electrowetting-based digital microfluidic devices. *Lab Chip* **2008**, *8*, 1342–1349.
- (128) Hayes, R. A.; Feenstra, B. J. Video-speed electronic paper based on electrowetting. *Nature* **2003**, *425*, 383–385.
- (129) Mugele, F.; Klingner, A.; Buehrle, J.; Steinhäuser, D.; Herminghaus, S. Electrowetting: a convenient way to switchable wettability patterns. *Journal of Physics: Condensed Matter* **2005**, *17*, S559–S576.
- (130) Mugele, F.; Baret, J.-C. Electrowetting: from basics to applications. *Journal of Physics: Condensed Matter* **2005**, *17*, R705–R774.
- (131) Bahadur, V.; Garimella, S. V. Electrowetting-Based Control of Droplet Transition and Morphology on Artificially Microstructured Surfaces. *Langmuir* **2008**, *24*, 8338–8345.
- (132) Verplanck, N.; Galopin, E.; Camart, J.-C.; Thomy, V.; Coffinier, Y.; Boukherroub, R. Reversible Electrowetting on Superhydrophobic Silicon Nanowires. *Nano Lett.* **2007**, *7*, 813–817.
- (133) Vrancken, R. J.; Kusumaatmaja, H.; Hermans, K.; Prenen, A. M.; Pierre-Louis, O.; Bastiaansen, C. W. M.; Broer, D. J. Fully Reversible Transition from Wenzel to Cassie–Baxter States on Corrugated Superhydrophobic Surfaces. *Langmuir* **2009**, *26*, 3335–3341.
- (134) Vrancken, R. J. Supporting Information Movies belonging to article, showing uplifting transition 3D Lattice Boltzmann model and real-time microscopy results <http://pubs.acs.org/doi/abs/10.1021/la903091s>.
- (135) Xia, Y.; Whitesides, G. M. Soft Lithography. *Angewandte Chemie International Edition* **1998**, *37*, 550–575.
- (136) Priest, C.; Albrecht, T. W. J.; Sedev, R.; Ralston, J. Asymmetric Wetting Hysteresis on Hydrophobic Microstructured Surfaces. *Langmuir* **2009**, *25*, 5655–5660.
- (137) Schäfle, C.; Brinkmann, M.; Bechinger, C.; Leiderer, P.; Lipowsky, R. Morphological Wetting Transitions at Ring-Shaped Surface Domains. *Langmuir* **2010**, *26*, 11878–11885.

- (138) Furuta, T.; Sakai, M.; Isobe, T.; Matsushita, S.; Nakajima, A. Sliding of Water Droplets on Hydrophobic Surfaces with Various Hydrophilic Region Sizes. *Langmuir* **2011**, *27*, 7307–7313.
- (139) Dorrer, C.; R uhe, J. Advancing and Receding Motion of Droplets on Ultrahydrophobic Post Surfaces. *Langmuir* **2006**, *22*, 7652–7657.
- (140) Wang, X.-P.; Qian, T.; Sheng, P. Moving contact line on chemically patterned surfaces. *Journal of Fluid Mechanics* **2008**, *605*.
- (141) McHale, G.; Shirtcliffe, N. J.; Aqil, S.; Perry, C. C.; Newton, M. I. Topography Driven Spreading. *Phys. Rev. Lett.* **2004**, *93*, 036102.
- (142) Ishino, C.; Reyssat, M.; Reyssat, E.; Okumura, K.; Qu er e, D. Wicking within forests of micropillars. *Europhysics Letters (EPL)* **2007**, *79*, 56005.
- (143) Mickel, W.; Joly, L.; Biben, T. Transport, phase transitions, and wetting in micro/nanochannels: A phase field/DDFT approach. *The Journal of Chemical Physics* **2011**, *134*, 094105–094105–14.
- (144) Ledesma-Aguilar, R.; Nistal, R.; Hern andez-Machado, A.; Pagonabarraga, I. Controlled drop emission by wetting properties in driven liquid filaments. *Nat Mater* **2011**, *10*, 367–371.
- (145) Alexeev, A.; Verberg, R.; Balazs, A. C. Patterned Surfaces Segregate Compliant Microcapsules. *Langmuir* **2007**, *23*, 983–987.
- (146) Usta, O. B.; Alexeev, A.; Balazs, A. C. Fork in the Road: Patterned Surfaces Direct Microcapsules to Make a Decision. *Langmuir* **2007**, *23*, 10887–10890.
- (147) Kusumaatmaja, H.; Pooley, C. M.; Girardo, S.; Pisignano, D.; Yeomans, J. M. Capillary filling in patterned channels. *Phys. Rev. E* **2008**, *77*, 067301.
- (148) Kusumaatmaja, H.; Yeomans, J. M. Anisotropic hysteresis on ratcheted superhydrophobic surfaces. *Soft Matter* **2009**, *5*, 2704–2707.
- (149) Chu, K.-H.; Xiao, R.; Wang, E. N. Uni-directional liquid spreading on asymmetric nanostructured surfaces. *Nat Mater* **2010**, *9*, 413–417.
- (150) Barahman, M.; Lyons, A. M. Ratchetlike Slip Angle Anisotropy on Printed Superhydrophobic Surfaces. *Langmuir* **2011**, *27*, 9902–9909.
- (151) Roach, P.; Shirtcliffe, N. J.; Newton, M. I. Progress in superhydrophobic surface development. *Soft Matter* **2007**, *4*, 224–240.
- (152) Nosonovsky, M.; Bhushan, B. Hierarchical roughness makes superhydrophobic states stable. *Microelectronic Engineering* **2007**, *84*, 382–386.
- (153) Courbin, L.; Denieul, E.; Dressaire, E.; Roper, M.; Ajdari, A.; Stone, H. A. Imbibition by polygonal spreading on microdecorated surfaces. *Nat Mater* **2007**, *6*, 661–664.

- (154) Blow, M. L.; Kusumaatmaja, H.; Yeomans, J. M. Imbibition through an array of triangular posts. *Journal of Physics: Condensed Matter* **2009**, *21*, 464125.
- (155) Blow, M. L.; Yeomans, J. M. Anisotropic imbibition on surfaces patterned with polygonal posts. *Philosophical Transactions of the Royal Society A: Mathematical, Physical and Engineering Sciences* **2011**, *369*, 2519–2527.
- (156) Tekin, E.; Smith, P. J.; Schubert, U. S. Inkjet printing as a deposition and patterning tool for polymers and inorganic particles. *Soft Matter* **2008**, *4*, 703.
- (157) Derby, B. Inkjet Printing of Functional and Structural Materials: Fluid Property Requirements, Feature Stability, and Resolution. *Annual Review of Materials Research* **2010**, *40*, 395–414.
- (158) Calvert, P. Inkjet Printing for Materials and Devices. *Chemistry of Materials* **2001**, *13*, 3299–3305.
- (159) Vrancken, R. J. Geometry of micro-transfer printed polymerized mesogen structures. M.Sc. thesis, Eindhoven University of Technology: Eindhoven, 2006.
- (160) Gross, M.; Varnik, F.; Raabe, D. Fall and rise of small droplets on rough hydrophobic substrates. *EPL (Europhysics Letters)* **2009**, *88*, 26002.
- (161) Sbragaglia, M.; Peters, A. M.; Pirat, C.; Borkent, B. M.; Lammertink, R. G. H.; Wessling, M.; Lohse, D. Spontaneous Breakdown of Superhydrophobicity. *Phys. Rev. Lett.* **2007**, *99*, 156001.
- (162) *Simulating Complex Systems by Cellular Automata*, Hoekstra, A. G.; Kroc, J.; Sloot, P. M. A., Eds.; 1st ed.; Springer, 2010.
- (163) Zhang, J. Lattice Boltzmann method for microfluidics: models and applications. *Microfluidics and Nanofluidics* **2010**, *10*, 1–28.
- (164) Lee, T.; Lin, C.-L. A stable discretization of the lattice Boltzmann equation for simulation of incompressible two-phase flows at high density ratio. *Journal of Computational Physics* **2005**, *206*, 16–47.
- (165) Shan, X.; Chen, H. Simulation of nonideal gases and liquid-gas phase transitions by the lattice Boltzmann equation. *Phys. Rev. E* **1994**, *49*, 2941–2948.
- (166) Prenen, A. M. Polymeric microfilters by interference holography: development and applications. Ph. D. thesis, Eindhoven University of Technology, 2009.
- (167) Marmur, A. From Hydrophilic to Superhydrophobic: Theoretical Conditions for Making High-Contact-Angle Surfaces from Low-Contact-Angle Materials. *Langmuir* **2008**, *24*, 7573–7579.
- (168) Tsujii, K.; Yamamoto, T.; Onda, T.; Shibuichi, S. Super Oil-Repellent Surfaces. *Angewandte Chemie International Edition in English* **1997**, *36*, 1011–1012.

- (169) Shibuichi, S.; Yamamoto, T.; Onda, T.; Tsujii, K. Super Water- and Oil-Repellent Surfaces Resulting from Fractal Structure. *Journal of Colloid and Interface Science* **1998**, *208*, 287–294.
- (170) Li, H.; Wang, X.; Song, Y.; Liu, Y.; Li, Q.; Jiang, L.; Zhu, D. Super-“Amphiphobic” Aligned Carbon Nanotube Films. *Angewandte Chemie International Edition* **2001**, *40*, 1743–1746.
- (171) Nicolas, M.; Guittard, F.; G ribaldi, S. Synthesis of Stable Super Water- and Oil-Repellent Polythiophene Films. *Angewandte Chemie International Edition* **2006**, *45*, 2251–2254.
- (172) Hoefnagels, H. F.; Wu, D.; de With, G.; Ming, W. Biomimetic Superhydrophobic and Highly Oleophobic Cotton Textiles. *Langmuir* **2007**, *23*, 13158–13163.
- (173) Ahuja, A.; Taylor, J. A.; Lifton, V.; Sidorenko, A. A.; Salamon, T. R.; Lobaton, E. J.; Kolodner, P.; Krupenkin, T. N. Nanonails: A Simple Geometrical Approach to Electrically Tunable Superlyophobic Surfaces. *Langmuir* **2007**, *24*, 9–14.
- (174) Cao, L.; Price, T. P.; Weiss, M.; Gao, D. Super Water- and Oil-Repellent Surfaces on Intrinsically Hydrophilic and Oleophilic Porous Silicon Films. *Langmuir* **2008**, *24*, 1640–1643.
- (175) Zimmermann, J.; Rabe, M.; Artus, G. R. J.; Seeger, S. Patterned superfunctional surfaces based on a silicone nanofilament coating. *Soft Matter* **2008**, *4*, 450–452.
- (176) Steele, A.; Bayer, I.; Loth, E. Inherently Superoleophobic Nanocomposite Coatings by Spray Atomization. *Nano Lett.* **2008**, *9*, 501–505.
- (177) Leng, B.; Shao, Z.; de With, G.; Ming, W. Superoleophobic Cotton Textiles. *Langmuir* **2009**, *25*, 2456–2460.
- (178) Tuteja, A.; Choi, W.; Mabry, J. M.; McKinley, G. H.; Cohen, R. E. Robust omniphobic surfaces. *Proceedings of the National Academy of Sciences* **2008**, *105*, 18200 – 18205.
- (179) Tuteja, A.; Choi, W.; McKinley, G. H.; Cohen, R. E.; Rubner, M. F. Design Parameters for Superhydrophobicity and Superoleophobicity. *MRS Bulletin* **2008**, *33*, 752–758.
- (180) Feng, X. J.; Jiang, L. Design and Creation of Superwetting/Antiwetting Surfaces. *Advanced Materials* **2006**, *18*, 3063–3078.
- (181) Sun, T.; Feng, L.; Gao, X.; Jiang, L. Bioinspired Surfaces with Special Wettability. *Acc. Chem. Res.* **2005**, *38*, 644–652.
- (182) Wu, D.; Vrancken, R. J.; Loenen, van, B. G. H.; Benthem, R. van; With, de, G.; Ming, W. Lipophobicity on Hierarchically Structured Superhydrophobic Surfaces. *Polym. Mater. Sci. Eng.* **2007**, *97*, 418–419.
- (183) Cassie, A. B. D. Contact angles. *Discuss. Faraday Soc.* **1948**, *3*, 11–16.

- (184) Bormashenko, E.; Stein, T.; Whyman, G.; Bormashenko, Y.; Pogreb, R. Wetting Properties of the Multiscaled Nanostructured Polymer and Metallic Superhydrophobic Surfaces. *Langmuir* **2006**, *22*, 9982–9985.
- (185) Marmur, A. Wetting on Hydrophobic Rough Surfaces: To Be Heterogeneous or Not To Be? *Langmuir* **2003**, *19*, 8343–8348.
- (186) Ming, W.; Leng, B.; Hoefnagels, H. F.; Wu, D.; With, de, G.; Shao, Z. Toward superlyophobic surfaces. In: Contact Angle, Wettability, and Adhesion; Koninklijke Brill NV: Leiden, 2009; Vol. 6, pp. 191–206.
- (187) Leng, B. Bioinspired morphology control – the function of several biomolecules in mineralization and the design of superhydrophobic/superoleophobic surfaces. Ph. D. thesis, Fudan University: Shanghai, 2009.
- (188) Yasuda, T.; Okuno, T.; Yasuda, H. Contact Angle of Water on Polymer Surfaces. *Langmuir* **1994**, *10*, 2435–2439.
- (189) Neumann, A. W. Contact angles and their temperature dependence: thermodynamic status, measurement, interpretation and application. *Advances in Colloid and Interface Science* **1974**, *4*, 105–191.
- (190) Holmes-Farley, S. R.; Bain, C. D.; Whitesides, G. M. Wetting of functionalized polyethylene film having ionizable organic acids and bases at the polymer-water interface: relations between functional group polarity, extent of ionization, and contact angle with water. *Langmuir* **1988**, *4*, 921–937.
- (191) Lafuma, A.; Quere, D. Superhydrophobic states. *Nat Mater* **2003**, *2*, 457–460.
- (192) Mognetti, B. M.; Yeomans, J. M. Capillary filling in microchannels patterned by posts. *Phys. Rev. E* **2009**, *80*, 056309.
- (193) Mognetti, B. M.; Yeomans, J. M. Using electrowetting to control interface motion in patterned microchannels. *Soft Matter* **2010**, *6*, 2400–2402.
- (194) Noh, J. H.; Noh, J.; Kreit, E.; Heikenfeld, J.; Rack, P. D. Toward active-matrix lab-on-a-chip: programmable electrofluidic control enabled by arrayed oxide thin film transistors. *Lab on a Chip* **2012**, *12*, 353.
- (195) Kreit, E.; Mognetti, B. M.; Yeomans, J. M.; Heikenfeld, J. Partial-post laplace barriers for virtual confinement, stable displacement, and >5 cm s⁻¹ electrowetting transport. *Lab on a Chip* **2011**, *11*, 4221.
- (196) Kreit, E.; Dhindsa, M.; Yang, S.; Hagedon, M.; Zhou, K.; Papautsky, I.; Heikenfeld, J. Laplace Barriers for Electrowetting Thresholding and Virtual Fluid Confinement. *Langmuir* **2010**, *26*, 18550–18556.
- (197) Vrancken, R. J.; Bastiaansen, C. W. M.; Broer, D. J.; Ming, W.; With, de, G. The effects of size ratio, pressure and defects on the wetting state transitions and

- stability of raspberry-like dual-scale structured lyophobic surfaces. *In preparation* **2012**.
- (198) Leng, B.; Vrancken, R. J.; With, de, G.; Ming, W. Experiments and comparison to Gibbs energy model of a triple-scale structured superhydrophobic surface. *In preparation* **2012**.
- (199) Eggers, J.; Lister, J. R.; Stone, H. A. Coalescence of Liquid Drops. *Journal of Fluid Mechanics* **1999**, *401*, 293–310.
- (200) Menchaca-Rocha, A.; Martínez-Dávalos, A.; Núñez, R.; Popinet, S.; Zaleski, S. Coalescence of liquid drops by surface tension. *Phys. Rev. E* **2001**, *63*, 046309.
- (201) Narhe, R.; Beysens, D.; Nikolayev, V. S. Contact Line Dynamics in Drop Coalescence and Spreading. *Langmuir* **2004**, *20*, 1213–1221.
- (202) Narhe, R. D.; Beysens, D. A.; Pomeau, Y. Dynamic drying in the early-stage coalescence of droplets sitting on a plate. *EPL (Europhysics Letters)* **2008**, *81*, 46002.
- (203) Paulsen, J. D.; Burton, J. C.; Nagel, S. R. Viscous to Inertial Crossover in Liquid Drop Coalescence. *Phys. Rev. Lett.* **2011**, *106*, 114501.
- (204) Ristenpart, W. D.; McCalla, P. M.; Roy, R. V.; Stone, H. A. Coalescence of Spreading Droplets on a Wettable Substrate. *Phys. Rev. Lett.* **2006**, *97*, 064501.
- (205) Sellier, M.; Trelluyer, E. Modeling the coalescence of sessile droplets. *Biomicrofluidics* **2009**, *3*, 022412–022412–14.
- (206) Tanner, L. H. The spreading of silicone oil drops on horizontal surfaces. *Journal of Physics D: Applied Physics* **1979**, *12*, 1473–1484.
- (207) Horsten, F. Coalescence induced mixing of ink jetted drops. B.Sc. Thesis, Fontys Applied University of Technology: Eindhoven, 2007.
- (208) Dongen, M., van; Vrancken, R. J.; Horsten, F.; Ketelaars, P. H. J. M.; Bernards, J. UV-mediated coalescence and mixing of inkjet printed drops. *In preparation* **2012**.
- (209) Deegan, R. D.; Bakajin, O.; Dupont, T. F. Capillary flow as the cause of ring stains from dried liquid drops. *Nature* **1997**, *389*, 827–829.
- (210) Liu, D.; Vrancken, R. J.; Perelaer, J.; Schubert, U. S.; Broer, D. J.; Toonder, J. Coffee rings in a three-component inkjet printed drop with binder, solvent and magnetic nanoparticles. *In preparation* **2012**.
- (211) Capolino, F. *Metamaterials Handbook - Two Volume Slipcase Set: Theory and Phenomena of Metamaterials*; 1st ed.; CRC Press, 2009.

Appendix B: Nederlandse samenvatting

Het beïnvloeden van druppelvormen: theorie, experimenten en toepassingen in printing, zelf-reinigende lakken en microscopische vloeistof systemen

Nauwkeurig controle over de vorm van druppels die geplaatst worden op een vast oppervlak, is belangrijk voor veel toepassingen zoals het (inkjet) printen van functionele materialen, microscopische vloeistof systemen of intelligente lakken. In dit proefschrift wordt aangetoond dat er een grote variatie aan verschillende druppelvormen kan worden verkregen door het zorgvuldig patroneren van deze oppervlakken op micrometer lengteschalen, gecombineerd met de gecontroleerde plaatsing van de druppels. Dit geldt zowel voor isotrope als vloeibaar kristallijne vloeistoffen.

De druppelvorm wordt grotendeels bepaald door thermodynamische vergelijkingen. De relevante energetische termen van deze vergelijkingen zijn geïdentificeerd voor de verschillende lengteschalen van de druppels en de microstructuren op het oppervlak. Voor niet-vloeibaar kristallijne vloeistoffen zijn dit respectievelijk de potentiële energie van de zwaartekracht, de diverse oppervlakte energieën en de contactlijnenergie. Om de gevolgen van de diverse patroneringen te onderzoeken, is gekozen om te kijken naar druppels van kleiner dan 1 mm in doorsnede. Een combinatie van experimenten, numeriek modelleren en theoretische analyse wordt gebruikt om de vaak verrassende druppelvormen en tevens de invloed van de methode van aanbrengen van de druppels te onderzoeken.

Op oppervlakken gepatroneerd met parallelle groeven wordt de druppelvorm uitgerekte parallel aan de groeven, indien de druppel wordt aangebracht met behulp van een non-contact printmethode, zoals inkjet printen of zorgvuldig aanbrengen met behulp van een (injectie-)naald. Als de druppels echter worden aangebracht in een (in eerste instantie) uitgesmeerde vorm, bijvoorbeeld als ze op het oppervlak worden gedrukt door een contact-print methode zoals *micro-transfer printing*, dan is de uiteindelijke druppelvorm juist uitgerekte loodrecht op de groeven. Dit verschil wordt veroorzaakt doordat er vrijwel geen druppelvormhysterese is als gevolg van *pinning* van de contactlijn parallel aan de groeven en juist zeer sterke hysterese loodrecht op de groeven.

Als nematische thermotrope vloeibare kristallen worden aangebracht op parallel gegroefde oppervlakken door middel van *micro-transfer printing*, dan zijn de verkregen druppelvormen wederom uitgerekte in de richting loodrecht op de groeven. De mate van langgerektheid is zeer vergelijkbaar met die van niet-vloeibaar kristallijne materialen geprint onder vergelijkbare experimentele condities. Dit ondanks het feit dat de additionele energie, geassocieerd met de uitlijning van de vloeibare kristallen (in de bulk en aan het oppervlakte

van de druppel), lager is voor parallel uitgerekte druppels.

In dit proefschrift wordt voor het eerst een nieuwe en zeer praktische methode experimenteel aangetoond om waterdruppels een transitie te laten maken tussen twee belangrijke toestanden van oppervlaktebenutting. Dit zijn de volledig benutte ('Wenzel'-) toestand en een toestand waarbij de druppel deels 'zweeft' op de gasfase die zich tussen de uitstekende vaste delen van het oppervlak bevindt ('Cassie-Baxter'-toestand). De nieuwe transitie is van de Wenzel- naar de Cassie-Baxter- toestand. De omgekeerde transitie is al bekend uit de literatuur en veel eenvoudiger te realiseren. Bij de nieuwe methode wordt gebruik gemaakt van gegroefde oppervlakken en tevens wordt de intrinsieke contacthoek met behulp van een aangelegde elektrische spanning tijdelijk verlaagd. De transitie met deze methode is hier voor het eerst experimenteel aangetoond en is wezenlijk praktischer dan de enige eerder aangetoonde techniek, waarbij de druppel lokaal wordt gekookt om deze uit de groeven omhoog te laten komen. Het exacte mechanisme van de transitie is in detail onderzocht met behulp van numerieke simulaties. De analyse toont aan dat deze methode alleen onder zorgvuldig gekozen omstandigheden bruikbaar is: het is een vereiste om lokale *pinning* van de contactlijn te voorkomen, zeker als andere mogelijkheden om krachten op de contactlijn uit te oefenen, zoals mechanische vibraties, niet kunnen worden gebruikt.

Met behulp van het inkjet printen van waterdruppels zijn een aantal bijzondere druppelvormen gerealiseerd, waaronder achthoeken, zeshoeken, vierkanten en quasi-driehoekige vormen. Hiervoor wordt gebruik gemaakt van oppervlakken gepatroneerd met pilaren met afmetingen van enkele micrometers. Door deze micropilaren polygonale vormen te geven en op de juiste manier te plaatsen op een regelmatig rooster, vloeien de druppels uit in bovengenoemde bijzondere vormen. Deze anisotrope vloeit wordt veroorzaakt doordat het druppeloppervlak in verschillende richtingen anders loslaat van de pilaren als gevolg van de lokaal variërende vorm. Dit loslaten (*de-pinning*) is ook afhankelijk van het uit- of juist terugvloeien van de druppel. Door inkjet experimenten met druppels te combineren met microscopische observaties van de druppelvorm, en deze te vergelijken met numerieke simulaties, is verder inzicht verkregen in de lokale *pinning* en het loslaten van het druppeloppervlak.

Een belangrijke toepassing van zgn. intelligente lakken is het zelfreinigend maken van materialen, zoals autoruiten, textiel of scheepsrompen. Vloeistofafstotende oppervlakken zijn hier een praktisch voorbeeld van, met belangrijke industriële toepassingen. Een hiervoor geschikt oppervlak is een recent experimenteel gerealiseerd oppervlak bedekt met zogenaamde framboosvormige silicium nano-deeltjes, omhuld met vloeistofafstotend polymeer. In dit proefschrift wordt een theoretische analyse gepresenteerd van de stabiliteit van de (deels zwevende) druppeltoestand van dit nieuwe oppervlak. Door van dit soort oppervlakken alle mogelijke benuttingstoestanden en de transities hiertussen zorgvuldig te bestuderen, is meer inzicht verkregen in de benodigde randvoorwaarden om stabiele

vloeistofafstotende oppervlakken te creëren. Deze analysemethode is uitgebreid om in de toekomst andere gepatroneerde oppervlakken te kunnen analyseren op vergelijkbare wijze.

Tot slot worden een aantal mogelijke nieuwe toepassingen kort besproken in een technische beschouwing, waarbij ook nieuwe ontwikkelingen van het vakgebied worden betrokken.

Appendix C: Acknowledgements

Coming to the end of a Ph.D. project is a time of mixed feelings. On the one hand, there is a feeling of joy and accomplishment. It is an exciting time of new beginnings. On the other hand, it is also a time for some goodbyes, although by no means permanent! The list of people I would like to thank is long I know, but there you go...

My gratitude goes out to Dick, Bert and Cees, who as (co-)promoters have given me the opportunity to do this project on very short notice, and whose commitment gave me the confidence to complete the project on a very tight time-schedule. Dick, it was a pleasure finally working more closely with you, after being part of the PICT/SFD group in many roles in the past. Bert, thank you for the interesting theoretical discussions, with always a new view on the problems at hand. And of course Cees: you helped me take on many adventures and learn a great deal about science, business and most importantly remembering to have enough fun in the process. Truly, never a dull moment!

Also, I'm indebted to my committee members: Julia Yeomans, Marshall Ming, Eric Nies, Catarina Esteves and Emiel Hensen. Your quick responses and insightful comments to the thesis have been a great help in the process. I look forward to defending my work to you.

I have had the pleasure to work with many scientific collaborators, without whom my research would never have gotten far. Halim, it was great visiting Oxford and discussing science with you on many occasions. The first microscopy observation of the predicted Wenzel-to-Cassie transition was really a high-five moment for us, even though you were on the other side of the Channel. Your inquisitive nature and critical thinking together with your kindness and sincerity will undoubtedly help you to achieve great things in your scientific career. Marshall, it was a serendipitous meeting that set us on a path to try and model your very interesting raspberry structures. Through many changes and relocations it was always great to be back in touch and the energy never left, even through some inevitable delays. My best to you and your family! Bart, after a long time, it is about time to present the model which you have worked on with great efforts a few years ago. Without you, we could not have gotten to this point. Matthew, thank you for letting me join you in your research on polygonal posts. Matching experiments with theory is a challenging task and your insights into (de-)pinning mechanisms have really expanded my understanding of these phenomena on a fundamental level. After meeting with you, Julia, at a modelling conference in Amsterdam, it was great to hear that you were enthusiastic to start collaborations with your group. The numerical models that are being developed in your group have made all the difference in understanding the myriad of drop behaviours, and your commitment to my research felt as a one long sustained compliment.

Ko and An, thank you for your help in preparing those crucial lithographic samples.

Olivier, your theoretical input on the transition paper helped to comprehend and trust the numerical model results, before daring to go for the experimental confirmation. Jolke, for many afternoon experiments, discussions and coffees. Danqing and Jaap, for starting with me in a nice side-project on the coffee-drop effect. I'm confident that the exciting results so far will lead to a nice publication. Martijn, Peter and Jan, whom I've worked successfully before in a different role and who have helped me continue as part of the RAAK-PRO community. Thank you all for the support over the years and best of luck in completing your own thesis Martijn. I trust the manuscript will coalesce into a nice publication soon. Catarina and Camille, with whom I hope to validate my models on a new and exciting nano-particle surface. Lastly, I had many great discussions early on with Paul van der Schoot, who helped me whenever I was in a tight spot, and who pointed me towards this interesting field at the start of the project. Paul, even though you may not know this, but without you all this may never have happened.

Over the years I was fortunate to work with and (co-)supervise scientific projects from a number of students: Frank, Kenny, Xiao, TingTing, Rene and Gerold. Not all your work is part of this thesis, nor was it intended to be. But I learned a lot from our projects and I hope to have helped you as you helped me.

During these last years I was lucky to be part of no less than three research groups at TU/e: SFD (formerly PICT), SMG and SKT. I always felt at home and welcome in your communities. At the risk of forgetting anyone dear, my best goes to Casper, Teun, Joost, Paul 'the Limburg connection', Mike, Debarshi, Camille 'Baracuda', Nicole, Yang, Albert, Ineke, Elly, Imanda, Jelle, Tamara, Jules, Marjolijn, Marjolein, Ties, Mian, Amol 'C-C bond', Jos, Piet, Pauline, Natalia, Irén, Xiaoran, Laurens, Ivelina, My, Peter, Patrick, Stephanie, Shufen, Antonio, Tom, Chris, Blanca and of course Bob 'Margaret' the thatcher.

To my paranymphs and 'partners in crime', Nico and Thijs: you were always there for me, in our many adventures, challenges and successes. Being part of such a good team was more than I could have hoped for. Now it is time for new adventures, which we will experience together and also on our own. But first you're there to see me through the defence and afterwards celebrate as only 'those crazy guys from Validus' can.

At Validus I had the opportunity to work together with a number of very talented and smart people, who helped me grow as a scientist and engineer but also in many other respects. Completing this Ph.D. is definitely also a result of the great time I had working with all of you. Ewald, our brainstormings were always very insightful and your level-headed approach to problem solving is inspiring. I'm going to miss working together, and of course your famous coffee. Mariette, your intuition for business development and marketing, and your warm touch in forming our team made a lasting impression (and clearly not only on me!). Charles, you really became the nestor of the team, and I consider you, your energy and good humour after such a long and distinguished career, as an example to live by. Pit, for

being one step ahead of any problem on so many occasions, as well as being such an all-round nice person to work with. I'm also indebted to Anke, Dirk-Jan, Thijs, Mark ('Marky Mark'), Kasia and Vincent for all their efforts and enthusiasm. I also had the benefit to learn a great deal from my investors, advisors, business partners, research consortium members, suppliers, bankers, lawyers, business school classmates, fellow entrepreneurs, accountants and customers, many of whom in confidence and privacy. Thank you all, you know who you are...

Working together with the professionals of Océ Technologies, I learned that putting one drop in its proper place (with the right morphology of course), is neither the beginning nor the end of the story. Many steps along the way from the lab to commercial production benefitted from the insights and support from Marcel, Hylke, Jev, Eelco, Eric, Karel, Wilbert, Daan, Mircea and many others. You helped me gain engineering and project management experience by setting an example of professionalism to strive for.

At the end of the day, what meaning does life have without sharing and enjoying the time one has together with family and friends? It is always a struggle to work on all these exciting things I've been involved with, while trying to keep in touch and do justice to your friendship and love: my best to everyone from Daedalus, Perspectief, Natuurkunst, Bernardinus, Freya, Astrid and Mike, Maaïke and Michiel, Arnoud and Linda, Alexander and Danielle and everyone I woefully forgot. Everyone in the Baecke family, Louis, José, Sergio, Nancy, Emma, Jens, Ankie, Johan, Niels and course little Britt. Jeanette, zonder jouw steun en liefde vanaf de eerste dag was dit alles mij nooit gegund. Petra and Marjolein, André and Steffi, to many wonderful days ahead. And finally Elleke, who came into my life at a time of hard work and change, and stayed with me ever since. For your love, kindness, sense of humour, support and trust, I'm forever grateful.

– Robert Vrancken, Eindhoven, April 2012

Appendix D: Curriculum Vitae

Robert Vrancken was born on the 21st of August 1981 in Heerlen, The Netherlands. After graduating as class valedictorian in secondary school ('Gymnasium') at Bernardinuscollege (Heerlen) in 1999, he studied Applied Physics at Eindhoven University of Technology (TU/e) where he received his first year degree ('propedeuse') *cum laude*. During his studies, Robert was active as Treasurer of the Student Physics Society "Johannes Diderik van der Waals" in 2001-2002 on a full-year scholarship. After that, he was Fundraising Manager for the Natuurkunst Foundation in 2002-2004. He raised over 400.000€ with his team for an artwork by Dutch artist Alex Vermeulen, which was erected on the university campus. Besides this, Robert was a board member of the Applied Physics division of the Royal Dutch Institute of Engineers (KIVI NIRIA).



After completing an internship on dusty plasmas and publishing an article on this work (2003-2004), he completed an international internship on high vapour pressure plasma deposition of organo-metallic precursors at the Colorado School of Mines under the guidance of Prof. Colin Wolden and Prof. Richard van de Sanden (2005).

He received his Masters degree in Applied Physics in 2006 for his thesis titled 'Geometry of micro-transfer printed polymerised mesogens structures' under the guidance of Prof. Cees Bastiaansen at the department of Chemical engineering and Chemistry. Concurrent with his graduation, Robert co-founded Validus Technologies B.V. as a spin-off of the research of his graduation project and became its Chief Technology Officer (2007-2011). After winning several national and international business plan competitions, as part of the management team of Validus he raised over 2.000.000€ in two rounds of venture capital, bank loans and government grants and completed the development of the technology with his team, culminating in two successful pilots.

In 2010 he obtained the executive Master of Business Innovation degree at TiasNimbas Business School. In 2011 he started a Ph.D. project at the department of Chemical Engineering and Chemistry under the guidance of Prof. Dick Broer, Prof. Bert de With and Prof. Cees Bastiaansen. The results of this work are described in this thesis.

Appendix E: List of publications and patents

Publications related to this work

M. A. H. van Dongen, R. Vrancken, F. Horsten, P. Ketelaars, J. Bernards, *UV-mediated coalescence and mixing of inkjet printed drops*, in preparation (2012)

D. Liu, R. J. Vrancken, J. Perelaer, U. S. Schubert, D. J. Broer, J. den Toonder, *Coffee ring effect of a three-component inkjet printed drop with binder, solvent and magnetic nanoparticles*, in preparation (2012)

R. J. Vrancken, W. Ming, C. W. M. Bastiaansen, D. J. Broer, G. de With, *Causes of decreased stability of lyophobic wetting states on dual-scale structured superhydrophobic surfaces*, in preparation (2012)

R. J. Vrancken, M. Blow, H. Kusumaatmaja, K. Hermans, A. M. Prenen, C. W. M. Bastiaansen, D. J. Broer, J. Yeomans, *Anisotropic wetting and de-wetting of drops on substrates patterned with polygonal posts*, in preparation (2012)

R. J. Vrancken, B. G. H. van Loenen, G. de With, W. Ming, *Gibbs Energy Analysis of Meta-Stability of Wetting States On Dual-Scale Structured Superhydrophobic Surfaces*, in preparation (2012)

R. J. Vrancken, H. Kusumaatmaja, K. Hermans, A. M. Prenen, O. Pierre-Louis, C. W. M. Bastiaansen and D. J. Broer, *Fully Reversible Transition from Wenzel to Cassie–Baxter States on Corrugated Superhydrophobic Surfaces*, *Langmuir*, 26 (5), 3335–3341, (2010)

M. E. Koekoek, T. Meijer, R. J. Vrancken, *Digital printing of multilevel optical variable Devices for Document Security & Brand Protection*, Proceedings of the Optical Document Conference II, 357-367, San Francisco, United States (2010)

H. Kusumaatmaja, R. J. Vrancken, C. W. M. Bastiaansen and J. M. Yeomans, *Anisotropic Drop Morphologies on Corrugated Surfaces*, *Langmuir* 24, 7299 (2008)

D. Wu, R. J. Vrancken, B. G. H. van Loenen, R. A. T. M. van Benthem, G. de With, W. Ming, *Lipophobicity on Hierarchically Structured Superhydrophobic Surfaces*, *Polym. Mat. Sci. Eng.*, 97, 419 (2007)

C. W. M. Bastiaansen, T. Meijer, R. J. Vrancken, *Security device with multiple authentication features*, PCT/EP2008/001924, Applicant Eindhoven University of Technology, Priority date filing 13-3-2007

C. W. M. Bastiaansen, T. Meijer, R. J. Vrancken, *Inkjettable polymerisable liquid crystalline mixture*, PCT/EP2008/001868, Applicant Eindhoven University of Technology, Priority date filing 13-3-2007

C. W. M. Bastiaansen, T. Meijer, R. J. Vrancken, *Polarization selective scattering security device and method for manufacturing*, PCT/EP2008/001867, Applicant Eindhoven University of Technology, priority date filing 13-3-2007

W. Ming, D. Wu, R. Vrancken, B. van Loenen, R. van Benthem, G. de With, *Nature-Inspired Superhydrophobic Coatings*, Proceedings of the Smart Coatings Conference, Orlando Florida (2007)

R. Vrancken, *Geometry of micro-transfer printed polymerised mesogen structures*, Master Thesis (great distinction), Laboratory for Polymers in Advances Systems, Department of Chemical Engineering and Chemistry and Laboratory for Molecular Biosensors for Medical Diagnostics, Department of Applied Physics, Eindhoven University of Technology (2006)

Publications not related to this work

R. J. Vrancken, G. V. Paeva, G. M. W. Kroesen and W. W. Stoffels, *Dust void formation above rectangular and circular potential traps in an rf plasma*, Plasma Sources Sci. Technol. 14, 1-8, (2005)

Appendix F: List of symbols

Geometry

x	cartesian or polar coordinate
y	cartesian or polar coordinate
z	cartesian or polar coordinate
r	polar or spherical coordinate
ϕ	azimuthal angle
θ	polar angle

Thermodynamics

σ_{ij}	surface energy of the $i - j$ interface per unit surface
Ω_{ij}	surface area of the $i - j$ interface of the drop
i, j	subscripts denoting the solid, liquid or vapour phase
G	Gibbs energy
\tilde{G}	dimensionless Gibbs energy
$A(\mathbf{x})$	position dependent contact line energy

Observables of drop

δ	intrinsic contact angle (“Young contact angle”)
β	observed (apparent) contact angle
β_a	observed advancing contact angle
β_r	observed receding contact angle
β_b	hysteresis in observed contact angles
β_x, β_y	observed contact angle in (arbitrary) x, y direction
$\beta_{\parallel}, \beta_{\perp}$	observed contact angles parallel / perpendicular to corrugations
r	radius of drop at the solid surface
r_x, r_y	radius of drop in (arbitrary) x, y direction
r_{\parallel}, r_{\perp}	radius of drop parallel / perpendicular to corrugations
V	drop volume

h	drop height
e	horizontal elongation of the drop
ζ	dimensionless drop height
k	principal axis of a spherical drop

Observables of surface

R	surface roughness as defined by Wenzel
f	surface solid fraction as defined by Cassie and Baxter
f_s	solid surface fraction function
f_v	vapour surface fraction function
\tilde{z}_0	maximum surface corrugation height
χ	aspect ratio of the corrugation height versus width - conversely, groove depth versus pitch (groove spacing)

Liquid crystal thermodynamics

$\mathbf{n}(\mathbf{x})$	position dependent director field
k_1	splay elastic constant
k_2	twist elastic constant
k_3	bend elastic constant
K	elastic constant in equal constants approach
ω_j	dimensionless anchoring strength on $i - j$ interface

Lattice Boltzmann model

\mathbf{u}	local velocity
\mathbf{P}	pressure tensor
ν	kinematic viscosity
Ψ	continuum energy function
$\psi(\rho)$	bulk free energy
ρ	density
ρ_l, ρ_v	liquid / vapour density
ρ_c	critical density
p	pressure

Appendix

p_c	critical pressure
T	lattice Boltzmann temperature
T_c	critical temperature
β	numerical parameter determining density ratio between vapour and liquid (as used in lattice Boltzmann model, not to be confused with apparent contact angle)
$l.u.$	lattice units, unit of length in lattice Boltzmann model
l_0	length scale (lattice Boltzmann model)
t_0	time scale (lattice Boltzmann model)
m_0	mass scale (lattice Boltzmann model)

Hierarchical surface model parameters

r	sphere radius
η	sphere packing factor
η_n	sphere packing factor on level n
\tilde{h}	dimensionless vapour height
\tilde{h}_n	dimensionless vapour height on level n
k, l	wetting states, single ('Cassie' = 'C' or 'Wenzel' = 'W') or dual ('Wenzel-Cassie' = 'WC', etc.)
$\tilde{B}_{k \rightarrow l}$	dimensionless energy barrier to transition from state k to l
$\Delta\tilde{G}_{k \rightarrow l}$	dimensionless energy barrier between state k compared to l
$\delta_{k \rightarrow l}^*$	Intrinsic contact angle at which $\tilde{B}_{k \rightarrow l} = \Delta\tilde{G}_{k \rightarrow l}$
$\delta_{k=l}^*$	Intrinsic contact angle at which $\Delta\tilde{G}_{k \rightarrow l} = 0$